IS-T-1845

Optical and Magneto-optical Properties of Single Crystals of RFe*2* (R=Gd, Tb, Ho, and Lu) and GdCo*2* Intermetallic Compounds

by

Lee, Seong-Jae

PHD Thesis submitted to Iowa State University

Ames Laboratory, U.S. DOE

Iowa State University

Ames, Iowa 50011

Date Transmitted: February 12, 1999

PREPARED FOR THE U.S. DEPARTMENT OF ENERGY

UNDER CONTRACT NO. W-7405-Eng-82.

DISCLAIMER

TABLE OF CONTENTS

LIST OF FIGURES

ACKNOWLEDGEMENTS

First of all, I would like to express my sincere thanks to my advisor, Prof. David W. Lynch, for his excellent guidance, fruitful discussions, and a critical reading of my dissertation. Without his support, I could not have accomplished this thesis. I also extend my appreciation to my co-advisor Prof. Paul Canfield for useful discussions and guidance in sample growing. I wish to express my thanks to Prof. Bruce N. Harmon for the valuable discussions about my project and computer programming.

Special thanks go to Prof. Karl A. Gschneidner and Prof. Kenneth E. Lassila, my committee members, and Prof. Constantine Stassis, my former advisor, for their help and encouragement. I am also indebted to Dr. Stefan Zollner, Dr. Zai Chen, Dr. Xindong Wang, Dr. V. P. Antropov, and Dr. L. L. Miller for their useful theoretical and experimental discussions. I am also appreciative of Prof. Joo-Yull Rhee, Prof. Sa-Yong Hong, and Prof. Kwang-Joo Kim for their help and useful discussions during their visits to the Ames Laboratory. I especially thank my colleagues and friends, Mr. Rüdiger Lange and Mr. Tyson Hoffmann for the useful discussions on the magneto-optics projects.

I am deeply appreciative to my parents and parents-in-law for their caring and encouragement. I also would like to thank my wife, Sung-Hye yoon Lee and my daughter, Sharon Lee. My wife has been very supportive and encouraging throughout my Ph.D. work.

This work was performed at Ames Laboratory under Contract No. W-7405-Eng-82 with the U.S. Department of Energy (DOE). The United States government has assigned

the DOE Report number IS-T 1845 to this thesis.

ABSTRACT

We have studied the diagonal and off-diagonal optical conductivity of RFe_2(R=Gd, Tb, Ho, Lu) and $GdCo_2$ single crystals grown by the flux method. Using spectroscopic ellipsometry we have measured the dielectric function from 1.5 to 5.5 eV. The magneto-optical parameters (Kerr rotation and ellipticity) were obtained using a magneto-optical Kerr spectrometer at temperatures between 7 and 295 K and applied magnetic fields between 0.5 to 1.6 T. The apparatus and calibration method are described in detail. Using magneto-optical data and optical constants we derive the experimental value of the off-diagonal conductivity components. Theoretical calculations of optical conductivities and magneto-optical parameters were performed using the tight binding-linear muffin tin orbitals method within the local spin density approximation. We applied this TB-LMTO method to $LuFe_2$. The theoretical results obtained agree well with the experimental data. The oxidation effects on the diagonal part of the optical conductivity were considered using a three-phase model. The oxidation effects on the magneto-optical parameters were also considered by treating the oxide layer as a nonmagnetic thin transparent layer. These corrections change not only the magnitude but also the shape of the optical conductivity and the magneto-optical parameters.

1 INTRODUCTION

The demand for high-density storage media is increasing due to new multimedia development and the huge amount of data generated in the science and technology area. Magnetic tape and disks have been used as major storage media, but recently several new mass storage media have been developed. Among them, optical data storage techniques are the most promising and already some of them are being used widely for mass storage such as the CD-ROM. Optical storage techniques have three major advantages over traditional magnetic tapes or disks: large storage capacity, removability, and great reliability [1]. In optical storage, diffraction-limited optics is used, so for higher storage density, short wavelengths are required. Currently 800 nm diode lasers are used, but diode lasers generating shorter-wavelength light are being developed, so the storage density can be increased more in the future. The reliability of optical storage media is great because the optical head and the storage medium do not touch each other, which can save data without loss or degradation of the medium. Currently, there are three kinds of optical storage, read only, write-once-read-many (WORM), and rewritable disk. The information written on the read-only disk can not be changed. But in the WORM method, data can be written only once with a strong laser beam and read many times with a weak laser beam. The last optical storage technique is the magneto-optical (MO) recording method based on the magneto-optical polar Kerr effect. This is the topic of this thesis. It provides rewritability of the magnetic medium. This technique is similar to the read-only and WORM in that it uses an optical laser but it differs from the other two optical storage methods in that it employs a magnetic field

like the traditional hard disk or floppy disk. Therefore the MO recording method is a combination of optics and magnetic technology. The process of erasing and writing in MO recording is achieved by heating a spot on the disk with a strong laser beam until the temperature of the spot reaches the Curie temperature where the coercivity H_c vanishes, then changing the magnetization orientation of the spot by a biasing magnetic field. Then turning off the laser beam cools down the medium which keeps its magnetic moment orientation. The written spots typically have the diameter of the laser spot (1 μm). A typical laser pulse time is 100 ns. To read information stored on the disk, a weak laser beam is used. If a weak linearly polarized laser beam shines on the MO layer, the reflected beam becomes elliptically polarized with the major axis rotated slightly relative to the polarization axis of the incident beam, clockwise or anticlockwise according to the magnetization direction of the focused spot. These opposite rotations can be used as the binary code for digital recording. The physical principle underlying MO recording is a magneto-optical effect. Magneto-optical effects involve the interaction of polarized light with magnetic materials. The interaction of light with a magnetized material will change the polarization of the incident light. The incident light can interact with the magnetized materials by transmission through or by reflection from the magnetized surface. In the transmission case, if the magnetization is parallel to the propagation direction of light, it is called the Faraday effect [2], and when the magnetization is perpendicular to the propagation direction of light, it is called the Voigt effect or Cotton-Mouton effect. In the reflection case, that is, if the incident light is reflected by a magnetized surface, it is called the magneto-optic Kerr effect [3]. The reflection geometry is more appropriate in real magneto-optical recording applications, so much research has focused on the Kerr effect. In the Kerr effect the reflected light becomes elliptically polarized even at normal incidence. The major axis of the reflected light is rotated from the polarization axis of the incident light. The angle of rotation is called the Kerr angle and the ratio of the minor to the major axis of the ellipse of polarization is

called the ellipticity. Figure 1-1 shows a diagram of the Kerr rotation and ellipticity. These two magneto-optical parameters are measurable quantities with a magneto-optical Kerr spectrometer (MOKS). There are three types of Kerr-effect configuration: in the polar Kerr effect, the magnetization is perpendicular to the reflecting surface. In the longitudinal and transverse Kerr effect, the magnetization is parallel to the surface. In the longitudinal configuration the magnetization is parallel to the plane of incidence, while in the transverse geometry the magnetization is perpendicular to it. Figure 1-2 shows the three possible magneto-optical Kerr effect (MOKE) geometric configurations. Among these three configurations the polar geometry gives the largest Kerr effect. To be a good candidate material for a MO disk, a material should meet several conditions. First a large perpendicular magnetic anisotropy is needed to have the magnetization vector perpendicular to the surface of the media. This is a very important condition for a MO recording system based on the polar Kerr effect. Without anisotropy, the magnetic moment prefers to lie in the plane of the recording layer to minimize the magnetostatic energy. Second, the material should have a large Kerr rotation to enhance the signal-to-noise ratio. The material also should have enough coercivity to resist temperature changes or external magnetic fields, but not too large a coercivity to allow the erasing process with a powerful laser. Additional conditions are described in many other references. For real applications, rare-earth transition-metal alloys have been used due to their superior properties as MO recording materials [4]. Transition metal multilayers are also being investigated for new MO materials for short wavelength lasers. For example Co/Pt films are found to have good signal-to-noise ratios in the blue range. The samples we measured are mainly single crystals grown by a flux method. Single crystals have several advantages in magneto-optic measurements over polycrystalline samples in that they have a higher purity which is manifested in reproducibility of data with samples from different growths. But there are a couple of disadvantages of single crystals compared to polycrystalline samples. The first is the usually small sizes of grown

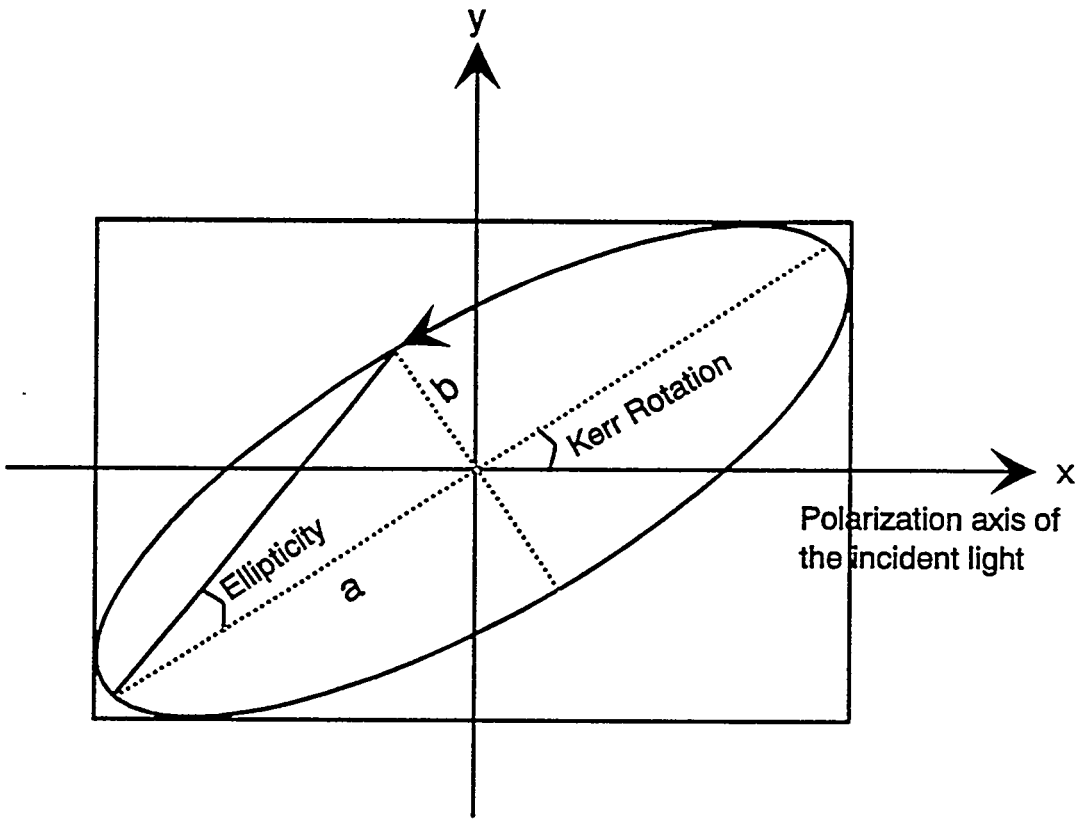

Figure 1.1 Polarization state of reflected light with Kerr rotation θ_K and ellipticity ϵ_K. The polarization axis of the incident light is along the x axis. The ellipticity is defined as the ratio of the minor axis b to the major axis a of the elliptically polarized light i.e. $\tan\epsilon_K$=b/a. Usually this ratio is small so we can use $\tan\epsilon_K=\epsilon_K$, and ϵ_K is expressed in degrees or radians.

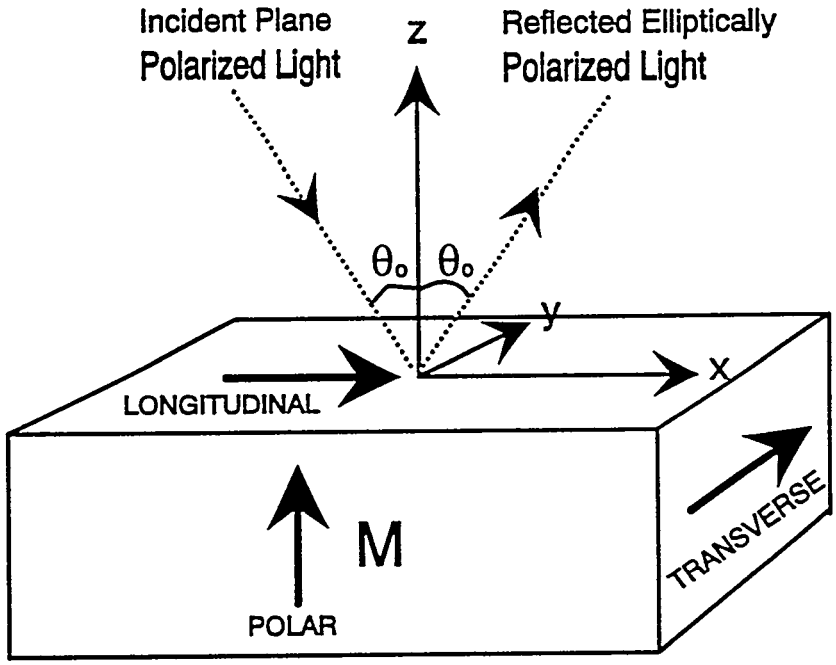

Figure 1.2 Magnetization orientations for the three magneto-optical Kerr effect configurations. θ_0 is the angle of incidence. Among these three configurations, the polar Kerr configuration produces the largest Kerr signal.

single crystals which cause difficulties in mounting on the sample holder and aligning the sample in MOKS and ellipsometry. The small size of the sample could reduce the intensity of the reflected light beam from the sample, especially in the UV region, leading to a limit of the experimental spectral range. The second is the many steps for the sample preparation of single crystals. In the case of polycrystals, the preparation steps are simpler and produce large surface areas. The reasons for the greater reliability of MOKE data measured with single crystals over those from polycrystals will be discussed in detail in Chapter 9.

Understanding the microscopic origin of the Kerr effect is essential to find new materials for magneto-optical storage applications. For the theoretical analysis, obtaining a wide spectral range of optical and magneto-optical experimental data is necessary. Using optical and magneto-optical data we can derive the off-diagonal optical conductivity component which is proportional to the Kerr rotation and compare it with ab-initio calculations based on the local spin density approximation (LSDA). In Chapter 2 we present an experimental description of MOKE, including principle, instrumentation and the calibration method. Also a brief summary of ellipsometry for the diagonal component of the optical conductivity measurements is presented. Finally the sample preparation method is discussed. In Chapter 3 we derive the macroscopic and microscopic theories of magneto-optical effects. The intraband and interband contributions to the magneto-optical effects are described in detail. In Chapter 4 we have studied the electronic and optical properties of non-magnetic rare-earth intermetallic compounds $LuAl_2$ and $YbAl_2$. Even though, they do not show magneto-optical effects, the studying of their electronic and optical properties is useful for investigating the role of the fully occupied 4f electrons. We obtained the real part of the diagonal optical conductivity by ellipsometry and compared it with the theoretical optical conductivity obtained by the local density approximation (LDA). The good agreement between theory and experiment tells us that the theory of LDA is valid for $LuAL_2$ and $YbAl_2$. The differences

of absolute magnitudes of optical conductivity between theory and experiment may be caused by oxidation effects on the surface. To check this, we employed the three-phase model treating the oxide layer on the bulk sample as a nonmagnetic thin dielectric layer with an effective refractive index n_{eff} and thickness d_{layer}. With this model, we estimated that the absolute magnitude of the experimental optical conductivity with clean surface is enhanced considerably. In Chapter 5 we present the calculated the Kerr rotation and ellipticity of $LuFe_2$ by the TB-LMTO method within the LSDA and compare them with experimental data. The tight-binding linear muffin-tin orbital method based on the LSDA used for theoretical analysis is presented. With Kubo's linear response theory, the optical conductivity tensor components from interband transitions can be determined. Some of the magneto-optical properties of 3d-based transition metals or intermetallic compounds have been successfully explained by ab-intio calculations based on the local spin density approximation(LSDA). However, the ab-intio calculations on f-electron compounds has not been so successful with the LSDA due to the strongly correlated f-electrons. In the case of full f shells (Lu, Yb), a first-principles LSDA calculation treating 4f electrons as valence electrons describes several experimental results well. Both theory and experiment agree quite well. In Chapter 6 the electronic, magnetic, optical and magneto-optical properties of $GdCo_2$ are studied. Rare earth materials exposed to air are easily oxidized. We consider the effect of oxidation on the Kerr rotation and ellipticity. The discussion of oxidation is presented in this chapter. In Chapter 7, $GdFe_2$ intermetallic compounds are discussed in detail. Through these analyses we explain the role of rare-earth and transition atoms in MOKE systematically and in more detail. The comparisons between $GdCo_2$ and $GdFe_2$ are presented in Chapter 8. The diagonal part of their optical conductivities are very similar, but the off-diagonal optical conductivities are quite different. The difference is believed to come from the different hybridization strengths in Gd-Co and Gd-Fe. The detailed comparison will be discussed in Chapter 8. In Chapter 9, the imaginary parts of the off-diagonal optical conductivity

of $HoFe_2$ and $TbFe_2$ are obtained using the MOKE and ellipsometry experimental data. The imaginary parts of the off-diagonal optical conductivity are compared with the theoretical values obtained from the TB-LMTO based on the LSDA. From these studies, the 4f electron involvement in optical interband transitions could be determined. In Chapter 10 the conclusions of this thesis will be stated.

2 EXPERIMENT

Magneto-optical Kerr spectrometer

Introduction

To understand the physical processes which cause the magneto-optical Kerr effect, we need to measure MOKE spectra. The methods of measuring the magneto-optical parameters, Kerr rotation θ_K and ellipticity ϵ_K, can be divided into two groups: the null method [5] and the intensity method [6, 7]. The basic idea of the computer-controlled null method is to compensate the Kerr rotation of the sample by rotating an analyzer which is crossed with respect to the fixed polarizer. At the first stage, the analyzer and polarizer are mounted in high-precision computer-controlled stepper-motor rotary stages and are crossed to each other. A modulator (Faraday or piezo) with a modulation frequency f positioned between the polarizer and analyzer modulates the polarization of the incident light. The signal component at 2f, detected by a 2-phase lock-in amplifier, is proportional to $\sin(\Delta\theta + 2\phi)$ where $\Delta\theta = -2\theta_K$ and ϕ is the transmission axis of the analyzer. By rotating the analyzer we can find a transmission axis of the analyzer which is equal to the major axis of the elliptically polarized light. The amount of rotation of the analyzer then corresponds to the Kerr rotation. The ellipticity ϵ_K is measured by inserting a Soleil-Babinet compensator [8, 9] between the sample and the modulator.

The intensity method also employs the modulator and lock-in amplifier. This method is generally highly sensitive. For the MOKE study we used the intensity method which

makes a simultaneous measurement of the two magneto-optical parameters, Kerr rotation and ellipticity, possible. The principle of the technique, calibration and experimental details will be described in the next sections.

Principles of the technique

A schematic diagram showing essential parts of the magneto-optical Kerr spectrometer (MOKS) is shown in Fig. 2. The direction of propagation of the incident light is along the z-axis. The light is linearly polarized by a polarizer whose transmission axis makes an angle of 45° with respect to the vertical axis, i.e. the optical axis of the modulator. This linearly polarized light passes through the photoelastic modulator (PEM) [10] and experiences a periodically varying relative phase shift δ between orthogonal amplitude components. The relative phase shift has the form $\delta = \delta_0 \sin \omega t$, where δ_0 is the peak relative phase difference and ω is the modulation angular frequency of the PEM (50 kHz in our experiment). δ_0 is proportional to V/λ, where V is the voltage applied to the PEM and λ is the wavelength of the incident light. Throughout the entire scan δ_0 is kept constant by varying the voltage. After passing the PEM, the light is reflected from the magnetized sample or a reference aluminum mirror in the cryostat. The reflected light passes through an analyzer whose transmission axis is rotated ϕ from the x-axis as shown in Fig. 2. Finally the light beam goes through a 1/4-m monochromator [11] and is detected by a S-20 photomultiplier. The angle of incidence is kept below 4°. To subtract out the Faraday rotation of the optical windows of the cryostat which is added to the MOKE spectrum, we used an Al reference mirror which shows negligible Kerr rotation and ellipticity between 1-5 eV, even in high magnetic fields. Furthermore, to subtract the strain birefringence of the windows we need to measure with both (positive and negative) field directions because the strain effect in the windows is independent of

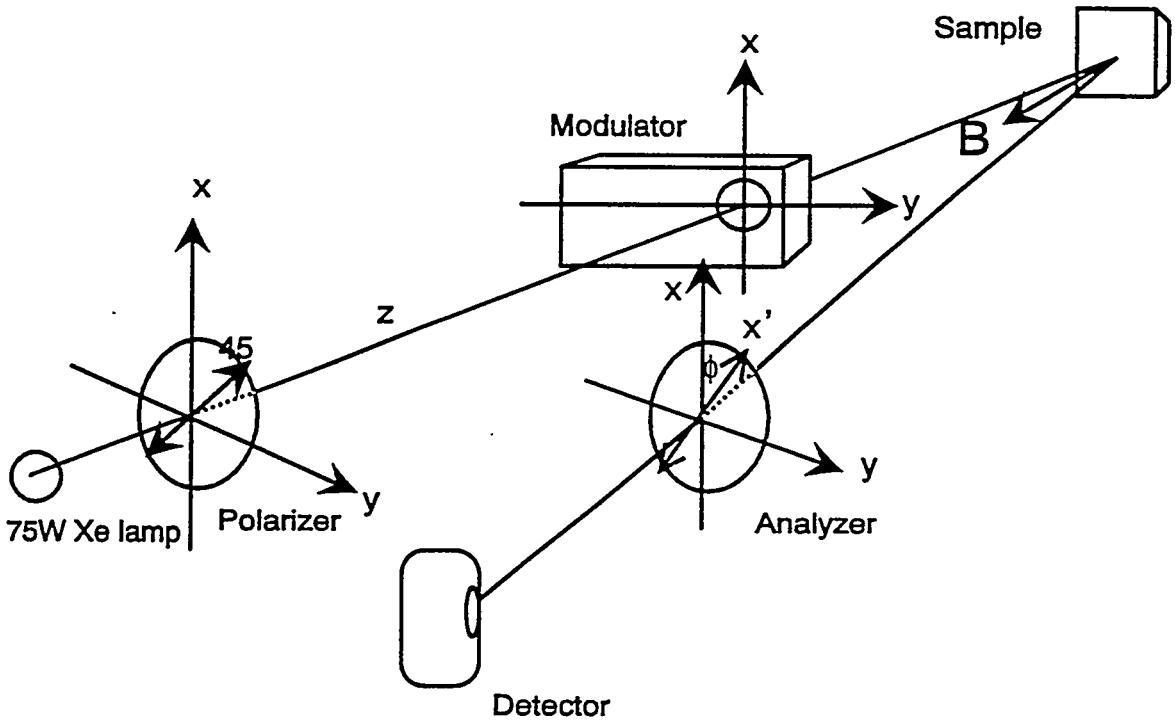

Figure 2.1 Schematic diagram of essential parts of the magneto-optical Kerr spectrometer.

magnetic field. Therefore the formula used for the Kerr rotation θ_K is given by

$$\theta_K = \left[(\theta_S^+ - \theta_M^+) - (\theta_S^- - \theta_M^-)\right]/2, \tag{2.1}$$

where $\pm$ are positive and negative magnetic fields, and the subscripts S, M designate the sample and reference mirror, respectively. The ellipticity ε_K is determined in the same way. Each spectrum we show is the result of 4 scans taken over a period of typically 4 hours. The transmitted electric field vector through the analyzer can be written in a simple form using the Jones matrix of each optical element [12]. We can express this as a simple product of Jones matrices of the optical elements. The details of Jones matrices of each optical elements are as follows. The electric field vector transmitted by the polarizer can be expressed as

$$PE_i = \begin{pmatrix} \cos\Psi \\ \sin\Psi \end{pmatrix} E_i, \tag{2.2}$$

where Ψ is the polarization angle of the polarizer. The Jones matrix for the modulator M is represented as follows:

$$M = \begin{pmatrix} 1 & 0 \\ 0 & e^{i\delta} \end{pmatrix}, \tag{2.3}$$

where δ is the modulator retardation. The reflection of light at near normal-incidence by a magnetized surface can be described by the Fresnel reflection coefficients $\tilde{r}_\pm = r_\pm e^{i\theta_\pm}$, where $\pm$ represents right and left circularly polarized light, respectively [12]. The Jones matrix representation of the sample in circular coordinates can be written as

$$S_0 = \begin{bmatrix} \tilde{r}_+ & 0 \\ 0 & \tilde{r}_- \end{bmatrix} \tag{2.4}$$

The above matrix is transformed into cartesian coordinates by the unitary transformation.

$$S = \frac{1}{\sqrt{2}} \begin{bmatrix} 1 & 1 \\ -i & i \end{bmatrix} \cdot S_0 \cdot \frac{1}{\sqrt{2}} \begin{bmatrix} 1 & i \\ 1 & -i \end{bmatrix} \tag{2.5}$$

The Jones matrix for the analyzer A is given by

$$A = \begin{pmatrix} 1 & 0 \\ 0 & 0 \end{pmatrix} \begin{bmatrix} \cos\phi & \sin\phi \\ -\sin\phi & \cos\phi \end{bmatrix} \tag{2.6}$$

where ϕ is the polarization angle of the analyzer. Therefore the amplitude of the electric field vector transmitted through the analyzer whose polarizing axis is rotated ϕ degrees from the x-axis is the product of each optical Jones matrix, that is E_f=ASMPE_i. With Ψ=45°, the final form of the electric field vector is

$$E_f = \frac{E_i}{2\sqrt{2}} \left\{ \tilde{r}_+ \left(1 + ie^{i\delta}\right) e^{i\phi} + \tilde{r}_- \left(1 - ie^{i\delta}\right) e^{-i\phi} \right\}. \tag{2.7}$$

The transmitted intensity is the squared magnitude of the transmitted electric field, that is,

$$I = E_f^* \cdot E_f. \tag{2.8}$$

The final result for the intensity is the following.

$$I = \frac{E_i^2}{4} \left(|r_+|^2 + |r_-|^2 + \sin\delta \left(|r_+|^2 - |r_-|^2 \right) + 2\,|r_+|\,|r_-| \cos\delta \sin\left(\Delta\theta + 2\phi\right) \right). \tag{2.9}$$

We use the following definitions to simplify the above equation:

$$R = \frac{1}{2}\left(|r_+|^2 + |r_-|^2 \right), \quad \Delta R = |r_+|^2 - |r_-|^2, \quad \Delta\theta = \theta_+ - \theta_-. \tag{2.10}$$

The following approximation holds for small MOKE signals.

$$|r_+|\,|r_-| \approx R. \tag{2.11}$$

Using the above two equations we can write the intensity in the following simple form.

$$I = I_0 \left(R + \frac{\Delta R}{2} \sin\delta + R \sin\left(\Delta\theta + 2\phi\right) \cos\delta \right). \tag{2.12}$$

The intensity I can be decomposed into components using the following expansion formula for $\sin\delta$ and $\cos\delta$.

$$\begin{aligned} \sin\delta &= \sin(\delta_0 \sin\omega t) = 2J_1(\delta_0) \sin\omega t + \cdots \\ \cos\delta &= \cos(\delta_0 \sin\omega t) = J_0(\delta_0) + 2J_2(\delta_0) \cos 2\omega t + \cdots, \end{aligned} \tag{2.13}$$

where $J_n(\delta_0)$ is an nth order Bessel function. By putting the above equations into I, we obtain

$$I = I_{DC} + I_\omega \sin\omega t + I_{2\omega}\cos 2\omega t + \cdots, \tag{2.14}$$

where

$$\begin{aligned} I_{DC} &= I_0 R\{1 + J_0(\delta_0)\sin(\Delta\theta + 2\phi)\} \\ I_\omega &= I_0 \Delta R J_1(\delta_0) \\ I_{2\omega} &= 2I_0 R J_2(\delta_0)\sin(\Delta\theta + 2\phi). \end{aligned} \tag{2.15}$$

To remove the effects in I_0 of the photomultiplier sensitivity, monochromator transmission, lamp spectrum, and the intensity reduction through reflection by the sample and the mirrors, we take the ratio of the modulated components to the dc component of the signal.

$$\begin{aligned} \frac{I_\omega}{I_{DC}} &= A\frac{J_1(\delta_0)\,\Delta R/R}{1 + J_0(\delta_0)\sin(\Delta\theta + 2\phi)}, \\ \frac{I_{2\omega}}{I_{DC}} &= B\frac{2J_2(\delta_0)\sin(\Delta\theta + 2\phi)}{1 + J_0(\delta_0)\sin(\Delta\theta + 2\phi)}, \end{aligned} \tag{2.16}$$

where A and B are gain factors which can be determined through a calibration procedures which will be explained later. The definitions of Kerr rotation and ellipticity are given by

$$\begin{aligned} \theta_K &= -\frac{1}{2}\Delta\theta, \\ \epsilon_K &= \frac{|r_+| - |r_-|}{|r_+| + |r_-|} = \frac{|r_+|^2 - |r_-|^2}{|r_+|^2 + |r_-|^2 + 2\,|r_+|\,|r_-|} \approx \frac{1}{4}\frac{\Delta R}{R}. \end{aligned} \tag{2.17}$$

From Eq. 2.15, the second term of the DC component is proportional to the Bessel function of order zero. The I_ω and $I_{2\omega}$ components are proportional to Bessel functions of order one and two respectively. The Bessel functions of order 0, 1 and 2 are shown in Fig. 2.2.

We choose the amplitude of the retardation δ_0 to satisfy $J_0(\delta_0) = 0$, where $\delta_0 = 2.405$ rad or 137.8°. This condition makes the second term of the DC component zero. Then

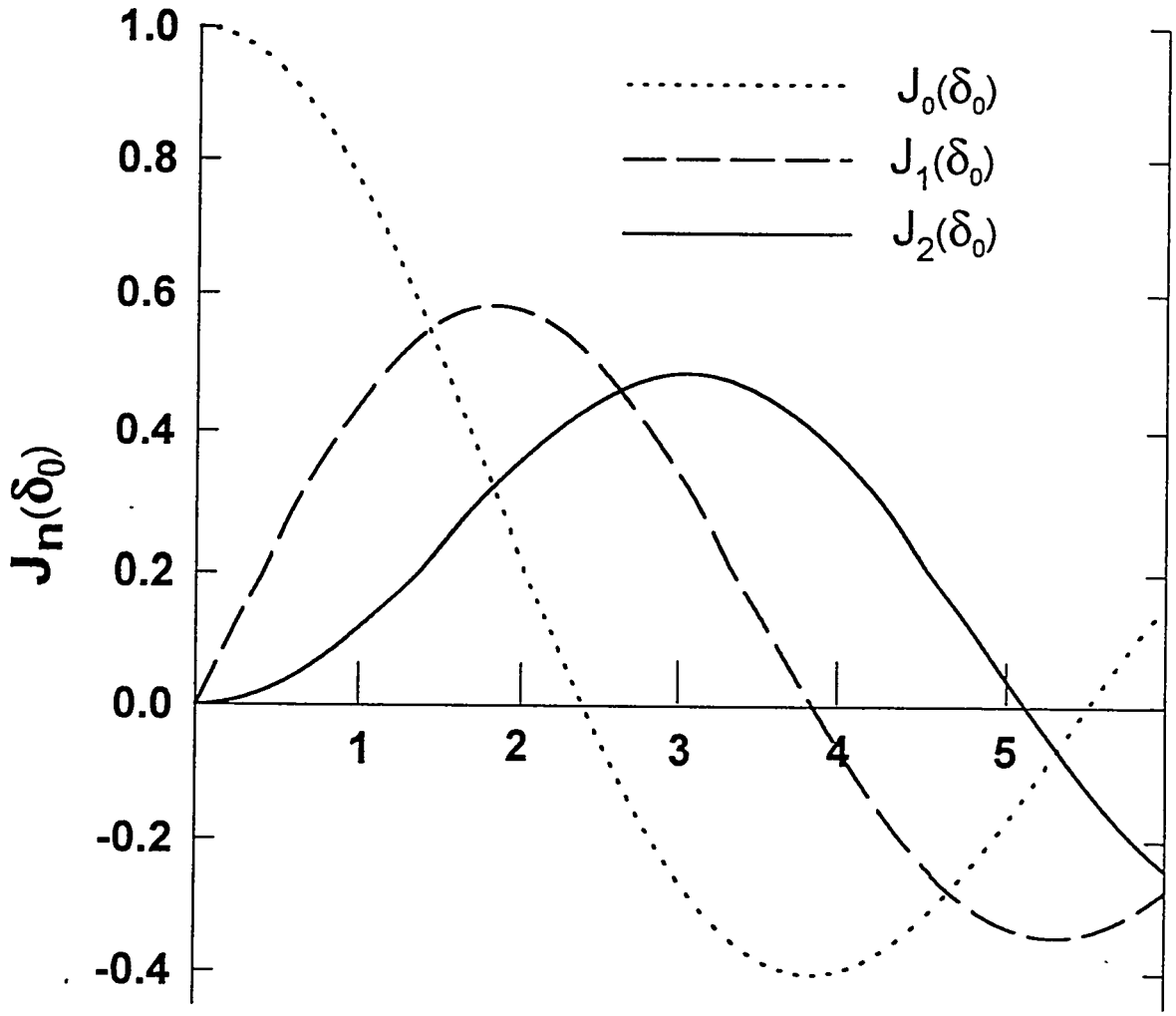

Figure 2.2 A graph showing Bessel functions of order 0, 1 and 2 as a function of ϕ_0. The horizontal axis units are radians.

the DC component does not depend on the magnitude of the Kerr rotation of the samples. With this δ_0, the values of $J_1(\delta_0)$ and $J_2(\delta_0)$ are within 90% of their maximum values. Using Eq. (2.16) and Eq. (2.17), we can derive the normalized I_ω and $I_{2\omega}$ components as:

$$\begin{aligned} \frac{I_\omega}{I_{DC}} &= AJ_1(\delta_0)\,\Delta R/R = 4AJ_1(\delta_0)\,\epsilon_K, \\ \frac{I_{2\omega}}{I_{DC}} &= 2BJ_2(\delta_0)\sin(\Delta\theta + 2\phi) \approx -4BJ_2(\delta_0)\,\theta_K. \end{aligned} \tag{2.18}$$

Therefore the Kerr rotation and ellipticity can be expressed in the following forms.

$$\begin{aligned} \theta_K &= -\frac{1}{4BJ_2(\delta_0)}\frac{I_{2\omega}}{I_{DC}}, \\ \epsilon_K &= \frac{1}{4AJ_1(\delta_0)}\frac{I_\omega}{I_{DC}} \end{aligned} \tag{2.19}$$

By using the above formulas, we can get the Kerr rotation and ellipticity from the experimentally measured values of I_{DC}, I_ω and $I_{2\omega}$. The calibration methods determining $4BJ_2(\delta_0)$, $4AJ_1(\delta_0)$ will be described in the next section.

Method of calibration

Calibration of the Kerr rotation

In the previous section we explained how to obtain the Kerr rotation and ellipticity from the DC, ω, and 2ω component of the detected intensity. In order to determine the gain factors $4AJ_1(\delta_0)$ and $4BJ_2(\delta_0)$, which depend on electronic amplification, sensitivity of the detector system, etc., we employed a direct calibration method which allows us to calibrate the instrument over the entire range of measurement. We used high precision computer-controlled rotary stages [13] to move the polarizer (P) and analyzer (A) prisms. The resolution is limited to 1/1000° which is sufficient for this kind of measurement. We place an aluminum reference mirror at the sample position.

As a first step we have to align the P-PEM-A setup. Therefore we set the retardation of the PEM to zero, i.e. turn it off, and find the minimum in the transmitted intensity.

This is done by fitting the DC intensity around the transmission minimum to a parabola. The crossed position for P and A can be determined within typically 0.005°.

After this procedure, we turn on the modulator and rotate the polarizer and the analyzer simultaneously until the signal component at 2f becomes zero. Now the polarizer is parallel to one of the two perpendicular principal axis of the modulator, and the analyzer is parallel to the other principal axis of the modulator. The face of the analyzer prism is set to be perpendicular to the reflected light beam to prevent the analyzer from deviating the beam upon rotation. We fix the analyzer and turn the polarizer to 45 degrees with respect to the analyzer. After finishing this procedure, which takes between 5 and 15 minutes, we perform the Kerr rotation calibration measurement. The mathematical expression for the Kerr rotation calibration is as follows. Because the Kerr rotation of the aluminum mirror is negligible through the spectral range (1 to 5.2 eV), if we rotate the polarization axis of the analyzer a small angle ϕ, then we can approximate Eq. 2.16 by

$$\frac{I_{2\omega}}{I_{DC}} = 2BJ_2(\delta_0)\sin(\Delta\theta + 2\phi) \approx 4BJ_2(\delta_0)\,\phi. \tag{2.20}$$

We obtain the following equations by rotating the polarization axis of the analyzer in clockwise and anticlockwise directions.

$$\begin{aligned} \left(\frac{I_{2\omega}}{I_{DC}}\right)_{+\phi} &= 4BJ_2(\delta_0)\,\phi, \\ \left(\frac{I_{2\omega}}{I_{DC}}\right)_{-\phi} &= -4BJ_2(\delta_0)\,\phi. \end{aligned} \tag{2.21}$$

The difference gives

$$\left(\frac{I_{2\omega}}{I_{DC}}\right)_{+\phi} - \left(\frac{I_{2\omega}}{I_{DC}}\right)_{-\phi} = 4BJ_2(\delta_0)\,2\phi. \tag{2.22}$$

We divide Eq. (2.22) by 2ϕ and get the final equation for the Kerr rotation calibration.

$$\left(\left(\frac{I_{2\omega}}{I_{DC}}\right)_{+\phi} - \left(\frac{I_{2\omega}}{I_{DC}}\right)_{-\phi}\right)/2\phi = 4BJ_2(\delta_0). \tag{2.23}$$

Using this method, the Kerr rotation can be calibrated over the whole energy range. Figure 2 shows the values of $4BJ_2(\delta_0)$ measured by setting $\phi = 1°$. As shown in Fig. 2,

the absolute magnitude of $4BJ_2(\delta_0)$ starts to decrease above 5.0 eV. This is due to the stray light in the UV range, especially above 5.0 eV. In Eq. 2.21, the I_{DC} component is fixed to 5 mV to normalize the I_ω and $I_{2\omega}$ components. As the photon energy increases in the UV range, the intensity of the reflected light from a reference mirror is getting weak due to the weak spectrum of the higher photon energy in the Xe lamp and low transmittance of optical elements at higher photon energy range. To maintain the DC voltage a constant value of 5 mV in the UV range, the power supply voltage to the photomultiplier should be increased, then the photomultiplier also increases more stray light. In this case, the DC component contributed by the stray light can not be ignored. At the same time the magnitude of the 2ω component also decreases, but we divide the $2\,\omega$ component still by fixed DC component which contains stray light contribution. This causes the ratio given in Eq. 2.21 to be reduced. As a result of this, the absolute magnitude of $4BJ_2(\delta_0)$ also decreases in the higher energy region (above 5 eV).

Calibration of Kerr ellipticity

For the entire ellipticity calibration we used a thin retardation plate made of sapphire, as proposed by Sato *et al.* [6, 7]. The thin sapphire plate is inserted between the PEM and the reference mirror. This gives an additional retardation δ_S, so the total retardation is expressed by

$$\delta_T = \delta_0 \sin \omega t + \delta_S, \tag{2.24}$$

where $\delta_S = 2\pi nl/\lambda$ is the retardation from the sapphire plate. The mathematical expression for the ellipticity calibration is as follows. For the mirror $\Delta R = 0$ and $\Delta\theta = 0$. Therefore the reflected intensity is

$$I = I_0 R\,(1 + \sin 2\phi \cos \delta_T) \tag{2.25}$$

By substituting Eq. 2.24 into Eq. 2.25, we derive the following equation,

$$I = I_0 R(1 - 2J_1(\delta_0) \sin \phi \sin \delta_S \sin \omega t \pm 2J_2(\delta_0) \cos \delta_S \cos 2\omega t). \tag{2.26}$$

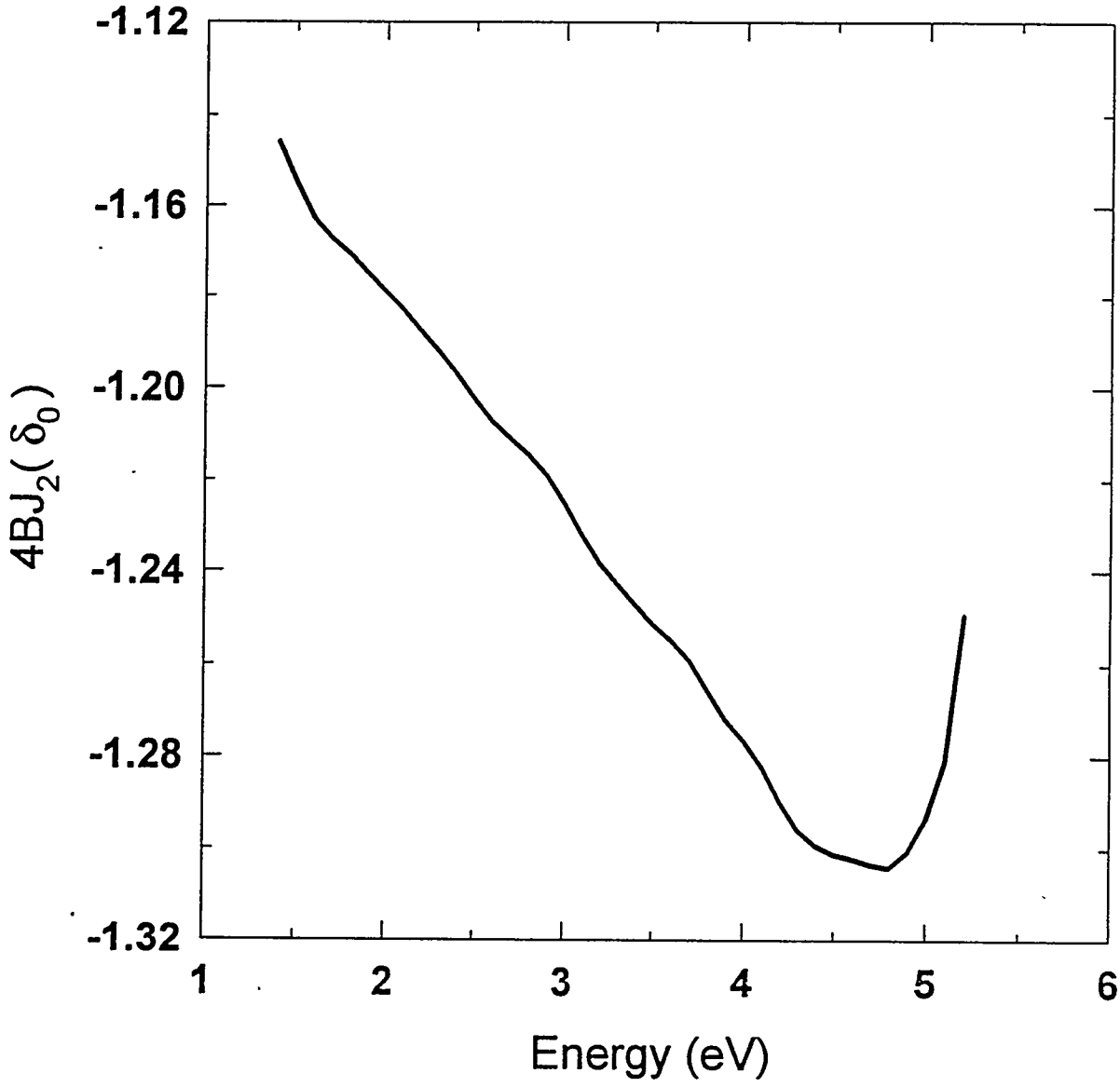

Figure 2.3 Spectrum of the calibration parameter for Kerr rotation with the analyzer angle $\phi = 1°$.

For small angles of $\pm\phi$, the ratio of I_{DC} to I_ω, becomes

$$\left(\frac{I_\omega}{I_{DC}}\right)_{\pm\phi} = \mp 2AJ_1(\delta_0)\phi \sin\delta_S. \tag{2.27}$$

Therefore

$$\left(\left(\frac{I_\omega}{I_{DC}}\right)_{+\phi} - \left(\frac{I_\omega}{I_{DC}}\right)_{-\phi}\right)/2\phi = -4AJ_1(\delta_0)\sin\delta_S. \tag{2.28}$$

This gives a direct value of $4AJ_1(\delta_0)$ for the ellipticity calibration. Figure 2.4 shows the values of -$4AJ_1(\delta_0)\sin\delta_S$ measured by setting $\phi = 1°$. The envelope function immediately gives the calibration values $\pm 4AJ_1(\delta_0)$.

Experimental details

A block diagram showing details of the magneto-optical Kerr spectrometer is shown in Fig. 2.5 The light source is a 75W Xe short-arc lamp [14]. Calcite prism polarizers are used for both the polarizer and analyzer. These polarizers, mounted in optical stages, are controlled by a high-precision stepping-motor controller. A Hinds photoelastic modulator(PEM) [10] is used for the polarization modulation of the light beam. The optical part of the PEM consists of an optical element and a transducer. Fused silica, which is commonly used in the visible, near UV, and near IR, is used for the optical element of the PEM. The fused silica bar is subjected to periodic vibrations by a quartz transducer. This vibration generates a time-varying birefringence in the silica bar with a frequency equal to a resonance frequency of the bar. The amplitude of the vibration is controlled by the Hinds PEM controller. Linearly-polarized light whose polarization axis is 45° from the vertical is incident on the center of the optical element of the PEM. The long axis of the modulator is along the horizontal axis. The incident polarized light can be decomposed into two components: E_x parallel to the modulator axis and E_y perpendicular to it. When the bar is under no stress, there will be no phase difference between the two perpendicular components. When the bar is under periodic stress, a sinusoidal, uniaxial strain is induced along the x-axis of the fused silica bar as shown in

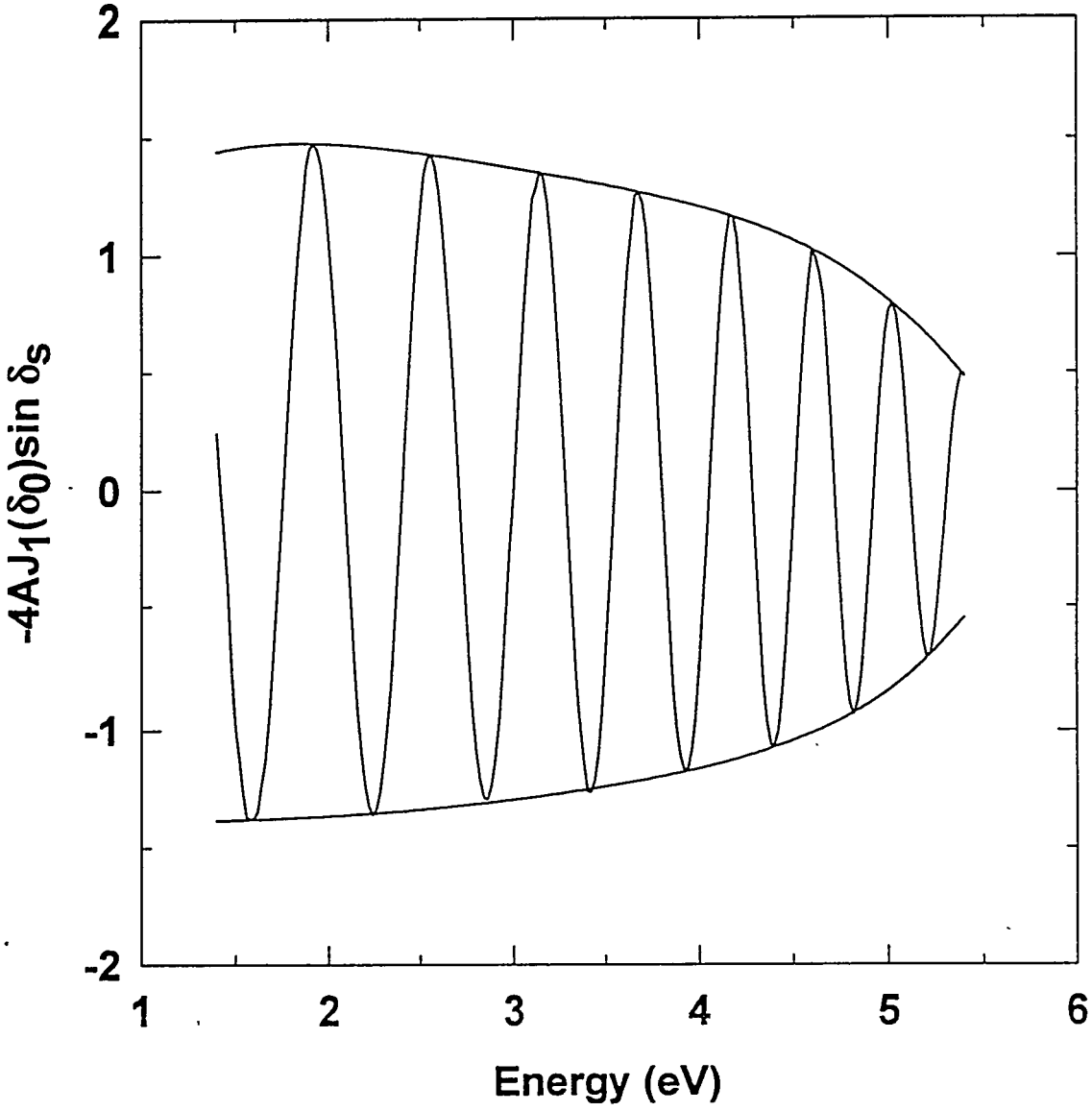

Figure 2.4 Spectrum of the calibration parameter for ellipticity with the method explained in the text.

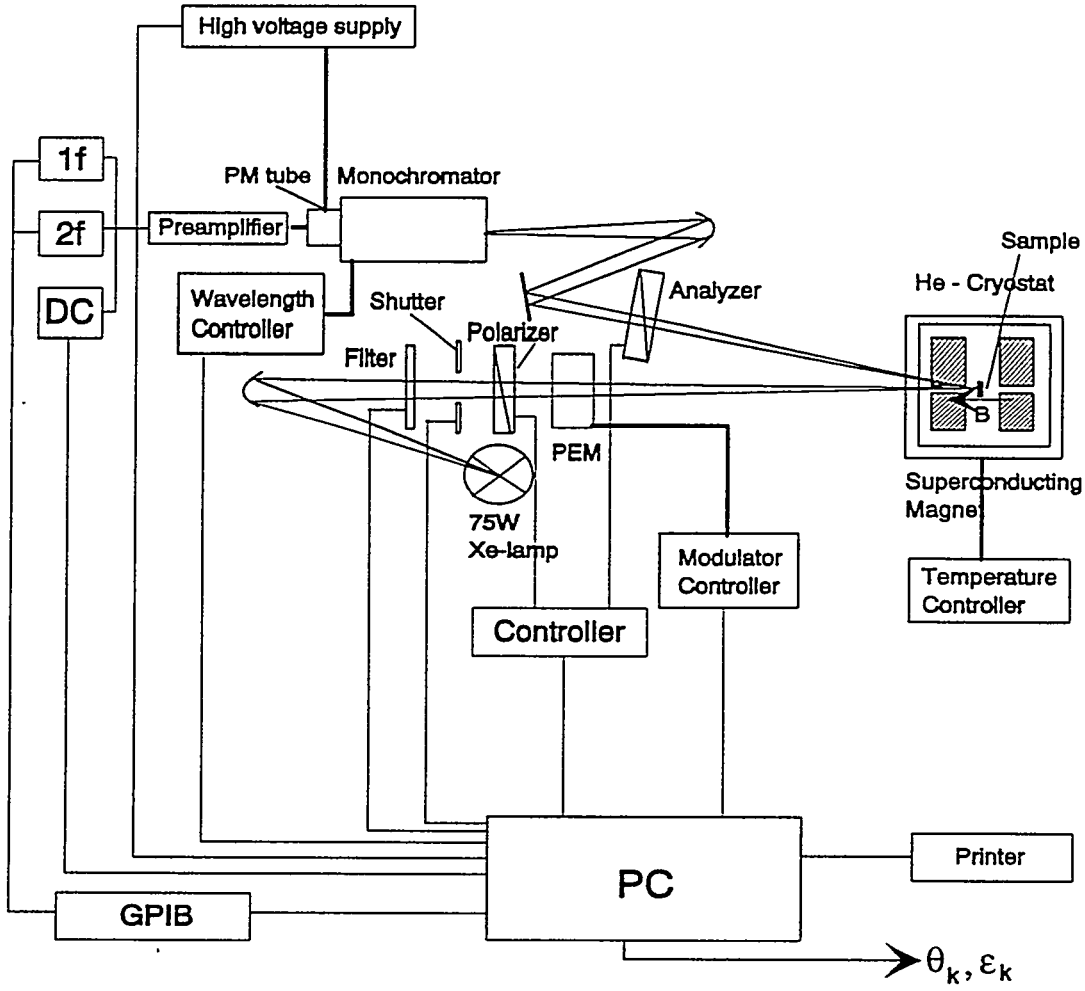

Figure 2.5 Block diagram of the magneto-optical Kerr spectrometer.

Fig. 2.6. As shown in Fig. 2.6, the incident light is polarized along 45° relative to the x-axis. Therefore the amplitude of the electric field vector before passing the PEM can be written as

$$\vec{E} = E_0 \left(\hat{i} + \hat{j}\right), \tag{2.29}$$

where $\hat{i}$ and $\hat{j}$ stand for the unit vectors along the x and y axes. After passing through the PEM, the amplitude of the electric field vector becomes

$$\vec{E} = E_0 \left(\hat{i} + e^{i\delta}\hat{j}\right), \tag{2.30}$$

where δ is the modulator retardation. The detail description of the principle of the PEM is as follows. When the bar is compressed, the polarization component parallel to the modulator axis moves a little bit faster than the vertical component. Then the horizontal component "leads" the vertical component after passing the modulator. If the bar is extended, then the polarization component parallel to the modulator axis moves a little bit slower than the vertical component. In this case, the vertical component "leads" the horizontal component after passing the modulator.

The instantaneous phase difference between the two orthogonal polarization components described above is called the retardation. The amplitude of the sinusoidal retardation as a function of time is called the peak retardation. When the peak retardation is exactly equal to one-fourth of the wavelength of the light, the PEM works as a quarter wave plate. The polarization state after the modulator changes between right circularly polarized and left circularly polarized, once each cycle. When the bar is under no strain, then the polarization state after the modulator is linear, that is no change in its polarization state. Between the positive and negative peak retardations, the light after the PEM becomes elliptically polarized light. The PEM also acts as a half-wave plate when the peak retardation is equal to one-half of the wavelength of the light. At the peak retardation, the polarization states are linearly polarized with the polarization axis rotated 90° from the incident linearly polarized light.

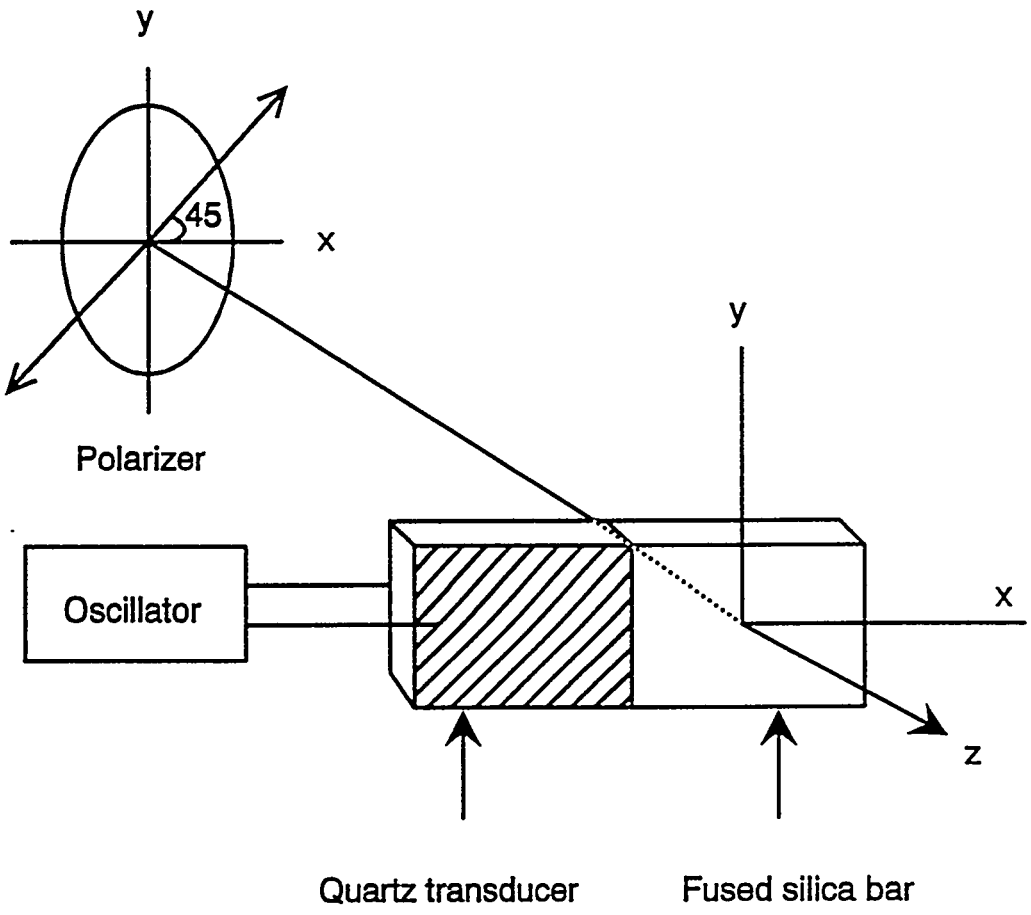

Figure 2.6 Schematic diagram of the optical part of the PEM.

For focusing and deflecting the light beam, we used UV-enhanced spherical concave mirrors with 0.5 m focal length and an UV enhanced plane mirror. The monochromator is a McPherson EU-700 scanning monochromator [11]. We use a plane holographic grating [15] with a ruling density of 1200 grooves/mm. The grating is optimized for the UV region, especially between 190-400 nm. The intensity in the UV range generated by the Xe lamp is very weak compared to that in the visible range. The long-wavelength stray light is intense enough to give a false DC signal when measuring in the UV range. The plane holographic gratings manufactured by a photolithographic process give gratings with straight, equidistant grooves with an approximately sinusoidal profile. These plane holographic gratings give low levels of stray light due to the lack of scattering centers. By using this grating, we do not have to use a filter for the UV range. Four glass filters, Schott WG305, GG395, and GG495 [16], are used in the wavelength ranges of 3500-4500 $\mathring{A}$, 4500-5500 $\mathring{A}$, and 5500-9000 $\mathring{A}$, respectively, to block out the contamination due to the second-and higher-order diffraction. A UV-enhanced, S20 response photomultiplier (Hamamatsu R562) is used as a detector.

For the generation of high magnetic fields we used a liquid helium cryostat [17] made by CRYO industries of America, shown in Fig. 2.7 which contains a superconducting magnet which can produce up to 7 Tesla. The magnet is a split solenoid which allows access for a sample from above. The magnetic field applied to the sample is perpendicular to the surface of the sample. The superconducting magnet should be immersed in liquid helium when running because it is made of NbTi whose critical temperature is 9.8 K. To hold liquid helium, the cryostat must be evacuated until the pressure of the vacuum space is down to approximately 10^{-5} Torr. Before introducing any liquid cryogens into the cryostat, all water should be removed from the nitrogen and helium reservoirs. If not removed, this water will freeze when cooled and could cause severe damage to the magnet and the cryostat. The cryostat has two reservoirs; nitrogen and helium. The function of the nitrogen reservoir is to reduce the consumption of liquid

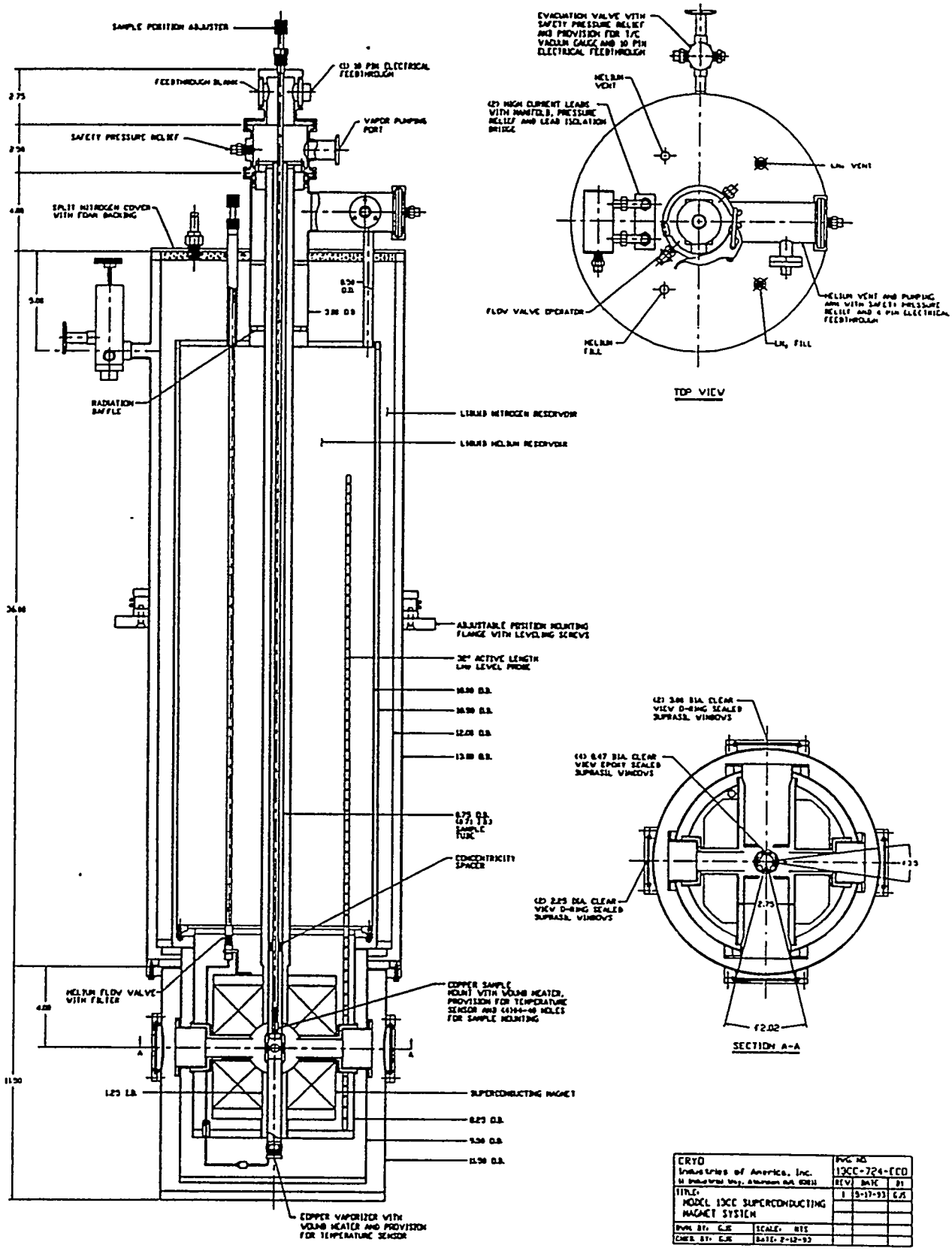

Figure 2.7 Liquid Helium Dewar.

helium. Before cooling the helium reservoir to liquid helium temperature, we need to make the temperature of the helium reservoir close to liquid nitrogen temperature. This will reduce the amount of liquid helium necessary to cool the superconducting magnet to liquid helium temperature. There are two methods of cooling the helium reservoir to liquid nitrogen temperature: direct and indirect. The direct method is to transfer liquid nitrogen into the helium reservoir. The advantage of this method is the fast cooling the superconducting magnet to liquid nitrogen temperature. But the disadvantage of this method is the removal of all of the liquid nitrogen after cooling. The other method is to fill the liquid nitrogen reservoir while keeping the helium reservoir overpressurized. After several days, the helium reservoir, and the superconducting magnet will be cooled down close to liquid nitrogen temperature due to radiation and conduction heat transfer. The level of liquid helium should be maintained above the superconducting magnet during the experiment.

The sample is mounted on the sample holder which is attached to the rod. The sample holder, shown in Fig. 2.8, is made of oxygen-free copper and has two brass windows. The Al reference mirror is mounted on the upper part of the sample holder and the sample is mounted on the lower part of the sample holder. The sample and Al reference mirror are fixed with 4 set screws through the copper windows which cover the sample and mirror. The Al reference mirror is used to cancel the Faraday rotation due to the two windows of the cryostat. The Al reference mirror is made by evaporating pure Al on a glass substrate from a tungsten boat. The reflected beam paths from the sample and the Al mirror should be the same and hit the same spot of the analyzer prism. Once the sample is inserted into the sample space of the cryostat, it is difficult to make the reflected paths of the sample and Al mirror identical. If we move the whole cryostat, then the windows also move which leads to different light paths in the windows between the sample and Al mirror. To overcome this difficulty, we designed a sample holder which allows some movement of the sample. The lower part of the sample holder is

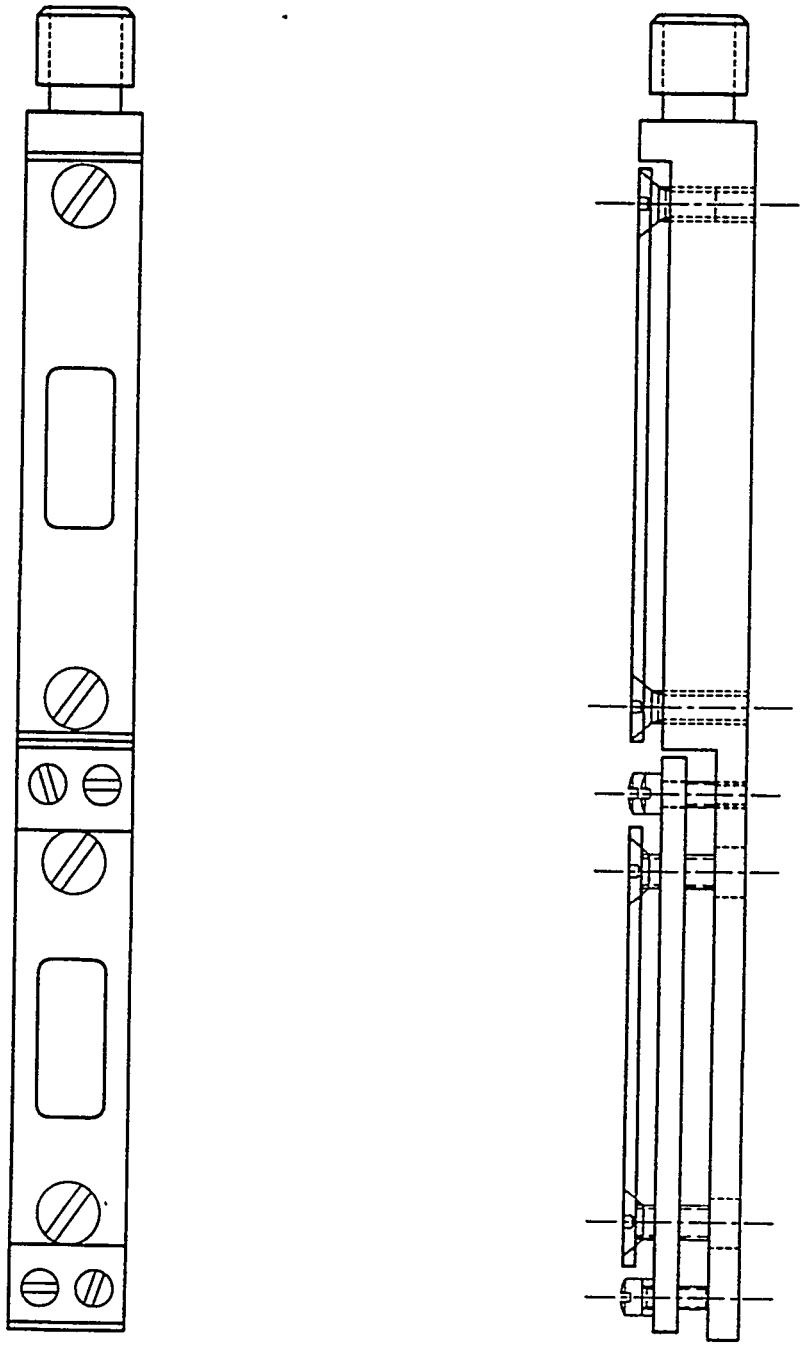

Figure 2.8 The assembly view of sample holder. The scale is double size.

adjustable with several degrees of freedom for optical alignment. In a real measurement, we measure the Al mirror in the cryostat first and we measure the sample by pulling the rod up slightly to put the light beam on the sample. We used an optical slider to simulate the alignment in the cryostat. Instead of moving vertically, the slider which holds the sample holder moves freely horizontally. By using a He-Ne laser beam, we mark on a wall-mounted screen the reflected laser beam from the reference mirror on the upper part of the sample holder. Then we move the slider horizontally until the laser beam hits the center of the sample. The reflected beam from the sample is usually off the marked dot. We then adjust the four screws around the sample holder to match the reflected laser beam spot from the sample with the spot from the Al mirror. After releasing the sample holder from the slider, we screw the sample holder to the end of the rod. The rod is slowly lowered into the sample space. Around the rod, several spacers are attached to prevent movement of the rod in the cryostat. We measure 4 times to get the Kerr rotation and ellipticity of a sample. We first measure the Faraday rotation in the two windows using the Al reference mirror, which shows zero Kerr rotation even at high magnetic fields with a positively applied magnetic field. After this measurement we switch the magnetic field without changing the alignment of the Al mirror. We do this to subtract out any birefringence induced mechanically or thermally in the cryostat windows. This birefringence does not change sign upon switching the magnet and will be cancelled out by subtracting data taken at negative field from data taken with positive field. After finishing the Al mirror measurements, we pull the rod up slightly to measure the sample. We measure the sample using the same procedure as the Al mirror. The method of changing samples is described in the Appendix.

Ellipsometry

Ellipsometry is widely used to characterize surfaces, interfaces, and thin films. The principle of ellipsometry is based on the fact that the state of polarization of light is changed on reflection. This change is directly related to the dielectric function of the reflecting material. In the case of reflectivity measurements, which measure the ratio of the reflected intensity to incident intensity of light from a sample at normal incidence, only the real part of the reflected field is measured. The imaginary part is obtained by Kramers-Kronig transformation of the real part where the analysis assumes that the real part is accuratly known to zero frequency. But measuring the exact absolute intensity is difficult. Furthermore the Kramers-Kronig analysis requires reflectivity over a wide energy range. Ellipsometry measures the phase and relative intensities, not absolute intensity, so a direct measurement of the real and imaginary part of the dielectric function is possible without the Kramers-Kronig transform technique. The diagram of a rotating analyzer ellipsometer is shown in Fig. 2.9. With rotating analyzer ellipsometry (RAE) [18, 19], one measures the complex reflectivity ratio

$$\rho = \frac{r_p}{r_s} = \left|\frac{r_p}{r_s}\right| e^{i\Delta} = \tan\Psi e^{i\Delta}, \tag{2.31}$$

where r_p, r_s are the complex amplitude reflection coefficients for p-and s-polarized light, and Ψ and Δ express the change in amplitude and phase between p and s components of polarized light reflected from a surface. Ψ and Δ are quantities directly measurable from ellipsometry.

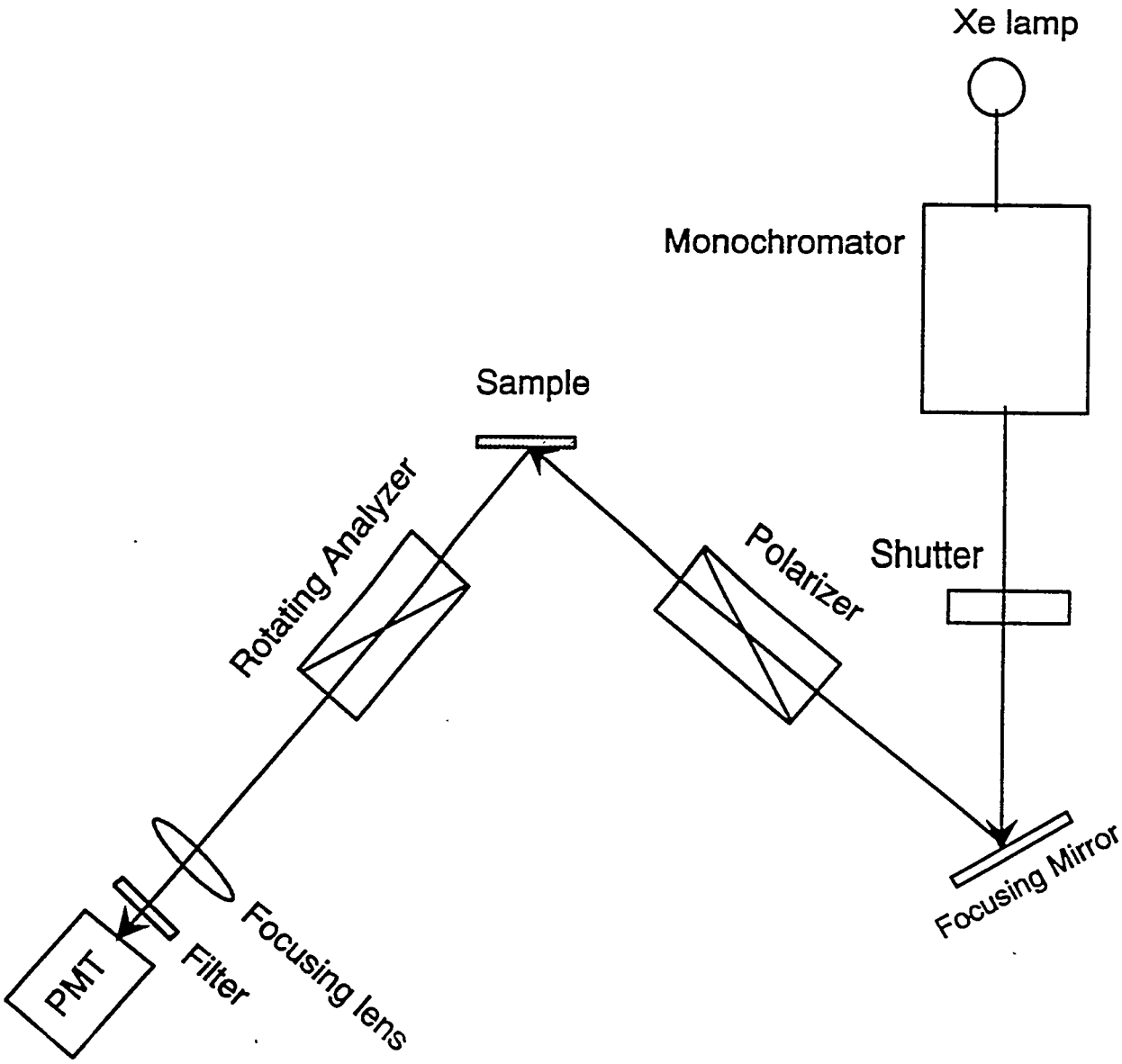

Figure 2.9 Schematic diagram of a rotating analyzer ellipsometer.

3 THEORY

Introduction

There are many theoretical approaches to understand the magneto-optical effects in solids [20, 21, 22, 23, 24]. We can divide the theories into two categories, macroscopic and microscopic. The macroscopic theory of the magneto-optical effects begins with the well-known Maxwell's equations. In the macroscopic description of magneto-optical effects, we derive relationships between macroscopic quantities like the dielectric tensor or optical tensor and magneto-optical parameters such as Kerr rotation and ellipticity. Even using the classical method, we can get some information about how magneto-optical phenomena appear in the solids. The microscopic theory of magneto-optical effects consists of two parts, description of intraband and interband transition contributions. Intraband transitions can be described by the Drude-Lorentz model and the description of interband transitions employs self-consistent relativistic spin-polarized electronic band structure calculations. From this electronic structure calculation we can derive the magneto-optical parameters. These macroscopic and microscopic analyses of magneto-optical effects can give us useful information for finding better magneto-optical media.

Sign conventions

The electromagnetic waves which are solutions of the wave equation can take their time-dependent part as exp($i\omega t$) or exp(-$i\omega t$). Depending on the choice of time dependence, the imaginary parts of the optical and magneto-optical constants have opposite signs. For example the complex refractive index $\tilde{n}$ takes the following forms

$$\begin{aligned} \tilde{n} &= n + ik \\ \tilde{n} &= n - ik \end{aligned} \tag{3.1}$$

according to the time dependence of the electromagnetic wave. With exp(-$i\omega t$) time dependence, the complex refractive index which has a positive imaginary part has to be used. Atkinson and Lissberger [25] discussed the sign conventions of the magneto-optical parameters in the Faraday and polar Kerr effects. Using a negative imaginary time exponent together with the dielectric tensor form of Eq. (3.2) has advantages over the positive imaginary time exponent. Therefore we adopted their sign conventions in describing the magneto-optical parameters in macroscopic theory and microscopic theory. That is, we chose the time dependence of the wave as exp(-$i\omega t$) and $\tilde{n} = n + ik$.

Macroscopic theory

If the magnetization vector points along the z-axis in a cubic crystal the complex dielectric tensor takes the following form

$$\overleftrightarrow{\tilde{\epsilon}} = \begin{pmatrix} \tilde{\epsilon}_{xx} & \tilde{\epsilon}_{xy} & 0 \\ -\tilde{\epsilon}_{xy} & \tilde{\epsilon}_{xx} & 0 \\ 0 & 0 & \tilde{\epsilon}_{zz} \end{pmatrix}, \tag{3.2}$$

where $\tilde{\epsilon}_{ij} = \epsilon_{1ij} + i\epsilon_{2ij}$ (i,j = x,y,z). The number of independent components in the complex dielectric tensor can be derived by using the invariance of the dielectric tensor under point symmetry operations [26]. The above dielectric tensor form is

applicable to any crystal systems which have at least three-fold rotational symmetry: hexagonal and trigonal, with a magnetic field applied along the z-axis. Because the optical conductivity tensor is simply related to the dielectric tensor we need to find the relationship between the magneto-optical parameters and either the dielectric tensor or the optical conductivity tensor. In this thesis we will find the relationship between the magneto-optical parameters and the optical conductivity tensor. In the case of magnetic materials, Maxwell's equations are written as

$$\vec{\nabla} \cdot \vec{D} = 4\pi\rho \tag{3.3}$$

$$\vec{\nabla} \times \vec{E} = -\frac{1}{c}\frac{\partial \vec{B}}{\partial t} \tag{3.4}$$

$$\vec{\nabla} \cdot \vec{B} = 0 \tag{3.5}$$

$$\vec{\nabla} \times \vec{H} = \frac{1}{c}\frac{\partial \vec{D}}{\partial t} + \frac{4\pi}{c}\vec{j}_f, \tag{3.6}$$

where $\vec{E}$, $\vec{D}$, $\vec{B}$ and $\vec{H}$ are the electric field, electric displacement, magnetic induction and magnetic field. Gaussian units are used. ρ is the charge density and $\vec{j}_f$ is the current density from free charges. In the optical region ($\nu = 10^{14} \sim 10^{15}\, Hz$) which is our major region of interest, we can set the permeability $\mu = 1$. The material equations are given by

$$\vec{D} = \overleftrightarrow{\epsilon} \cdot \vec{E} \tag{3.7}$$

$$\vec{B} = \vec{H} \tag{3.8}$$

$$\vec{j} = \overleftrightarrow{\sigma} \cdot \vec{E}, \tag{3.9}$$

where $\overleftrightarrow{\sigma}$ is the conductivity tensor. The contributions to the conductivity come from the free carriers and from the bound charges. The contribution from the latter to the current density is $\frac{\partial \vec{P}}{\partial t}$, where $\vec{P}$ is a polarization vector defined as the electric dipole moment per unit volume. Therefore the total current density can be written as

$$\vec{j}_{tot} = \vec{j}_f + \vec{j}_{bound} = \vec{j}_f + \frac{\partial \vec{P}}{\partial t}, \tag{3.10}$$

where $\vec{j}_{bound}$ is a current density from the bound carriers. We can treat the free charges in the electrically neutral solid as bound charges whose binding force is zero. Then the $\vec{j}_f$ term can be incorporated into the $\frac{\partial \vec{P}}{\partial t}$ term, that is

$$\vec{j}_{tot} = \frac{\partial \vec{P}}{\partial t} = \overleftrightarrow{\sigma} \cdot \vec{E} \,. \tag{3.11}$$

The polarization vector $\vec{P}$ is related to the electric field vector $\vec{E}$ and electric displacement vector $\vec{D}$ by

$$\vec{D} = \vec{E} + 4\pi \vec{P} \,. \tag{3.12}$$

We can rewrite Eq. (3.6) as follows

$$\begin{aligned} \vec{\nabla} \times \vec{H} &= \frac{1}{c}\frac{\partial \vec{E}}{\partial t} + \frac{4\pi}{c}\frac{\partial \vec{P}}{\partial t} + \frac{4\pi}{c}\vec{j}_f \\ &= \frac{1}{c}\frac{\partial \vec{E}}{\partial t} + \frac{4\pi}{c}\vec{j}_{tot} \\ &= \left((-i\omega)\frac{1}{c} + \frac{4\pi}{c}\overleftrightarrow{\sigma}\cdot\right)\vec{E} \,. \end{aligned} \tag{3.13}$$

With Eq. (3.4) and Eq. (3.6) we can derive the wave equation

$$\nabla^2 \vec{E} = -\frac{\omega^2}{c^2}\left(\overleftrightarrow{I} + \frac{4\pi i \overleftrightarrow{\sigma}}{\omega}\right)\cdot\vec{E} \tag{3.14}$$

$\overleftrightarrow{I}$ is the unit tensor. The dielectric tensor is related to the conductivity tensor by

$$\overleftrightarrow{\epsilon} = \overleftrightarrow{I} + \frac{4\pi i \overleftrightarrow{\sigma}}{\omega} \tag{3.15}$$

The solution of the wave equation has the form of plane waves $\vec{E} = E_o e^{i\left(\vec{k}\cdot\vec{r} - \omega t\right)}$, so $\nabla^2 \vec{E} = -k^2 \vec{E}$. Substituting $\nabla^2 \vec{E} = -k^2 \vec{E}$ and Eq. (3.15) in Eq. (3.14) gives

$$k^2 \vec{E} = \frac{\omega^2}{c^2}\overleftrightarrow{\epsilon}\cdot\vec{E} \,. \tag{3.16}$$

We can rewrite the above equation in Cartesian components as

$$k^2 E_i = \frac{\omega^2}{c^2}\sum_j \epsilon_{ij} E_j = k_o^2 \sum_j \epsilon_{ij} E_j \qquad (i,j = x,y,z)\,, \tag{3.17}$$

where k_o is the wave vector in vacuum. The ratio $\frac{k}{k_o}$ is the complex refractive index of the medium and is represented by $\tilde{n} = n + ik$. Then we can write Eq. (3.17) as

$$\tilde{n}^2 E_i - \sum_j \epsilon_{ij} E_j = 0 \qquad (i, j = x, y, z). \tag{3.18}$$

Substituting dielectric tensor (3.2) into Eq. (3.18) and setting the secular determinant equal to zero allows one to find the eigenvalues and eigenmodes, that is

$$\begin{vmatrix} \tilde{n}^2 - \tilde{\epsilon}_{xx} & -\tilde{\epsilon}_{xy} \\ \tilde{\epsilon}_{xy} & \tilde{n}^2 - \tilde{\epsilon}_{xx} \end{vmatrix} = 0. \tag{3.19}$$

Solving this secular equation leads to two $\tilde{n}^2$ eigenvalues, $\tilde{n}_+^2$ and $\tilde{n}_-^2$ as follows

$$\begin{aligned} \tilde{n}_+^2 &= \epsilon_{xx} + i\epsilon_{xy} \\ \tilde{n}_-^2 &= \epsilon_{xx} - i\epsilon_{xy}. \end{aligned} \tag{3.20}$$

By substituting $\tilde{n}^2 = \tilde{n}_\pm^2$ into the secular determinant, we can get the eigenmodes of light propagation in the medium where the magnetization is along the z-axis. For $\tilde{n}^2 = \tilde{n}_+^2$, we have $E_2 = iE_1$, which corresponds to left-circularly polarized light. The Jones vector representation for this is

$$\begin{pmatrix} 1 \\ i \end{pmatrix}. \tag{3.21}$$

For $\tilde{n}^2 = \tilde{n}_-^2$, we have $E_2 = -iE_1$, which corresponds to the right-circularly polarized light, with Jones vector representation

$$\begin{pmatrix} 1 \\ -i \end{pmatrix}. \tag{3.22}$$

These two eigenmodes propagate in the medium with different complex refractive indices $\tilde{n}_+$and $\tilde{n}_-$. These different complex refractive indices cause different phase velocities and different absorption between two modes. The difference of absorption between the two modes makes the transmitted light become elliptically polarized. The phase difference

between the right-and left-circularly polarized components leads to the rotation of the elliptically polarized light as it passes through the medium. The sign of the Faraday rotation θ_F and ellipticity ϵ_F is taken as positive if the sense of the rotation experienced by the transmitted elliptically polarized light is parallel to the magnetization direction as shown in Fig. 3.1. In Fig. 3.1 the incident light is linearly polarized along the x-axis. The linearly polarized light can be decomposed into right- and left-circularly polarized light. They experience different phase velocities and absorption. Combining the changed modes finally gives a Faraday rotation and ellipticity with a positive sign, corresponding to a clockwise rotation when viewed along the propagation direction, the same as that of the magnetization. For bulk samples, like single crystals or polycrystals, reflection measurements are generally used for studying magneto-optical effects. From the Fresnel equations the reflection coefficient $\tilde{r}$ for normal incidence is given by

$$\tilde{r} = \frac{\tilde{E}_r}{\tilde{E}_i} = \frac{\tilde{n} - 1}{\tilde{n} + 1}, \tag{3.23}$$

where $\tilde{E}_r$ is the amplitude of the reflected electric field and $\tilde{E}_i$ is the amplitude of the incident electric field. From this close relationship between the transmitted and reflected light, it is evident that right- and left-circularly polarized light will be eigenmodes of propagation of the reflected light as in the Faraday geometry. In that case the reflection coefficients for left and right circular polarization are given by

$$\tilde{r}_{\pm} = \frac{\tilde{n}_{\pm} - 1}{\tilde{n}_{\pm} + 1} = \frac{\sqrt{\tilde{\epsilon}_{\pm}} - 1}{\sqrt{\tilde{\epsilon}_{\pm}} + 1} \tag{3.24}$$

By using the above reflection coefficients for right-and left-circular polarized light, we can derive the relation between the dielectric tensor and the magneto-optical parameters such as the Kerr rotation and ellipticity. For incident light which is linearly polarized along the x-axis as shown, in Fig. 3.1, we can express linearly polarized light in terms of circularly polarized eigenmodes as

$$\tilde{E}_i = \frac{1}{2} E_o \left(\hat{e}_+ + \hat{e}_- \right), \tag{3.25}$$

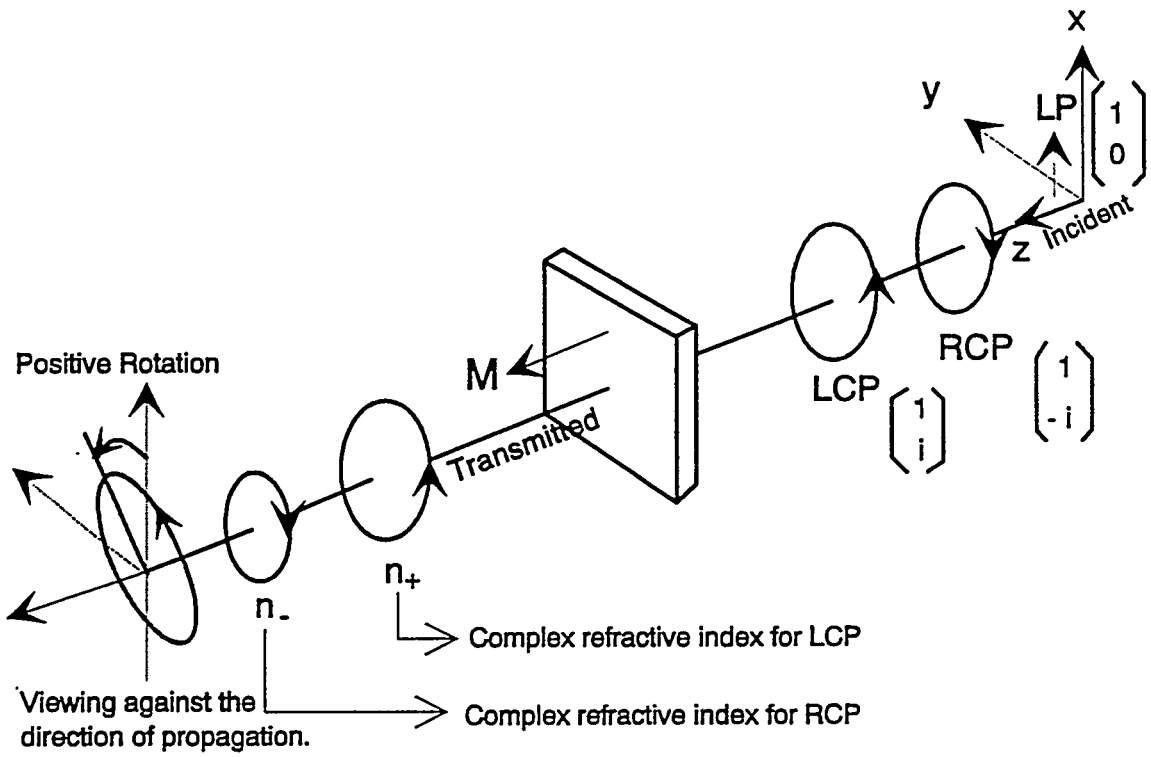

Figure 3.1 Faraday effect and sense of rotation

where

$$\begin{aligned} \hat{e}_+ &= \frac{1}{\sqrt{2}}(\hat{e}_x + i\hat{e}_y), \\ \hat{e}_- &= \frac{1}{\sqrt{2}}(\hat{e}_x - i\hat{e}_y). \end{aligned} \tag{3.26}$$

Then the reflected beam will be

$$\tilde{E}_r = \frac{1}{2}\left(\tilde{r}_+ \hat{e}_+ + \tilde{r}_- \hat{e}_-\right) \tag{3.27}$$

where $\tilde{r}_\pm$ are the reflection coefficients for left- and right-circularly polarized light respectively. If we express the reflected light in cartesian coordinates, then

$$\begin{aligned} \tilde{E}_r &= \frac{1}{2}\left\{\tilde{r}_+ (\hat{e}_x + i\hat{e}_y) + \tilde{r}_- (\hat{e}_x - i\hat{e}_y)\right\} \\ &= \frac{1}{2}\left\{\left(\tilde{r}_+ + \tilde{r}_-\right)\hat{e}_x + i\left(\tilde{r}_+ - \tilde{r}_-\right)\hat{e}_y\right\} \\ &= \frac{1}{2}\left(\tilde{r}_+ + \tilde{r}_-\right)\left\{\hat{e}_x + i\frac{\tilde{r}_+ - \tilde{r}_-}{\tilde{r}_+ + \tilde{r}_-}\hat{e}_y\right\}, \end{aligned} \tag{3.28}$$

which gives the complex Kerr rotation

$$\begin{aligned} \Psi &= i\frac{\tilde{r}_+ - \tilde{r}_-}{\tilde{r}_+ + \tilde{r}_-} \\ &= i\frac{\sqrt{\tilde{\epsilon}_+} - \sqrt{\tilde{\epsilon}_-}}{\sqrt{\tilde{\epsilon}_+}\sqrt{\tilde{\epsilon}_-} - 1} \\ &= i\frac{\sqrt{\tilde{\epsilon}_{xx} + i\,\tilde{\epsilon}_{xy}} - \sqrt{\tilde{\epsilon}_{xx} - i\,\tilde{\epsilon}_{xy}}}{\sqrt{\tilde{\epsilon}_{xx} + i\,\tilde{\epsilon}_{xy}}\sqrt{\tilde{\epsilon}_{xx} - i\,\tilde{\epsilon}_{xy}} - 1}. \end{aligned} \tag{3.29}$$

Since

$$\left|\tilde{\epsilon}_{xy}\right| \ll \left|\tilde{\epsilon}_{xx}\right|, \tag{3.30}$$

we can simplify the complex Kerr rotation as

$$\Psi = \frac{\tilde{\epsilon}_{xy}}{\left(1 - \tilde{\epsilon}_{xx}\right)\sqrt{\tilde{\epsilon}_{xx}}} \tag{3.31}$$

From the relation between $\overleftrightarrow{\epsilon}$ and $\overleftrightarrow{\sigma}$, the complex Kerr rotation can be expressed by the conductivity tensor components as

$$\Psi = \frac{-\tilde{\sigma}_{xy}}{\tilde{\sigma}_{xx}\sqrt{1 + \frac{i4\pi}{\omega}\tilde{\sigma}_{xx}}} \tag{3.32}$$

This is the formula we will use to calculate the complex Kerr angle. The above equation can be rewritten with optical constants as

$$\Psi = \frac{4\pi}{\omega}\left[\frac{\sigma_{xy}}{\left(1-(n+ik)^2\right)(n+ik)}\right] \tag{3.33}$$

where n and k are the refractive index and extinction index respectively which come from the diagonal optical conductivity. The Kerr rotation angle and ellipticity are the real part and imaginary part of the above equation, respectively. From the above equation, we see that the magneto-optical parameters (Kerr rotation and ellipticity) are directly related to the off-diagonal optical conductivity σ_{xy}. The off-diagonal optical conductivity is proportional to the product of the spin-orbit interaction Δ_{s-o} and the net spin polarization $\Delta n(\omega)$=$n_{\uparrow}(\omega) - n_{\downarrow}(\omega)$, that is, σ_{xy} is proportional to $\Delta_{s-o} \times \Delta n(\omega)$. If either Δ_{s-o} or $\Delta n(\omega)$ is zero, the off-diagonal optical conductivity will disappear and there will be no magneto-optical effects. The experimental values of the optical constants n and k can be obtained from ellipsometry and the magneto-optical parameters are obtained from the magneto-optical polar Kerr spectrometer. With these measured quantities, we can derive experimental spectra for the off-diagonal conductivity $\tilde{\sigma}_{xy}$. These experimental spectra are compared with the theoretical spectra from self-consistent electronic structure calculations. For this connection between optical and magneto-optical parameters and the off-diagonal conductivity, we rewrite the complex Kerr rotation and ellipticity in terms of complex refractive indices for right and left circularly polarized light. Using

$$\sqrt{\tilde{\epsilon}_{\pm}} = \tilde{n}_{\pm}, \tag{3.34}$$

from Eq. (3.29), we can rewrite Ψ as

$$\Psi = \theta_K + i\epsilon_K = i\frac{\tilde{n}_+ - \tilde{n}_-}{\tilde{n}_+\tilde{n}_- - 1} = i\,\tilde{\psi}\,. \tag{3.35}$$

From the above equation, we can derive the following relations

$$\theta_K = -Im\left(\frac{\tilde{n}_+ - \tilde{n}_-}{\tilde{n}_+\tilde{n}_- - 1}\right)$$

$$\epsilon_K = Re\left(\frac{\tilde{n}_+ - \tilde{n}_-}{\tilde{n}_+\tilde{n}_- - 1}\right) \tag{3.36}$$

By using Eq. (3.34) and the following equations,

$$\begin{aligned} \overleftrightarrow{\epsilon}_\pm &= \overleftrightarrow{I} + \frac{4\pi i \overleftrightarrow{\sigma}_\pm}{\omega} \\ \tilde{\sigma}_\pm &= \tilde{\sigma}_{xx} \pm i\,\tilde{\sigma}_{xy}, \end{aligned} \tag{3.37}$$

$\tilde{\psi}$ can be related to the conductivity by

$$\frac{-\tilde{\sigma}_{xy}}{i\,\tilde{\sigma}_{xx}\tilde{n}} = \frac{\tilde{n}_+ - \tilde{n}_-}{\tilde{n}_+\tilde{n}_- - 1}, \tag{3.38}$$

where we take the approximation that $\tilde{n} \cong \frac{1}{2}\left(\tilde{n}_+ + \tilde{n}_-\right)$. Using $\tilde{n}= n + ik$, and $\tilde{\sigma}_{ij}= \sigma_{1ij} + i\sigma_{2ij}$ Eq. (3.38) can be expressed as

$$\frac{-\tilde{\sigma}_{xy}}{i\,\tilde{\sigma}_{xx}\tilde{n}} = \frac{(B'\sigma_{1xy} - A'\sigma_{2xy}) + i\left(A'\sigma_{1xy} + B'\sigma_{2xy}\right)}{A'^2 + B'^2}, \tag{3.39}$$

where A' and B' are given by

$$\begin{aligned} A' &= \frac{\omega}{4\pi}\left(-k^3 + 3n^2k - k\right) \\ B' &= \frac{\omega}{4\pi}\left(-n^3 + 3k^2n + n\right). \end{aligned} \tag{3.40}$$

From Eq. (3.36)

$$\begin{aligned} \theta_K &= \frac{-A'\sigma_{1xy} - B'\sigma_{2xy}}{A'^2 + B'^2} \\ \epsilon_K &= \frac{B'\sigma_{1xy} - A'\sigma_{2xy}}{A'^2 + B'^2}. \end{aligned} \tag{3.41}$$

We can express σ_{1xy} and σ_{2xy} in terms of θ_K, ϵ_K, n and k as

$$\begin{aligned} \sigma_{1xy} &= \frac{\omega}{4\pi}\left(-A\theta_K + B\epsilon_K\right) \\ \sigma_{2xy} &= -\frac{\omega}{4\pi}(B\theta_K + A\epsilon_K), \end{aligned} \tag{3.42}$$

where

$$\begin{aligned} A &= -k^3 + 3n^2k - k \\ B &= -n^3 + 3k^2n + n \end{aligned} \tag{3.43}$$

Multiplying $\hbar$ to numerator and denominator in Eq. (3.42) and using $4\pi\hbar = 8.2714 \times 10^{-15} eV \cdot \sec$, we can express Eq. (3.42) in numerical values as

$$\begin{aligned} \sigma_{1xy} &= 0.1209 \times 10^{15} \left(-A\theta_K + B\epsilon_K\right) \cdot \left(\frac{\hbar\omega}{eV \cdot \sec}\right) \\ \sigma_{2xy} &= -0.1209 \times 10^{15} \left(B\theta_K + A\epsilon_K\right) \cdot \left(\frac{\hbar\omega}{eV \cdot \sec}\right), \end{aligned} \tag{3.44}$$

where $\hbar\omega$ is the photon energy in units of eV.

Microscopic theory

The dielectric tensor or conductivity tensor contains two physically distinct contributions, namely intraband and interband contributions. Intraband conductivity originates from electromagnetic-field-induced displacements of the free conduction electrons, described phenomenologically with an empirical Drude model. Intraband contributions are dominant in the IR part of the magneto-optical spectra and as the energy increases, their contribution to the conductivity become less important. Interband conductivity is caused by the direct band-to-band transitions. Interband conductivity is dominant at visible or UV part of the spectrum.

Intraband contributions to magneto-optical effects

The intraband contributions to the conductivity in nonmagnetic materials can be described by the simple Drude-Lorentz model. The equation of motion of an electron in an electric field $\vec{E}$ of the electromagnetic radiation and in an external static magnetic field $\vec{B}$ is written as

$$m^* \frac{d\,\vec{v}}{dt} + m^* \gamma\, \vec{v} = e\,\vec{E} + e\frac{\vec{v}}{c} \times \vec{B} \tag{3.45}$$

where m^* is the effective mass of the electron , γ is a damping constant and $\vec{v} = \frac{d\vec{r}}{dt}$. As in the Faraday geometry, the electric field vector can be written with right-and left-

circularly polarized components as

$$\tilde{E}_{\pm}=\tilde{E}_{\circ}\,\hat{e}_{\pm}e^{i(kz-\omega t)}, \tag{3.46}$$

where $\hat{e}_{\pm}$ is defined in Eq. (3.26). We assume that the time dependence of $\tilde{r}_{\pm}$ follows the time dependence of $\tilde{E}_{\pm}$. Then we have $\tilde{r}_{\pm}$, given by

$$\tilde{r}_{\pm}=\frac{e\,\tilde{E}_{\pm}}{m^{*}\omega\left(-\omega\pm\omega_{c}+i\gamma\right)}, \tag{3.47}$$

where $\omega_c = \frac{eB}{mc}$. The complex dielectric functions for right and left circularly polarized light are expressed as

$$\tilde{\epsilon}_{\pm}=1+\frac{4\pi Ne\,\tilde{r}_{\pm}}{\tilde{E}_{\pm}}. \tag{3.48}$$

Substituting Eq. (3.47) into Eq. (3.48) yields

$$\tilde{\epsilon}_{\pm}=1+\frac{4\pi Ne^{2}}{m^{*}\omega\left(-\omega\pm\omega_{c}+i\gamma\right)}. \tag{3.49}$$

$\tilde{\epsilon}_{\pm}$is related to its cartesian components by

$$\tilde{\epsilon}_{\pm}=\tilde{\epsilon}_{xx}\pm i\,\tilde{\epsilon}_{xy}\,. \tag{3.50}$$

From Eq. (3.49), we find the off-diagonal dielectric functions for right-and left-circularly polarized components of nonmagnetic materials in an applied magnetic field are split by the cyclotron frequency ω_c. Experimentally, this splitting of the plasma frequency ω_p by ω_c has been observed in the reflection spectra near the plasma minimum of silver [27] and doped InSb [28]. It agreed well with the result from the Drude-Lorentz model. The off-diagonal component of the dielectric tensor can be obtained from Eq. (3.50) as

$$\tilde{\epsilon}_{xy}=\frac{\tilde{\epsilon}_{+}-\tilde{\epsilon}_{-}}{2i}=\frac{-2\omega_{c}A}{\left(\omega-i\gamma\right)^{2}-\omega_{c}^{2}}, \tag{3.51}$$

where A=$\frac{1}{2i}\frac{4\pi Ne^{2}}{m^{*}\omega}$. From Eq. (3.15) we can derive the following relation between the off-diagonal conductivity and the off-diagonal dielectric tensor component:

$$\tilde{\sigma}_{xy}=\frac{\omega\,\tilde{\epsilon}_{xy}}{4\pi i}. \tag{3.52}$$

Using this, the imaginary part of the off-diagonal conductivity is

$$\sigma_{2xy} = -\frac{2\omega_c\omega\gamma\omega_p^2}{\left(\omega^2-\omega_c^2-\gamma^2\right)^2+4\omega^2\gamma^2}, \tag{3.53}$$

where $\omega_p^2 = \frac{4\pi Ne^2}{m^*}$ In the high frequency limit, $\sigma_{2xy} \propto \frac{1}{\omega^3}$ and we see that as the photon energy increases, the intraband contribution decreases quickly. In magnetically ordered materials, the phenomenological theory of the off-diagonal conductivity $\tilde{\sigma}_{xy}$ was expanded in the framework of a skew scattering theory by Erskine and Stern [29] and improved by Reim *et al.* [30]. They added a new term not included in the Drude model. They have shown that the off-diagonal conductivity can be expressed as

$$\tilde{\sigma}_{xy} = \frac{\omega_p^2}{4\pi} < \sigma_z > \left\{\frac{-\Omega}{\Omega^2+(i\omega+\gamma)^2} + \frac{|p_o|}{ev_o}\left(1-\frac{i\omega\left(\gamma+i\omega\right)}{\Omega^2+\left(\gamma+i\omega\right)^2}\right)\right\}, \tag{3.54}$$

where Ω is the skew-scattering frequency which arises from the spin-orbit asymmetric scattering, $< \sigma_z >= \frac{(n_\uparrow - n_\downarrow)}{(n_\uparrow + n_\downarrow)}$ is the spin polarization. $\gamma = \frac{1}{\tau}$ is the damping term, v_o is the Fermi velocity, ω_p is the plasma frequency, and $|p_o|$ is the maximum value of the dipole moment per unit cell due to spin-orbit interactions. The absorption part of $\tilde{\sigma}_{xy}$can be obtained by simple calculation from Eq. (3.54) and the result is given by

$$\sigma_{2xy} = \omega_p^2 < \sigma_z > \left[\frac{2\gamma\Omega\omega}{\left(\Omega^2+\gamma^2-\omega^2\right)^2+4\gamma^2\omega^2} - \frac{|p_o|}{ev_o}\frac{\omega\gamma\left(\Omega^2+\gamma^2+\omega^2\right)}{\left(\Omega^2+\gamma^2-\omega^2\right)^2+4\gamma^2\omega^2}\right]. \tag{3.55}$$

The first term is identical to the classical Drude-Lorenz term except that $< \sigma_z > \Omega$ replaced the cyclotron frequency ω_c. This first term gives a $\frac{1}{\omega^3}$ frequency dependence for $\omega \gg \Omega, \gamma$ as in the classical Drude-Lorenz model. The second term of Eq. (3.55) is proportional to $\frac{1}{\omega}$ for $\omega \gg \Omega, \gamma$. The total absorption part of σ_{2xy} is the sum of intraband and interband contributions, that is

$$\sigma_{2xy}^{tot} = \sigma_{2xy}^{Inter} + \sigma_{2xy}^{Intra}, \tag{3.56}$$

where σ_{2xy}^{Inter} is the absorption part of σ_{2xy} due to interband transitions. For $\omega \gg \Omega, \gamma$, the $\sigma_{2xy}^{Intra} \cong \frac{C}{\omega}$, therefore

$$\sigma_{2xy} = \sigma_{2xy}^{Inter} + \frac{C}{\omega}. \tag{3.57}$$

By multiplying both sides by ω, we obtain

$$\omega\sigma_{2xy}^{Inter} = \omega\sigma_{2xy}^{tot} - C. \tag{3.58}$$

That is, by subtracting the constant intraband background of intraband contributions from the measured absorptive part of the off-diagonal conductivity, we can have only the interband transitions. Erskine and Stern [29] have estimated the constant intra-band contribution C to $\omega\sigma_{2xy}^{tot}$ in Gd to be about 1.1 in units of (10^{29} sec^{-2}).

Interband contributions to magneto-optical effects

The macroscopic diagonal and off-diagonal part of the conductivity tensor are related to microscopic optical transitions through the Kubo formula within the one-particle band theory. A detailed derivation can be found in Wang's thesis [31]. By using Kubo's linear response theory [32], one obtains the following forms for the interband contribution to the conductivity tensor.

$$\tilde{\sigma}_{xx}(\omega) = \frac{ie^2}{m^2 h\Omega}\sum_k\sum_{n,l} f(\omega_l)(1-f(\omega_n))\left(\frac{\left|\pi_{nl}^{+}\right|^2+\left|\pi_{nl}^{-}\right|^2}{2\omega_{nl}}\right)\left(\frac{1}{\omega-\omega_{nl}+i\epsilon}+\frac{1}{\omega+\omega_{nl}+i\epsilon}\right) \tag{3.59}$$

$$\tilde{\sigma}_{xy}(\omega) = \frac{e^2}{m^2 h\Omega}\sum_k\sum_{n,l} f(\omega_l)(1-f(\omega_n))\left(\frac{\left|\pi_{nl}^{+}\right|^2-\left|\pi_{nl}^{-}\right|^2}{2\omega_{nl}}\right)\left(\frac{1}{\omega-\omega_{nl}+i\epsilon}-\frac{1}{\omega+\omega_{nl}+i\epsilon}\right), \tag{3.60}$$

where $f(\omega)$ is the Fermi distribution function and l, n stand for the occupied and unoccupied energy band states at wave vector k, respectively. The momentum operator is expressed by

$$\vec{\pi}=\vec{p}+\frac{\hbar}{4mc^2}\vec{\sigma}\times\vec{\nabla}V \tag{3.61}$$

and

$$\pi^{\pm} = \frac{1}{\sqrt{2}}(\mp\pi_x + i\pi_y). \tag{3.62}$$

$\pi_{nl}^{\pm}(k)$ are matrix elements of the left and right circularly polarized components of the momentum operator respectively. In Eq. (3.61), $\vec{p}$ is the momentum operator and

$\vec{\sigma} \times \vec{\nabla} V$ represents the spin-orbit contribution to the matrix element. It is well known that in determining the magneto-optical effect the spin-orbit interaction which causes a splitting of the degeneracies of the energy bands at high simmetry points or lines in k-space. and an exchange splitting in the magnetic materials play major roles [33]. The form of spin-orbit interaction added to the one-electron Hamiltonian is written as

$$H_{SO} = \frac{h}{8m^2c^2\pi} \vec{p} \cdot \left(\vec{\sigma} \times \vec{\nabla} V \right) \tag{3.63}$$

where $\vec{\nabla} V$ is the electric field generated by an effective potential due to not only all of the other electrons in the solid but also the nuclear cores and $\vec{\sigma}$ is the Pauli spin operator. The spin-orbit interaction H_{SO} couples the spin-up and spin-down states and doubles the size of the Hamiltonian matrix from that of the scalar relativistic one spin Hamiltonian matrix. In addition, spin-orbit interaction couples the orbital angular magnetic momentum of the electron to its own spin magnetic moment. The crystalline field, having the symmetry of the crystal, acts on a particular lattice atom surrounded by the symmetrically located neighbouring atoms in the crystal. Therefore the shape of the orbitals in the particular atom will be changed into asymmetrical form from the symmetrical shape in the isolated atom due to the crystalline field. This is a kind of coupling between the electron orbital and the crystal lattice. The spin-spin coupling originating from the exchange interaction is isotropic, that is, it is not dependent on the angle between the axis of the spin and the crystal lattice. Therefore there will be no crystal anisotropy by the spin-spin coupling alone. Due to the spin-orbit coupling, the crystal lattice and the spin are coupled by a mediation of the orbital of electron. This leads to a crystalline anisotropy in that the physical properties are dependent on the different directions of the crystal axes. One example is the magnetization curves for single crystals of iron, nickel, and cobalt. The magnetization curves are different for different crystal axes. As a consequence, the spin-orbit interaction causes a reduction in the symmetry of the crystal and removes the accidental degeneracies of the electronic

structure at high symmetry points or lines in k-space. The splitting due to the spin-orbit interaction is an essential part of the magneto-optical Kerr effect (MOKE). The effects of the spin-orbit interaction on the physical properties have been studied by many authors [34, 35]. The other important contributions to the magneto-optical effects are the exchange effects arising from the Stoner's band model of ferromagnetism, accounting for the splitting of the degeneracy of spin-up and spin-down states. Erskine and Stern [29] showed how the spin-orbit interaction and exchange splitting affect the absorptive part of the off-diagonal conductivity by using an atomic picture. From these theoretical analyses, the origin of magneto-optical effects of the rare earth-transition intermetallic compound will be studied in the next chapters. The tight-binding linear muffin tin orbital method based on the local spin-density approximation will be dealt with in the following chapters.

4 OPTICAL PROPERTIES AND ELECTRONIC STRUCTURE OF $LuAl_2$ AND $YbAl_2$

Introduction

The electronic, magnetic and optical properties of the RAl_2 (R=Rare Earth) intermetallic compounds have been investigated theoretically and experimentally by many authors [36, 37]. Particularly, the role of 4f electrons in determining the physical characteristics of these materials is still under investigation. Jarlborg *et al.* [38] calculated the energy band structure of $CeAl_2$, $LaAl_2$ and YAl_2 using the linear muffin-tin orbital (LMTO) method, neglecting spin-orbit coupling for the valence states. They found that the rare-earth atoms are the dominant factor in determining the electronic structure near the Fermi energy because the f-bands are located close to the Fermi level. Kim and Lynch [39] measured the optical properties of $CeAl_2$ and $LuAl_2$ using rotating-polarizer-analyzer ellipsometry and reflectivity measurements in the 0.04-4.5 eV region at room temperature. They found that the optical conductivity of $CeAl_2$ has structures at 0.1 eV and 1.0 eV while $LuAl_2$ has no structure below 1eV. The difference in optical conductivities between $CeAl_2$ and $LuAl_2$ comes from the different electronic structures of $CeAl_2$ and $LuAl_2$, especially the 4f states. In the case of $CeAl_2$, the positions of 4f electrons are located near the Fermi level while for $LuAl_2$, the positions of 4f electrons are located well below the Fermi level. Therefore in the case of $CeAl_2$, the 4f states can contribute to the interband transitions. But for $LuAl_2$, the interband contributions by the 4f states are ignorable because the positions of the 4f electrons are located well below the Fermi level.

Metallic Lu is trivalent with a hcp crystal structure while metallic Yb is divalent with a stable hcp crystal structure below room temperature. Above room temperature, a fcc crystal structure becomes more stable. The electronic structure for the elemental Yb in metallic state has been calculated by the relativistic LMTO method [40]. The calculated 4f bands are separated by the spin-orbit interaction, $4f_{5/2}$ and $4f_{7/2}$, and the location of the fully occupied split bands is at 0.3 eV and 1.64 eV below the Fermi energy, respectively. X-ray photoemission measurements for evaporated films of ytterbium showed that the 4f levels are split and they are located at 1.4 ± 0.4 eV and 2.7 ± 0.4 eV below the Fermi level [41]. They interpreted the split a being due to the spin-orbit interaction in the 4f levels. The difference of the 4f levels between theory and experiment is about 1 eV, which is not so bad when we consider that Yb is a rare-earth material. The direct comparison between the calculated one-electron density of states (DOS) based on LDA and the XPS spectral weight which shows the DOS final states of the system may be not adequate. This is true for highly correlated systems like rare-earths. For this system, the intra-atomic Coulomb correlation U is large, therefore the Koopmans' theorem can not be applicable [42]. Furthermore if the rare-earth has an unfilled open shell like Gd, the XPS final-state spectrum is determined not only by the electron emitted but also by the remaining electrons in the unfilled shell. Therefore describing the final state spectrum with the one-electron approximation is not appropriate for an open shell 4f system. The theoretical estimation of the 4f-electron excitation energies which can be measured by XPS and BIS has been performed by taking the total energy difference between the initial ground state and the final excited state obtained by the self-consistent LDA calculations [43]. But for the closed shell, the final XPS spectral weight can be compared with the DOS obtained by an one-electron approximation based on the LDA because for the closed shell, one hole is generated after one electron emitted from the 4f shell and the final state can be described by the single hole. There is no intra-atomic Coulomb repulsion for this one-hole state. For these reasons, a first-principles LDA calculation

for Lu and Yb metals treating 4f electrons as valence electrons describes several experimental results well. Tibbetts and Harmon [44] calculated the electronic structure of hcp Lu using a linearized augmented plane wave (LAPW) method with the Hedin-Lundqvist local density approximation for the exchange and correlation. The shape of the their calculated Fermi surfaces was in good agreement with the experimental Fermi surface. Min *et al.* [45] have calculated the electronic structure and structural properties of Lu at normal or under pressure with the self-consistent LMTO within a LDA. They calculated the total energies E_{tot}, Wigner-Seitz radii r_{WS}, bulk moduli B, and the cohesive energies E_{coh} by treating the 4f electrons as either valence and core electrons. The differences of the above physical quantities between the different treatments of 4f electrons are very small for Lu. This is because the 4f states of Lu are located well below the Fermi level. and the hybridization of 4f states with the other valence electrons is negligible. In the case of Yb, the situation is more complicated than Lu because the positions of 4f states in the electronic structure are close to the Fermi level. In this case we can not treat the 4f electrons as core electrons in optics calculations because the 4f states near the Fermi level can be involved in interband optical transitions. Also for rare-earths, the magnetic properties come from the electrons in the open 4f-shells. Therefore treating the 4f electrons of the rare-earths as valence electrons seems to be more appropriate for optics and magneto-optics calculations. The rare-earth can be combined with transition metals such as Fe, Co to become intermetallic compounds. These compounds, which are the topics for the next chapters, show many interesting electronic, optical, magnetic, and magneto-optical properties [46, 47]. In this chapter, instead of the 3d metals, a nonmagnetic material, Al, will be combined with rare-earths (Lu, Yb). The crystal structures of intermetallic compounds $LuAl_2$ and $YbAl_2$ are cubic Laves C15 and nonmagnetic. Compared to $LuAl_2$, $YbAl_2$ shows many interesting physical properties due to the ambivalent character of Yb. When Yb forms intermetallic compounds such as $YbAl_2$ and $YbAl_3$, the valence of Yb changes, i.e. the ground state of $YbAl_2$ can not be

described as only divalent, but a combination of divalent Yb^{2+} ($4f^{14}$) and trivalent Yb^{3+} ($4f^{13}$) configurations. Therefore if v is a mean valence of $YbAl_2$, the mathematical form of the ground state of $YbAl_2$ can be written as (3-v)($4f^{14}$)+(v-2)($4f^{13}$) [48]. For $YbAl_2$, the mean valence, v of Yb changes from 2.0 at -200°C, to 2.08 at room temperature, and 2.44 at 600°C [49]. Oh [50] *et al.* observed the valence change in $YbAl_2$ from XPS and BIS spectra. Their valences for $YbAl_2$ are generally larger than those of [49]. The two peaks A and B in the final state of $YbAl_2$ in Fig. 1 of ref. [50] correspond to $4f^{14} \rightarrow 4f^{13}$ and $4f^{13} \rightarrow 4f^{12}$, respectively. From the intensity ratio between the two spectral weights, the valence v can be obtained [50]. The trivalent peak B ($4f^{13} \rightarrow 4f^{12}$) is located about 9 eV below the Fermi level and the divalent peak A ($4f^{14} \rightarrow 4f^{13}$) is located close to the Fermi level and split due to the spin-orbit interaction. The detailed study of the 4f states of $YbAl_2$ compared to that of $LuAl_2$ will be discussed with the analysis of density of states obtained by the TB-LMTO method based on the LDA. $LuAl_2$ can be a good reference material for the investigation of the involvement of 4f electrons [39] in the optical transitions in $YbAl_2$ because the 4f states of $YbAl_2$ are located close to the Fermi energy while those of $LuAl_2$ are located well below the Fermi energy. Therefore, by comparing optical spectra in the low-energy region one can get information on the role of 4f electrons in optical transitions. Another difference between $LuAl_2$ and $YbAl_2$ related to the 4f states is the electronic specific heat coefficient which gives information on the electronic density of states at the Fermi level. The electronic specific heat coefficient of $YbAl_2$ is three times bigger than that of $LuAl_2$, even though the number of conduction electrons is smaller than that of $LuAl_2$. This strongly indicates that the Yb 4f-states contribute to the density of states at the Fermi level. Therefore studying the electronic properties of $LuAl_2$ and $YbAl_2$ within the LDA formalism can be useful, although any involvement of 4f bands in the optical properties would have to be carefully examined. The mean valence of $YbAl_2$ changes as temperature varies. At zero temperature the ground state of $YbAl_2$ is divalent. The theoretical calculations are performed at zero

temperature. Therefore in the calculation of the theoretical optical conductivity, we treated $YbAl_2$ as in the divalent configuration in the ground state. But the experiment was performed at room temperature, so Yb in $YbAl_2$ may be not be divalent at room temperature. But since the effect of trivalent Yb appears well below the Fermi level, which is beyond the experimental spectral range in optical measurements, we can treat $YbAl_2$ as divalent. Details will be discussed in the Results and Discussion part.

It is well known that the magneto-optical Kerr effect (MOKE) is proportional to the product of the spin-orbit interaction and the exchange splitting which causes the net spin polarization. The 4f shells of $LuAl_2$ and $YbAl_2$ are fully occupied, so the exchange splitting is zero. As a result of this, even though the spin-orbit splitting is large, the MOKE will not appear in these metals. The theoretical calculations show also that the MOKE for these non magnetic materials are almost zero throughout the whole energy range. Even though they do not show MOKE, the study of the theorerical and experimental diagonal part of the optical conductivity for $LuAl_2$ and $YbAl_2$ could be a starting point for the R(=rare-earth)Fe_2 and $GdCo_2$ intermetallic compounds which have the same cubic Laves $MgCu_2$ crystal structure, the samples for MOKE study in this thesis. Rare earths and their intermetallic compounds exposed to air can not avoid of oxidation on the surface. The treatment of oxidation on the surface of the rare-earth compounds is covered in this chapter. For this, effects of oxidation on the sample surface were included by the three-phase model. We found by this model that the thin oxide layer reduces the magnitude of the optical conductivity. The real part of the diagonal conductivity calculated by the TB-LMTO method within the LDA formalism, and the density of states (DOS) and band structure of $LuAl_2$ and $YbAl_2$ will be presented in this chapter. The agreement between theory and experiment is excellent, except for magnitude differences in optical conductivities.

Sample preparation and characterization

Single crystals have some advantages in optical measurement over polycrystalline samples or thin films in that they have a higher purity which is manifested in reproducibility of data with samples from different growths. The disadvantage of single crystals is frequently their small size, leading to difficulty in alignment in ellipsometry measurements. Single crystals of $YbAl_2$ and $LuAl_2$ were prepared via two different flux growth techniques. In the case of $YbAl_2$, elemental Yb and Al in the ratio of $Yb_{.55}Al_{.45}$ was placed in a Ta crucible which was placed in a sealed quartz tube, then heated to $1190°C$ and slowly cooled to 750°, at which temperature the crystals were removed from the melt. The reason for not doing arc-melt of YbAl is due to the low vapor pressure of Yb. The Al-Yb phase diagram is shown in Fig. 4.1. The crystals grown by this technique are octahedral, with typical dimensions of $2 \times 2 \times 0.5\ mm^3$. However, when applied to $LuAl_2$, this technique produces small, intergrown crystals. Hence, $LuAl_2$ was grown from a third element flux, in this case indium (In). The ternary melt was cooled slowly to $725°C$, at which temperature the crystals were removed from the flux. These crystals were larger than those produced from the binary melt, and had both octahedral and plate-like morphologies. In the case of the plate-like samples, the growth direction is along [111]. The surface of the grown single crystal is a little bit dim due to remnant flux on the surface of the crystal. We used only an alumina of 0.05 μm diameter to remove any possible remnant flux on the surface of the single crystal. After a short period of polishing, the surface of the single crystal became mirror-like and did not require further treatment. X-ray powder diffraction patterns of $LuAl_2$ and $YbAl_2$ were obtained by crushing the single crystals. The patterns are shown in Fig. 4.2 and Fig. 4.3. The lower limit for presence of second phases in X-ray pattern is below 1 % for both samples.

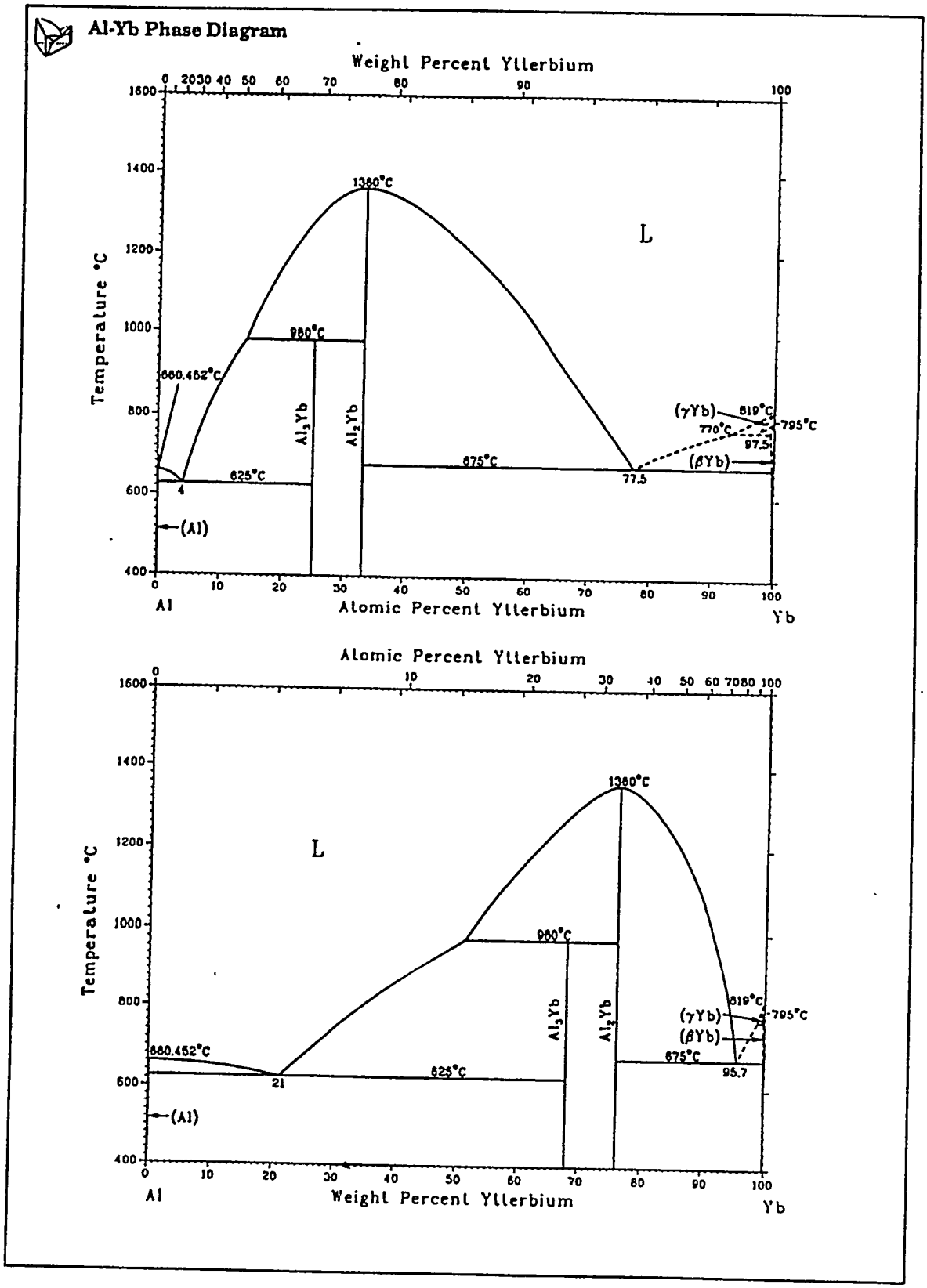

Figure 4.1 Al-Yb Phase Diagram [51].

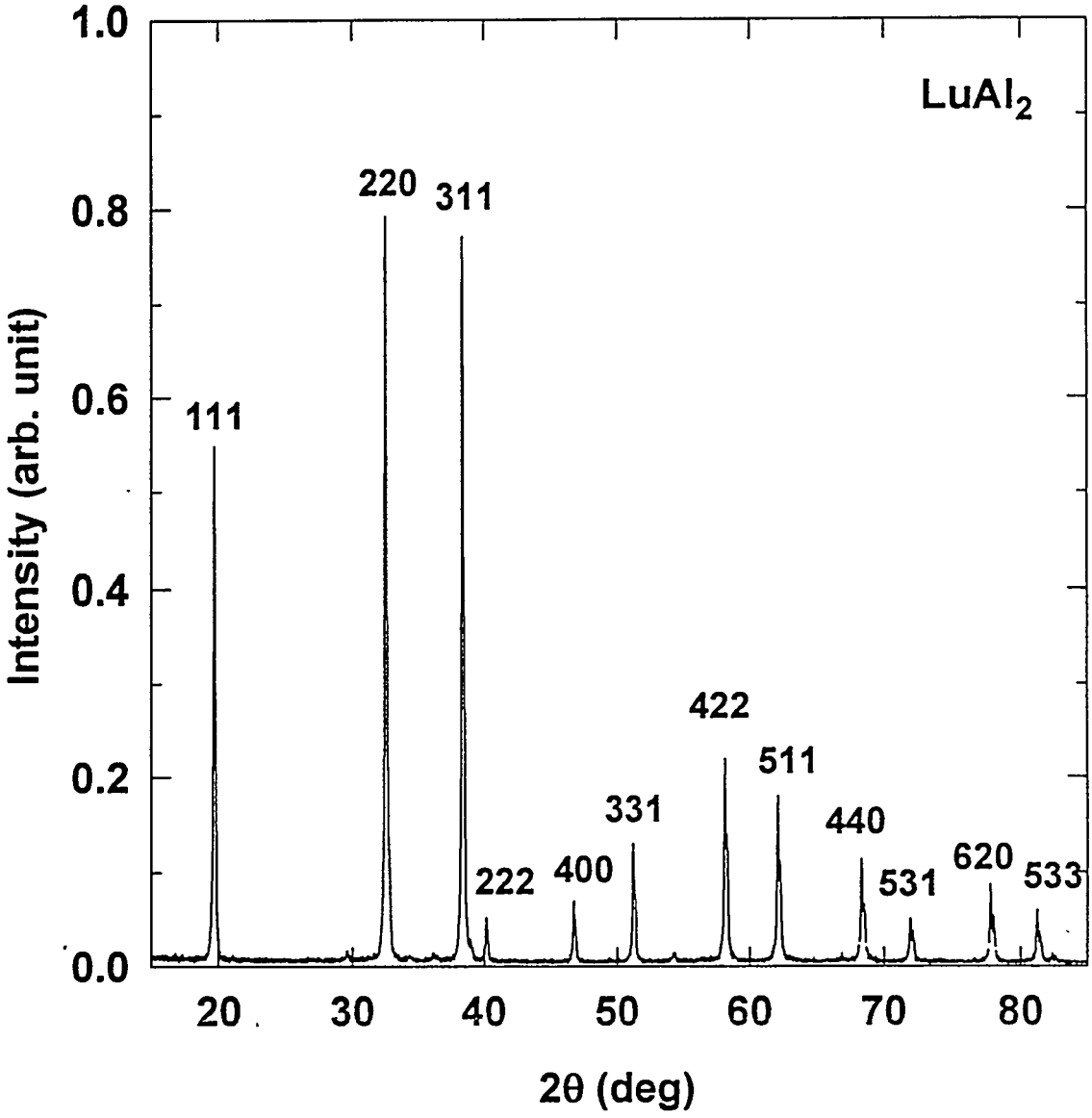

Figure 4.2 Powder X-ray diffraction pattern of crushed $LuAl_2$ single crystal. The peaks are indexed to a fcc unit cell with a lattice parameter a=7.7465$\mathring{A}$.

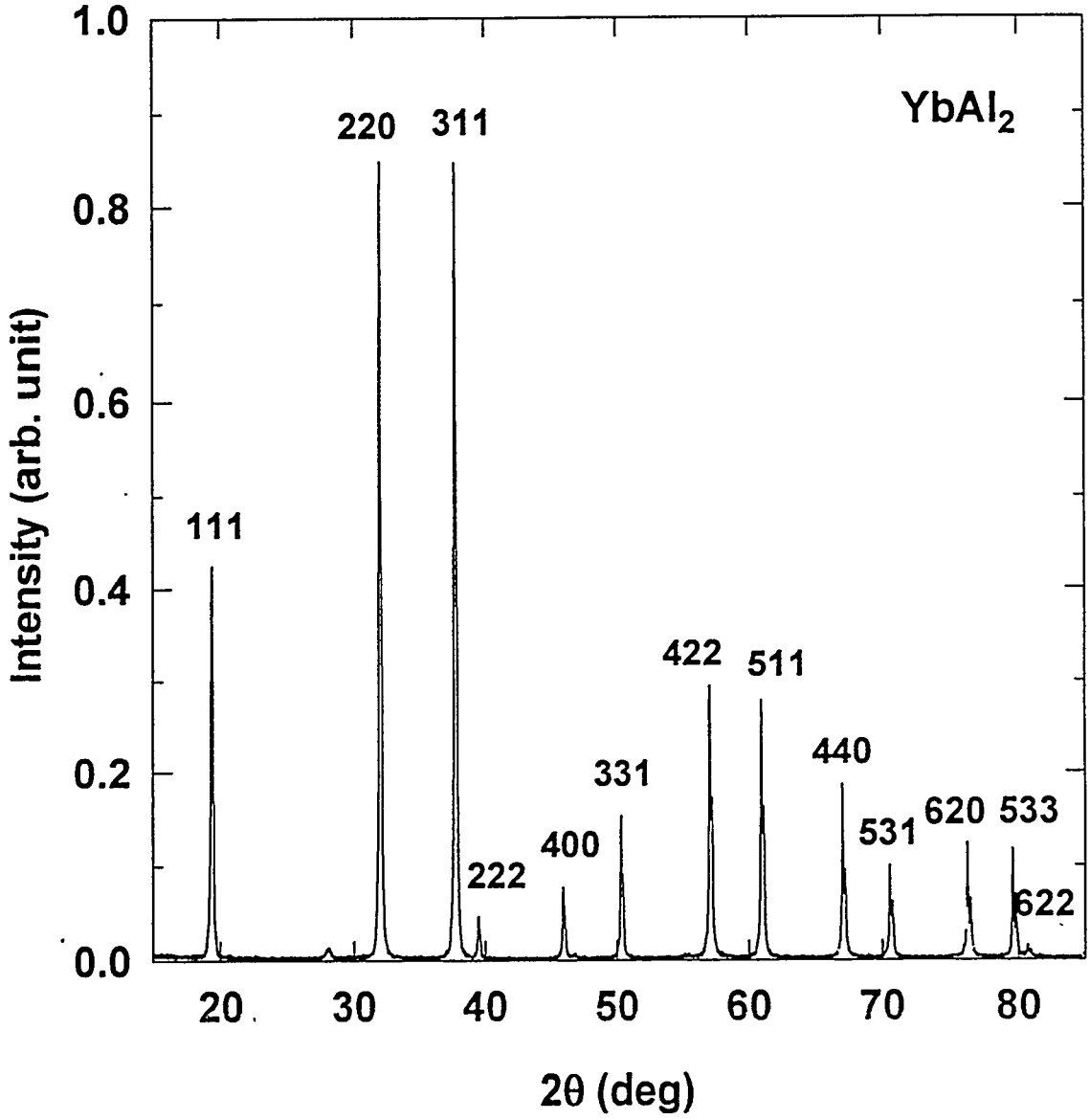

Figure 4.3 Powder X-ray diffraction pattern of crushed $YbAl_2$ single crystal. The peaks are indexed to a fcc unit cell with a lattice parameter a=7.8846$\mathring{A}$.

Band structure calculations

$LuAl_2$ and $YbAl_2$ have the C15 crystal structure. The lattice constants used for $LuAl_2$ and $YbAl_2$ were 14.6436 a.u. (7.7465 $\mathring{A}$) and 14.9047 a.u. (7.8846 $\mathring{A}$), respectively. We treated the 4f electrons of the rare earth atoms as valence electrons throughout the whole calculation. The exchange-correlation potential has been included in the local density approximation (LDA) with the von Barth-Hedin form [52]. The k-integrated functions have been evaluated by the tetrahedron technique with 144 k-points in the irreducible Brillouin zone which is $\frac{1}{48}$ of the Brillouin zone. Once the self-consistent potential and charge are obtained, the real part of the optical conductivity can be easily calculated. In cubic systems it is necessary to calculate only one of the three diagonal components of the conductivity tensor. For the paramagnetic state, we can rewrite Eq. (3.58) as

$$\sigma_{xx} = \frac{\pi e^2}{3m^2\omega} \sum_{f,i} \int_{BZ} d^3k \frac{2}{(2\pi)^2} |p_{fi}|^2 \times f_i(k) \times (1 - f_f(k)) \times \delta(E_f(k) - E_i(k) - \hbar\omega) \tag{4.1}$$

where BZ denotes Brillouin zone, $f(k)$ is the Fermi distribution function and i, f stand for the occupied and unoccupied energy band states at wave vector k, respectively.

$$p_{fi} = \frac{\hbar}{i} \langle f | \nabla | i \rangle \tag{4.2}$$

is the dipole matrix element between the occupied $E_i(k)$ and unoccupied $E_f(k)$ one-electron states. The calculated spectra are unbroadened quantities. The electrons generally interact with other electrons, especially in strongly correlated systems. These correlated interacting electrons are described by the quasiparticle picture. This quasiparticle picture describes the more realistic situation and can be described by self-energy terms. The self energy is usually momentum and energy dependent. The self energy consists of two parts. The real part represents a shift of the spectra and the imaginary part describes the broadening of the spectra caused by the finite lifetime of a state. We set a single empirical energy-dependent broadening parameter as q=AE where E is

the incident photon energy and A=0.1 has been used. From the energy bands and the TB-LMTO eigenvectors, we calculated the total and orbital projected density of states.

Two-phase and three-phase models

With ellipsometry we can measure the complex reflectivity ratio. This complex reflectivity ratio ρ is related to the dielectric function ϵ by

$$\epsilon = \sin^2\phi_o + \sin^2\phi_o \tan^2\phi_o \left[\frac{1-\rho}{1+\rho}\right] \tag{4.3}$$

where ϕ_o is the angle of incidence and ϵ an ρ are complex quantities. The dielectric function given in Eq. 4.1 is obtained using the two-phase model, that is, the system consists of an isotropic ambient and an isotropic semi-infinite, homogeneous solid. The interface between them is assumed to be abrupt and flat. Once we have the experimental data, ρ and ϕ_o, then we can obtain a dielectric function derived by the two-phase model. In real situations, the two-phase model may not be appropriate in describing a system. A sample exposed to air can be oxidized. A native oxide layer can form on top of the bulk sample. This layer on the surface makes us use a three-phase model for describing the real system. The effective dielectric function of the oxidized sample can be simulated with the three-phase model. In order to do that we need the dielectric functions of the clean bulk sample and its oxide. A good example of the three-phase model of a native oxide layer is air-SiO_2-Si which has been studied by many authors [53, 54, 55]. Rossow [56] has simulated the effective dielectric function of GaAs using the dielectric functions of GaAs and its oxide. They found the height of the imaginary part of the dielectric function of the oxidized sample, especially near the E_2-gap, is affected, that is, the magnitude of the peak at 4.7 eV is reduced greatly as the oxide thickness increases. Conversely, with the dielectric functions of an oxidized sample and its oxide one can obtain the dielectric function of the clean sample. The complex reflectance ratio for the

three-phase model [12] is given by the following equation:

$$\rho = \tan\Psi \exp(i\Delta) = \frac{r_{01p} + r_{12p}e^{i2\beta}}{1 + r_{01p}r_{12p}e^{i2\beta}} \times \frac{1 + r_{01s}r_{12s}e^{i2\beta}}{r_{01s} + r_{12s}e^{i2\beta}} \tag{4.4}$$

where the subscripts 0, 1 and 2 in the above equations represent the ambient, the layer and bulk sample, and p and s stand for p and s polarization respectively. The reflection coefficients for p and s polarized light between the i-j interface are given by

$$r_{ijp} = \frac{\epsilon_j\sqrt{\epsilon_i - \sin^2\phi_o} - \epsilon_i\sqrt{\epsilon_j - \sin^2\phi_o}}{\epsilon_j\sqrt{\epsilon_i - \sin^2\phi_o} + \epsilon_i\sqrt{\epsilon_j - \sin^2\phi_o}}, \tag{4.5}$$

$$r_{ijs} = \frac{\sqrt{\epsilon_i - \sin^2\phi_o} - \sqrt{\epsilon_j - \sin^2\phi_o}}{\sqrt{\epsilon_i - \sin^2\phi_o} + \sqrt{\epsilon_j - \sin^2\phi_o}}. \tag{4.6}$$

For example r_{01p} is the reflection coefficient for p polarized light at the interface from ambient to layer. The phase shift β is given by

$$\begin{aligned} \beta &= \frac{2\pi d_{layer}}{\lambda} n_1 \cos\phi_1, \\ \beta &= \frac{2\pi d_{layer}}{\lambda}\sqrt{n_1^2 - n_o^2\sin^2\phi_o} \quad , \end{aligned} \tag{4.7}$$

where λ is the wavelength of the incident polarized light, ϕ is the angle of incidence in ambient medium and ϕ_1 is the angle of refraction in the oxide layer n_1. By the Snell's law, ϕ_0, ϕ_1, and ϕ_2, which are angles between the directions of propagations of the plane waves in the ambient (n_o), layer (n_1), bulk substrate (n_2) and the the normal to the layer and the clean bulk sample are related each other by

$$n_o \sin\phi_0 = n_1 \sin\phi_1 = n_2 \sin\phi_2 \tag{4.8}$$

To describe the three-phase model system, we need 6 parameters. Three are the (complex) refractive indices of the ambient (n_o), layer (n_1) and bulk substrate (n_2). These refractive indices will be real or complex depending on whether there is absorption or not. The other three are the thickness of the layer (d_{layer}), angle of incidence (ϕ_o) and wavelength of incident light (λ). In each measurement at one wavelength λ and one

angle of incidence ϕ_o, we can determine only one complex unknown parameter or two real unknown parameters of the three-phase model system. For example, the complex refractive index of the pure bulk, n_2, can be determined only if the oxide overlayer thickness d_{layer} and refractive index n_1 are known. The two unknown optical parameters can be obtained by minimizing

$$M = \sum_{i=1}^{i_{max}} |\rho_i^m - \rho_i^c(n_o, n_1, n_2, d_{layer}, \phi_o, \lambda)|^2 \tag{4.9}$$

where ρ_i^m is the ratio of the complex-amplitude reflection coefficients for p- and s-polarized light as defined in Eq. 2.31 for the ith measurement on a three-phase model system, ρ_i^c is the computed value of this ratio from Eq. 4.4 and i_{max} is the number of measurements. For $LuAl_2$ we measured from 1.5 - 5.6 eV with an energy step of 0.02 eV, therefore $i_{max} = 206$. For $YbAl_2$ we measured from 1.4 - 5.2 eV with the same energy step and $i_{max} = 191$. For this nonlinear least-squares fitting, the well-known Levenberg-Marquardt algorithm [57] has been employed. In Eq. 4.9, the refractive index n_o of the ambient air is 1. The angle of incidence ϕ and the wavelength λ are known parameters. Therefore there are three unknown parameters (two real and one complex), that is, the refractive index of the overlayer n_1, the thickness of the overlayer d_{layer}, and the complex refractive index of the clean bulk substrate n_2. But with the algorithm of Eq. 4.9, we can determine only one complex parameter or two real parameters of the three phase model system. Our concern is to get the optical constants or the dielectric function of the clean bulk substrate. We need to know the refractive index n_1 of the thin native oxide overlayer covering the bulk sample exposed to air and the overlayer thickness d_{layer}. There are many difficulties in obtaining accurate information on these. Therefore we assumed a constant value of the refractive index of the oxide layer and varied the thickness of the oxide layer, as will be discussed detail later. With this information, the algorithm adjusts the unknown three-phase model parameters (complex refractive index of the clean bulk substrate) iteratively until the difference between the measured

complex reflectance ratio and the complex reflectance ratio determined from three phase model, Eq. 4.4, is minimized, that is converged. From this procedure, we can get the best results for the one complex or two real unknown parameters of the three-phase model system. In our case these are the complex refractive index (or dielectric function or optical conductivity) of the clean bulk sample which would be obtained in ultra-high vacuum chamber if an optical surface were prepared in situ.

Oxide effects

In experiments, the effects of oxidation, surface roughness, defects, and contamination are contained in the measured data. A measured dielectric function ϵ containing all these effects is called the effective dielectric function or pseudodielectric function, written as $\langle\epsilon\rangle$. Theoretical models have been developed to treat inhomogeneous phases or oxidation problems. For the treatment of inhomogeneous phases, an effective-medium theory like that of Bruggemann [58] has been used. The generalized form of the Bruggemann effective-medium theory(BEMT) is [58]

$$\sum_i f_i \frac{\epsilon_i - \epsilon}{\epsilon_i + 2\epsilon} = 0, \tag{4.10}$$

where ϵ=$\langle\epsilon\rangle$ is the effective (measured) dielectric function and ϵ_i and f_i are the dielectric function and volume fraction of the ith medium respectively. The f_i's satisfy the relationship

$$\sum_i f_i = 1 \tag{4.11}$$

Rhee [59] used the BEMT and the three-phase model, where a rough overlayer was modeled as a mixture of voids and host material, to explain the optical conductivity in thin-film Ce samples. In treating rare-earth materials, we can not avoid oxidation problems. It is known that rare earth metals react with oxygen more easily than transition metals. The rate of oxidation depends on several variables. Among them, high

temperature and humidity increase the rate of oxidation. Light rare earths like Ce oxidize considerably faster than heavy rare earth metals (Gd, Lu, Yb, etc.) [60]. R_2O_3 (R=rare earth metal) is a typical composition for a rare earth oxide. In the case of Al, Al_2O_3 is the common oxide. The band gaps E_g of Lu_2O_3 and Yb_2O_3 are 5.4 eV and 5.1 eV respectively [61]. Al_2O_3 is also a wide band gap material. Zukowska [62] confirmed the formation of a Yb_2O_3 overlayer on the ytterbium layer surface after removing the ytterbium layer from the vacuum chamber by a structural examination. Zukowska *et al.* [63] estimated the thickness of the ytterbium oxide layer. They found it slowly increases up to 22 $\mathring{A}$ within 24 hours of exposure to air, and the oxide layer stabilized at a value of 33 $\mathring{A}$ after 48 hours. Burnham *et al.* [64] found the oxidation rate of ytterbium in air decreases quickly and estimated that the thickness of the oxide overlayer on ytterbium was about 90 $\mathring{A}$ after two months exposure to air, by extrapolation of their measurements. If we assume that the oxide dielectric layer is composed of Yb_2O_3 and Al_2O_3, then from the Bruggemann effective medium theory, the effective refractive index n_1 of the oxide overlayer can be obtained by the following equation,

$$f_{Yb_2O_3}\frac{n^2_{Yb_2O_3}-n^2_{eff}}{n^2_{Yb_2O_3}+2n^2_{eff}}+f_{Al_2O_3}\frac{n^2_{Al_2O_3}-n^2_{eff}}{n^2_{Al_2O_3}+2n^2_{eff}}=0 \tag{4.12}$$

and

$$f_{Yb_2O_3}+f_{Al_2O_3}=1 \tag{4.13}$$

where $f_{Yb_2O_3}$, $f_{Al_2O_3}$ are the relative volume fractions of Yb_2O_3 and Al_2O_3 in the oxide layer. If the relative volume fractions of Yb_2O_3 and Al_2O_3 and the refractive indices of the Yb_2O_3 and Al_2O_3 in the energy range we are interested in are known, then the effective refractive index n_{eff} of the oxide layer will be determined by the Eq. 4.12. The refractive index of the oxide layer can be considered as real in the visible region; the extinction index k=0, due to the wide band gaps of Yb_2O_3 [61], and Al_2O_3. The above is the simplest assumption for the surface oxide layer. But the real situation of the oxidized surface might be more complicated to handle with the BEMT. Yb_2O_3 or

Al_2O_3 is not only possible oxide layer on $YbAl_2$. $YbAlO_3$ or other forms of ternary oxide are possible as a native oxide layer on $YbAl_2$. $(YbAl)_2O_3$, a random mixture of Yb and Al, oxide layer is also a possible oxide layer. The dielectric functions for these oxide layers are not known. In order to estimate the optical constants of the clean bulk Yb_2Al_3 through the three phase model, we assumed a constant effective refractive index for the complicated oxide layer. for the refractive indices of the oxide layer is difficut The refractive indices of Al_2O_3 and Yb_2O_3 [65] are roughly 1.65 and 1.85 in the visible region. Therefore we assumed the effective refractive index of the oxide layer is in the range from 1.5 to 2.0. It is well known that the oxide thickness of Al_2O_3 saturates below $30\mathring{A}$ when Al is exposed to air. Because we did the ellipsometry experiment as soon as we grew the single crystals of $YbAl_2$ and $LuAl_2$, the thickness of the oxidation will not exceed 100 $\mathring{A}$ from [62]. So we varied the thickness of the unknown oxide layer from $50\mathring{A}$ to 100 $\mathring{A}$ in the three phase model simulation. Without being heated, the oxide layer of heavy rare earth intermetallic compounds usually does not grow quickly. Figure 4.4 and 4.5 show the diagonal component of the optical conductivity of pure bulk $LuAl_2$ and $YbAl_2$ obtained using the three-phase model according to different refractive indices and thickness of the oxide layer. In Fig. 4.4, the dotted line stands for the theoretical real part of the diagonal optical conductivity obtained using the TB-LMTO within the local density approximation (LDA) using a lifetime broadening proportional to energy. The 4f electrons of Lu are treated as valence electrons. The optical conductivity of clean $LuAl_2$ is simulated using the measured optical conductivity of the polycrystalline $LuAl_2$ with the assumed thickness and refractive index of the oxide layer. As shown in Fig. 4.4, as the refractive index increases the simulated optical conductivity of the clean bulk sample is increases. In Fig. 4.5, the theoretical real part of the diagonal optical conductivity obtained using the TB-LMTO within the LDA using a lifetime broadening proportional to energy is represented by short-dashed line. In the calculation, the 4f electrons of Yb are also treated as valence electrons like those of Lu. There is a big peak at 0.5 eV in the

theoretical optical conductivity of $YbAl_2$ which does not appear in $LuAl_2$. The optical conductivity at 0.5 eV obtained from theory is contributed mainly by the 4f states in Yb because if we treat the 4f as core electrons the peak at 0.5 eV almost disappears. In the case of $LuAl_2$, the differences in optical conductivity according to different treatments are ignorable. From this result we know that the optical conductivity of $YbAl_2$ is affected considerably, especially in the lower energy range, by the 4f states of Yb. The optical conductivity of clean $YbAl_2$ is simulated by using the measured optical conductivity of the single-crystal of $YbAl_2$ with an assumed thickness and refractive index of the oxide layer. We notice a small flat shoulder around 1.6 eV is shown in experiment and around 1.7 eV in theory in the optical conductivity.

Results and discussion

The calculated electronic band-structures of $LuAl_2$ and $YbAl_2$ are shown in Figs. 4.6 and 4.7. The Fermi energy E_F is marked by a horizontal dotted line and the positions of symmetry points are indicated by vertical lines. In both calculations we treated the 4f electrons of Lu and Yb as valence electrons. Two narrow flat 4f bands, separated due to spin-orbit interaction, lie 4 and 5.5 eV below the Fermi level for $LuAl_2$ and 0.2 and 1.8 eV below the Fermi level for $YbAl_2$, respectively. In the case of $YbAl_2$, a small fraction of the $4f_{7/2}$ bands extends to the Fermi level while the 4f electron bands are located well below the Fermi level for $LuAl_2$. The lowest two bands of $LuAl_2$ and $YbAl_2$, which are located between -10 to -6 eV, are mainly of Al s and p character. The theoretical partial densities of states of $LuAl_2$ and $YbAl_2$ are presented in Figs. 4.8 and 4.9, respectively. Due to the extended $4f_{7/2}$ state at the Fermi level in $YbAl_2$, the theoretical density of states of $YbAl_2$ at the Fermi level is twice as large as that of $LuAl_2$ for which the 4f electron states are located well below the Fermi level. The experimental electronic specific heat coefficient γ of $YbAl_2$ has been reported to be

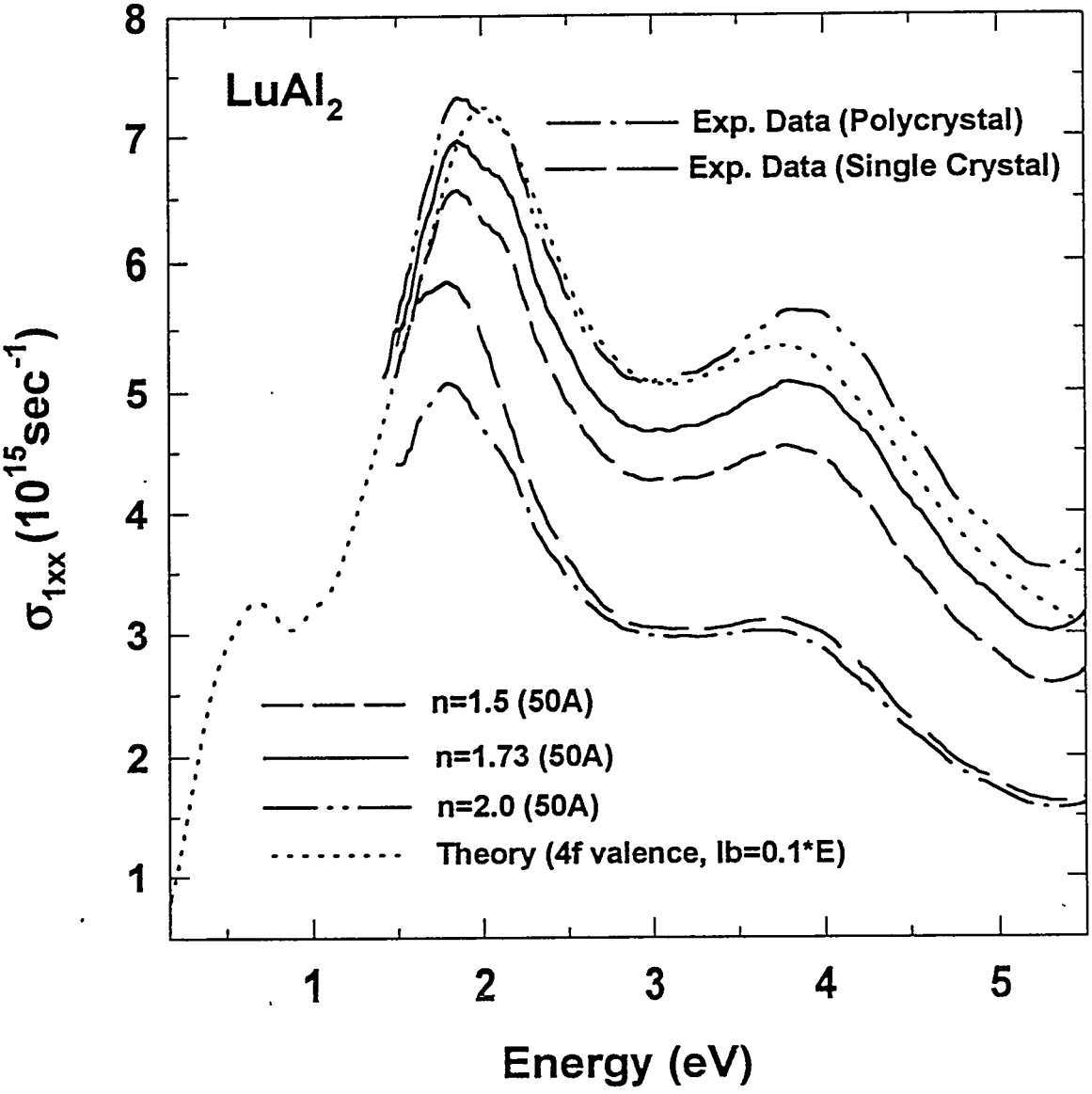

Figure 4.4 Diagonal component of the optical conductivity of $LuAl_2$. Theoretical data obtained from the TB-LMTO using a lifetime broadening proportional to energy. Experimental data were measured with a polycrystalline sample and single crystal samples. The diagonal components of the optical conductivity of the clean bulk $LuAl_2$ was obtained using the three-phase model using different refractive indices at $50\mathring{A}$ of oxide layer.

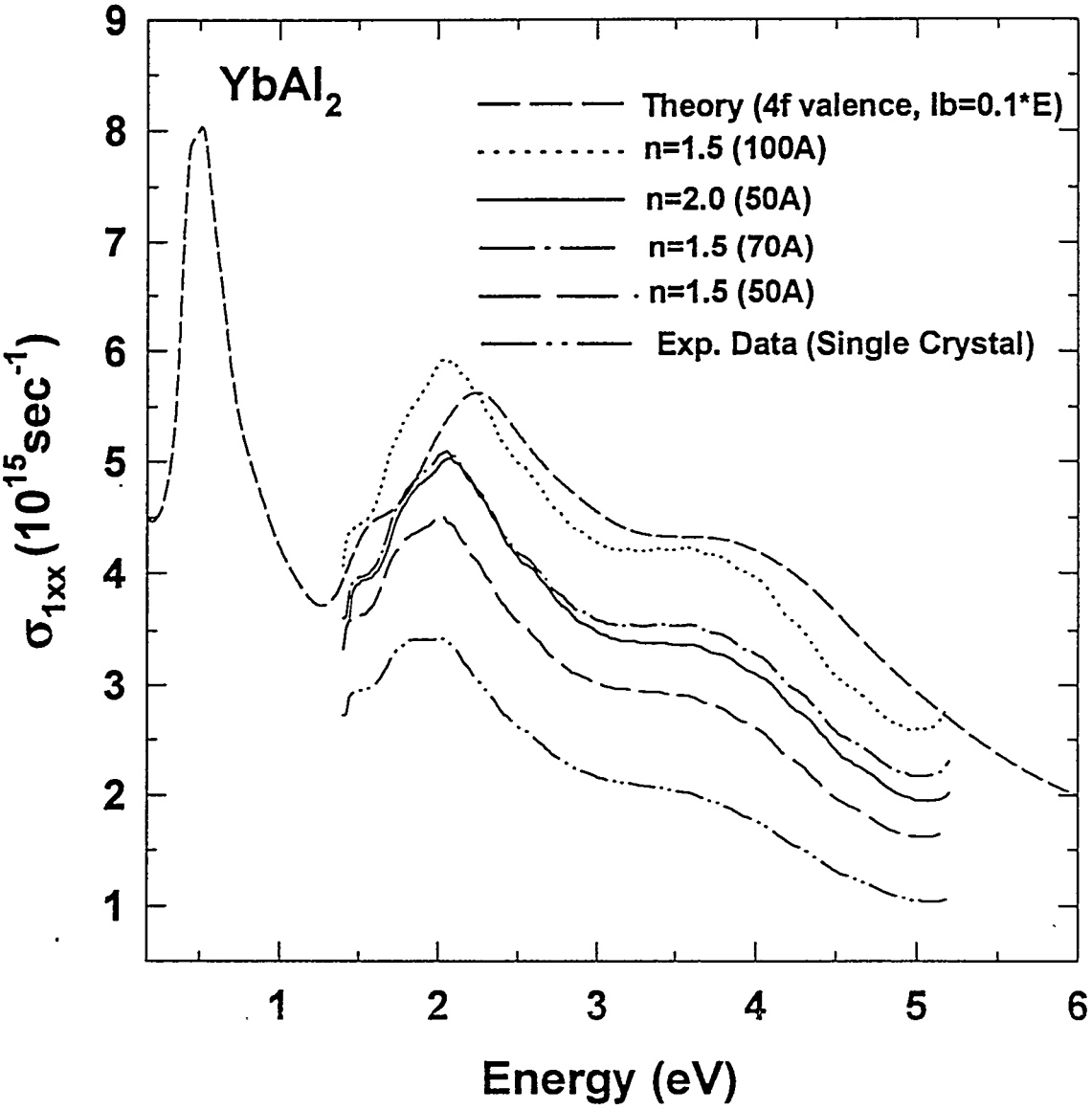

Figure 4.5 Diagonal component of the optical conductivity of $YbAl_2$. Theoretical data obtained from TB-LMTO using a lifetime broadening proportional to energy. Experimental data were measured with a single crystal sample. The diagonal component of the optical conductivty of the clean bulk $YbAl_2$ was obtained using the three-phase model with different refractive indices and thickness of the oxide layer.

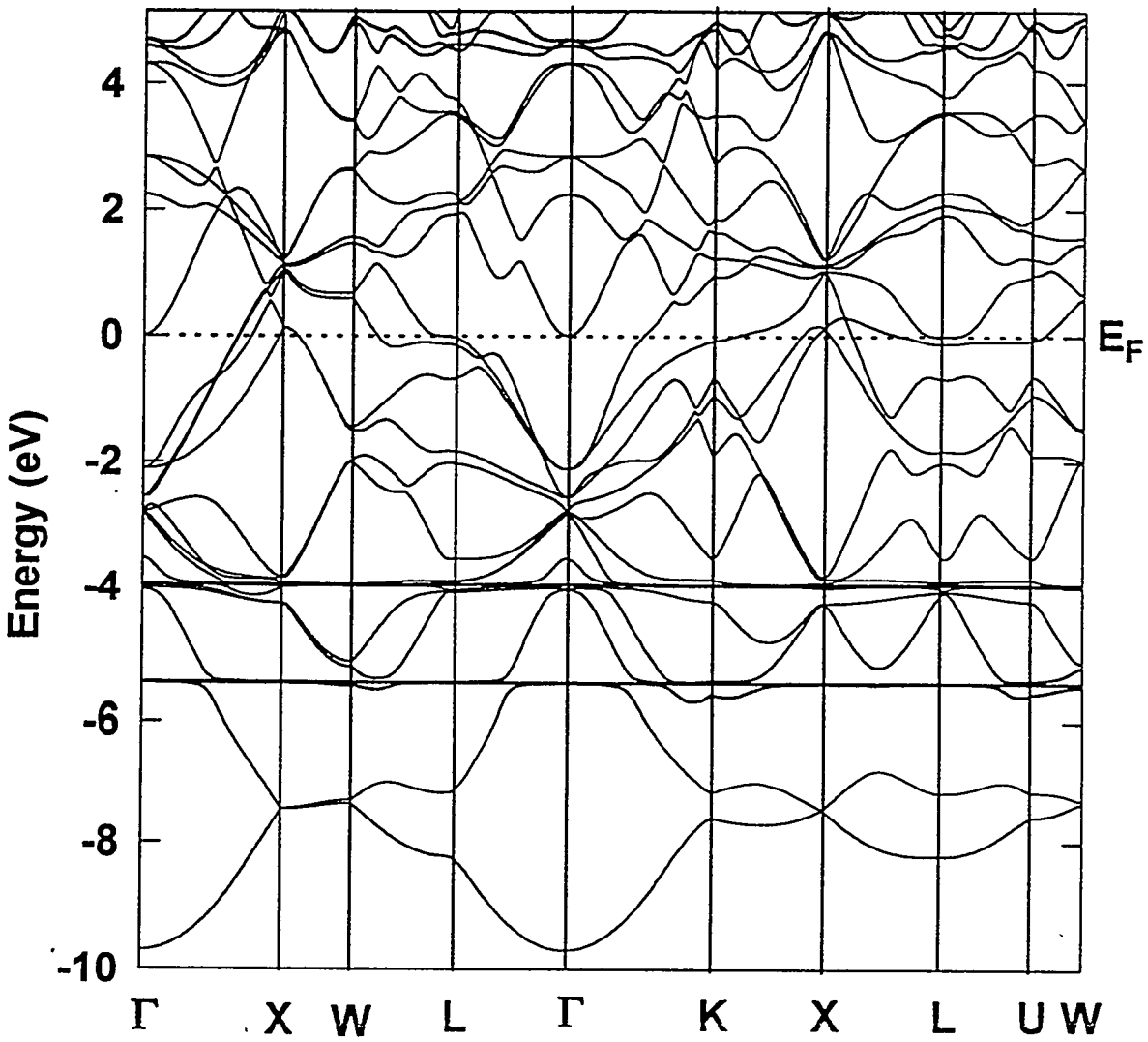

Figure 4.6 Band structure of $LuAl_2$ obtained from the self-consistent TB-LMTO with spin-orbit interaction included.

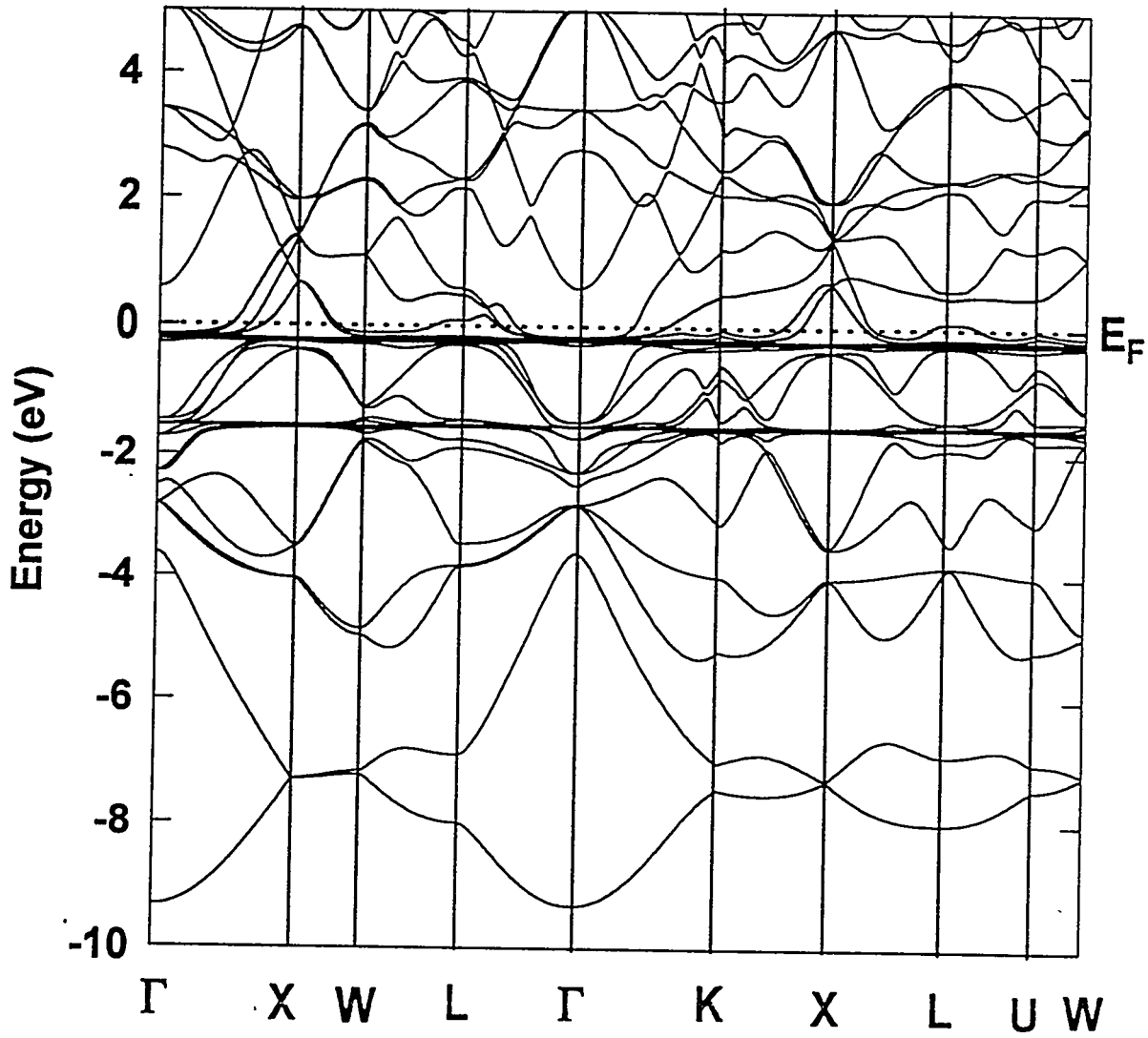

Figure 4.7 Band structure of $YbAl_2$ obtained from the self-consistent TB-LMTO with spin-orbit interaction included.

16.8 $mJK^{-2}mol^{-1}$ [66] while that of $LuAl_2$ is 5.6 $mJK^{-2}mol^{-1}$ [67]. The theoretical electronic specific heat coefficient γ of $YbAl_2$ and $LuAl_2$ are 7.81 $mJK^{-2}mol^{-1}$ and 4.08 $mJK^{-2}mol^{-1}$ with the TB-LMTO method, respectively. The experimental electronic specific heat coefficient of $YbAl_2$ is larger than the theoretical value. The theoretical partial density of states for $LuAl_2$ and $YbAl_2$ obtained from TB-LMTO with LDA in the atomic sphere approximation (ASA) are shown in Figs. 4.8 and 4.9, respectively.

BIS(Bremsstrahlung Isochromat Spectroscopy) is the counterpart of XPS (X-ray photoemission spectroscopy). It reveals information on the unoccupied density of states above the Fermi level [68]. Oh *et al.* [50] studied the electronic structure of $YbAl_2$ using XPS and BIS at different temperatures. Their purpose of the experiments was to tell whether the final 4f spectral weights can also lie on the right side of the Fermi level as suggested by the mixed-valence configuration. For this, they measured the BIS spectra of $LuAl_2$ for comparison with that of $YbAl_2$. By comparing the two BIS spectra, they found small peak, supposed to be the 4f states of $YbAl_2$, on the right side of the Fermi level. The valence band spectrum of $YbAl_2$ taken by Oh *et al.* [50] is shown in Fig.1 of ref. [50]. The big peak, split due to the spin-orbit interaction, is located close to the Fermi level, one at 1.8 eV below the Fermi energy and the other at 0.2 eV below the Fermi level. The peak extended out to the Fermi energy. These big experimental peaks correspond to $4f^{14} \rightarrow 4f^{13}$ spectral weight. The partial density of states obtained from the TB-LMTO with LDA in the atomic sphere approximation (ASA), shown in Fig. 4.9, also shows two big peaks contributed by 4f states of Yb in $YbAl_2$. The two peaks are separated by 1.7 eV from spin-orbit interaction. The positions of the 4f states and the spin-orbit splitting are quite similar in both experiment and theory. Figure 3 of ref. [50] shows the BIS spectrum of $YbAl_2$ measured at 120K. Our calculated DOS of $YbAl_2$ shown in Fig. 4.9 shows that the tail of the DOS of the $4f_{7/2}$ states is extended beyond the Fermi energy, which correspond to peak A in Fig. 3 of ref. [50]. Peak B in Fig. 3 of [50], located 1.8 eV above the Fermi level, is mainly due to Yb-5d states,

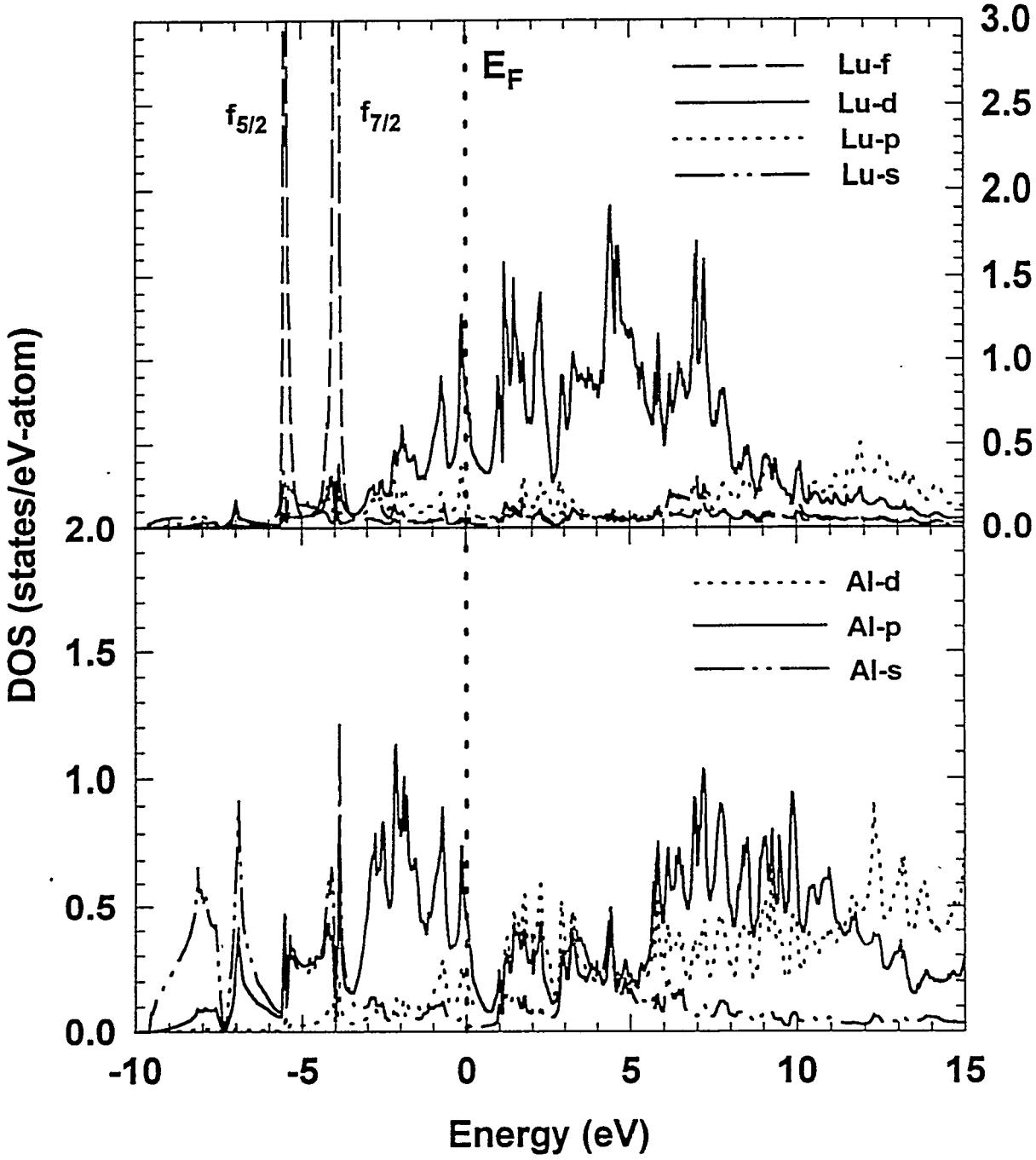

Figure 4.8 Partial density of states obtained from the TB-LMTO with LDA in the atomic sphere approximation (ASA). The upper and lower panel show the DOS on the Lu and Al site in states/eV atom

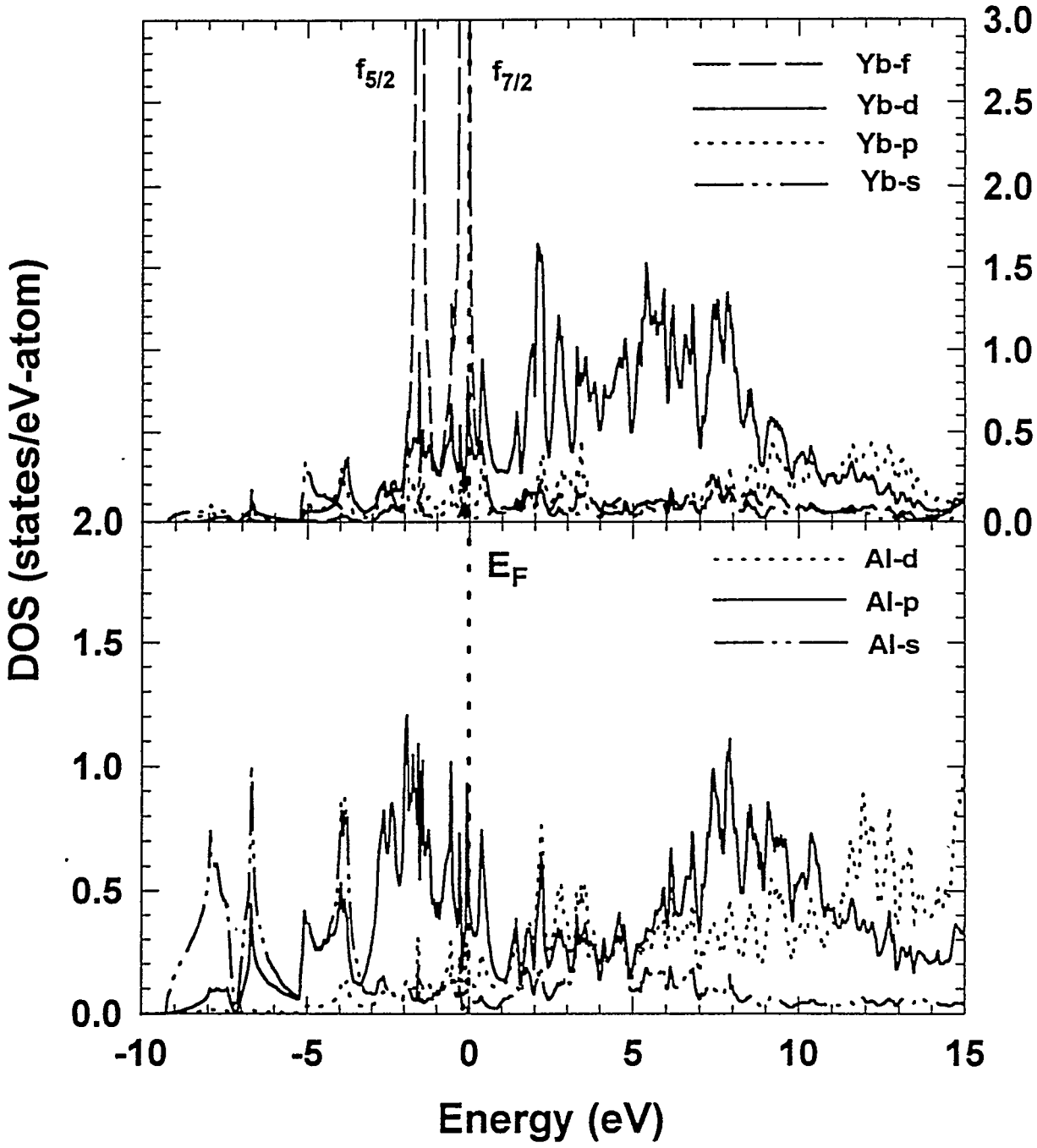

Figure 4.9 Partial density of states obtained from the TB-LMTO with LDA in the atomic sphere approximation (ASA). The upper and lower panel show the DOS on the Yb and Al site in states/eV atom

as shown in Fig. 4.9. The BIS spectrum of $LuAl_2$ measured by Oh *et al.* [50] has three peaks, at 2 eV, 5 eV, and 7.8 eV respectively. These peaks are considered to be contributed by Lu-5d states, as shown in Fig. 4.8. The calculation of the DOS, was for zero temperature. At zero temperature, the Yb in $YbAl_2$ is divalent. In Figs. 1 and 2 of [50], the intensity changes with temperature due to the valence change. But the peak positions are almost the same between 120K and 460K, while peak the intensity changes a little. The intensity measured at 120K is close to that of divalent Yb. Even though as the temperature increases, the intensity changes due to the valence change, the theoretical calculation for $YbAl_2$ at zero temperature explains the positions of XPS and BIS peaks in the experimental data for $YbAl_2$. The measured optical conductivities of $LuAl_2$ and $YbAl_2$ show similar features in our measurement range. There are two peaks for both samples. The sharp peak appears at 1.8 eV and a flat, broad peak appears from 2.8 to 3.8 eV for $LuAl_2$. For $YbAl_2$ the first peak appears at 1.9 eV and a flat, broad peak appears from 3.1 to 3.6 eV. But there is a difference in the lower energy range in the theoretically calculated optical conductivities. Around 0.5 eV, there is a big peak in $YbAl_2$ while there is no such noticeable structure in $LuAl_2$. $LuAl_2$ has a small shoulder at 0.8 eV. Both in theory and experiment $LuAl_2$ has a slightly larger feature in the 4 eV energy region. This difference comes from the different electronic configurations of the Lu and Yb atoms. In both, the 4f states are fully occupied, but Lu has one more valence electron. Therefore the Lu 5d occupied DOS is wider than that of $YbAl_2$. From the analysis of DOS, the feature around 3.5 eV in $LuAl_2$ is due partly to interband transition contributions from occupied Lu 5d states to unoccupied Lu 6p states. The big peak in the theoretical optical conductivity of $YbAl_2$ at 0.5 eV may come from interband transitions with the 4f states of Yb involved. But the 4f electrons of $LuAl_2$ are located well below the Fermi level, so there is no corresponding feature in the low energy region.

Ellipsometry is surface sensitive in that the measured optical conductivity is not

correct if the surface is oxidized. We considered this oxide overlayer by using the three-phase model with the assumption that the overlayer has an effective refractive index n_{eff} and thickness d_{layer}. As already discussed, as the refractive index gets larger, the optical conductivity of the clean bulk sample, determined from measurements on the oxidized sample, increases, and as the thickness of the oxide layer increases the optical conductivity of the pure bulk sample also increases. For $LuAl_2$ as the oxide thickness increases, the feature around 4.0 eV becomes more prominent. It agrees well with the theoretical calculation around 4.0 eV. The theoretical optical conductivity of $YbAl_2$ was obtained from the electronic structure which was calculated at zero temperature, while the experiment was performed at room temperature. As already discussed, Yb in $YbAl_2$ is divalent at low temperature, but changes its valence as the temperature increases. However, at room temperature there is no noticeable difference between the theoretical and experimental values. If we were to measure the optical conductivity of $YbAl_2$ at high temperature, then the optical conductivity at 0.5 eV, which shows a big peak involving the f states, may show a difference between the values measured at high temperature and values calculated at zero temperature due to the 4f valence change of Yb at high temperatures.

Conclusions

The optical conductivities of polycrystal and single-crystal $LuAl_2$, and single-crystal $YbAl_2$ have been measured between 1.5 - 5.6 eV for $LuAl_2$ and 1.4 - 5.2 eV for $YbAl_2$, using a rotating analyzer ellipsometer. We compared the experimental data with theoretical spectra obtained using the self-consistent TB-LMTO method. We also considered the effect of an oxide overlayer on the optical response using a three-phase model. We found the oxide overlayer on the sample reduces the magnitude of the optical conductivity and smoothed out some features. The difference between the electronic structure of

$LuAl_2$ and $YbAl_2$ is that the 4f states of $YbAl_2$ are located near the Fermi energy level while those of $LuAl_2$ are located well below the Fermi level. The 4f electrons near the Fermi level contribute the large peak at 0.5 eV in the theoretical optical conductivity of $YbAl_2$. This peak has not yet been measured. Therefore it is a proposal that could be examined by IR ellipsometry or IR reflectivity measurements.

5 OPTICAL AND MAGNETO-OPTICAL PROPERTIES OF $LuFe_2$

Introduction

The magnetic, electronic, and optical properties of rare-earth transition-metal (RT) intermetallic compounds have been studied because of their technologically important applications such as permanent magnets and magneto-optical media. But there are many obstacles in doing reseach on RT intermetallic compounds theoretically and experimentally. Incorporating the 4f electrons of rare earth compounds into the self-consistent band theory formalism is difficult due to their strongly correlated behavior. The oxidation of rare earth materials makes optical investigations difficult. The 4f shell of $LuFe_2$ is completely occupied. Therefore there are no complicated contributions from the f electrons. In the case of full f shells (Lu, Yb), many experimental results are well described by first-principles local spin-density approximation (LSDA) calculations [69]. In this chapter, the theoretical and experimental studies of the electronic, magnetic, optical and magneto-optical properties of $LuFe_2$ will be presented.

Sample preparation and characterization

Laves phase compounds AB_2 can be divided into three crystal types, the hexagonal C14, and C36, and the cubic C15 types, in Strukturbericht notation. Crystals with the C36 structure are very rare. $LuFe_2$ crystallizes in the cubic Laves phase with the

rare-earth atoms arranged in the diamond structure consisting of two fcc structures displaced from each other by one-fourth of a body diagonal. The Al atoms are on sites of rhombohedral symmetry ($\bar{3}m$), in a tetrahedral arrangement with four rare-earth atoms as next-nearest neighbors. Rare-earth atoms have 12 Al atoms as nearest neighbors. This $MgCu_2$(C15) structure type belongs to space group O_h^7-$Fd3m$ with 24 atoms per conventional unit cell. Figure 5.1 shows the crystal structure of $LuFe_2$. For magneto-optical experiments, we grew single crystals of $LuFe_2$ by the flux method [70]. The single crystals grown from the flux method have fewer defects and impurities due to the clean environment for growth offered by molten metal fluxes. Using single crystals in experiments has several advantages over using polycrystal or thin film samples because many of the microscopic and macroscopic phenomena can be manifested only with single crystal materials. For example, we can obtain magnetization curves along different crystal directions to determine the easy and hard axes only with single crystals. Cho [71] recently successfully has grown single crystals of RNi_2B_2C (R=Y, Gd, Dy, Ho, Er, and Tm) by using the flux method and investigated the anisotropic intrinsic properties which can be manifested only through the study with single crystals. A couple of disadvantages of single crystals are often their small sizes and the many steps for sample preparation. The small size of the single crystal leads to the difficulty of mounting the sample on the sample holder, alignment of the sample and reduction of the reflected light intensity due to the small surface area. Polycrystals are easier to preapare and the surface areas are large. But the typical disadvantages of polycrystalline samples in magneto-optical measurements are their surface qualities. A button-shaped polycrystalline sample prepared by arc-melting is not usually flat and shiny enough to do optical measurements. Therefore mechanical polishing is required to achieve a smooth and mirror-like surface. While polishing with abrasives, the surface could be deformed and scratched. The scratched surface causes diffuse scattering, especially of ultra-violet light. The deformed surface causes strain-induced birefringence which could alter the real

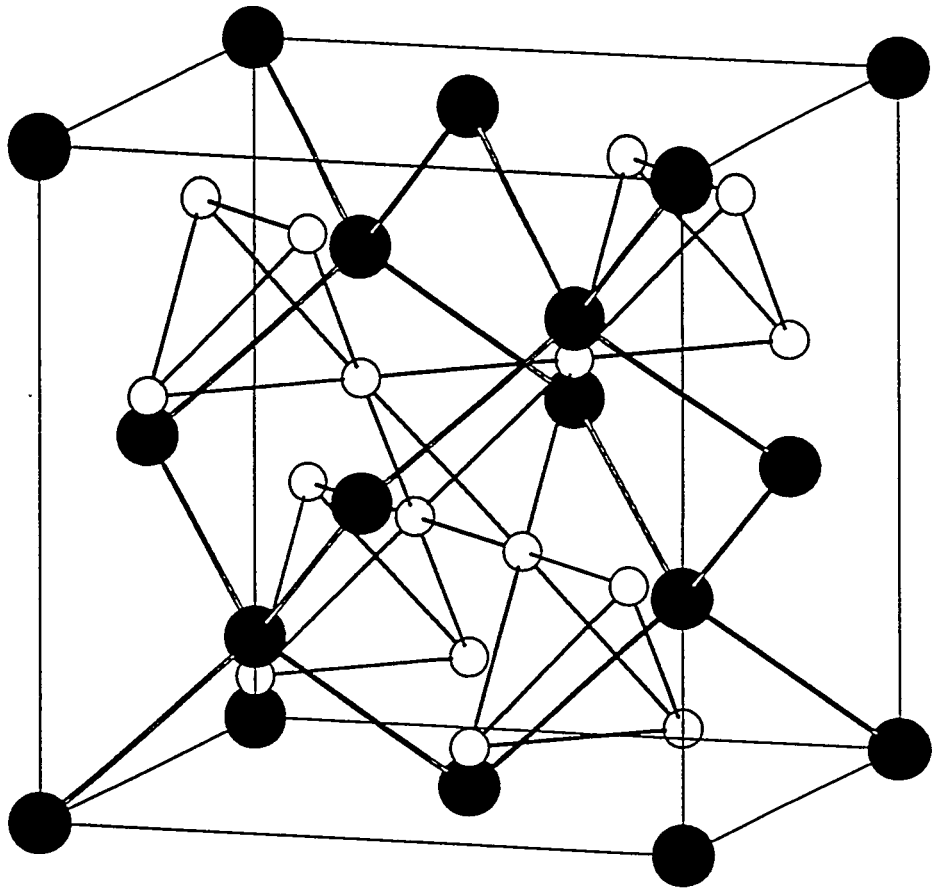

Figure 5.1 Crystal structure of $LuFe_2$. The large black circles denote the sites of Lu atoms and the small open circles denote the sites of Fe atoms

signal. To remedy these effects, sample annealing follows mechanical polishing to relax the deformed surface. But the high annealing temperature expedites the oxidation on the surface of the rare-earth materials which may lose their luster due to the oxidation. Chemical etching could dissolve one component more than the other component. In the case of thin films, the advantages are their smooth and large surface area. But the birefringence induced by different thermal contraction of the substrate and the film could lead to the wrong MOKE signal. Another disadvantage of the thin films is their tendency to corrode on temperature change. The surface of single crystals of $LuFe_2$ is flat and mirror like, so no further surface treatment like mechanical polishing is necessary. The detailed procedure for growing single crystals of $LuFe_2$ by the flux method is as follows. A button-shaped polycrystalline sample of the composition $Lu_{0.6}Fe_{0.4}$ is prepared by arc-melting under Ar gas on a water-cooled copper hearth. The button, wrapped in Ta foil, is sealed in a quartz tube under a partial pressure of Ar and then heated to $1190°C$ within 2 hours and slowly cooled to $1020°C$. The crystal grows during the cooling step from $1190°C$ to $1020°C$ over 60 hours. Figure 5.2 shows the temperature and time schedule for the growth of single crystal of $LuFe_2$. At a temperature of $1020°C$, the crystals are removed from the flux and the plate-like crystals are obtained. This flux method yields single crystals of $LuFe_2$ as large as $4 \times 2 \times 0.5mm^3$. The lower limit for presence of second phases in X-ray pattern is 3% to 5%. The measured lattice parameter of $7.221\mathring{A}$ is in accordance with published data and used for the theoretical calculation.

Theory

Band structure calculation

The tight binding-linear muffin tin orbital (TB-LMTO) method based on the atomic-sphere- approximation(ASA) with the inclusion of spin-orbit coupling was used for the

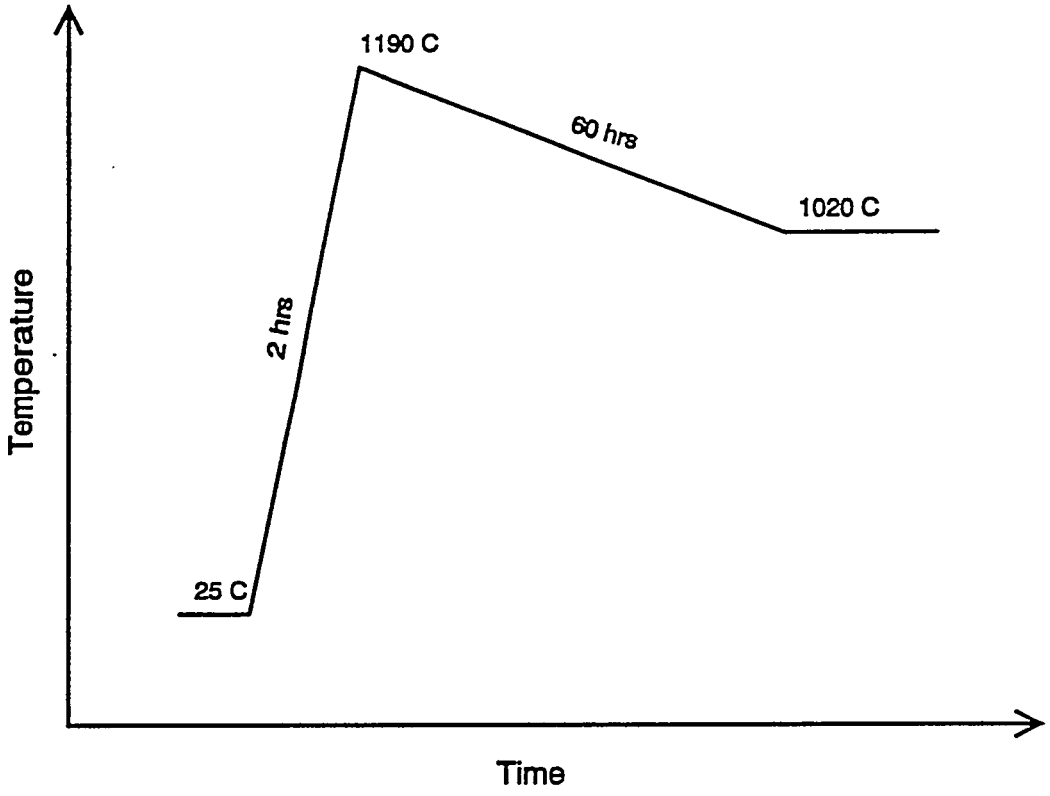

Figure 5.2 Temperature and time schedule for the growth of single crystal of $LuFe_2$. The starting sample is a button of polycrystalline $Lu_{0.6}Fe_{0.4}$ prepared by arc-melting.

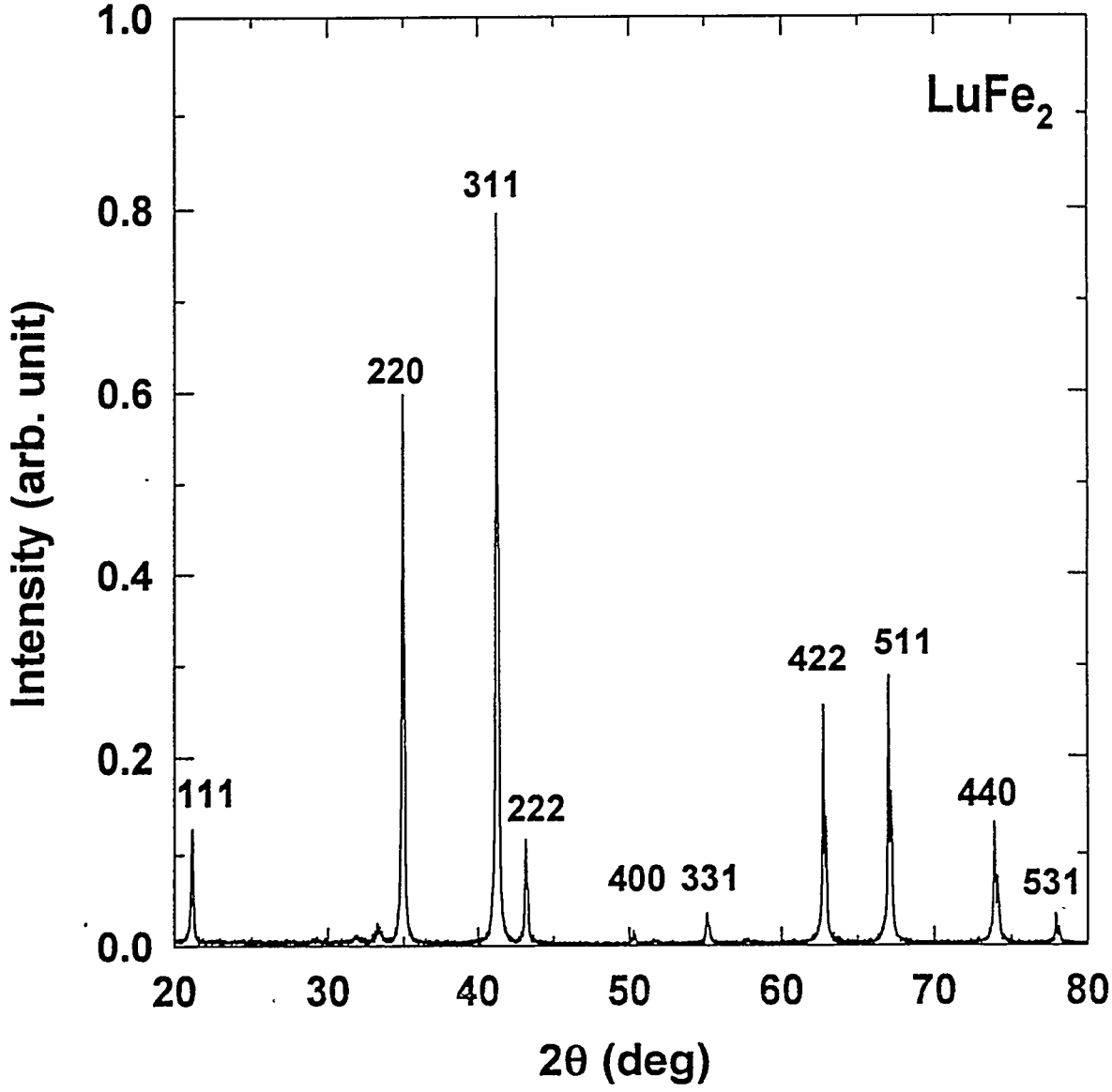

Figure 5.3 Powder X-ray diffraction pattern of crushed $LuFe_2$ single crystal. The peaks are indexed to a fcc unit cell with a lattice parameter a=7.221$\mathring{A}$

band structure calculation. The potential parameters and the structure matrix [72] are necessary for the conventional LMTO band structure calculation [73]. The screened structure matrix of the TB-LMTO method is obtained by transforming the unscreened structure matrix of the conventional LMTO. The transformed screened structure matrix S^{α} of the TB-LMTO is short ranged, up to second-nearest neighbor contributions are counted, while the unscreened structure matrix S° of LMTO is long ranged. It is well known that as the packing ratio of the crystal increases, the accuracy of the band structure calculation is improves for the TB-LMTO method. The structure of $LuFe_2$, the C15 crystal type, is appropriate for the TB-LMTO method because it is a closely packed structure with high symmetry. For the band structure calculation of $LuFe_2$, we used the measured lattice constant mentioned above. We treated the 4f electrons of the rare-earth atoms as valence electrons throughout the whole calculation. The exchange-correlation potential has been included in the local spin density approximation (LSDA) with the von Barth-Hedin form. The k-integrated functions have been evaluated by the tetrahedron technique with 144 k-points in the irreducible Brillouin zone. Once the self-consistent potential and charge are obtained, the diagonal and off-diagonal parts of the optical conductivity can be calculated easily. In cubic systems it is necesasary to calculate only one of the three diagonal components of the conductivity tensor. We used Kubo's linear response theory [32] to obtain the interband contributions to the conductivity, Eqs. (3.59) and (3.59). The calculated values are unbroadened quantities. To reproduce the experimental values, it is necessary to broaden the calculated spectra. But the exact form of the broadening function is not known for each compound. From comparison between theory and experiment, we used for $LuFe_2$ a constant lifetime broadening of 0.3 eV. From the energy bands and the TB-LMTO eigenvectors, we calculated the total and orbital projected density of states.

Specific heat

The electronic specific heat coefficient value γ in the low-temperature limit is proportional to the density of states at the Fermi energy E_F and is given by

$$\gamma = \frac{\pi^2}{3} D(E_F) k_B^2 (1 + \lambda) \tag{5.1}$$

where k_B is Boltzmann's constant and λ is the mass enhancement factor incorporating the interactions of an electron with other electrons or phonons. The experimental value for γ of $LuFe_2$ is 12.8 (mJ/K^2mole) by Butera *et al.* [74]. The calculated value by the TB-LMTO method is 6.81 (mJ/K^2mole), similar to that obtained by Yamada *et al.* [75] using the empirical tight-binding method. From Eq. (5.1) we have $\lambda = 0.88$.

Magnetic moment

$LuFe_2$ orders ferrimagnetically and has a Curie temperature of 570 K [76]. SQUID mesurements confirmed that an applied magnetic field of 1.0T is sufficient to saturate the magnetic moments of $LuFe_2$ at 5K as shown in Fig. 5.4. The saturation magnetization is $2.46\mu_B/LuFe_2$ and therefore smaller than the magnetic moment determined by neutron scattering by Givord *et al.* [77] who measured $2.85\mu_B/LuFe_2$. Recently Kasamatsu *et al.* [78] carried out magnetic moment measurements of Lu in $LuFe_2$ by high pressure ^{175}Lu NMR measurements at 4.2K. From this experiment they suggested that Lu may carry a negative magnetic moment as predicted by self-consistent band calculations. The partial densities of states of Fe and Lu are shown in Figs. 5.5 and 5.6.

We can explain the negative magnetic moment of Lu with the density of states. Because the 6s and 6p states of Lu are featureless and broad, we focus on the 5d states on the Lu atom. Yamada [75] and Brooks [79] explained the negative sign of the magnetic moment of Lu through the analysis of hybridization between the 5d states on Lu atoms and 3d states on Fe atoms. Their explanation is as follows, which can be confirmed by

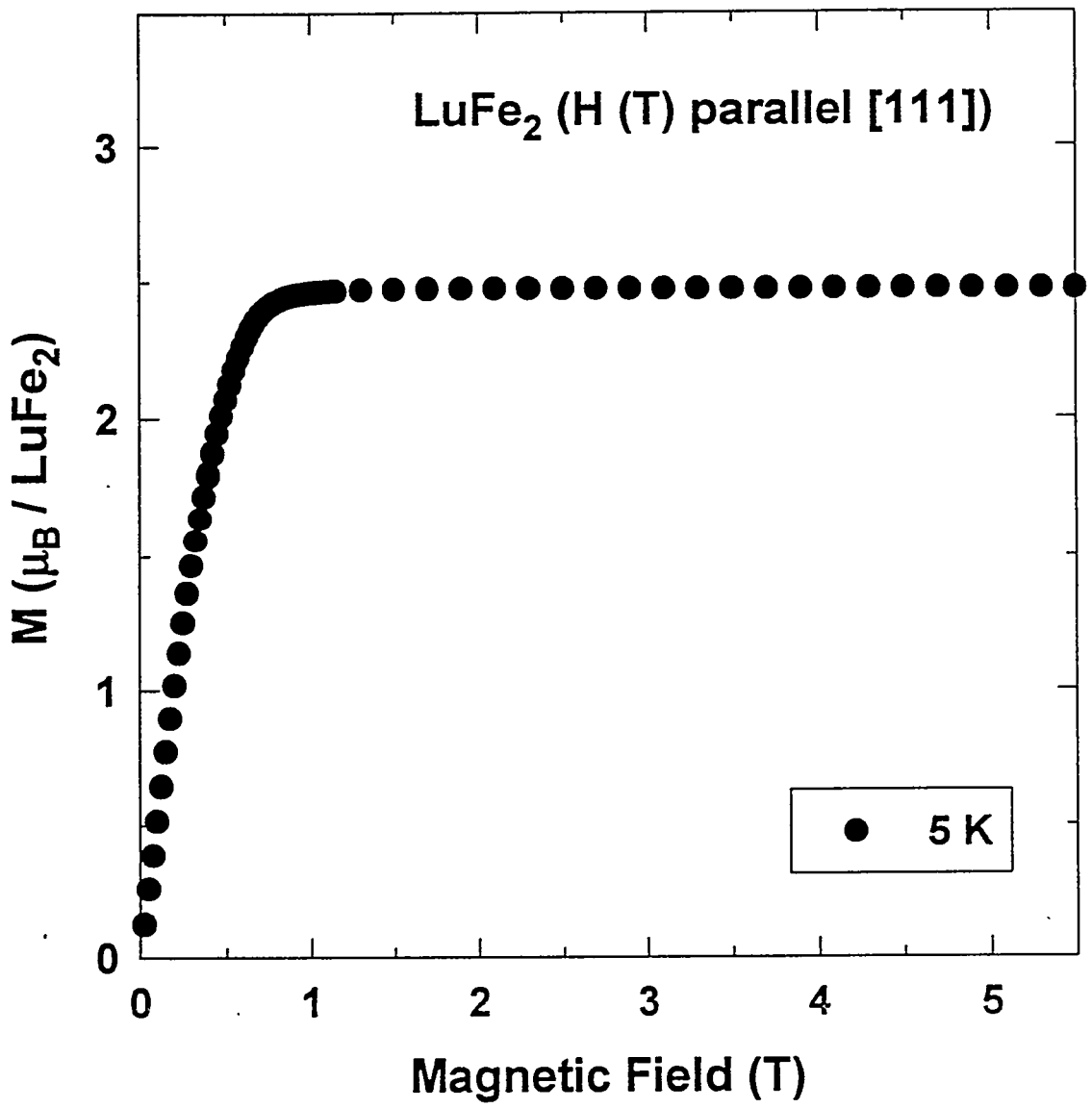

Figure 5.4 Magnetization of $LuFe_2$ at 5K. The magnetic field H was applied parallel to [111].

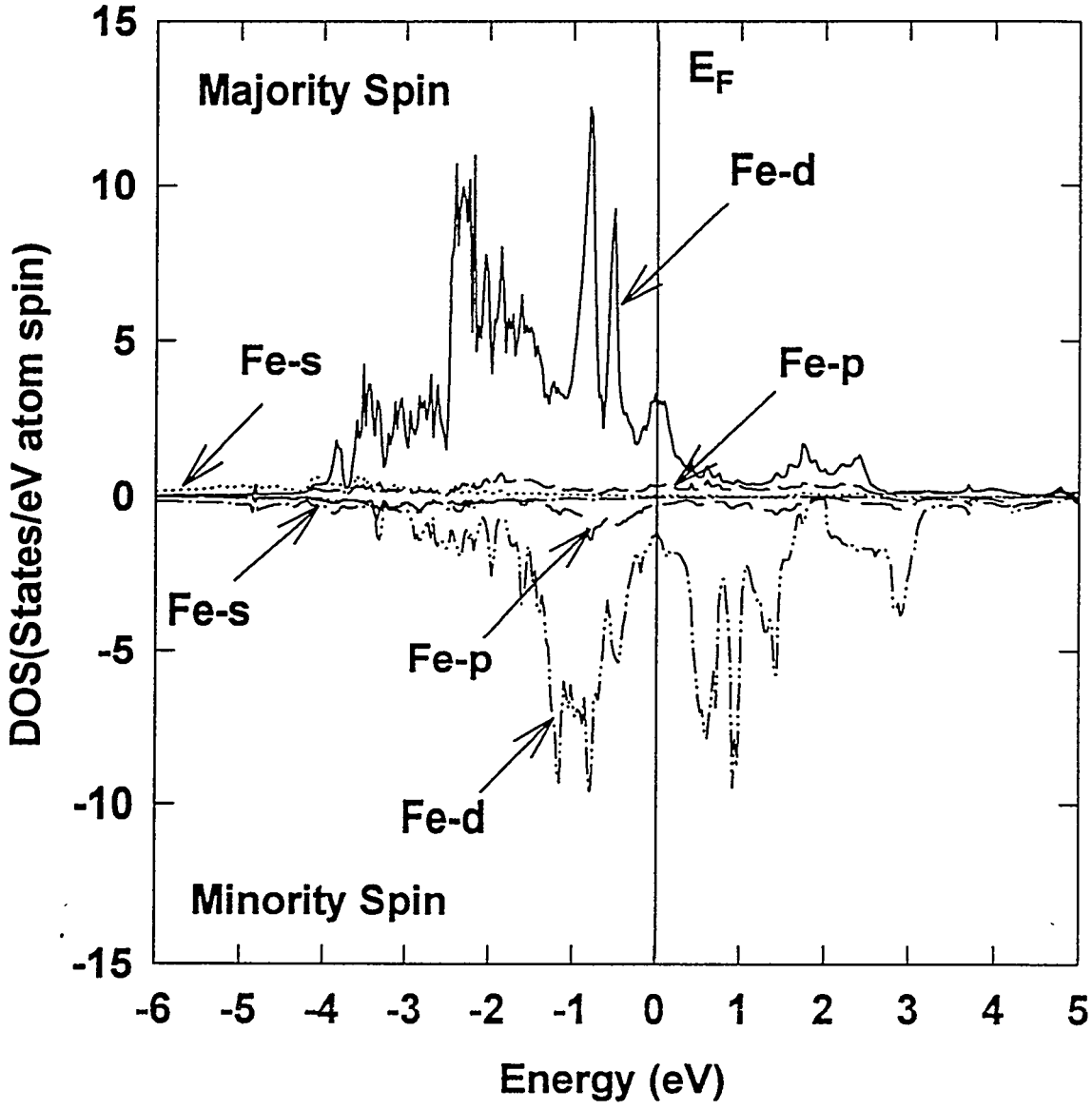

Figure 5.5 Calculated spin-polarized partial density of states (DOS) for Fe using the TB-LMTO including spin-orbit interaction.

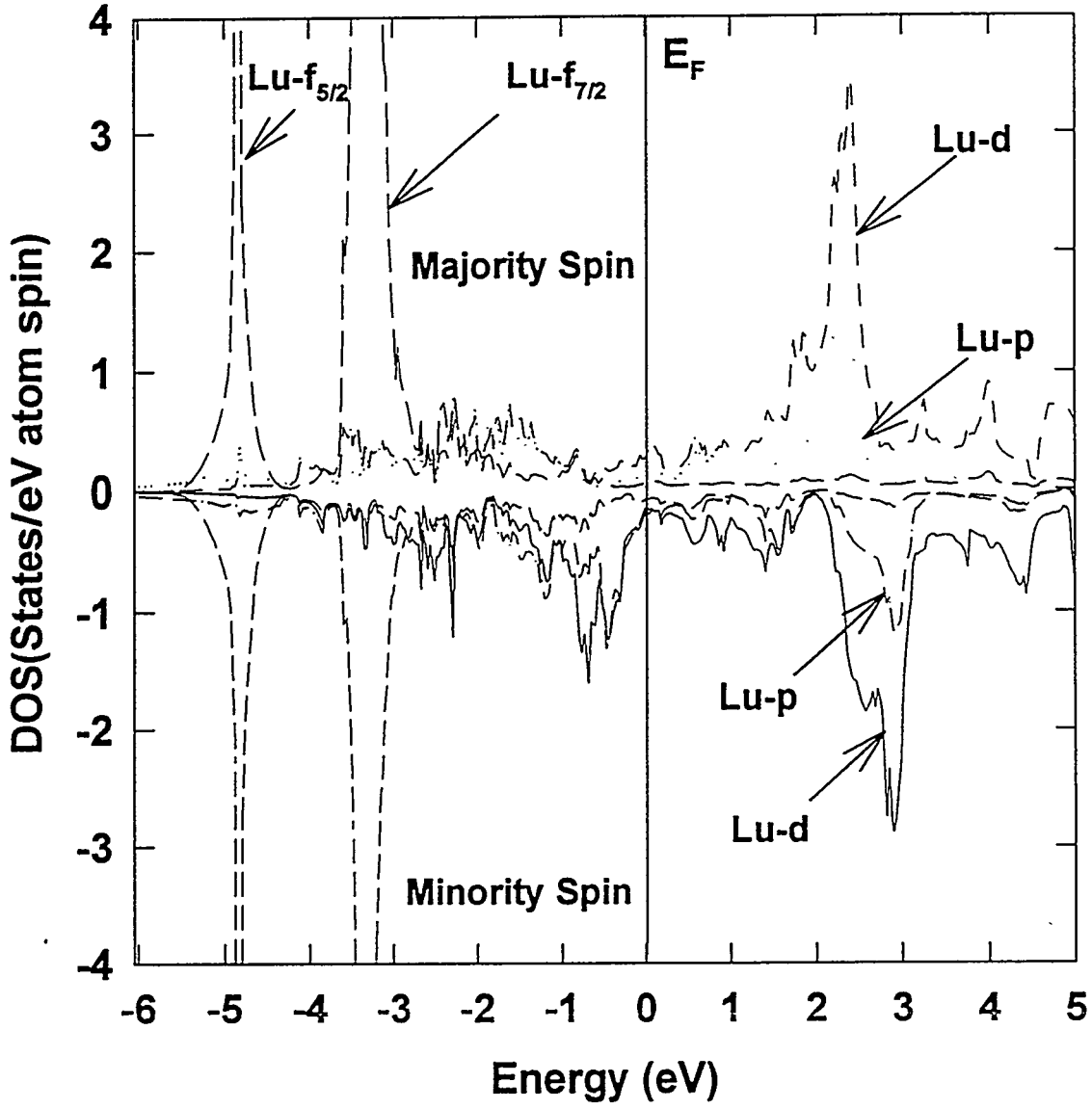

Figure 5.6 Calculated spin-polarized partial density of states (DOS) for Lu using the TB-LMTO including spin-orbit interaction. Two peaks in the DOS are split by spin-orbit interaction.

Figs. 5.5 and 5.6. The energy of Lu the 5d states is higher than that of the Fe 3d states. In a saturated ferromagnetic state, the majority spin states and minority spin states of Fe 3d are shifted in opposite directions by exchange splitting, as shown in Fig. 5.5. The hybridization between the minority spin states of Fe 3d and Lu 5d is stronger than that of the majority spin states of Lu 5d and Fe 3d due to the smaller energy separation of the former pair. This stronger hybridization of the minority spin states causes the minority occupations of Lu 5d to become larger than the majority occupations of Lu 5d shown in Fig. 5.6. Therefore the net magnetization of Lu is negative and the crystal becomes a ferrimagnetic material.

Result and discussion

Using a rotating analyzer ellipsometer we measured the dielectric function of $LuFe_2$ between 1.5 and 5.5 eV and calculated the diagonal part of the optical conductivity from the optical constants. In Fig. 5.7 we show the results together with the absorptive part of $\tilde{\sigma}$ obtained from the TB-LMTO, where we included a lifetime broadening of 0.3 eV. The shapes of the calculated and measured spectra agree well. The amplitude of the experimental conductivity is lower than expected, possibly due to a native oxide overlayer. Figure 5.8 displays the experimental Kerr rotation and ellipticity measured at different temperatures and magnetic fields between 1.4 and 4.0 eV. The minimum Kerr rotation appears near 3 eV.

As the field increases, the magnitude of the Kerr rotation increases, but there is no essential change of shape of the spectrum. The solid lines in Figs. 5.8 and 5.9 show calculated values of the Kerr rotation and ellipticity. In this calculation, we treated the 4f electrons of Lu as valence electrons. Two narrow spin-orbit split 4f bands ($4f_{5/2}$ and $4f_{7/2}$) lie about 4.8 and 3.3 eV below the Fermi level, respectively, as shown in Fig. 5.6. These results are similar to those obtained for elemental Lu by Min *et al.*

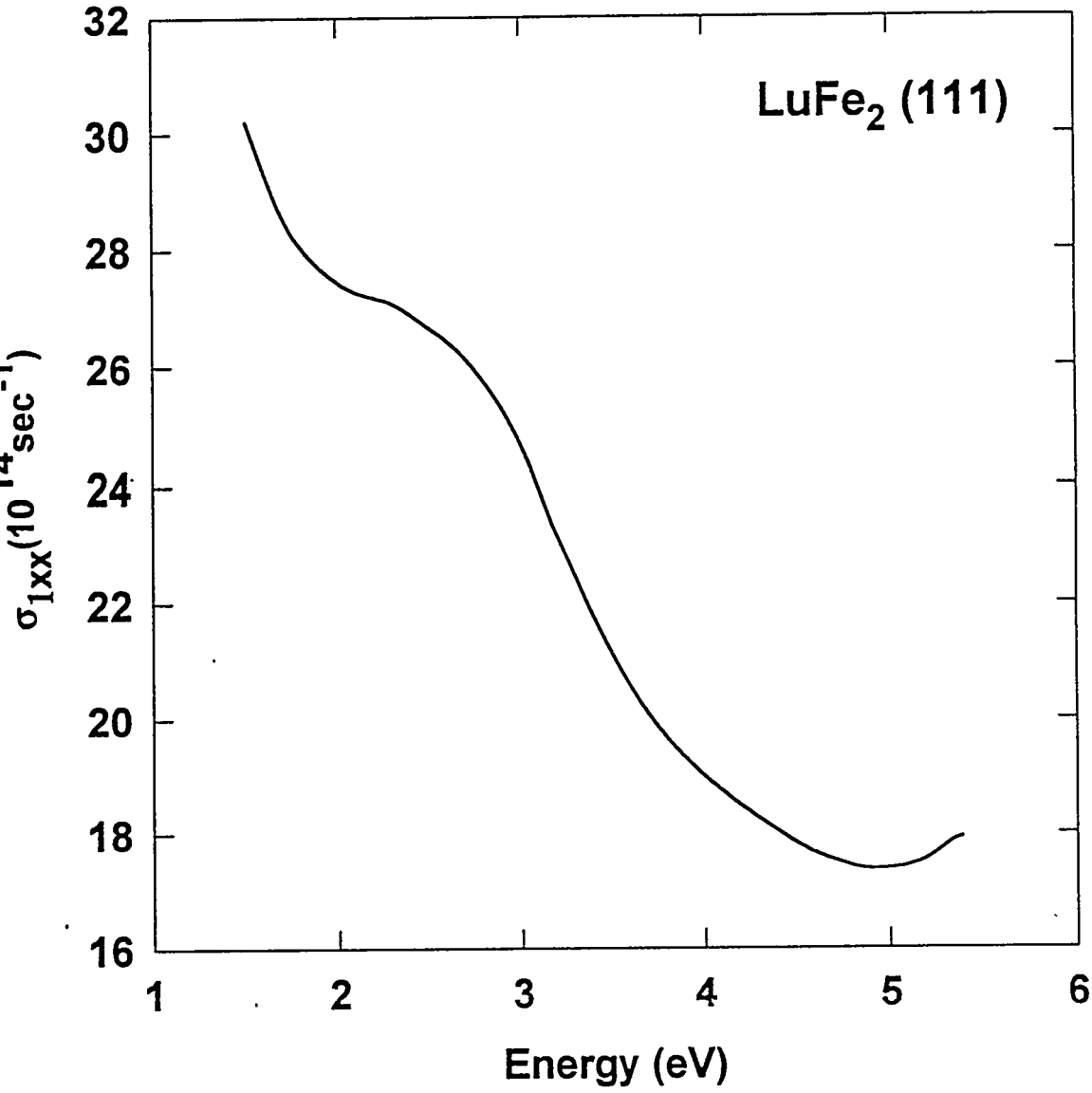

Figure 5.7 Diagonal component of the optical conductivity of $LuFe_2$ measured at room temperature with a rotating analyzer ellipsometer.

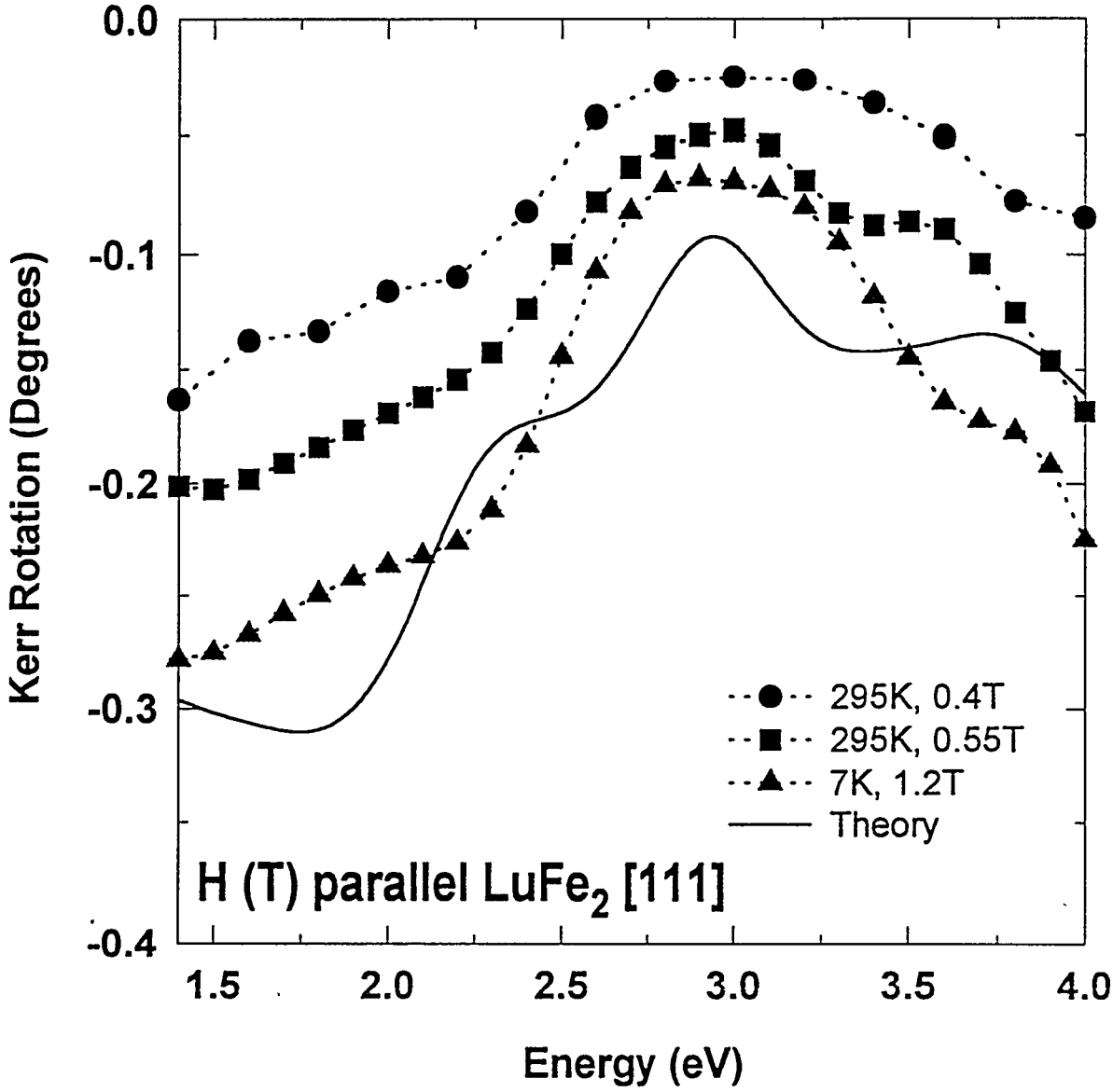

Figure 5.8 Polar Kerr rotations of $LuFe_2$ measured at different temperatures and magnetic fields. The solid line shows the result obtained from the TB-LMTO with a lifetime broadening of 0.3 eV.

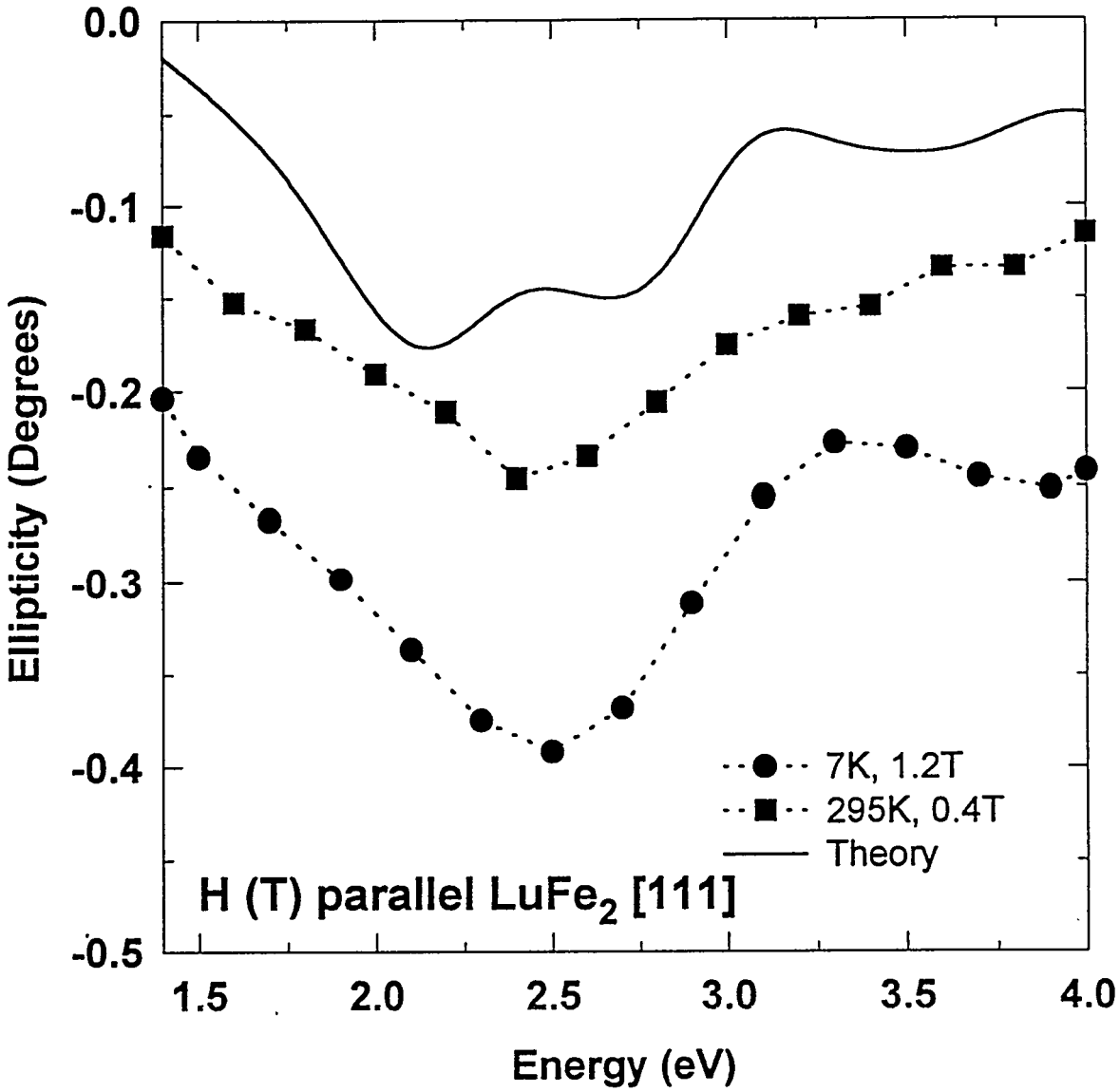

Figure 5.9 Ellipticity of $LuFe_2$ measured at different temperatures and magnetic fields. The solid line shows the result obtained from the TB-LMTO with a lifetime broadening of 0.3 eV.

[69] When we compare experimental and theoretical Kerr rotation spectra, we notice that the theoretical and experimental values agree well in magnitude and shape in the measured range. The agreement between theory and experiment for RFe_2 (R=Gd, Ho, Tb) was not as good. This is attributed to the problem of treating the 4f bands within the LSDA formalism, whereby partially occupied 4f bands are positioned at the Fermi level. Only negligible Lu 4f conduction electron states are occupied near the Fermi level, which indicates that the electronic configuration is transition metal-like. Around 3.5 eV, there is a small shoulder in the experimental data as shown in Fig. 5.8. In the theoretical results we see the same flat shoulder appear between 3.3 and 3.7 eV. This occurs only when we treat the 4f electrons of Lu as valence electrons. When we treat them as core electrons, the flat shoulder does not appear in the calculated Kerr rotation. Figure 5.7 shows the spectra of $\omega\sigma_{2xy}$ derived from experimental data of $(\theta_K, \varepsilon_K)$ and (n, k), and theoretical values from the TB-LMTO calculations. $\omega\sigma_{2xy}$ is proportional to the difference of the absorption rates for LCP and RCP light. $\omega\sigma_{2xy}$ has a large value at 1.5 eV as shown in Fig. 5.10, Therefore transitions relating to LCP light are stronger in this region. From the density of states analysis this peak in σ_{2xy} near 1.5 eV likely originates from Fe-(4p$\rightarrow$3d) and Lu-(6p$\rightarrow$5d) interband transitions near E_F.

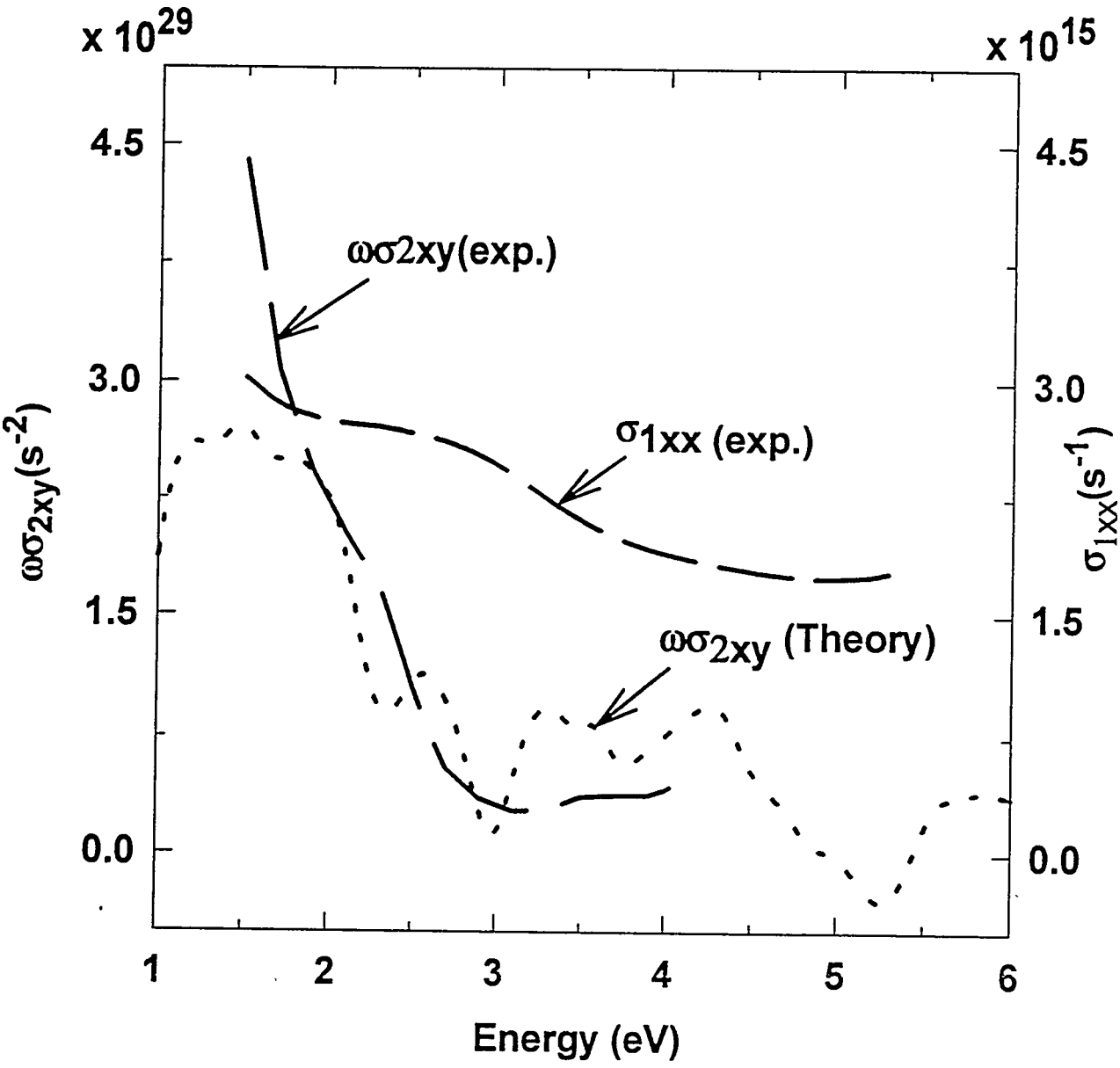

Figure 5.10 Experimental spectra of $\omega\sigma_{2xy}$ and σ_{1xx} obtained from Kerr spectroscopy and ellipsometry. The dotted line is the theoretical value of $\omega\sigma_{2xy}$ from the TB-LMTO calculation. A reduced lifetime broadening of 0.2 eV was used to enhance the structure of the calculated conductivity. No Drude contributions were included in the theoretical results.

6 THE OPTICAL AND MAGNETO-OPTICAL PROPERTIES OF $GdCo_2$ SINGLE CRYSTAL

Introduction

The rare-earth-transition-metal (RE-TM) intermetallic compounds have been studied extensively because of their useful technological applications. Many permanent magnets and magneto-optical storage media are made of RE-TM compounds. Studying the electronic, magnetic and magneto-optical properties of $GdCo_2$ which has the cubic Laves-phase structure, can give insights for more complicated RE-TM intermetallic compounds. The spin-polarized electronic structure is an essential part to understanding the magnetic and magneto-optical properties of $GdCo_2$. The Gd in $GdCo_2$ has 4f electrons, which makes electronic structure calculations difficult due to the strongly correlated 4f electrons. The experimental value for the energy separation between the spin up 4f bands and spin-down 4f bands of elemental Gd is 12 eV. But theory based on the LSDA gives only 5 eV because the LSDA does not include many-electron correlation effects. These incorrect positions of the 4f bands relative to the Fermi level induce incorrect interband transitions between f and d orbitals in the magneto-optics calculations. To avoid this problem, sometimes treating the 4f electrons as core electrons when performing self-consistent LSDA calculation is employed [80]. Jaswal [81] calculated the self-consistent electronic structure of simple structural models of Gd_2Co and compared it with their X-ray photoemission measurements on a-$Gd_{65}Co_{35}$. Calculating a realistic atomic model of a-$Gd_{65}Co_{35}$ glass is extremely difficult, therefore they simulated the $Gd_{65}Co_{35}$ glass

with a CaF_2 and a body-centered-tetragonal (BCT) crystalline structures of the same composition and the average mass density as that of glass. Their calculation for the simulated Gd_2Co structures produced the wrong positions of 4f electrons of Gd in the electronic structure due to the strong intra-atomic Coulomb correlation energy which is not well considered in the one-electron LSDA. To incorporate the many-body correlation effects of localized 4f states in Gd_2Co, they employed a Slater transition-state analysis [82] and calculated the change in the total energy of the Gd_2Co. Through this process, a correction term δ to Koopman's theorem appeared. By adding the calculated value $\delta = 3.3\ eV$ for the Gd atom to the DOS obtained from the LSDA, the Gd-4f level for Gd_2Co was in reasonable agreement with the XPS of a-$Gd_{65}Co_{35}$. Antropov [83] *et al.* employed the so called LDA+U [84] method which includes the Coulomb parameter U for the 4f electrons explicitly. They used the full-potential scalar-relativistic LMTO technique [85] in calculating the electronic band structure of Gd and CeSb. The calculated results for Gd are in remarkably good agreement with experimental data. The theoretical energy separation between the spin up 4f bands and spin-down 4f bands is 11.5 eV which agrees well with the experimental value of 12 eV. Furthermore, the 4f spin-down bands are removed from near the Fermi level, leading to great improvement in the off-diagonal component of the optical conductivity, which is directly related to the magneto-optical parameters. From the analysis of the LDA+U calculation, they found almost all of the magneto-optical spectrum is due to p-to-d interband transitions. Even up to 10 eV, the contributions from f electrons are negligible. But so far there have been no reports of LDA+U calculations for $GdCo_2$.

Magnetic properties of $GdCo_2$

$GdCo_2$ shows interesting magnetic properties [86, 87] From neutron diffraction, it is found that the magnetic moments of Gd and Co atoms are aligned in opposite directions

[88]. Gignoux [89] measured the magnetic moment of $GdCo_2$ at 4.2K with a sample which consists of 80% single crystalline domain and the rest a polycrystalline Gd_2Co_3 phase. At 4.2 K, the easy axis of $GdCo_2$ is the [001]. They found also the energy anisotropy is very weak, that is, the magnetization anisotropy is negligible within experimental accuracy. The measured saturated magnetic moment is $5.3\mu_B$ per $GdCo_2$ a value higher than that of polycrystalline $GdCo_2$ measured at the same temperature, 4.2K (4.89 μ_B per $GdCo_2$ [90]). The SQUID measurement for single-crystal $GdCo_2$ obtained from the flux method is shown in Fig. 6.1. As shown in Fig. 6.1, the magnetic moment of $GdCo_2$ at 7K is 5.47 μ_B per $GdCo_2$. This value is larger than those of the imperfect single crystal of Ginoux and polycrystalline sample. The theoretical magnetic moment calculated with the TB-LMTO based on the LSDA is 5.45 μ_B per $GdCo_2$. In our theory we treated the 4f electrons as valence electrons. The Gd magnetic moment is 7.2 μ_B and Co magnetic moment is 0.88 μ_B.

Sample preparation and characterization

While the magnetic properties of $GdCo_2$ have been studied extensively, the magneto-optical properties of single-crystal $GdCo_2$ have not been reported, probably due to the difficulties of growing single crystals of rare earth-cobalt compounds [91]. Katayama *et al.* [92] measured the polar Kerr rotation of a single crystal of $GdCo_5$ and amorphous films of $Gd_{21}Co_{79}$. Even though their compositions are similar, the features are quite different, especially in the UV region. The amorphous materials have no periodicity; therefore Bloch's theorem is not applicable. Therefore for comparison with theory, it is best to measure with single crystals which keep long range periodicity. For the growth of single crystals of $GdCo_2$, the flux-growth technique has been used. The detailed procedure for growing single crystals of $GdCo_2$ by the flux method is as follows. The melting points of Gd and Co are $1313°C$ and $1495°C$, respectively as shown in Fig. 6.2,

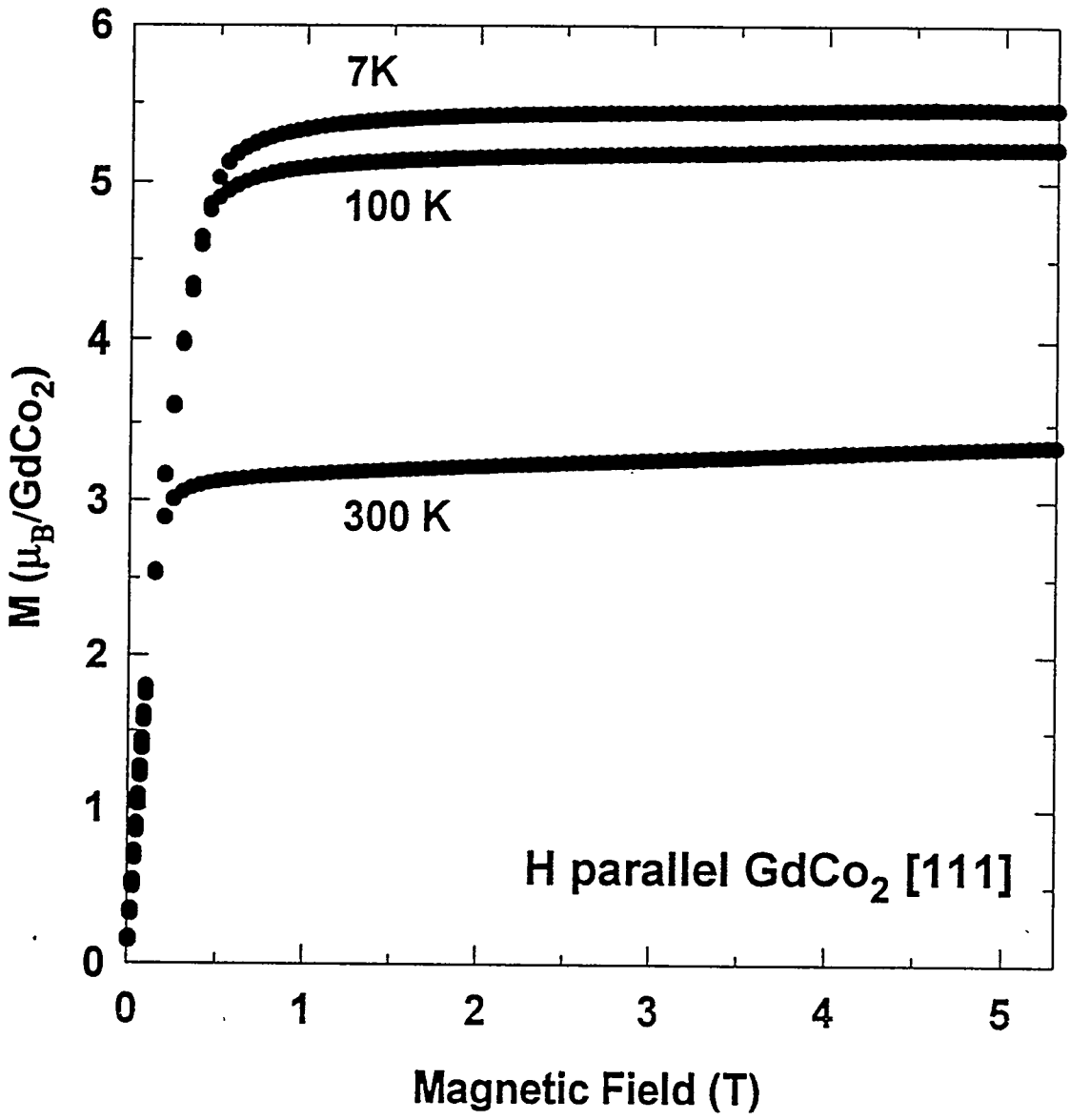

Figure 6.1 Magnetization measurements of $GdCo_2$ at 7K, 100K, and 300K.

therefore we need to do arc-melting first. A button-shaped sample of stoichiometric polycrystalline $Gd_{.55}Co_{.45}$ is prepared by arc-melting under Ar gas on a water-cooled copper hearth. The button, wrapped in Ta foil, is sealed in a quartz tube under a partial pressure of Ar and then heated to 1140 $°C$. The mixture was cooled from 1140 $°C$ to 950 $°C$ within 2 hours and slowly cooled from 950 $°C$ to 700 $°C$ over a period of 132 hours. The crystal grow during the cooling step. At a temperature of 700 $°C$, the crystals of $GdCo_2$ were removed from the melt. The size of the crystals are typically $2 \times 1 \times 1mm^3$.

From the X-ray diffraction measurement shown in Fig. 6.3, a lattice constant of $7.272\mathring{A}$ was determined and used for the TB-LMTO calculation. The crystal size is too small to mount on the sample holder for introduction into the cryostat. The Curie temperature of $GdCo_2$ is 440 K [93] which is above room temperature, and the magnetic moment of $GdCo_2$ is saturated at a magnetic field of 0.5T at room temperature as seen in Fig. 6.1. The single crystal of $GdCo_2$ was measured out of the cryostat using a $Nd_2B_{14}Fe_2$ permanent magnet [94] which can generate a magnetic field of 0.5T.

Oxidation effects

Rare-earth materials are oxidized when exposed to air, even at room temperature. Lee *et al.* [95] have studied the oxidation of RCo_2 (R=Gd, Tb, Dy) and $GdNi_2$ compounds by magnetic analysis. By heating to $750K$ for one hour in air, they found that rare-earth transition-metal intermetallic compounds oxidize readily to form free transition metal and a rare-earth oxide, possibly R_2O_3. The transition metal atoms diffused to form clusters of free transition metal, even at room temperature. But the mechanism of the diffusion process, the degree of oxidation, and the nature of the rare-earth oxide were not determined from their experiments. Shen [96] *et al.* have investigated the oxidation of Gd-Co and Gd-Fe amorphous films by XPS. From the XPS depth profiles,

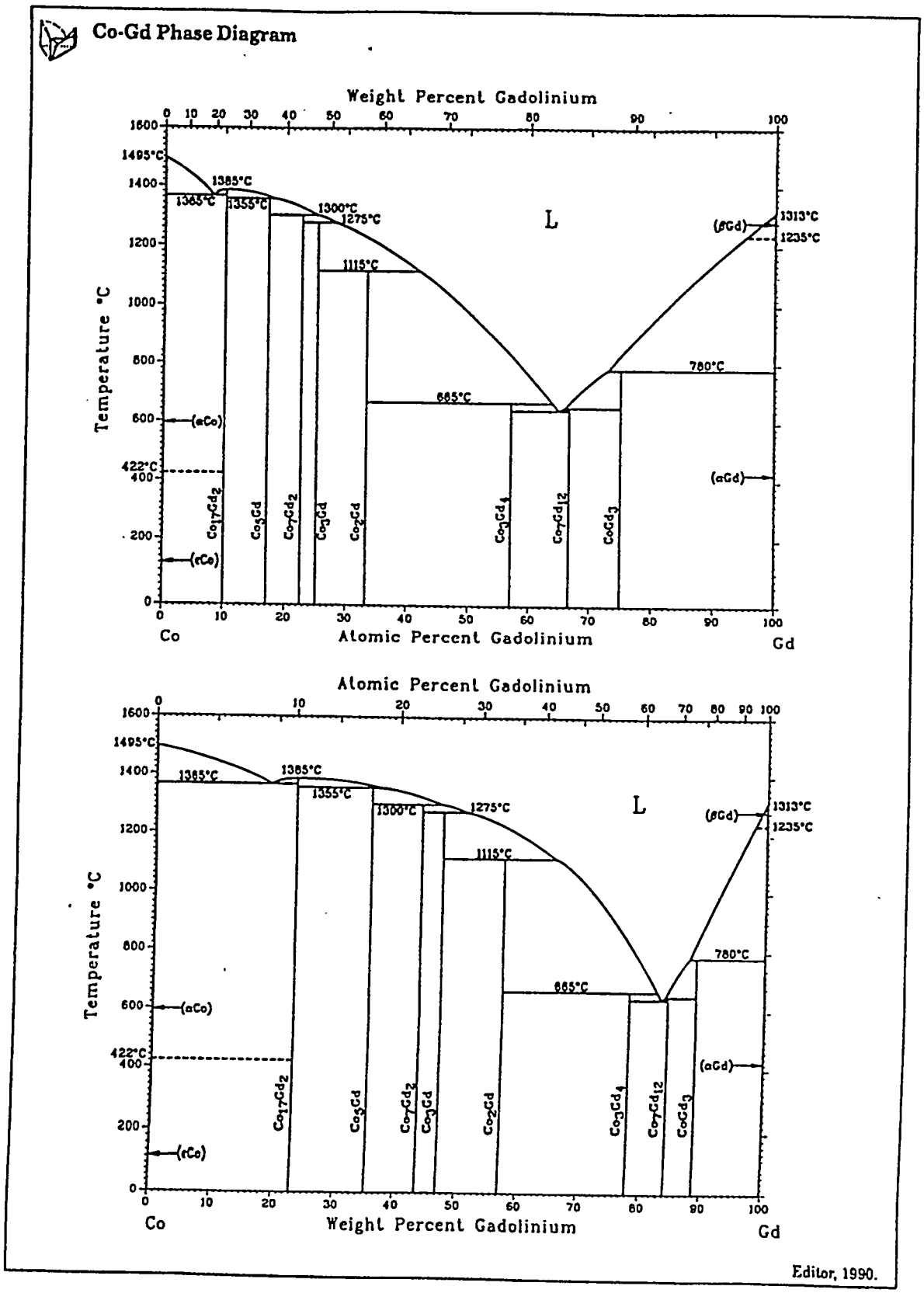

Figure 6.2 Co-Gd Phase Diagram [51].

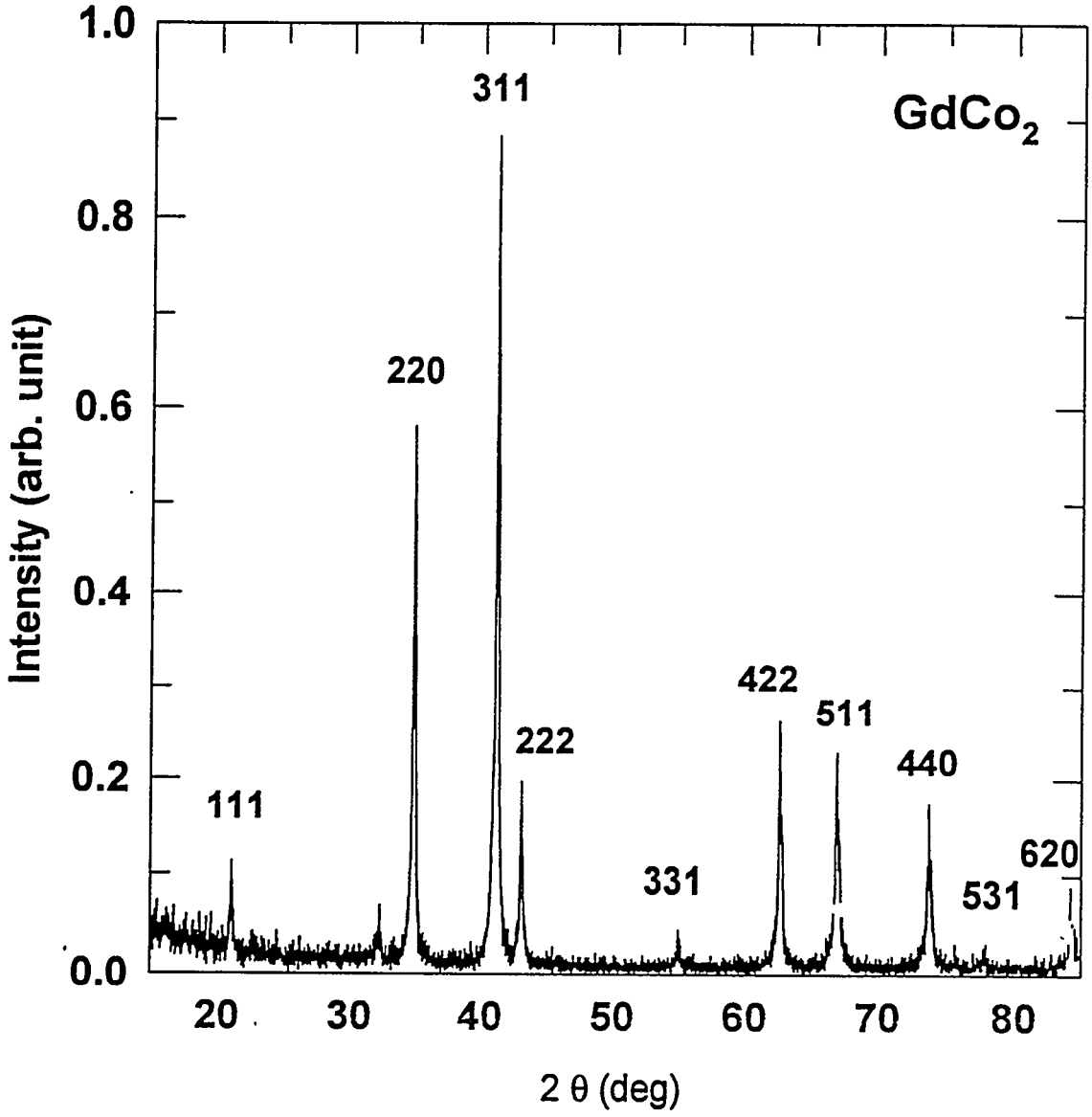

Figure 6.3 Powder X-ray diffraction pattern of crushed $GdCo_2$ single crystal. The peaks are indexed to a fcc unit cell with a lattice parameter a=7.272$\mathring{A}$.

surface segregation of Gd was observed even at room temperature. They suggested this segregation of the oxidized Gd leads to the reduction of the Co oxide. Dover *et al.* [97] have studied the effects of oxidation on the magnetic properties of unprotected Tb-Fe thin films with Auger electron spectroscopy (AES). They prepared amorphous Tb-Fe thin films by dual magnetron cosputtering. They found the films with no overcoating to develop an oxide layer about 8 nm thick upon exposure to air at room temperature. It developed roughly in one day, then ceased further growth. Buschow [98] *et al.* measured the polar Kerr rotation of M_xCo_{1-x} intermetallic compounds where M is La, Y or Gd. They measured the Kerr rotation of polycrystalline $GdCo_2$, $GdCo_3$, $GdCo_5$, Gd_2Co_{17} with an applied field of 1.15 T at room temperature (Fig. 3 of ref.([98]). They also measured several amorphous $Gd_{1-x}Co_x$ samples with x=0.62, 0.75, 0.87, 1.00 (Fig. 4 of ref. [98]). As shown in those figures, the Kerr rotation features of amorphous $Gd_{1-x}Co_x$ become less clear as the concentration ratio x decreases compared to those of polycrystalline samples. Because $GdCo_2$ is ordered ferrimagnetically and dominated by the Gd-sublattice at room temperature, the Gd magnetic moments in $GdCo_2$ are parallel to the applied magnetic field and the Co magnetic moments in $GdCo_2$ are antiparallel to the applied magnetic field. Unlike $GdCo_2$, the Co magnetic moments are dominant in $GdCo_3$, $GdCo_5$, and Gd_2Co_{17}. Therefore the Co magnetic moments are parallel to the applied magnetic field for these compounds. Buschow *et al.* have reversed the directions of the vertical axes which represents the Kerr rotation $2\theta_K$ of $GdCo_2$ to make the orientation of the Co magnetic moments in $GdCo_2$ parallel to the applied magnetic field, as in other Co-rich compounds, for the purpose of comparison of Kerr rotation spectra of the other Co-rich compounds. Co, Ni, and Fe are well known materials whose Kerr rotations are negative in the IR, visible, and near UV region, while the Kerr rotation of elemental Gd is positive [29]. One can expect a positive Kerr rotation for $GdCo_2$ if we can neglect the couplings between Gd and Co in $GdCo_2$ because the magnetic moments of Gd and Co are ferrimagnetically ordered. Mathematically we can express

this as $\theta_{Kerr} = \theta_{Gd} - \theta_{Co}$. That is the Kerr rotation of Gd is positive and the Kerr rotation of Co is negative. Therefore the subtraction gives a positive Kerr rotation. This is a kind of independent sublattice-model which ignores couplings between Gd and Co. This model is incorrect because the electronic structure and density of states of $GdCo_2$ are dependent on the hybridization between the majority Gd-5d bands and the minority Co-3d bands. Therefore the Kerr rotation of $GdCo_2$ which is dependent on the electronic structure of the magnetic materials, can not be simply described by adding the Kerr rotations of individual atoms with opposite sign. Katayama [92] analyzed the Kerr rotation of polycrystalline $GdFe_2$ samples, following the idea of independent sublattice model, that is, neglecting other types of atoms in the compound, and just added the Kerr rotation contributions from each elemental atom, Gd and Fe. As shown in Fig. 6.4, the Kerr rotation of $GdCo_2$ is not positive in the whole spectral range. The Kerr rotation crosses from positive to negative at 3.8 eV. Figure 6.4 shows the Kerr rotation and ellipticity of a single crystal of $GdCo_2$ measured at room temperature with an applied magnetic field of 0.5T. On the contrary, the Kerr rotation crosses from positive to negative at 3.7 eV. The Kerr rotation of the $Gd_{.25}Co_{.75}$ amorphous alloy in Fig. 4 of Buschow's paper [98] agrees with the Kerr rotation of $GdCo_2$ in Fig. 3 in the same paper [98]. Therefore the Kerr rotations of $GdCo_2$ and $GdCo_3$ in Fig. 3 of Buschow's paper [98] have to be switched. The $GdCo_3$ Kerr rotation spectrum in Fig. 3 of Buschow's paper [98] should be compared with our single-crystal $GdCo_2$ Kerr rotation spectrum. Their Kerr rotation data are similar to our data in that the Kerr rotation of their polycrystalline $GdCo_2$ crosses zero at 3.6 eV, but the difference is that their magnitude is smaller than ours. We could not compare the ellipticity data because they did not measure ellipticity. To calculate the off-diagonal conductivity component, we have to have the experimental optical constants. We used rotating analyzer ellipsometry to measure the optical constants. Figure 6.5 shows the optical conductivity in units of 10^{14}/ sec.

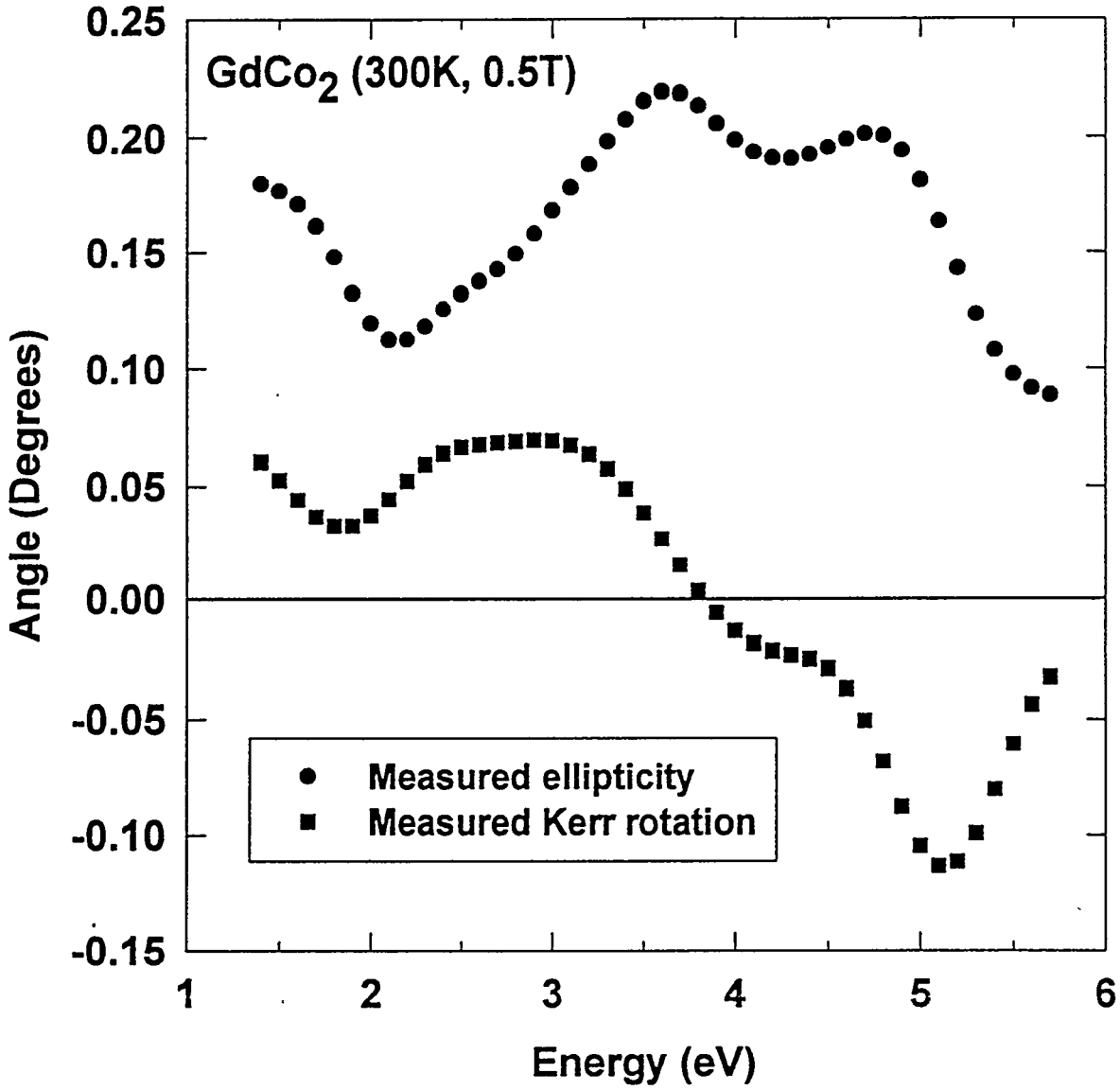

Figure 6.4 Kerr rotation and ellipticity of single crystal of $GdCo_2$ measured with an applied field of 0.5T at room temperature.

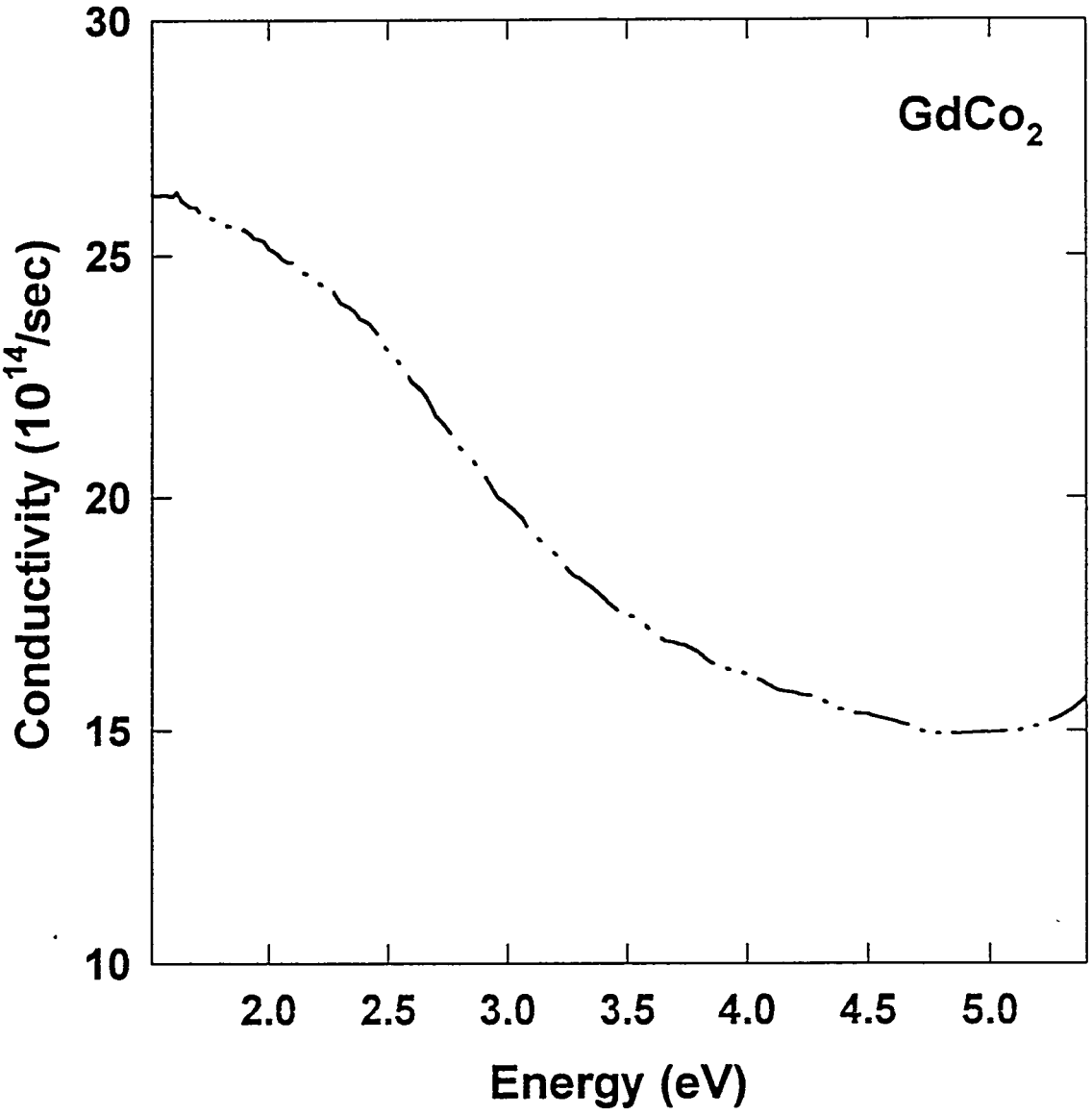

Figure 6.5 The real part of the diagonal optical conductivity in units of 10^{14}/ sec measured at room temperature.

The Kerr rotation of the alloy sample $Gd_{1-x}Co_x$(x=0.62) was found to be changed, especially in the UV region, when exposed to air for an extended period of time [98]. This indicates that oxidation affects the magneto-optical properties of the sample. For the effect of oxidation on the diagonal part of the optical conductivity, we used the three-phase model which was explained in detail in chapter 4. We assumed that the native oxide layer on $GdCo_2$ is a transparent dielectric with an effective refractive index n and thickness d. The results are shown in Fig. 6.6 with different refractive indices and thickness of the oxide layer.

To treat the effect of an oxide overlayer on the Kerr rotation and ellipticity, we modified Chen *et al.*'s general expression for the magneto-optical polar Kerr effect in a bilayer system [99, 100]. Their expression could be used for magnetic materials with an oxide layer if we replace the dielectric coating SiO by the oxide layer [99]. Because we used different time dependence ($\sim e^{-i\omega t}$) and magneto-optics notation, their equations should be modified. The derivation is summarized as follows. The normally incident polar Kerr effect in a magnetic medium is characterized by the response for right and left circular polarized light. The complex refractive indices corresponding to left (+) and right (-) circular polarized light are given by

$$\tilde{n}_{\pm} = \tilde{n}_m \left(1 \pm \frac{Q}{2}\right), \qquad |Q| \ll 1 \tag{6.1}$$

where $\tilde{n}_m = n + ik$. $\tilde{n}_m$ denotes a complex refractive index in the unmagnetized state of the medium. Q is a complex number called the Voigt parameter, which is related to $\tilde{\epsilon}_{xx}$ and $\tilde{\epsilon}_{xy}$ by

$$Q = i\frac{\tilde{\epsilon}_{xy}}{\tilde{\epsilon}_{xx}}. \tag{6.2}$$

Assuming that the light is incident from the non-magnetic medium whose complex refractive index is $\tilde{n}_0$ onto the magneto-optic medium, the $\tilde{r}_{\pm}$ in a two-medium system will be

$$\tilde{r}_{\pm} = r_{\pm}e^{i\delta_{\pm}} = \frac{\tilde{n}_o - \tilde{n}_{\pm}}{\tilde{n}_o + \tilde{n}_{\pm}} = \tilde{r}\tilde{\rho}_{\pm}, \tag{6.3}$$

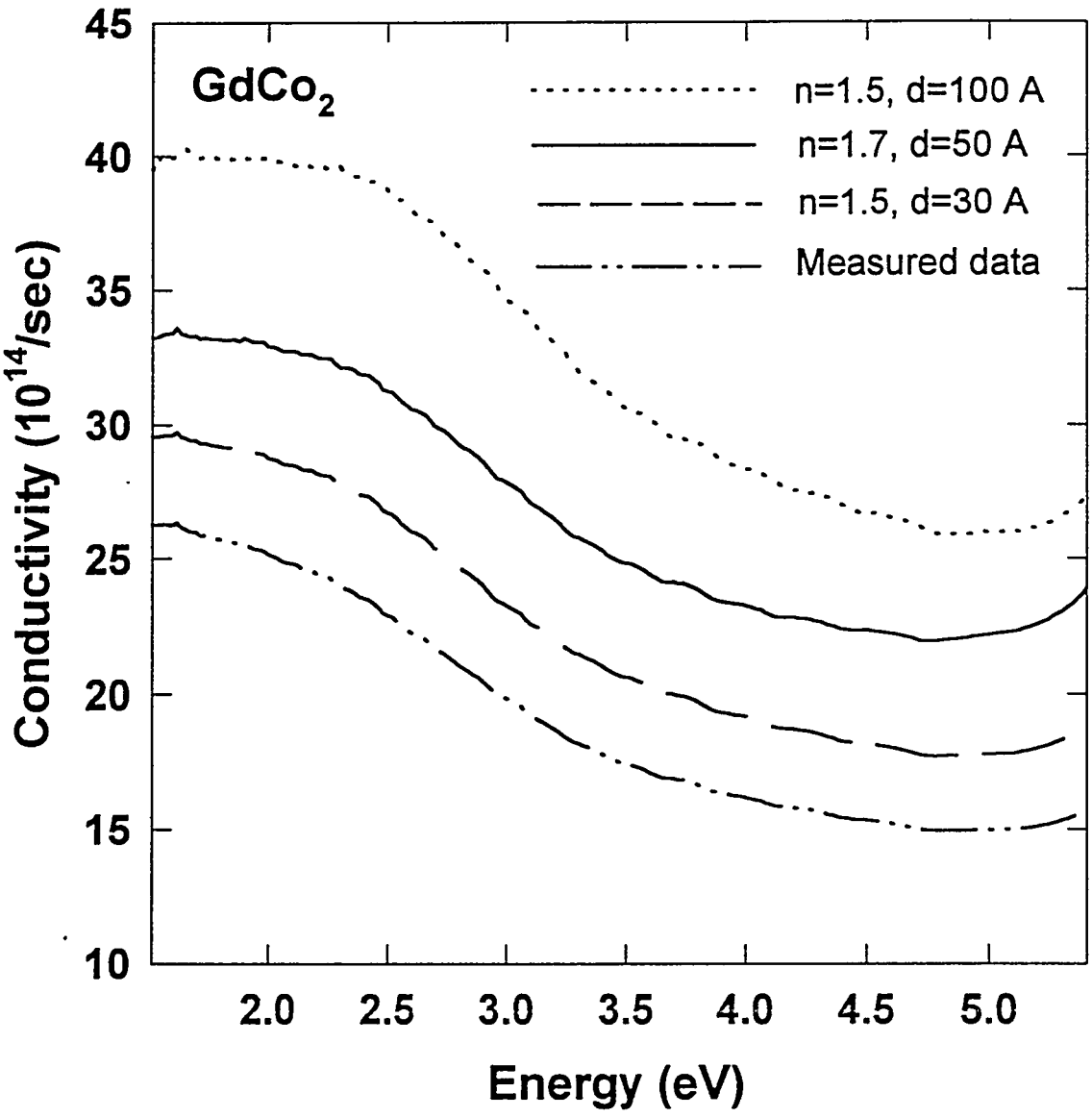

Figure 6.6 The real part of the diagonal optical conductivity with different refractive indices and thickness of the oxide layer.

where $\tilde{r}$ is the ordinary reflection coefficient for the magneto-optic medium when there is no magnetization,

$$\tilde{r} = re^{i\varphi} = \frac{\tilde{n}_o - \tilde{n}_m}{\tilde{n}_o + \tilde{n}_m}, \tag{6.4}$$

and $\tilde{\rho}_\pm$ is a complex quantity related to the pure MOKE. From Eqs. 6.1, 6.3, and 6.4, we can derive the following equation,

$$\tilde{\rho}_\pm = \frac{\tilde{r}_\pm}{\tilde{r}} = \rho_\pm e^{i\theta_\pm} = \frac{\left(1 \mp \frac{\tilde{n}_m \frac{Q}{2}}{\tilde{n}_o - \tilde{n}_m}\right)}{\left(1 \pm \frac{\tilde{n}_m \frac{Q}{2}}{\tilde{n}_o + \tilde{n}_m}\right)}. \tag{6.5}$$

Because $|Q| \ll 1$, we can expand the denominator and finally have the form,

$$\tilde{\rho}_\mp \simeq \left(1 \pm \frac{\tilde{n}_m \frac{Q}{2}}{\tilde{n}_o - \tilde{n}_m}\right)\left(1 \mp \frac{\tilde{n}_m \frac{Q}{2}}{\tilde{n}_o + \tilde{n}_m}\right). \tag{6.6}$$

By ignoring Q^2 we have the following form,

$$\tilde{\rho}_\pm = 1 \mp \frac{\tilde{n}_o Q \tilde{n}_m}{\tilde{n}_o^2 - \tilde{n}_m^2} = 1 \mp \tilde{\eta} Q, \tag{6.7}$$

where

$$\tilde{\eta} = \frac{\tilde{n}_o \tilde{n}_m}{\tilde{n}_o^2 - \tilde{n}_m^2} = \frac{\sqrt{\epsilon_o}\sqrt{\epsilon_m}}{\epsilon_o - \epsilon_m}. \tag{6.8}$$

Using Eq. 3.29 and Eq. 6.3, one can get a relation between the complex Kerr rotation $\Psi = \theta_K + i\epsilon_K$ and $\tilde{\eta}Q$ as,

$$\Psi_K = \Theta_K + i\epsilon_K = -i\tilde{\eta}Q. \tag{6.9}$$

If the non-magnetic medium is air, then $\epsilon_0 = 1$ and $\epsilon_m = \epsilon$, In that case, a simple calculation leads to the complex Kerr rotation given in Eq. 3.31. For a system consisting of two interfaces, one with the ambient and a dielectric overlayer and the other the dielectric overlayer and the magneto-optic substrate, the complex Kerr rotation for the system can be obtained using Fresnel's equations. The refractive index of the ambient (air) is 1. Let $\tilde{n}_o$ and $\tilde{n}_\pm^m$ be the complex refractive index of the dielectric overlayer and

the complex refractive index of the magneto-optic substrate respectively. The complex reflection amplitudes $\tilde{r}_1$ for the first interface (air/dielectric overlayer) is given by

$$\tilde{r}_1 = \frac{1-\tilde{n}_o}{1+\tilde{n}_o}. \tag{6.10}$$

The complex reflection amplitudes $\tilde{r}_\pm$ for the second interface (dielectric overlayer/MO substrate) is given by

$$\tilde{r}_\pm = \frac{\tilde{n}_o - \tilde{n}_\pm}{\tilde{n}_o + \tilde{n}_\pm} = \tilde{r}\tilde{\rho}_\pm = \tilde{r}\left(1 \mp \tilde{\eta}Q\right) = \tilde{r}\left(1 \mp i\Psi\right), \tag{6.11}$$

where Ψ is the complex Kerr rotation for the magneto-optic substrate located below the dielectric overlayer and $\tilde{r}$ is defined in Eq. 6.4. The total reflection amplitude for overlayer system is expressed as

$$\tilde{r}_\pm^{tot} = \left|r_\pm^{tot}\right| e^{i\delta_\pm} = \tilde{r}^{tot}\left(1 \mp i\Psi^{tot}\right) = \frac{\tilde{r}_1 + \tilde{r}_\pm e^{i\beta}}{1 + \tilde{r}_1\tilde{r}_\pm e^{i\beta}}, \tag{6.12}$$

where

$$\beta = \frac{4\pi\tilde{n}_o d}{\lambda}. \tag{6.13}$$

Here d denotes the thickness of the dielectric overlayer and λ is the wavelength of the incident light. By inserting Eqs. 6.10 and 6.11 into Eq. 6.13, we have

$$\tilde{r}_\pm^{tot} = \frac{\tilde{r}_1 + \tilde{r}\tilde{\rho}_\pm e^{i\beta}}{1 + \tilde{r}_1\tilde{r}\tilde{\rho}_\pm e^{i\beta}}. \tag{6.14}$$

After some calculation, ignoring 2nd-order terms in the expansion, the above equations can be written in the following simple form,

$$\tilde{r}_\pm^{tot} \simeq \tilde{r}^{tot}\left(1 + A + B\right), \tag{6.15}$$

where

$$\tilde{r}^{tot} = \frac{\tilde{r}_1 + \tilde{r}e^{i\beta}}{1 + \tilde{r}_1\tilde{r}e^{i\beta}}, \tag{6.16}$$

which is an ordinary reflection coefficient for the dielectric overlayer system, and

$$A = \frac{\mp i\tilde{r}\Psi e^{i\beta}}{\tilde{r}_1 + \tilde{r}e^{i\beta}}. \tag{6.17}$$

$$B = \frac{\pm i\tilde{r}_1\tilde{r}e^{i\beta}\Psi}{1 + \tilde{r}_1\tilde{r}e^{i\beta}}. \tag{6.18}$$

From Eqs. 6.13 and 6.16,

$$\mp i\Psi_K^{tot} \simeq A + B. \tag{6.19}$$

Therefore

$$\Psi_K^{tot} = \frac{\tilde{r}e^{i\beta}\left(1 - \tilde{r}_1^2\right)\Psi}{\left(\tilde{r}_1 + \tilde{r}e^{i\beta}\right)\left(1 + \tilde{r}_1\tilde{r}e^{i\beta}\right)}. \tag{6.20}$$

By replacing the complex Kerr rotation with the Kerr rotation and ellipticity, we have

$$\Psi_K^{tot} = \theta_K^{tot} + i\epsilon_K^{tot} = \frac{\tilde{r}e^{i\beta}\left(\theta_K + i\epsilon_K\right)\left(1 - \tilde{r}_1^2\right)}{\left(\tilde{r}_1 + \tilde{r}e^{i\beta}\right)\left(1 + \tilde{r}_1\tilde{r}e^{i\beta}\right)}. \tag{6.21}$$

By simple calculation, we can have the pure complex Kerr rotation $\theta_K + i\epsilon_K$, which is the Kerr rotation of the substrate, corrected for the effect of the oxide overlayers, as follows,

$$\theta_K + i\epsilon_K = \frac{\left(\tilde{r}_1 + \tilde{r}e^{i\beta}\right)\left(1 + \tilde{r}_1\tilde{r}e^{i\beta}\right)\left(\theta_K^{tot} + i\epsilon_K^{tot}\right)}{\left(1 - \tilde{r}_1^2\right)\tilde{r}e^{i\beta}}, \tag{6.22}$$

where $\tilde{r}_1$, $\tilde{r}$, and β are defined in Eqs 6.10, 6.12, and 6.14 respectively. As an approximation, if $\tilde{n}_0 = 1$ and d$\rightarrow$ 0, which corresponds to air, that is no oxide overlayer, then $\tilde{r}_1 = 0$ and $\beta \rightarrow 0$. From this, $e^{i\beta} \rightarrow 1$. This situation corresponds to the pure bulk state, that is no oxidation at all. Therefore the effective Kerr rotation which contains the oxidation effect is just the Kerr rotation as would measure with an unoxidized sample,

$$\theta_K + i\epsilon_K = \theta_K^{tot} + i\epsilon_K^{tot}. \tag{6.23}$$

If d$\rightarrow \infty$ and $k_0 \neq 0$ then $e^{i\beta} \rightarrow 0$ and

$$\theta_K + i\epsilon_K = \frac{\tilde{r}_1\left(\theta_K^{tot} + i\epsilon_K^{tot}\right)}{0}. \tag{6.24}$$

To satisfy this condition, the complex Kerr rotation will be given as $\theta_K^{tot} + i\epsilon_K^{tot} = 0$ This means that when the thickness of oxidation is infinite and the overlying material is absorbing, then the measured Kerr rotation will be zero. We applied this model to $GdCo_2$, and the results are shown in Fig. 6.7.

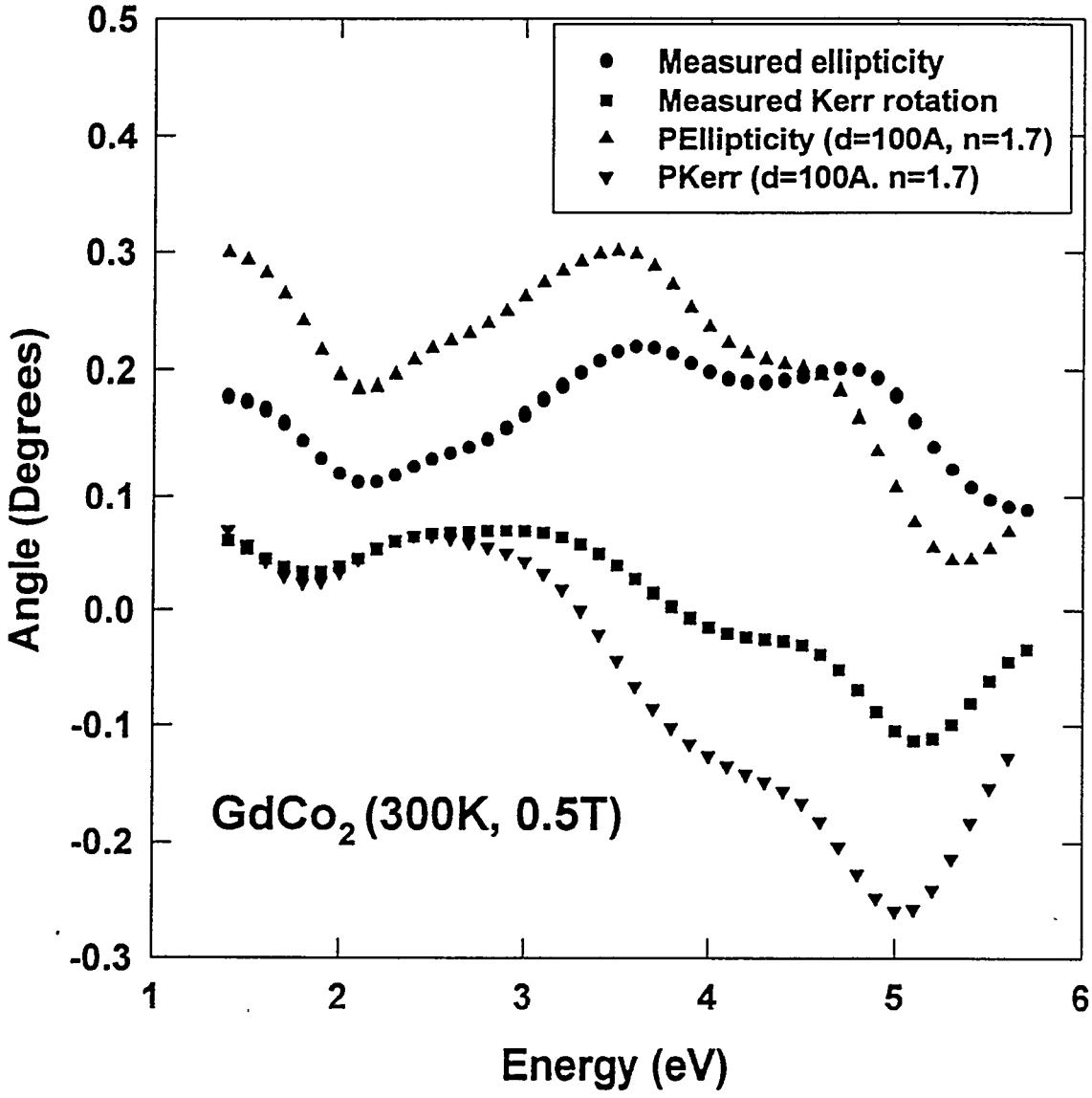

Figure 6.7 Oxidation effects on the Kerr rotation and ellipticity of crystal of $GdCo_2$. The solid circles and solid squares stand for the measured ellipticity and Kerr rotation of single crystal $GdCo_2$ at room temperature with an applied magnetic field of 0.5 T. The solid triangles up and down represent the simulated ellipticity and Kerr rotation of the clean bulk sample with an assumed 100 $\mathring{A}$ thickness and refractive index n=1.7 of the oxide layer.

7 MAGNETO-OPTICAL PROPERTIES OF $GdFe_2$

Introduction

The electronic configuration of rare-earth elements in the metallic state is $4f^{(n)}\,(5d6s)^3$ with only Eu and Yb having a $4f^{(n+1)}\,(5d6s)^2$ configuration [60]. Therefore the electronic configurations of the heavy rare earth elements differ only by the number of 4f electrons, increasing from 7(Gd) to 14(Lu), except Yb. The rare-earth-Fe_2(RFe_2) intermetallic compounds have high Curie temperatures and the cubic Laves-phase (C15) crystal structure. Due to these properties, Kerr rotation measurements at room temperature and theoretical calculations on these materials are possible. The experimental magneto-optic data are useful for checking the validity of the theoretical electronic structures of ferromagnetic intermetallic compounds. Katayama *et.al.* have measured the Kerr rotation of RFe_2(R=Gd, Er, Ho, Dy, and Tb) [92]. They measured at room temperature and 1.2T on polycrystalline samples prepared by arc melting, mechanically polished with fine γ-alumina solution. The samples were exposed to air while taking the data. A null-type automatic Kerr spectrometer was employed. This report on the Kerr rotation measurements on RFe_2 presents the only Kerr rotation data measured with the polar Kerr geometry with bulk samples that we can compare with our single-crystal data. They did not measure the ellipticity. Mukimov *et.al.* [101] measured the magneto-optical equatorial spectra of RFe_2(R=Gd, Tb, and Er) prepared by arc melting. From the the magneto-optical equatorial spectra, they derived the off-diagonal optical conductivities for $GdFe_2$, $TbFe_2$ and $ErFe_2$. The theoretical calculation of the magneto-optical prop-

erties of materials requires quite accurate self-consistent band structure calculations, otherwise the wrong interband transitions could be deduced. As already described, obtaining an accurate band structure for intermetallic compounds containing 4f electrons, such as the rare-earth transition-metal compounds, is difficult due to the strongly correlated 4f electrons. Therefore experimental magneto-optic data could be useful for developing models for the electronic structure of 4f electrons.

Experiment

Sample preparation and characterization

The single crystals of $GdFe_2$ were grown by the flux growth technique. Polycrystalline samples of $GdFe_2$ were prepared by arc melting. The surfaces of the as-grown samples were mirror like, so no more surface preparation was necessary. The surfaces of the polycrystals were polished mechanically with abrasives, the final grade being a paste of $0.05\mu m$ diameter alumina, and then cleaned with acetone and methanol. Finally, the samples were dried with dry N_2. The X-ray diffraction pattern of the single crystal of $GdFe_2$ is shown in Fig. 7.1. The crystals are well-defined single phase and the lattice constants obtained from the patterns are in accordance with published data.

Magnetic properties of rare earth-transition intermetallic compounds

The rare-earth-Fe_2(RFe_2) intermetallic compounds have many interesting magnetic properties. Understanding the magnetic behavior of RFe_2 compounds is important for permanent magnet and magneto-optical storage media applications. The Curie temperature of RFe_2 is the highest among the RT_2(T=Fe, Co, Ni) compounds. For example, the Curie temperatures of $GdFe_2$ is 790K [76]. In the case of the RCo_2 compounds, only the Curie temperature of $GdCo_2$ is above room temperature. The Curie temperatures of RNi_2 are all below 100K [102]. These different Curie temperatures among the RT_2 in-

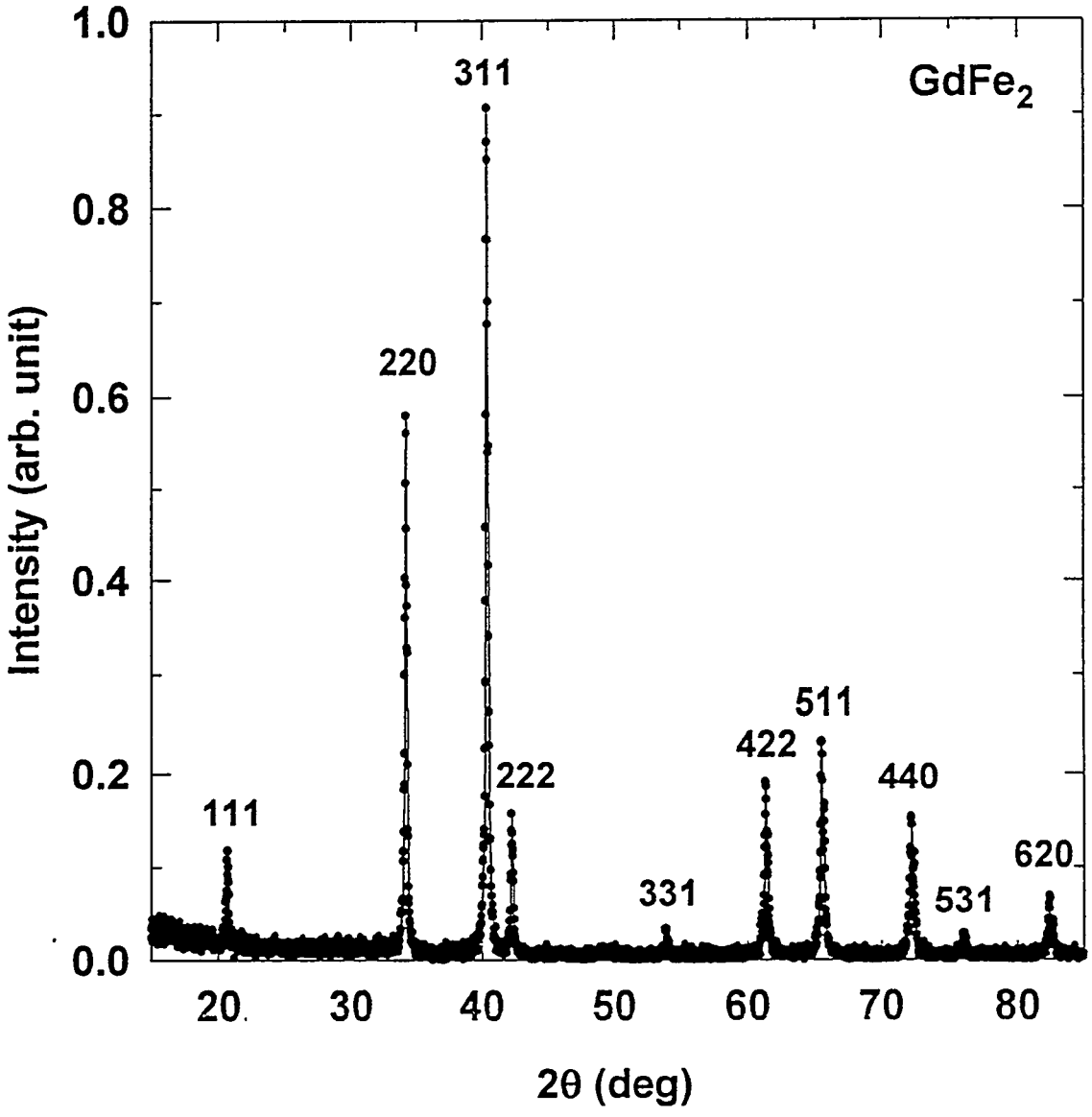

Figure 7.1 Powder X-ray diffraction pattern of crushed $GdFe_2$ single crystal. The peaks are indexed to a fcc unit cell with a lattice parameter a=7.405$\mathring{A}$.

termetallic compounds come from different interactions between the rare-earth 4f (R-4f) sublattice and the transition metal 3d (T-3d) sublattice. Among the R-R, R-T and T-T sublattice interactions, the R-4f and T-3d interactions couple the directions of the 4f and 3d spins oppositely. The mechanism for this was suggested by Campbell on the basis of experiment [103]. Brooks *et al.* [104] investigated the magnetic properties of RFe_2 with self-consistent energy-band structure calculations. From a detailed analysis of their calculation, they derived that the magnitude of the interaction depends on the R-5d spin induced by the hybridization with the M-3d bands. Their explanation for the coupling of R-4f and Fe-3d can be summarized as follows. The ferromagnetic 3d bands are split between spin-up and spin-down bands, depending on the degree of exchange splitting. The spin-up 3d bands are lowered and the spin-down 3d bands are raised, compared to the energy bands of the paramagnetic state. Due to the lowered spin-up 3d bands, the hybridization between spin-up 3d and spin-up R-5d states is reduced. Before hybridization with the 3d bands, the R-5d states were empty and located above the Fermi level. Contrary to the spin-up 3d bands, the spin-down 3d bands come close to the R-5d band as a result of 3d band splitting. Therefore the hybridization between spin-down 3d bands and R-5d bands is increased. From the increased hybridization, we can expect that the charge transfer from Fe-3d character to R-5d character between spin-down bands is greater than between the spin-up bands. Therefore the spin magnetic moment of Fe-3d and the spin magnetic moment of R-5d are aligned in opposite directions, that is ferrimagnetically. The local intra-atomic exchange interaction between R-4f and R-5d spins always couples the spins in a ferromagnetic state. The local exchange is always ferromagnetic between 5d and 4f electrons in the whole RE series. Therefore the 4f magnetic moment of rare earth atoms is always aligned opposite to that of the Fe-3d. The R-5d electrons in rare-earth atoms play a very important role in the coupling of the two sublattices. The total magnetic moment of a rare-earth atom depends on the quantum number J, given by $J=L\pm S$. For light rare earths $J=L-S$. As a result of this

relation between the orbital quantum number and spin quantum number, the magnetic moments are parallel with the magnetic moments of Fe-3d atoms. For heavy rare earth atoms, J=L+S, from Hund's rule, that is the total magnetic moment of heavy rare earth atom is always parallel to the spin magnetic moments of rare earth atom. As a result of this fact, the magnetic moments of heavy rare-earth atoms are antiparallel to the Fe-3d magnetic moments. The simple expression for the interaction between R-M can be written as the Heisenberg type,

$$E_{RM} = -J_{RT} S_R S_T, \tag{7.1}$$

where J_{RT} is the exchange coupling between the neighboring R and T spins. S_R and S_T stand for the spin moments of the rare-earth and transition metal, respectively. Liu *et al.* [105] have studied the magnetic coupling by means of the high field free-powder method (HFFP) with which one can determine the intersublattice-coupling strength. From their experimental data, the exchange coupling J_{RT} decreases in the sequence of Fe, Co, Ni. This tendency was described theoretically using the tight-binding scheme [106]. This antiparallel alignment of 3d and 4f can be confirmed by magnetization measurements. Figure 7.2 shows the magnetization measurement of single crystal of $GdFe_2$.

In Fig. 7.2, the magnetic moment of $GdFe_2$ per formula measured by a SQUID at 5K is 3.5 μ_B. This experimental value agrees reasonably well with the calculated magnetic moment if we assume the magnetic moment of Gd is 7.0 μ_B and Fe is 1.7 μ_B. This is a reasonable approximation because Gd has only spin magnetic moments and the magnetic moment of elemental Fe is 2.1 μ_B. There are two Fe atoms per formula unit, so the magnetic moment per formula unit will be $(7.0\text{-}2\cdot1.7)\mu_B$=3.6 μ_B. If the 4f and 3d electrons ordered ferromagnetically, then the experimental magnetic moment will be more than 10 μ_B. This result confirms that the 3d-4f are coupled ferrimagnetically.

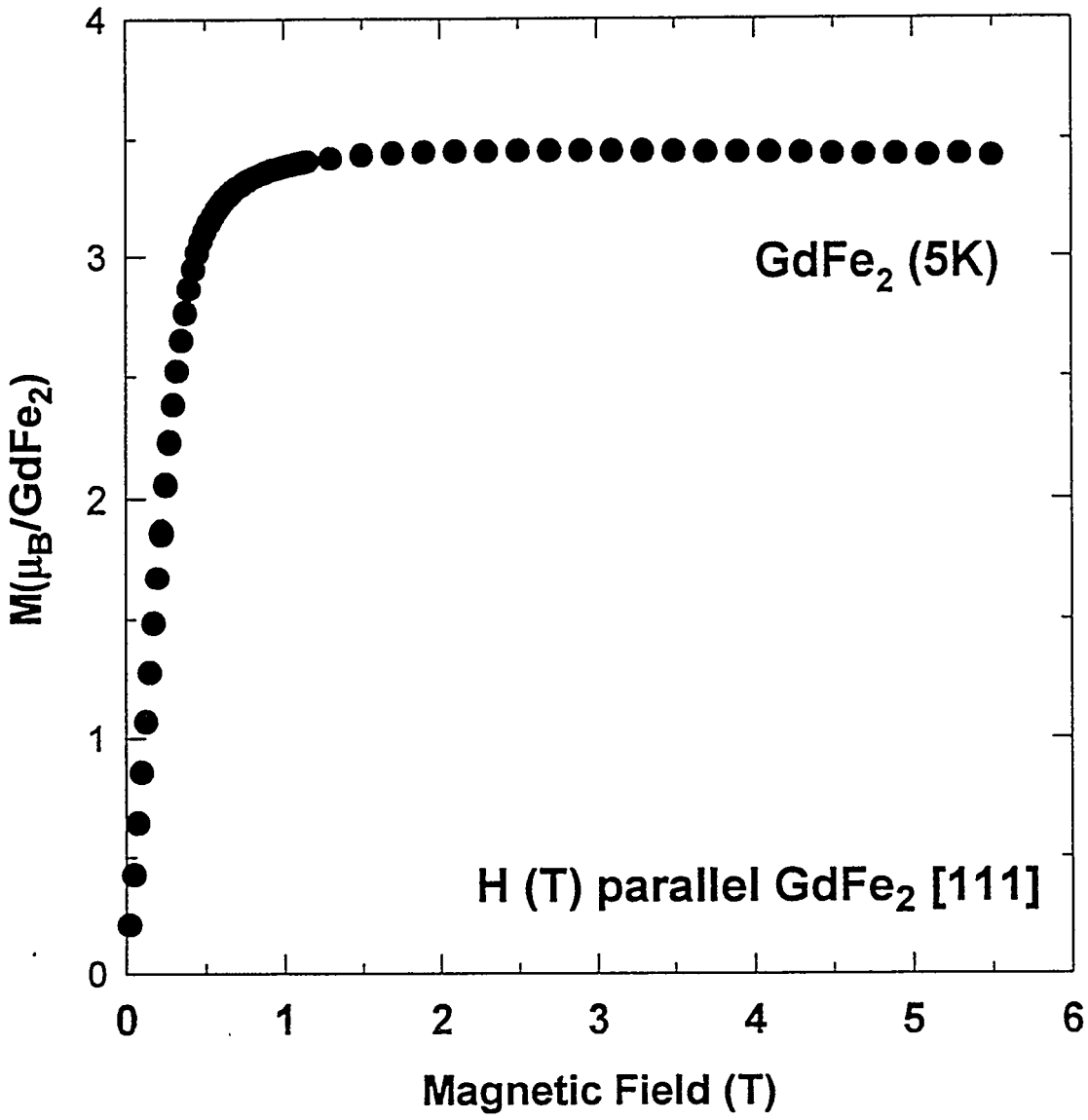

Figure 7.2 Magnetization measurements of $GdFe_2$ at 5K.

Experimental results and discussion

The real part of the diagonal optical conductivity for $GdFe_2$ was measured using a rotating analyzer ellipsometer. These optical constants were used for the off-diagonal optical conductivity with the magneto-optical Kerr rotation and ellipticity data. The measured results are shown in Fig. 7.3. A broad peak was found between 2.0-3.0 eV. The magnitude of the optical conductivity may be reduced by the oxidation of the surface of the samples. Sharipov *et al.* [107] measured the real part of the diagonal optical conductivity of polycrystalline $GdFe_2$. The measured spectra shown in Fig. 2 of [107] have a similar broad peak between 2.0 eV and 3.0 eV. The spectra of $TbFe_2$ and $HoFe_2$, which will be discussed in Chapter 9, have similar features in the real part of the diagonal optical conductivities. Heavy rare earths exhibit the same optical behavior [108, 109] in the range 1.5 to 6 eV. The metallic heavy rare earths have the same trivalent electronic configuration $5d6s^2$, except Yb which is divalent. They differ only in the number of 4f electrons. The similar optical behavior among the rare earths or RFe_2 compounds implies that the involvement of the 4f states in the diagonal optical conductivity may be ignorable. The Kerr rotations of single crystal and polycrystalline $GdFe_2$, measured at different temperatures and magnetic fields, are shown in Fig. 7.4. As shown in Fig. 7.2, the magnetic moment of single crystal $GdFe_2$ is fully saturated with an applied magnetic field of 1.4 T at 5 K. We made polycrystalline $GdFe_2$ by arc melting and polished it mechanically for the optical measurements. The measured Kerr rotation at room temperature with an applied magnetic field 0.5 T is shown in Fig. 7.4. The Kerr rotation of single crystal $GdFe_2$ measured at higher magnetic field shows clearer features and larger magnitude than that measured at lower magnetic field. When we compared the Kerr rotations between single crystal and polycrystalline $GdFe_2$ measured at the same temperature and applied magnetic field, we found there are differences in the high-energy region between the polycrystalline sample and the single crystal sample.

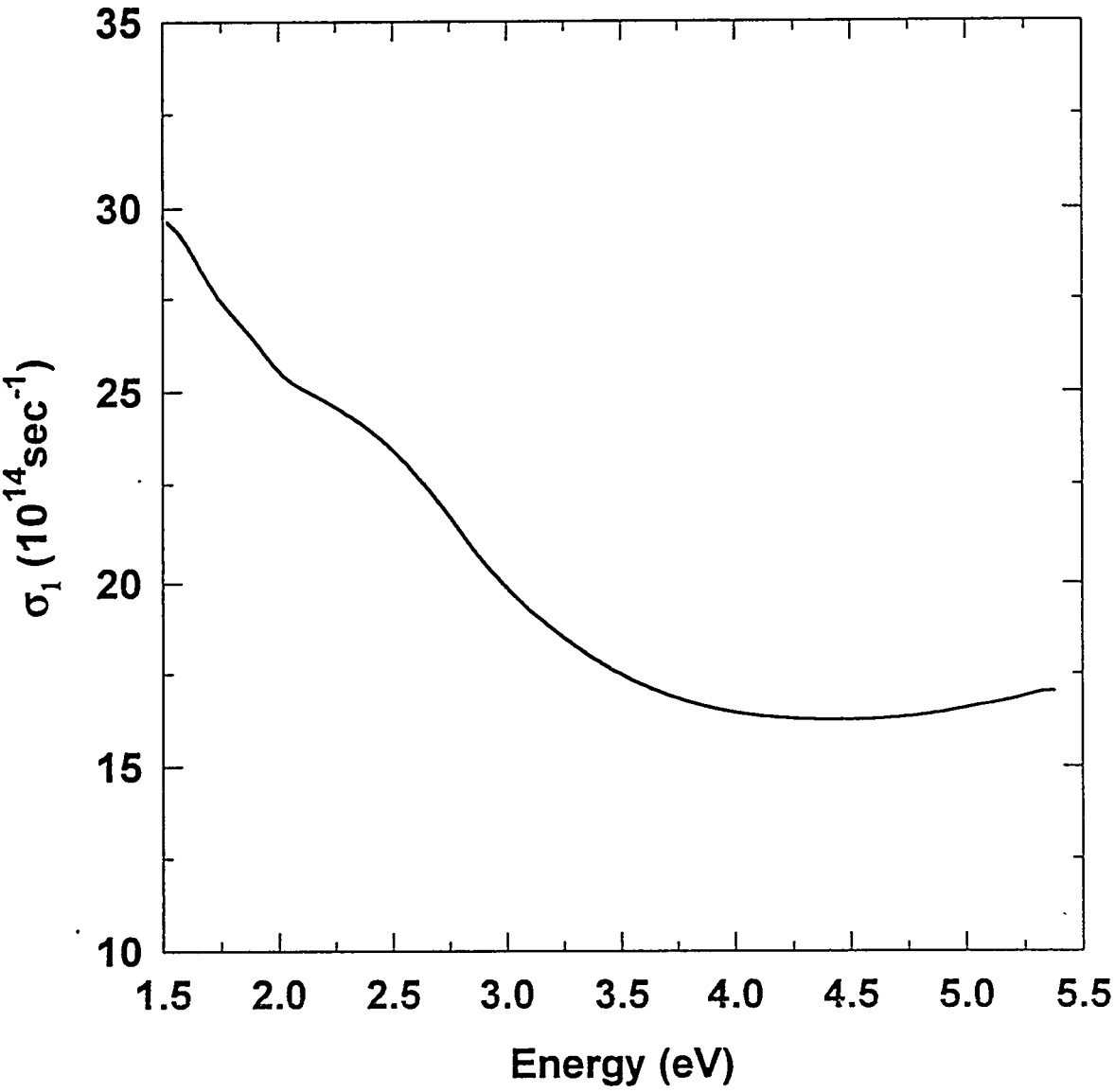

Figure 7.3 Real part of the diagonal optical conductivity for $GdFe_2$ single crystal measured at room temperature.

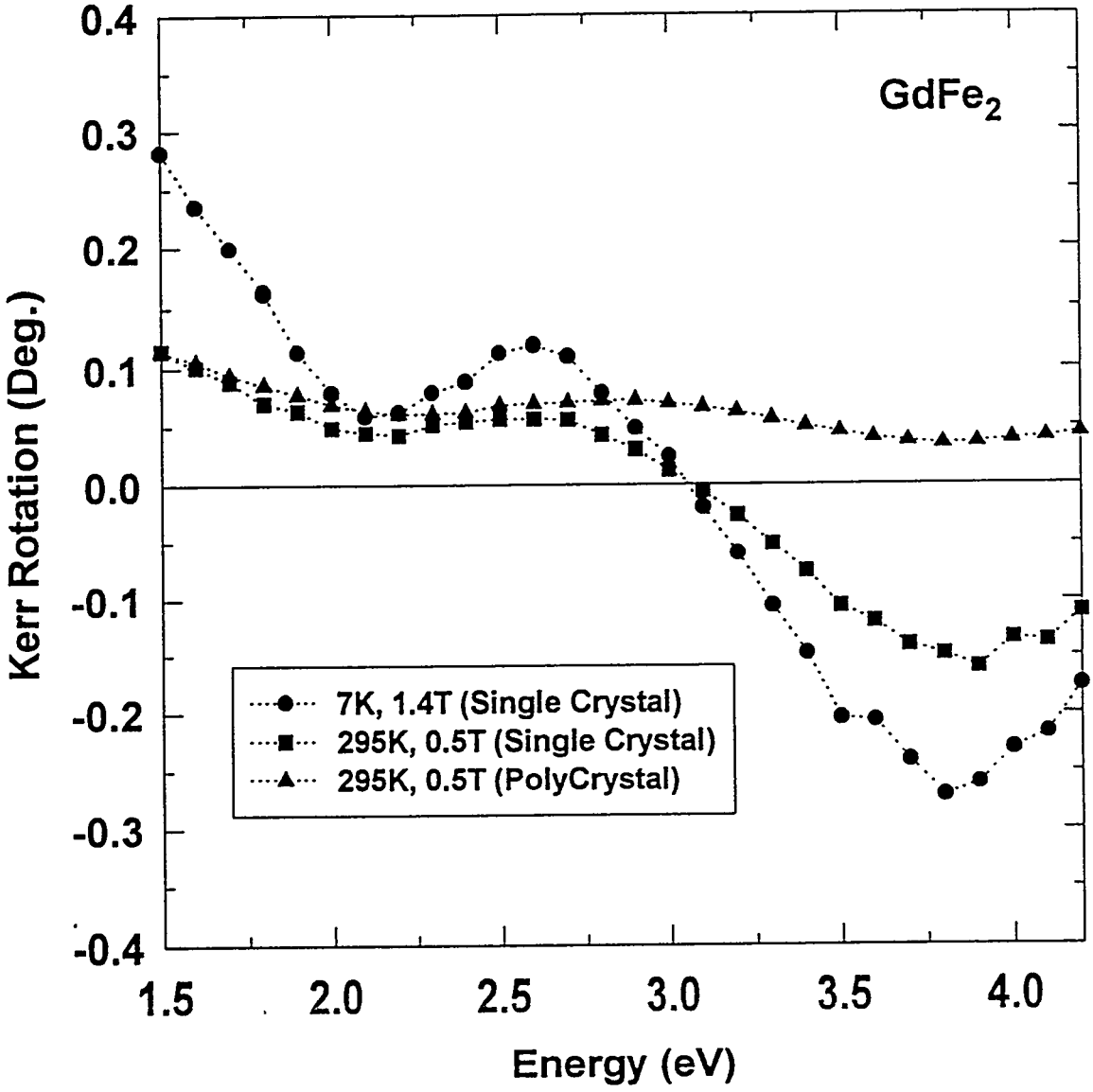

Figure 7.4 The Kerr rotations of single crystal and polycrystalline $GdFe_2$ measured at temperatures of 7K and 295K with applied magnetic fields of 1.4T and 0.5T.

The Kerr rotation of a single crystal of $GdFe_2$ is negative above 3.2 eV while that of polycrystalline $GdFe_2$ remains positive. The absolute magnitude of the Kerr rotation of single crystal $GdFe_2$ is much larger than that of polycrystalline $GdFe_2$ in the high-energy region. The Kerr rotation of polycrystalline $GdFe_2$ measured by Katayama [92] at room temperature with a magnetic field of 1.2 T stays positive with a magnitude between 0.1 and 0.2° in the range 1.65 eV - 5.0 eV. The measured Kerr rotation and ellipticity at room temperature with an applied magnetic field 0.5 T are shown in Fig. 7.5.

The solid squares represent the Kerr rotation and the solid circles stand for the ellipticity of polycrystalline $GdFe_2$. The other spectra are the Kerr rotations and ellipticities obtained using a bilayer model to consider the effect of oxidation on the MOKE. In the measured Kerr rotation with polycrystalline $GdFe_2$, there are two weak peaks at 2.7 eV and 4.6 eV. The Kerr rotation crosses zero at 5.0 eV and becomes negative above 5.0 eV. The Kerr rotation measured by Katayama [92] varies between 0.1° and 0.2°, while our Kerr rotation varies within 0° - 0.1° between 1.4 eV to 5.0 eV. Above 5.0 eV the Kerr rotation we measured becomes negative while that of Katayama stays positive at 5.0 eV. Their Kerr rotation values of $GdFe_2$ seem to be shifted up about 0.1 ° from ours in the measured spectral range. It is well known that shorter-wavelength light is more sensitive to the surface state than longer-wavelength light because the penetration depth of shorter-wavelength light is much smaller than that of longer-wavelength light [98]. Therefore this oxidation effect on the MOKE may cause the discrepancy in the Kerr rotation in the higher energy region between the polycrystalline and single crystal samples. To test the effects of oxidation on the MOKE, we applied the bilayer model employed in Chapter 6. We obtained the Kerr rotation and ellipticity of the clean surface of the sample using the bilayer model. The triangles pointing up and down stand for the ellipticity and Kerr rotation obtained using the bilayer model with the assumption that the thickness of the oxide layer is 100 $\mathring{A}$ and the effective refractive index n=1.5. The open circles and the open squares stand for the ellipticity and Kerr

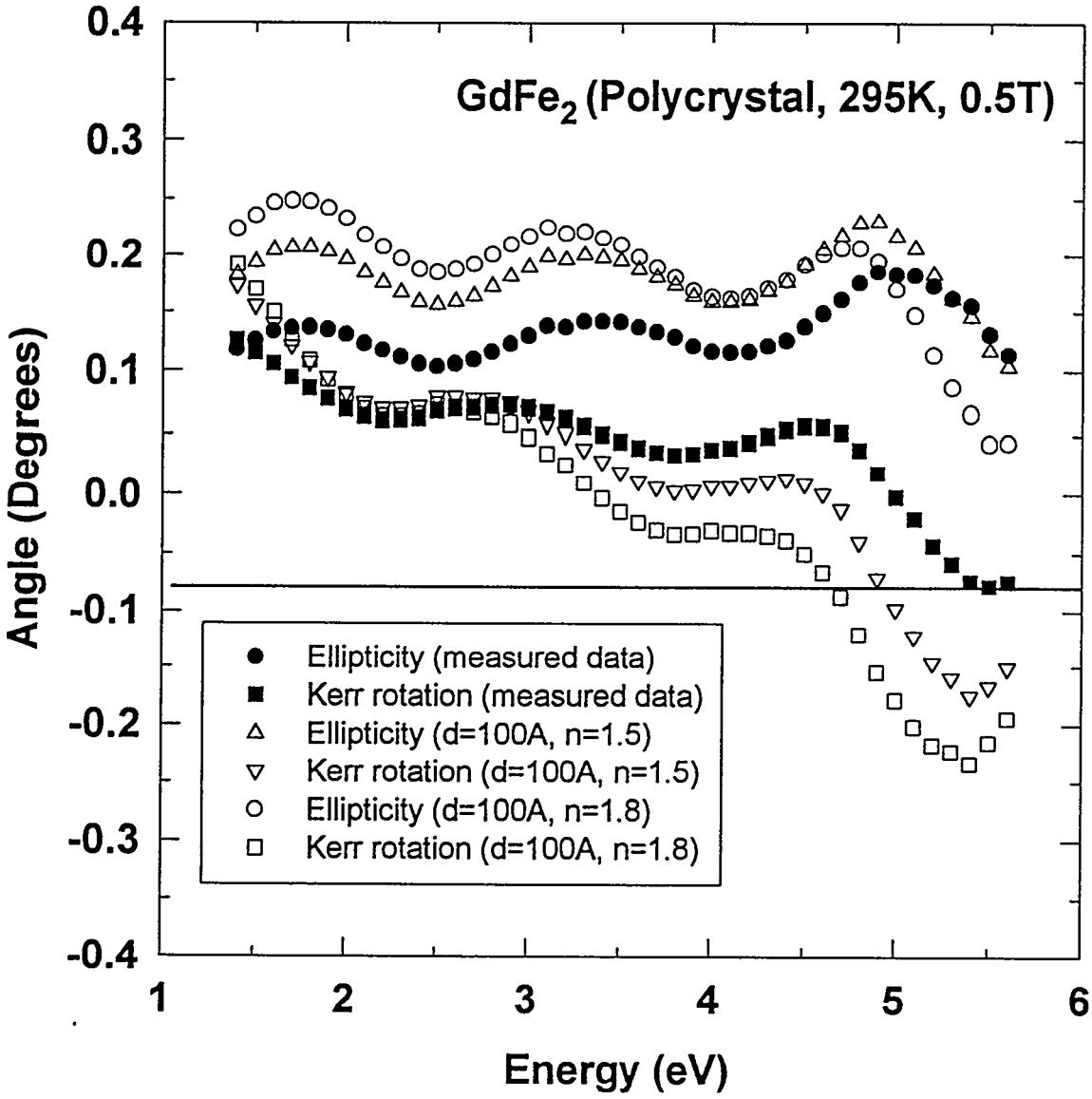

Figure 7.5 The Kerr rotation and ellipticity of polycrystalline $GdFe_2$ measured at room temperature with an applied magnetic field of 0.5 T. The triangles pointing up and down stand for the ellipticity and Kerr rotation obtained using the bilayer model with the assumption that the thickness of the oxide layer is 100 $\mathring{A}$ and the effective refractive index n=1.5. The open circles and the open squares stand for the ellipticity and Kerr rotation obtained using the bilayer model with the assumption that the thickness of the oxide layer is 100 $\mathring{A}$ and the effective refractive index n=1.8.

rotation obtained using the bilayer model with the assumption that the thickness of the oxide layer is 100 $\mathring{A}$ and the effective refractive index n=1.8. As shown in Fig. 7.5, the sign of the Kerr rotation of an oxide-free sample becomes negative in the higher energy region, which agrees with the Kerr rotation of the single crystal. The advantage of using single crystals over the polycrystals in MOKE measurements will be discussed in detail in Chapter 9. Buschow *et al.* [98] observed that oxidation changes the Kerr rotation of $Gd_{1-x}Co_x$ (x=0.62) amorphous alloys in the UV region. To compare the MOKE in more detail between single crystals and polycrystals, we plotted in Figs. 7.6 and 7.7 the experimental values of σ_{1xy}, σ_{2xy}, and $\omega\sigma_{2xy}$ of single-crystal $GdFe_2$ and polycrystalline $GdFe_2$ measured at the same temperature and applied magnetic field.

The weak broad peaks are marked by arrows in both samples. The signs of σ_{2xy} and $\omega\sigma_{2xy}$ of polycrystalline $GdFe_2$ are negative in the measured spectral range, while those of single crystal $GdFe_2$ become positive above 3.2 eV. The σ_{2xy} and $\omega\sigma_{2xy}$ spectra of the single crystal have more clear features that those of the polycrystal. The off-diagonal optical conductivity is important because it is related directly to the magneto-optical Kerr effect. The joint density of states function $J_{\alpha\beta}(\omega)$ is related to $\omega\sigma_{2xy}$ by [29]

$$\omega\sigma_{2xy} = \frac{\pi e^2}{4m^2\hbar}\,\bar{F}_{\alpha\beta}\cdot J_{\alpha\beta}(\omega) \tag{7.2}$$

where $\bar{F}_{\alpha\beta}$ is an average matrix element defined by Eq. (5) of [29]. If $\bar{F}_{\alpha\beta}$ is a constant, independent of ω, then $\omega\sigma_{2xy}$ is directly proportional to the joint density of states. From a model calculation on Gd, Eskine *et al.* [29] found that below 4.5 eV, where p-to-d transitions are dominant, $\bar{F}_{\alpha\beta}$ is approximately constant, but above 4.5 eV, where d-to-f transitions start contributing, $\bar{F}_{\alpha\beta}$ does change [29]. Therefore the direct proportionality between $\bar{F}_{\alpha\beta}$ and $\omega\sigma_{2xy}$ does not hold if the f states are involved in the off-diagonal optical transitions for Gd. The joint density of states is high if the unoccupied energy band and the occupied band are separated by a nearly constant energy. At these k points, interband transitions are strong. For the analysis of these experimental data, we need

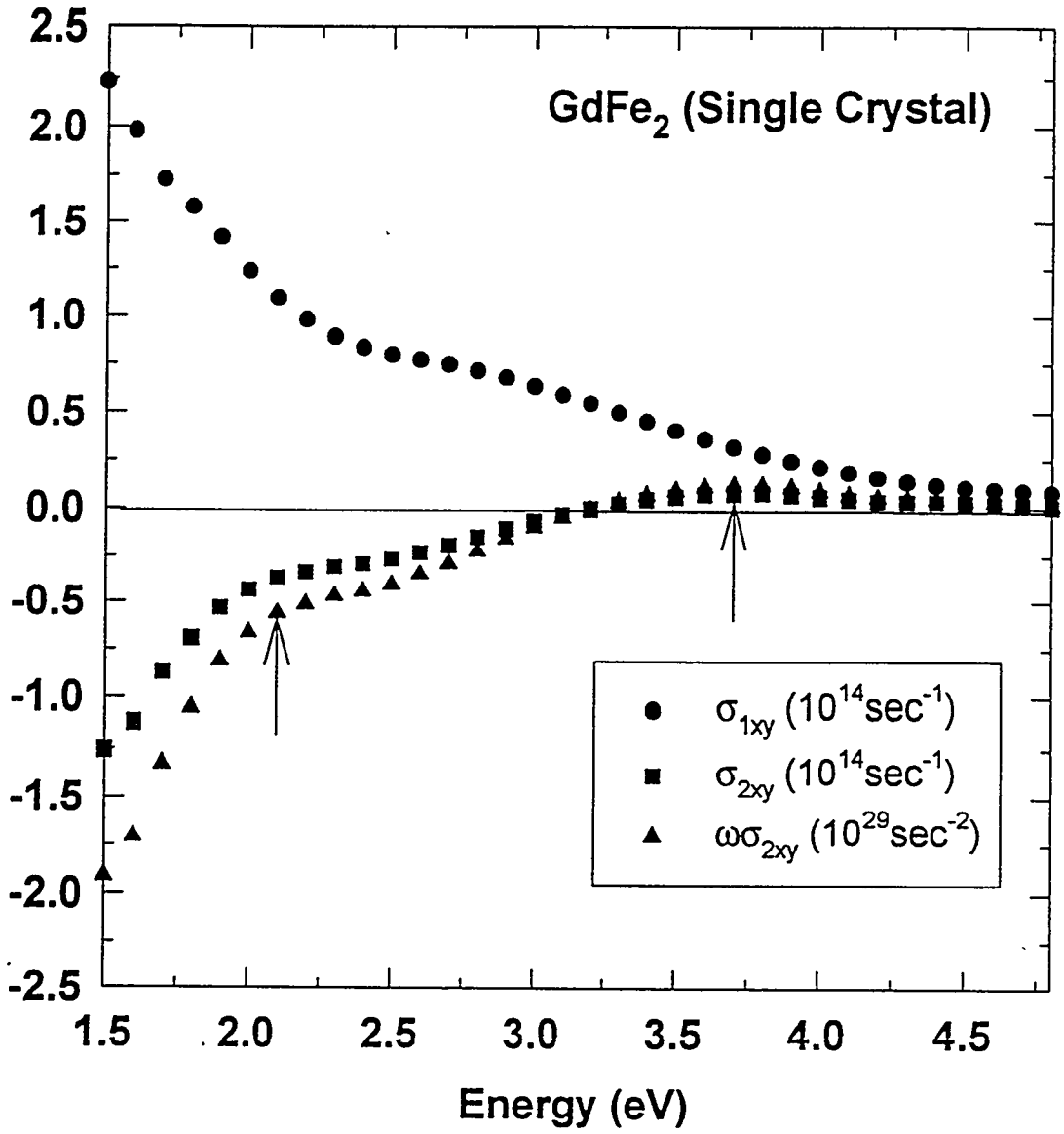

Figure 7.6 The experimental σ_{1xy}, σ_{2xy}, and $\omega\sigma_{2xy}$ values of single crystal of $GdFe_2$ from experimental Kerr rotation, ellipticity measured at room temperature with an applied magnetic field of 0.5 T and optical constants measured at room temperature with no magnetic field applied. The arrows stand for the peak positions in the experimental $\omega\sigma_{2xy}$.

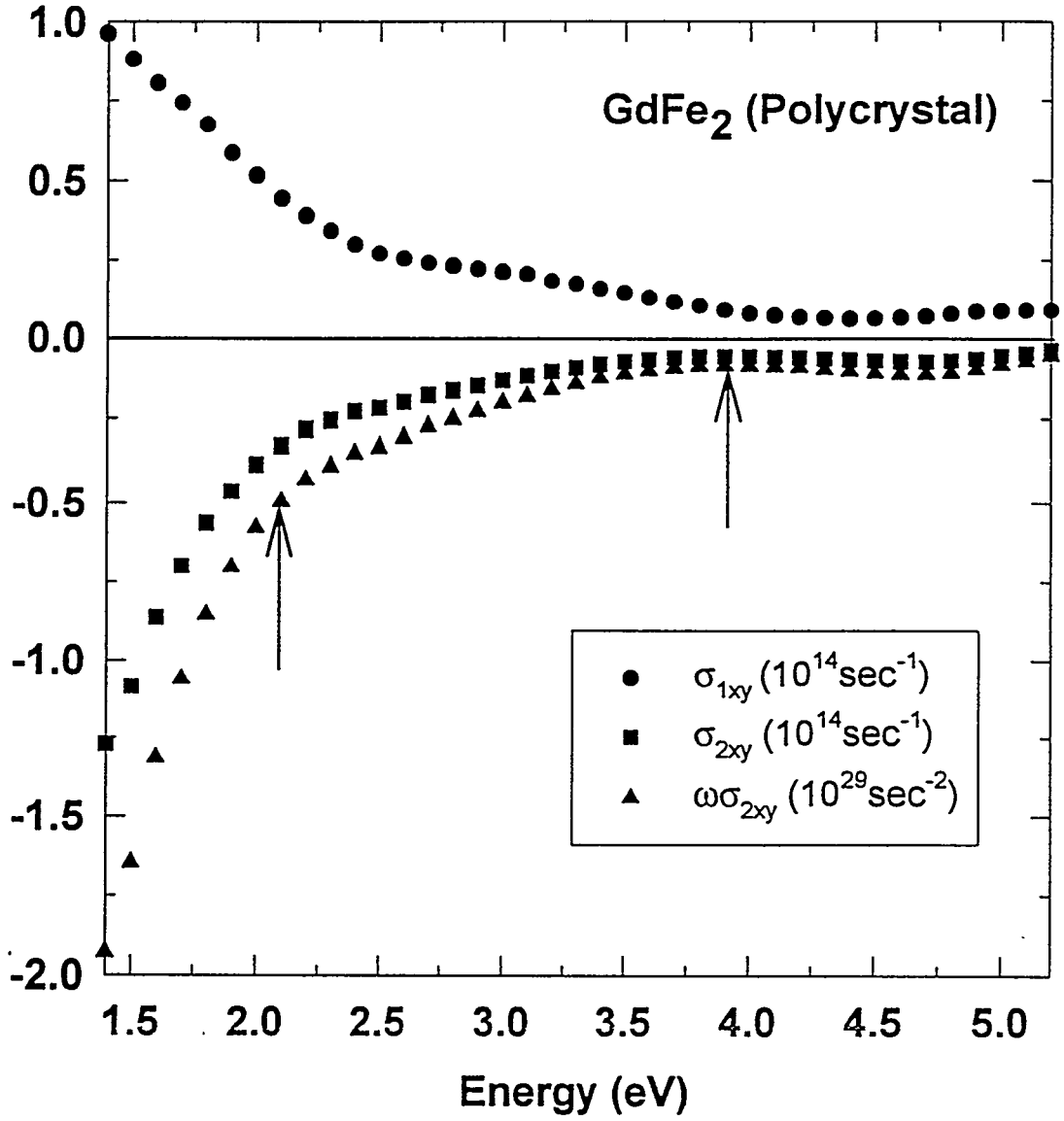

Figure 7.7 The experimental σ_{1xy}, σ_{2xy} and $\omega\sigma_{2xy}$ values of polycrystal of $GdFe_2$ from experimental Kerr rotation, ellipticity measured at room temperature with an applied magnetic field of 0.5 T and optical constants measured at room temperature with no magnetic field applied.

an accurate electronic structure and density of states of $GdFe_2$. The DOS calculated using the TB-LMTO with LSDA are plotted in Chapter 8 compared with that of $GdCo_2$. Antropov *et al.* [83] calculated the off-diagonal part of the optical conductivity for Gd with the LSDA+U. They obtained good agreement with experimental data, while their results with the standard LSDA completely disagree with the experimental data. The LDA+U removes the 4f unoccupied states from the vicinity of the Fermi energy and this greatly improves the off-diagonal optical conductivity. It is difficult to analyze the experimental data with the theoretical DOS obtained with the LSDA due to the incorrect positions of the 4f states in the electronic structure and the hybridization of these incorrect 4f states with the conduction electrons, which could cause incorrect interband optical transitions. To compare the theoretical off-diagonal optical conductivity with the experimental data of $GdFe_2$, we used the TB-LMTO method based on the LSDA. Figure 7.8 shows the theoretical results for the absorptive part of the off-diagonal optical conductivity obtained from the electronic structure of $GdFe_2$.

To test the involvement of the 4f states in σ_{2xy}, we calculated σ_{2xy} with the f-to-d and d-to-f interband transitions turned on and off. The solid line represents σ_{2xy} with the f-to-d and d-to-f transitions included, and the dotted line stands for the σ_{2xy} with the f-to-d and d-to-f transitions excluded. The dash-dot line represents σ_{2xy} with the inclusion of a self-energy correction of -0.2. This value produces a theoretical diagonal optical conductivity which agrees with the experimental diagonal optical conductivity. As shown in Fig. 7.8, there are no big differences among them. In the case of $TbFe_2$ and $HoFe_2$, which will be discussed in Chapter 9, we have found big differences between inclusion and exclusion of the 4f states in σ_{2xy}. The differences between $GdFe_2$ and $HoFe_2$, $TbFe_2$ are caused by the different position of the unoccupied 4f states of the rare earths relative to the Fermi energy. The exchange-correlation energy splitting Δ_{ex} is largest for Gd and decreases as the number of 4f electrons increases [110]. On the contrary, the spin-orbit energy splitting Δ_{so} increases as the number of 4f electrons

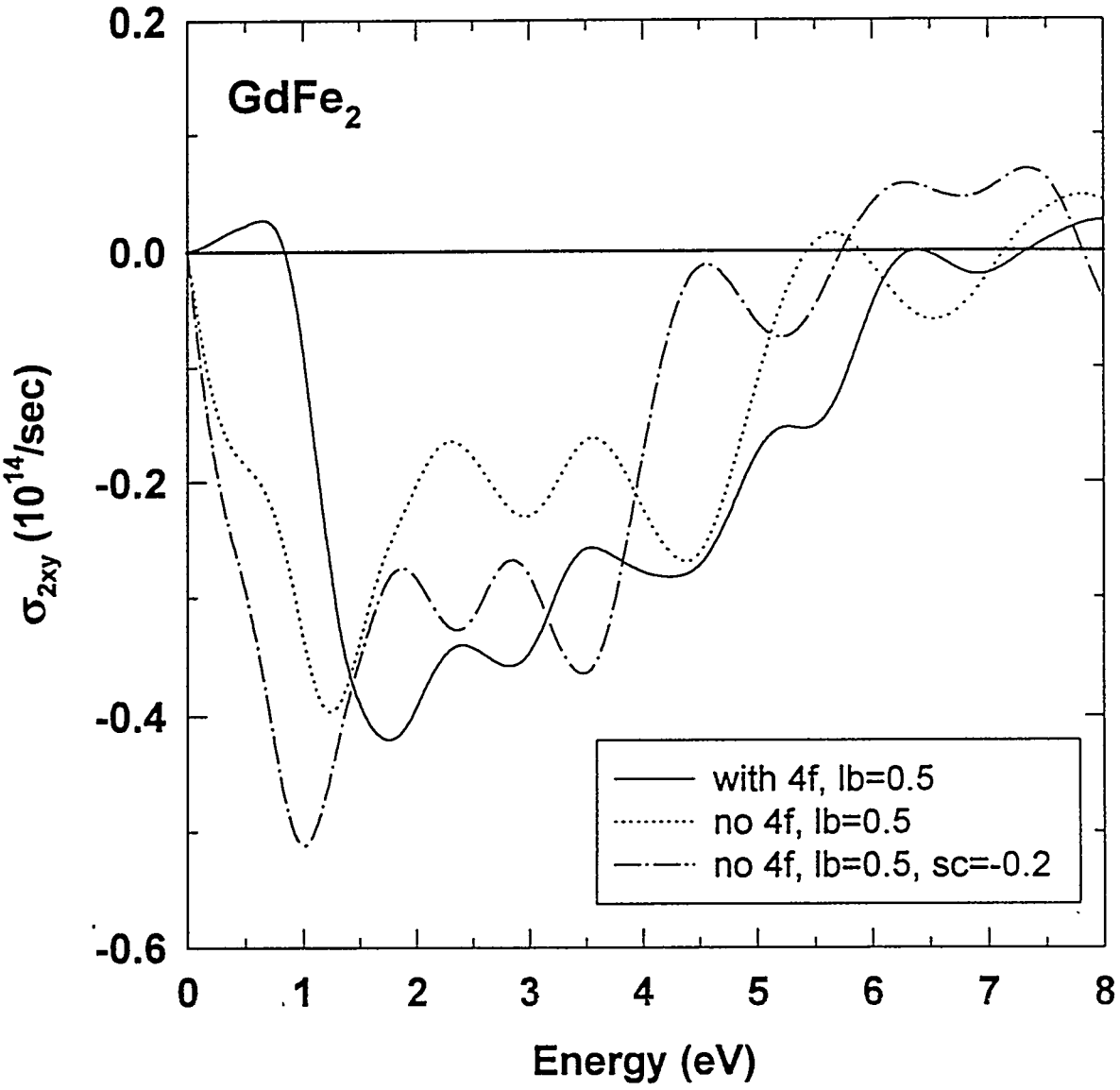

Figure 7.8 The theoretical σ_{2xy} calculated using TB-LMTO based on LSDA. The solid line represents the σ_{2xy} with d-to-f and f-to-d interband transitions included. The dotted line represents the σ_{2xy} with d-to-f and f-to-d interband transitions not included. The dash-dot line represents the σ_{2xy} with the inclusion of a self-energy correction of -0.2 with d-to-f and f-to-d interband transitions not included. For all calculations, a constant lifetime broadening parameter of 0.5 eV is used.

increases [110]. Due to the large exchange-correlation energy splitting, the occupied 4f states below the Fermi energy and the unoccupied 4f states above the Fermi energy are separated the most among the heavy rare earth compounds. In theoretical calculations, the unoccupied 4f states of $GdFe_2$ are located above 1.3 eV relative to the Fermi energy while those of $HoFe_2$ and $TbFe_2$ are located at the Fermi energy. But these 4f positions relative to the Fermi energy obtained by LSDA theory are always smaller than the experimental values because the large Coulomb correlation interaction, U, of 4f electrons in rare earths is not considered in LSDA. To remedy this problem, the LDA+U method has been introduced [83]. Herbst *et al.* [111] have calculated the position of the excited 4f level above the Fermi energy. They estimate the unoccupied 4f states are located 3.6 eV above the Fermi energy in Gd. The unoccupied 4f states of $GdFe_2$ should not be different from those of Gd. Therefore the theoretical value of 1.3 eV above the Fermi energy is smaller than the expected experimental value due to the omission of U in the LSDA. Therefore σ_{2xy} in Fig. 7.7 is affected by the 4f states located close to the Fermi level which should be far away from the Fermi energy. Therefore we turned off the f-to-d and d-to-f transitions in σ_{2xy}, plotted as a dotted line in Fig. 7.8. With the f turned off, σ_{2xy} above 1 eV is shifted up, while below 1 eV, σ_{2xy} is shifted down slightly. When the self-energy correction term is included, σ_{2xy} is shifted toward the lower-energy region. The σ_{2xy} with self-energy correction term becomes positive between 5.5 eV to 7.8 eV. If we use a larger negative self-energy correction, we could reproduce the positive σ_{2xy} around 4.0 eV, but in that case the theoretical diagonal optical conductivity with that correction parameter is quite different from the experimental σ_{1xx}. Therefore we used the same self-energy correction term in both σ_{1xx} and σ_{2xy}. The σ_{2xy} with no f-to-d and d-to-f transitions seems to agree with experimental data better than the σ_{2xy} with f-to-d and d-to-f transitions. But the three cases plotted in Fig. 7.8 do not agree with the σ_{2xy} experimental data for the single crystal, which is positive above 3.2 eV. We need a more accurate method to calculate the electronic

structure of a system which has localized 4f electrons to explain the MOKE effects of the rare earth transition intermetallic compounds. Misemer [33] derived that the magneto-optical behavior has a linear dependence on the strength of the spin-orbit interaction parameter, but has no simple scaling relationship with magnetization. The smallest value of the spin-orbit energy splitting Δ_{so} of Gd among the heavy rare earths causes the smallest Kerr rotation and ellipticity of $GdFe_2$ among RFe_2 (R=heavy rare earths) compounds which is consistent with the Misemer's conclusion. If the phenomenological lifetime parameter $\epsilon = 0$, then the absorptive part of the off-diagonal optical conductivity takes the following form.

$$\sigma_{2xy}(\omega) = \frac{\pi e^2}{\hbar \omega m^2 \Omega} \sum_{n,l} f(\omega_l)(1 - f(\omega_n)) \frac{\left|\pi_{nl}^{+}\right|^2 - \left|\pi_{nl}^{-}\right|^2}{2} \delta(\omega - \omega_{nl}), \tag{7.3}$$

where $\pi_{nl}^{\pm}$ are the matrix elements of the circularly polarized components of the kinetic momentum operator and n, l stand for the occupied and unoccupied energy band states at wave vector k. The kinetic momentum operator given by Eq. 3.61 consists of two terms. The first term is the conjugate momentum, given by

$$p = \frac{m}{\hbar} \frac{\partial H}{\partial k}, \tag{7.4}$$

and the second term,

$$\frac{\hbar}{4mc^2} \sigma \times \nabla V, \tag{7.5}$$

comes from the spin-orbit contribution. It can cause "spin-flip" transitions. When $\sigma \times \nabla V$ in Eq. 7.5 is expanded, the terms containing σ_x and σ_y cause the spin-flips. Misemer [33] showed that the second term contributed by spin-orbit interaction is negligible by the following arguments. The matrix element of the operator p_{nl} between n and l and the matrix elements $(\nabla V)_{nl}$ are related by the following equation,

$$(E_n - E_l)\, p_{nl} = -i\hbar\, (\nabla V)_{nl}\,. \tag{7.6}$$

Substituting p_{nl} in the above equation into Eq. 3.61, then the matrix elements π_{nl} can be written as

$$\pi_{nl} = \left[\frac{-i\hbar}{E_{nl}}\hat{r}_{nl} + \frac{\hbar}{4mc^2}(\sigma \times \hat{r})_{nl}\right]\left(\frac{\partial V}{\partial r}\right)_{nl}, \tag{7.7}$$

where m is the mass of electron and $E_{nl} = (E_n - E_l)$. $(\sigma \times \hat{r})_{nl}$ in the second term is order of 1 and the order of E_{nl} is a few eV in the measured spectral range while that of $4mc^2$ is MeV. Therefore the second term is negligible compared to the first term. Wang *et al.* [112] included the spin-flip term of π in their matrix element calculation and found its contribution in all cases to be negligible in the half-metallic Heusler alloys. Therefore we can generally ignore the second term and replace π with p. Even though the direct spin-flip transitions caused by the spin-orbit term in the interaction Hamiltonian are negligible, the spin-mixing in the eigenstates of the Hamiltonian can cause transitions from one spin state to the other spin state. To test the spin-mixing contributions to the off-diagonal optical conductivity, Misemer [33] decomposed the off-diagonal optical conductivity into 4 terms using the property that the dipole operator p is diagonal in spin as

$$\sigma_{xy} = \sigma_{xy}(\uparrow\uparrow) + \sigma_{xy}(\downarrow\downarrow) + \sigma_{xy}(\uparrow\downarrow) + \sigma_{xy}(\downarrow\uparrow). \tag{7.8}$$

The parallel spin up term $\sigma_{xy}(\uparrow\uparrow)$ involves contributions from majority spin and and the parallel spin down term $\sigma_{xy}(\downarrow\downarrow)$ involves contributions from minority spin electrons, respectively. By a numerical test, they found the mixed terms $\sigma_{xy}(\uparrow\downarrow)$, $\sigma_{xy}(\downarrow\uparrow)$ are negligible. Therefore we can separate the absorption part of the off-diagonal optical conductivity as spin-up and spin-down contributions, that is,

$$\sigma_{2xy} = \sigma_{2xy}(\uparrow\uparrow) + \sigma_{2xy}(\downarrow\downarrow) \tag{7.9}$$

where $\sigma_{2xy}(\uparrow\uparrow)$ involves contributions from the majority spin and $\sigma_{2xy}(\downarrow\downarrow)$ involves contributions from the minority spin electrons only. From Eq. 7.3, one can see that the absorptive part of the off-diagonal optical conductivity is caused by the difference

in absorption for left- and right-circularly polarized light, that is,

$$\sigma_{2xy} \propto \left(\left| p_{nl}^{+} \right|^2 - \left| p_{nl}^{-} \right|^2 \right), \tag{7.10}$$

where $p^{\pm} = p_x \pm i p_y$ are the dipole matrix elements for left- and right-circularly polarized light respectively. When we consider the spin up and spin down contributions to σ_{2xy}, Eq. 7.10 can be decomposed as

$$\sigma_{2xy} \propto |\langle n\uparrow |p_+| l\uparrow\rangle|^2 - |\langle n\uparrow |p_-| l\uparrow\rangle|^2 + |\langle n\downarrow |p_+| l\downarrow\rangle|^2 - |\langle n\downarrow |p-| l\downarrow\rangle|^2 . \tag{7.11}$$

For simplicity, put

$$\begin{aligned} |\langle n\uparrow |p_+| l\uparrow\rangle| &= \left| p_{\uparrow}^{+} \right| \\ |\langle n\uparrow |p_-| l\uparrow\rangle| &= \left| p_{\uparrow}^{-} \right| \\ |\langle n\downarrow |p_+| l\downarrow\rangle| &= \left| p_{\downarrow}^{+} \right| \\ |\langle n\downarrow |p_-| l\downarrow\rangle| &= \left| p_{\downarrow}^{-} \right| . \end{aligned} \tag{7.12}$$

then we can rewrite Eq. 7.11, as

$$\sigma_{2xy} \propto \left| p_{\uparrow}^{+} \right|^2 - \left| p_{\uparrow}^{-} \right|^2 + \left| p_{\downarrow}^{+} \right|^2 - \left| p_{\downarrow}^{-} \right|^2 = \left(\left| p_{\uparrow}^{+} \right|^2 + \left| p_{\downarrow}^{+} \right|^2 \right) - \left(\left| p_{\uparrow}^{-} \right|^2 + \left| p_{\downarrow}^{-} \right|^2 \right). \tag{7.13}$$

That is, if the sign of σ_{2xy} is positive, that means the absorption of the majority and/or minority spin transitions relating to left circularly polarized (LCP) light is larger than that of right-circularly polarized light (RCP). On the contrary, if the sign of σ_{2xy} is negative, this implies that the transitions with majority- and/or minority spin electrons relating to RCP are greater than those for LCP.

For paramagnetic materials, there is no MOKE, therefore $\sigma_{2xy} = 0$ throughout the whole energy spectrum. To meet this condition, we find the following condition from Eq. 7.9,

$$\sigma_{2xy}(\uparrow\uparrow) = -\sigma_{2xy}(\downarrow\downarrow), \tag{7.14}$$

that is the majority contributions are cancelled out by the minority spin contributions. In a more detailed expression, we can write this condition from Eq 7.11 as

$$\begin{aligned} \left|p_{\uparrow}^{+}\right|^2 &= \left|p_{\downarrow}^{-}\right|^2 \\ \left|p_{\uparrow}^{-}\right|^2 &= \left|p_{\downarrow}^{+}\right|^2, \end{aligned} \tag{7.15}$$

For the paramagnetic state, even though the absorption rate is different between the LCP and RCP light in the same spin-majority or -minority state due to spin-orbit coupling, no MOKE arises because there is no exchange splitting which separates the majority and minority spin states. The spin-orbit coupling splits the degenerate states and the split states have different absorption rates according to the following selection rule

$$\Delta m_l = \pm 1. \tag{7.16}$$

The transitions with $\Delta m_l = +1$ correspond to LCP light and $\Delta m_l = -1$ correspond to RCP light respectively. Figure 7.4 shows the Kerr rotations of single crystal $GdFe_2$ and polycrystalline $GdFe_2$ measured at different temperatures and magnetic fields. The solid squares and the solid circles represent the Kerr rotations of single crystal $GdFe_2$ measured at room temperature with an applied magnetic field of about 0.5 T and measured at 7 K with an applied magnetic field of 1.4 T. The Kerr rotation measured out of the cryostat at room temperature with an applied magnetic field of 0.5 T has no Faraday rotation due to the windows and no strain-induced birefringence due to the thermal change or pressure change on the windows. Kerr rotations measured inside the cryostat and outside of the cryostat cross zero at the same energy, 3.1 eV. This means that the shift of the Kerr rotation due to strain or Faraday rotation measured inside the cryostat is negligible. The Kerr rotation measured inside the cryostat has a maximum value of about 0.3° at 1.5 eV and a minimum value of about -0.3° at 3.8 eV, crossing zero at 3.1 eV, while the Kerr rotation measured out of the cryostat has a maximum value of

about 0.12° at 1.5 eV and a minimum value of about -0.15° at 3.9 eV, crossing zero at 3.1 eV. From these comparisons between measurements at inside and outside the cryostat, one can see very similar features, except the magnitudes of Kerr rotation due to different magnitudes of magnetic fields. The measurement out of the cryostat has no strain and Faraday effects, therefore the similar features imply that the Kerr rotation measured inside of the cryostat and obtained through Eq. (2.1) after four measurements reasonably cancelled the Faraday rotation and strain effects. The Faraday rotation is cancelled using an Al mirror and the strain effects of nonmagnetic origin are removed by subtracting the positive and negative magnetic field measurements. σ_{2xy} of single crystal and polycrystalline $GdFe_2$ are shown in Figs. 7.6 and 7.7. The signs of σ_{2xy} for polycrystal of $GdFe_2$ and the single crystal of $GdFe_2$ are opposite above 3.2 eV until 4.7 eV which is the highest energy of the single crystal spectrum. The sign of σ_{2xy} of the single crystal is positive between 3.2 eV and 4.7 eV. According to Eq. 7.10, majority and/or minority spin transitions related to LCP light may be stronger than RCP light in this energy spectrum while for the polycrystal, the sign of σ_{2xy} is negative in this energy spectrum, leading to opposite conclusions. If σ_{2xy} is positive, then according to Eq. 7.10, LCP absorption is dominant and from the selection rule Eq. 7.16, the transitions which satisfy $\Delta m_l = +1$ will be dominant. If σ_{2xy} is positive, the opposite case occurs. The different signs in σ_{2xy} imply transitions originating from different orbital characters in the electronic structure of ferromagnetic materials. single crystal data are believed to manifest intrisic properties of MOKE due to several reasons which will be discussed in Chapter 9. But this discrepancy in sign of σ_{2xy} between single crystal and polycrystal of $GdFe_2$ should be analyzed more carefully.

Conclusions

It has been shown in this chapter that magneto-optical data combined with ellisometry data can be used for checking the validity of the electronic structure of the ferromagnetic material which have 4f electrons. The single crystal of $GdFe_2$ grown by the flux method produces positive σ_{2xy} above 3.2 eV while that of polycrystalline $GdFe_2$ gives negative σ_{2xy} above 3.2 eV. We used a bilayer model to check the effects of oxidation on MOKE. We found that by removing the oxide layer analytically, the Kerr rotation becomes negative which is agrees with the single crystal data. This negative Kerr rotation makes σ_{2xy} positive. The theoretical σ_{2xy} with LSDA can not estimate well the experimental data of σ_{2xy}. We need a more accurate method beyond LSDA to calculate the electronic structure of strongly correlated systems to explain the MOKE effects in the rare earth transition intermetallic compounds.

8 COMPARISON OF $GdFe_2$ AND $GdCo_2$

The crystal structures of $GdFe_2$ and $GdCo_2$ are cubic Laves-phase structures. The lattice constant of $GdFe_2$ is $7.405\mathring{A}$ while that of $GdCo_2$ is $7.272\mathring{A}$. $GdFe_2$ and $GdCo_2$ are ferrimagnetic, that is, the magnetic moments of Fe or Co align antiparallel to those of Gd atoms. But their Curie temperatures are different, 790K for $GdFe_2$ [76] and 404K for $GdCo_2$ [113]. This indicates that the exchange interaction between the Co moments is smaller than that for the Fe moments. Cannon *et al.* [114] found that the Co-Gd coupling in $GdCo_2$ is significantly stronger than the Fe-Gd coupling in $GdFe_2$. They diluted the Gd sublattice of $GdFe_2$ and $GdCo_2$ with yttrium to see the effect of the Gd moments on the Fe or Co moments. They found the Co sublattice magnetization depends on the population of the Gd sublattice, which indicates that the Gd-Co interaction is not negligible compared to the Co-Co interaction. But the magnetic moment of Fe is not strongly affected by the magnetic moment of Gd. The experimental magnetic moment of Fe in $GdFe_2$ is $2.1\mu_B$ [115] and the magnetic moment of Co is $1.05\mu_B$ [116]. From Fig. 6.1, the magnetic moment of $GdCo_2$ per formula unit is $5.5\mu_B$. From this value, we can derive the magnetic moment of Co with the assumption that the magnetic moment of Gd is $7.5\mu_B$. The reason for assuming a Gd magnetic moment of $7.5\mu_B$ is due to the polarization of the Gd-d states which is approximately $0.5\mu_B$. This assumed value for the Gd-5d moment agrees with the theoretical result from the TB-LMTO method. Then the magnetic moment of Co will be $1.0\mu_B$ by the following calculation. $M_{Co} = (M_{Gd} - M_{GdCo_2})/2$ where $M_{GdCo_2} = 5.5\mu_B$ and $M_{Gd} = 7.5\mu_B$. This value agrees with the experimental data by Lemaire [116]. The same analysis applied to $GdFe_2$ (Fig.

7.3) gives the magnetic moment of Fe as about $2.0\mu_B$. The magnetic moments of elemental Fe and Co are $2.21\mu_B$ and $1.\dot{6}6\mu_B$ respectively [117]. We see the magnetic moment of Co in $GdCo_2$ is significantly reduced compared to the magnetic moment of Co metal. Huq [118] argued that the reduction of the Co magnetic moment in $GdCo_2$ is due to the filling of the magnetic 3d band of Co by the conduction electrons contributed from the Gd atoms. This is confirmed by our band structure calculation on $GdCo_2$ which will be discussed later. It would be interesting to compare the optical and magneto-optical properties of $GdFe_2$ and $GdCo_2$ due to the different magnetic properties of $GdFe_2$ and $GdCo_2$. For the investigation of the optical properties, we used ellipsometry. The magnitude of the diagonal optical conductivity is larger than that of the off-diagonal optical conductivity $\left(\frac{\sigma_{xy}}{\sigma_{xx}} \approx 10^{-2} \sim 10^{-3}\right)$. In magnetic materials, we can divide the electrons into magnetic electrons, that is, d electrons in transition metals and d and f electrons in rare-earth metals which have unpaired electrons, and the free conduction electrons, that is, s and p electrons. The spin-orbit interaction and spin-polarization of s and p states are much smaller than the d and f states. Therefore we can expect $s \rightarrow p$ transitions to be negligible in the magneto-optical Kerr effect. The involvement of d and f states is essential in magneto-optical effects due to their strong spin-orbit interaction and spin polarization. Erskine *et al.* estimated that the spin-orbit interaction of d states is larger than p-character-conduction electrons by a factor of 50 in Gd [29]. But in the diagonal optical conductivity, the $s \rightarrow p$ transitions are dominant due to their large dipole matrix elements and the $d \rightarrow f$ transitions are ignorable due to small dipole matrix elements in Gd [29]. Therefore the electronic structures of magnetic materials which contain d or f electrons are more effectively investigated by measuring the off-diagonal optical conductivity due to its strong dependence on the spin-orbit interaction and spin-polarization which are manifested by d or f electrons rather than s or p electrons. Magneto-optical Kerr spectroscopy (MOKS) is a unique tool for investigating the electronic structure of magnetic materials which contain d or f electrons. With MOKS in the transverse con-

figuration, the off-diagonal dielectric tensor, ϵ_{xy} or off-diagonal optical conductivity, σ_{xy} can be obtained using some experimental parameters and ϵ_{xx} or σ_{xx} [119]. With MOKS in the polar configuration, the magneto-optical parameters (Kerr rotation and ellipticity) are obtained directly, but the off-diagonal conductivities are obtained through Eq. 3.43. One of the advantages of MOKS over electron emission and tunneling experiments is its lower sensitivity to surface effects [120]. The experimental spectra of the real part of the diagonal optical conductivity of single crystals of $GdFe_2$ and $GdCo_2$ measured at room temperature without an external applied magnetic field are shown in Fig. 8.1.

From the figure, we see that the two compounds have very similar features in the optical conductivity. Both of them have broad peaks. $GdFe_2$ has a broad peak between 2eV and 3 eV. $GdCo_2$ has a somewhat broader peak at the lower energy, between 1.7 eV and 2 eV. We calculated the real part of the diagonal optical conductivities of $GdFe_2$ and $GdCo_2$ using the TB-LMTO based on LSDA. These are shown in Fig. 8.2.

There are broad peaks in the theoretical conductivity around 3.0 eV in both $GdFe_2$ and $GdCo_2$. When an external magnetic field is applied perpendicularly to the sample surface, the magnetic moments of Gd align parallel to the external field and the magnetic moments of Fe or Co align antiparallel to the external field. Therefore the majority-spins of the Gd atoms will be coupled with the minority-spins of the Fe or Co atoms in the up-spin state and vice versa in the down-spin state. The theoretical total densities of states of $GdFe_2$ and $GdCo_2$ are shown in Figs. 8.3 and 8.4 respectively.

The big peaks in Figs. 8.3 and 8.4 are from Gd-4f states. The spin-up states are marked by an up-arrow and spin-down states are marked by down-arrows. The occupied Gd-4f states are located 3.5 eV below the Fermi level and the unoccupied Gd-4f states are located 1.3 eV above the Fermi level for both samples. The Gd-4f states are highly localized and the hybridization with other states is negligible. The projected densities of states of $GdFe_2$ on Gd and Fe sites are plotted in Figs. 8.5 and 8.6 respectively.

The projected densities of states of $GdCo_2$ on Gd and Co are plotted in Figs. 8.7 and

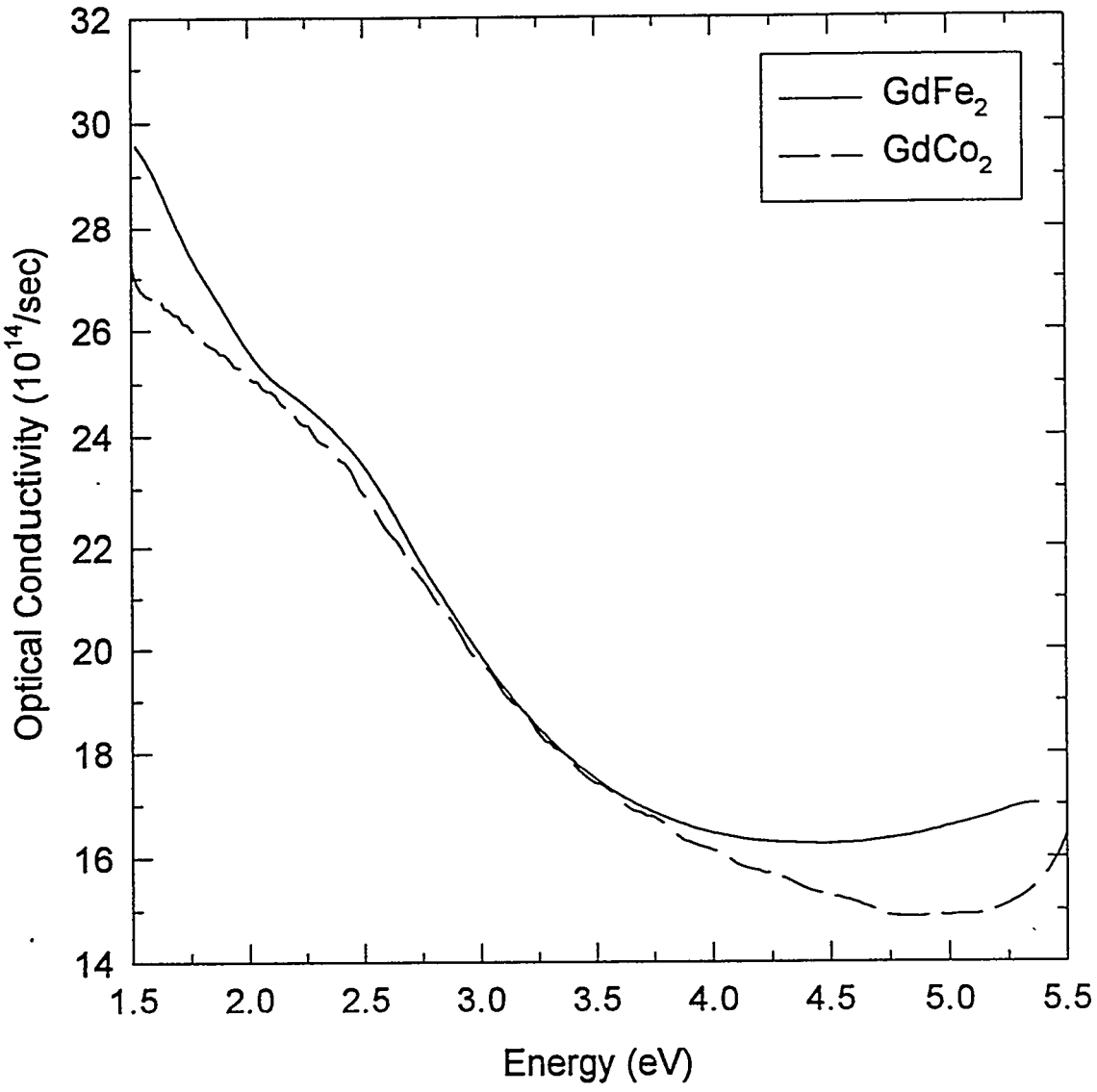

Figure 8.1 Real part of the diagonal optical conductivity for $GdFe_2$ and $GdCo_2$ single crystals measured at room temperature.

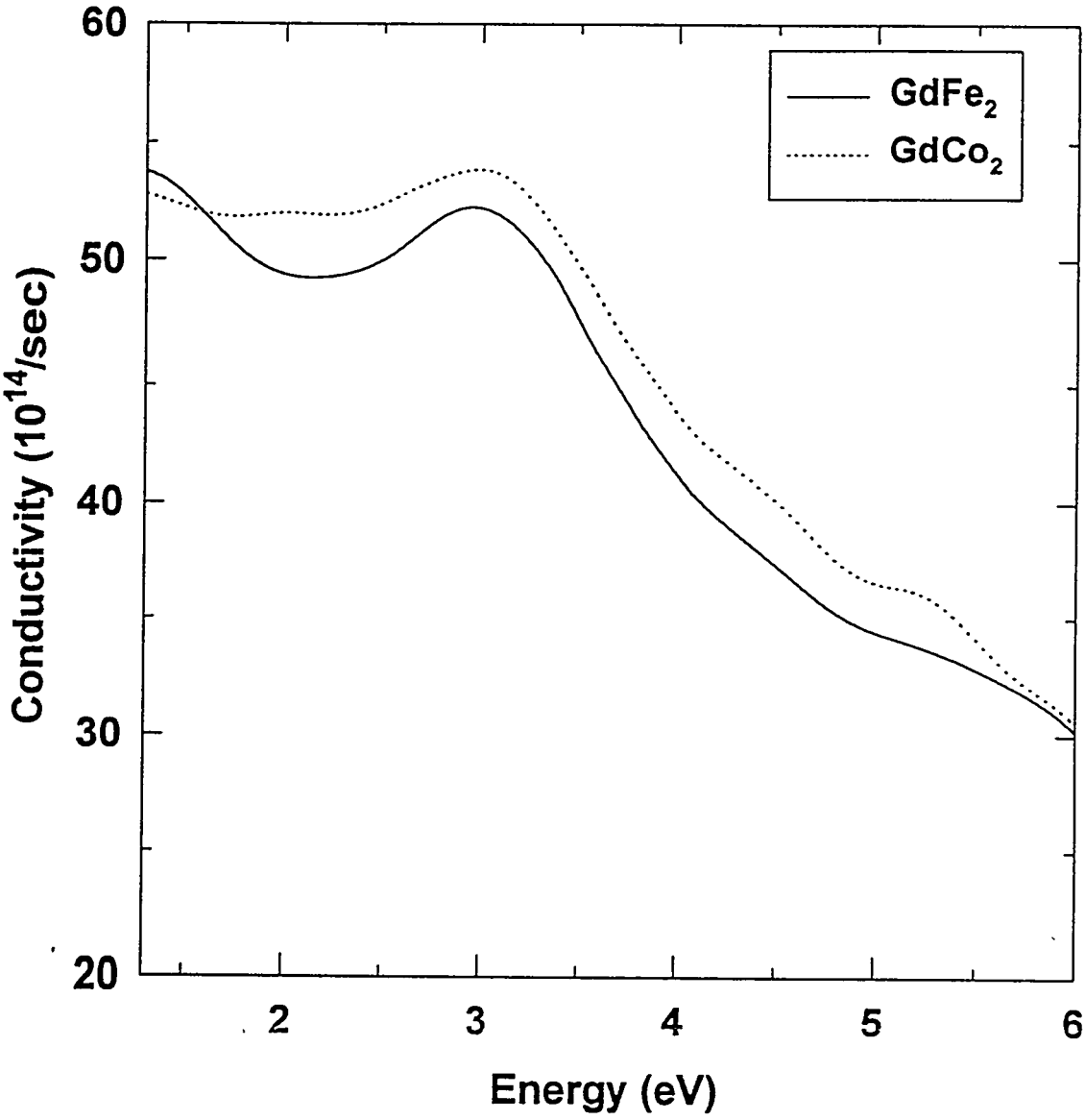

Figure 8.2 The real part of the diagonal optical conductivity for $GdFe_2$ and $GdCo_2$ calculated using the TB-LMTO method.

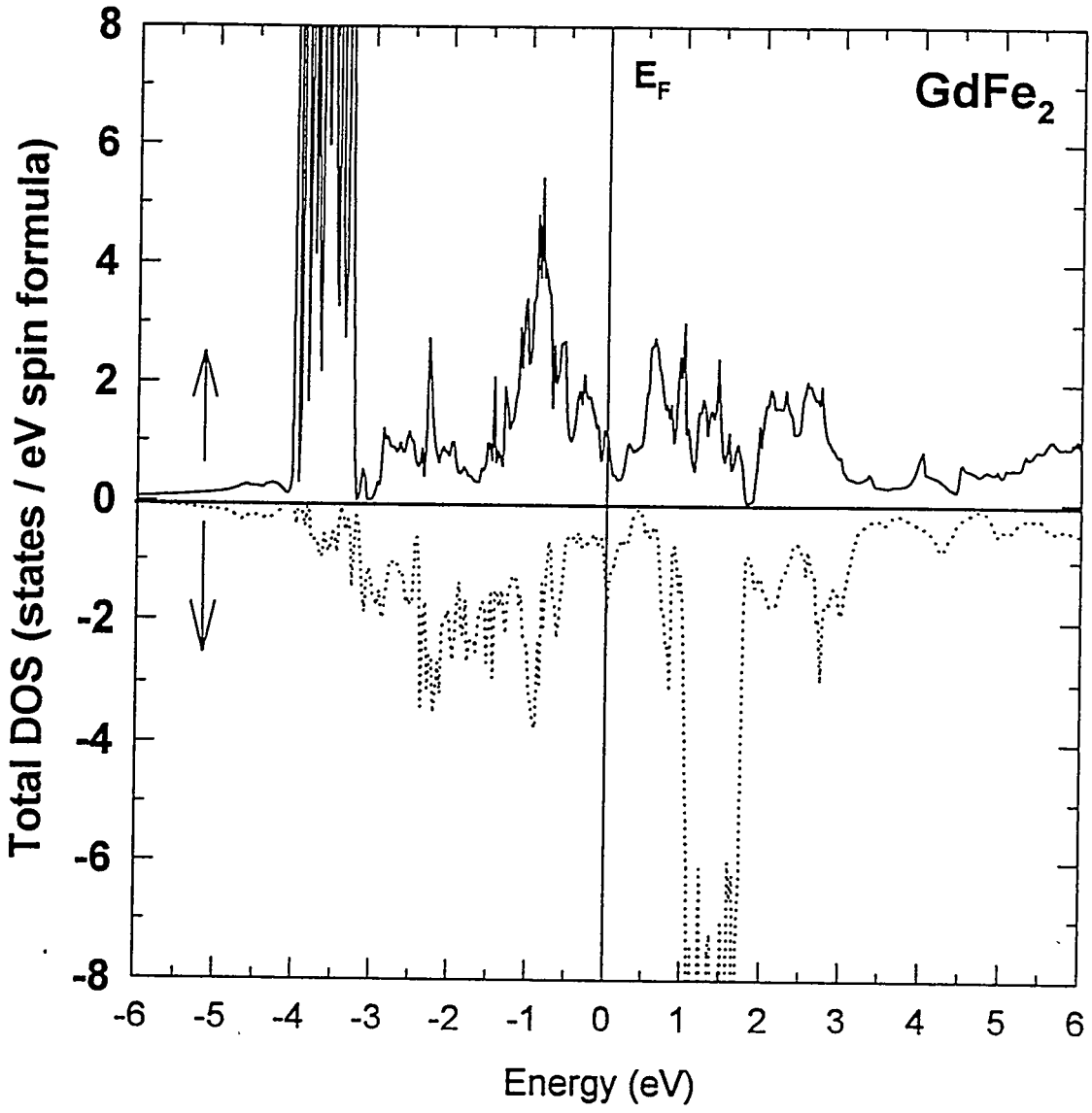

Figure 8.3 The total density of states of $GdFe_2$ calculated using the TB-LMTO method.

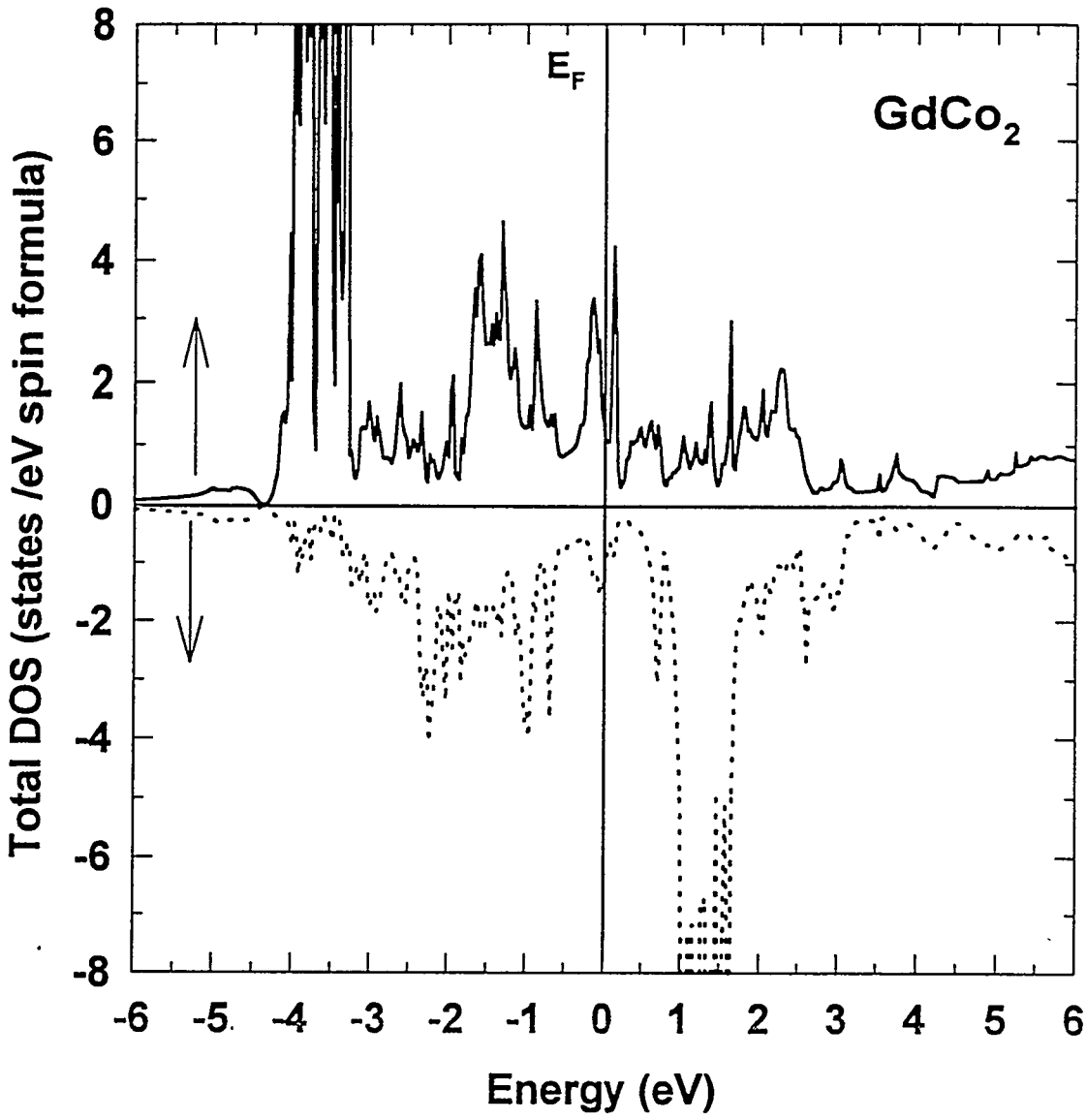

Figure 8.4 The total density of states of $GdCo_2$ calculated using the TB-LMTO method.

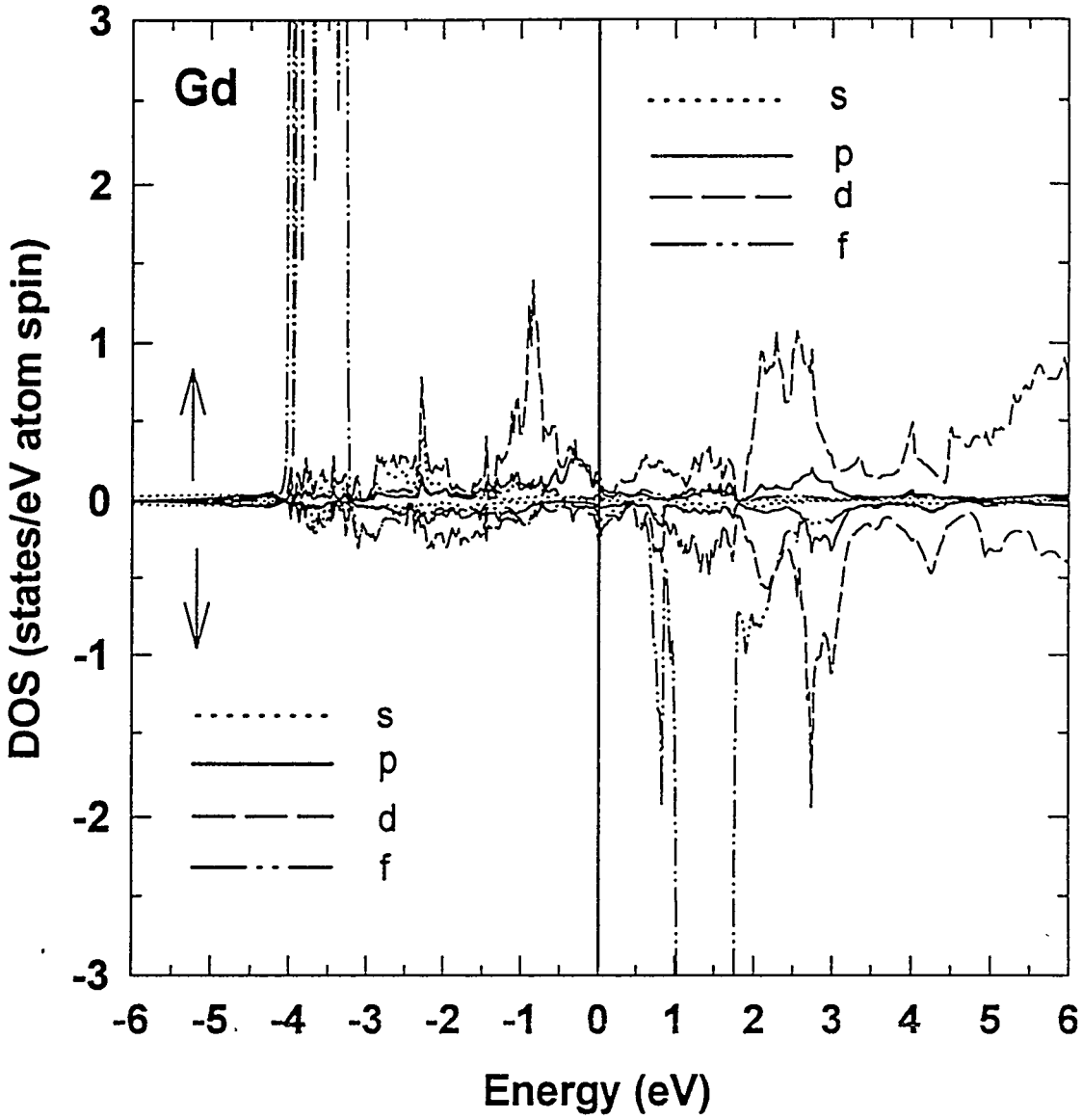

Figure 8.5 The calculated projected density of states of $GdFe_2$ on Gd sites using the TB-LMTO method.

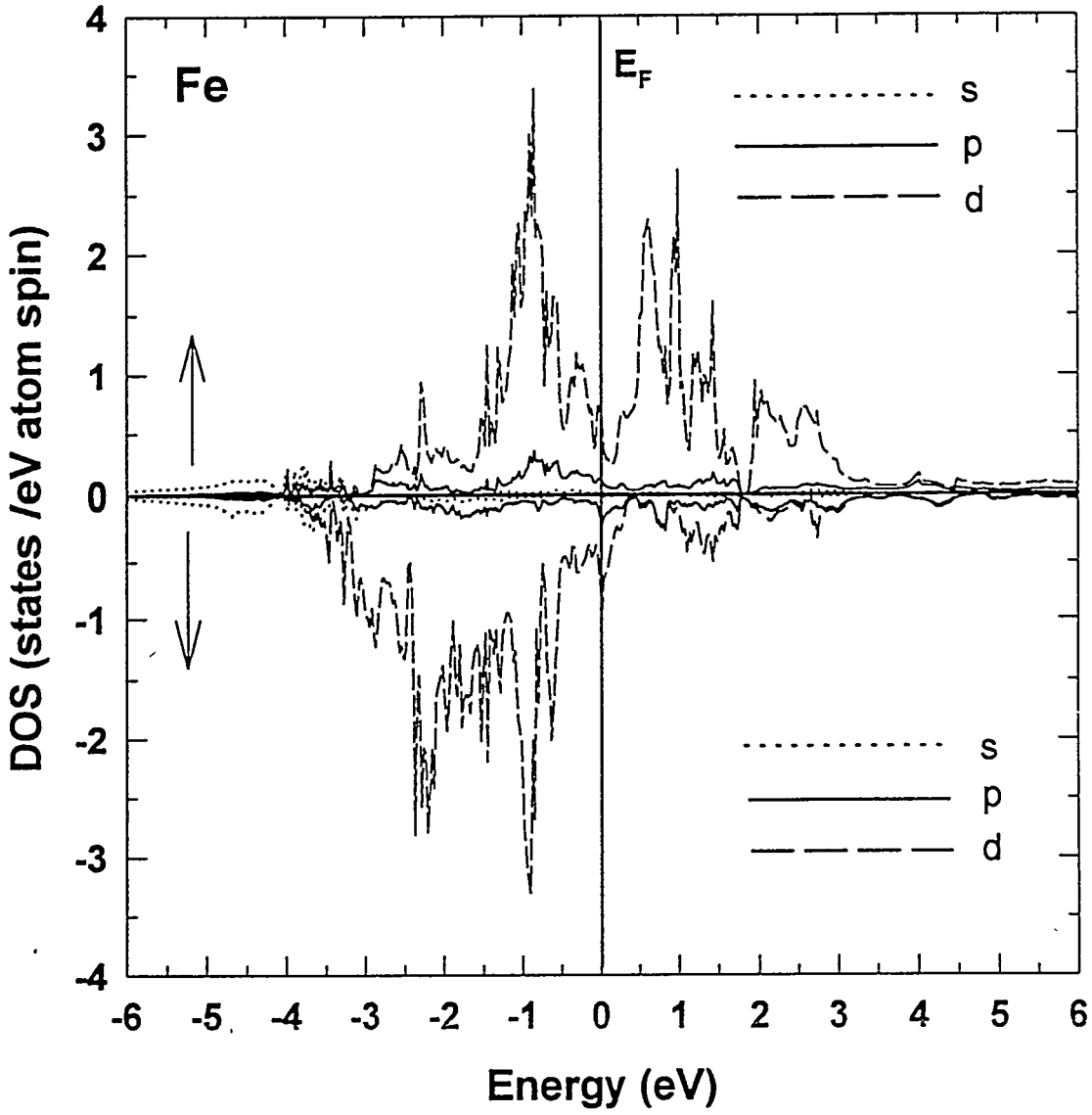

Figure 8.6 The calculated projected density of states of $GdFe_2$ on Fe sites using the TB-LMTO method.

8.8 respectively.

The 4f states of Gd in $GdFe_2$ and $GdCo_2$ are very similar as shown in Figs. 8.5 and 8.7, but the 5d states are quite different. This difference may come from the different coupling strength between Gd-Co and Gd-Fe. As already discussed, the coupling of the Gd-Co in $GdCo_2$ is significantly stronger than that of Gd-Fe in $GdFe_2$. The coupling is between the majority Gd-5d spins and the minority Fe(Co)-3d spins in the up state, therefore the 5d states of Gd and 3d states of Fe are expected to be mostly affected by the coupling. The change of the density of states of Gd or Fe(Co) in $GdFe_2$ and $GdCo_2$ relative to the those of Gd-metal and Fe(Co)-metal will be dependent on the coupling strength between Gd-Fe(Co). The unoccupied 3d states of Co-3d in the up state of $GdCo_2$ are shifted significantly to lower energy, even below the Fermi level, relative to those of elemental Co, which may be due to hybridization between Co-3d and Gd-5d states. This definitely reduces the magnetic moment of Co in $GdCo_2$, as proved by experiment [116]. But in the case of Fe in $GdFe_2$, the Fe-3d density of states does not change much compared to that of Fe-metal. The experimental density of states can be obtained using X-ray photoemission spectroscopy (XPS) for the occupied states and bremsstrahlung isochromat spectroscopy (BIS) for the unoccupied states. Dejuan *et al.* [121] have measured the binding energy, density of states and their temperature dependence of the 4d and 4f states of Tb and Gd ions of $TbFe_3$, $GdFe_2$ and $GdCo_2$ amorphous films by using XPS. The occupied Gd-4f levels at $400°C$, which is the crystallization temperature of $GdFe_2$ and $GdCo_2$, are 8.75 eV and 8.8 eV, respectively. Güntherodt *et al.* [122] measured the XPS spectrum of $Gd_{1-x}Fe_x$ amorphous alloys. From the XPS spectrum with x=0.67, the location of the 4f occupied states of Gd is 9.4 eV below the Fermi energy. The occupied Gd-4f states in amorphous alloys shifted by 0.65 eV toward lower energy from those of the crystalline phase in $GdFe_2$ from the above two experiments. As far as we know, there has been no report on the BIS or inverse photoemission spectroscopy (IPES) spectrum of $GdFe_2$ and $GdCo_2$. The locations of the occupied and

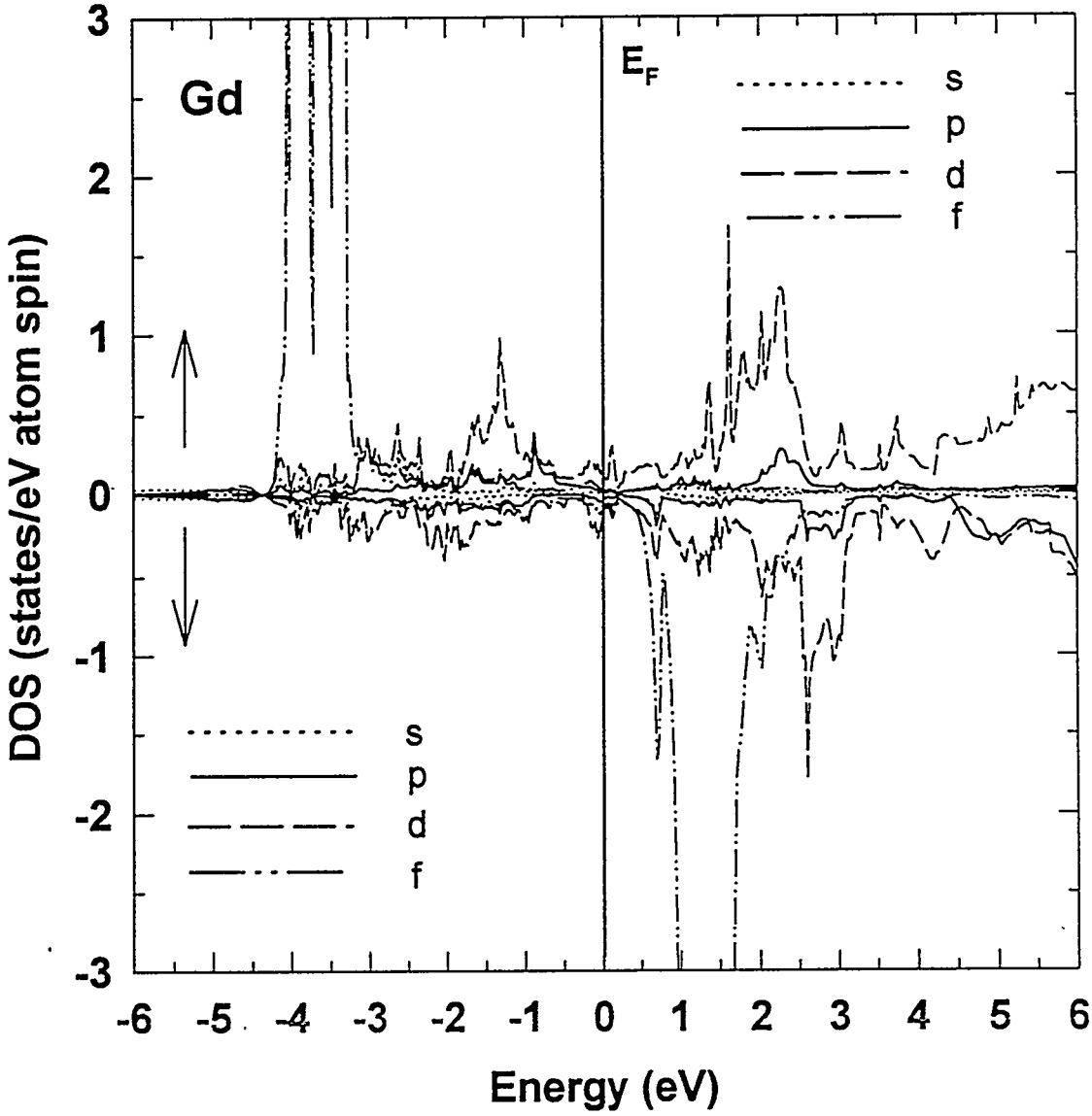

Figure 8.7 The calculated projected density of states of $GdCo_2$ on Gd sites using the TB-LMTO method.

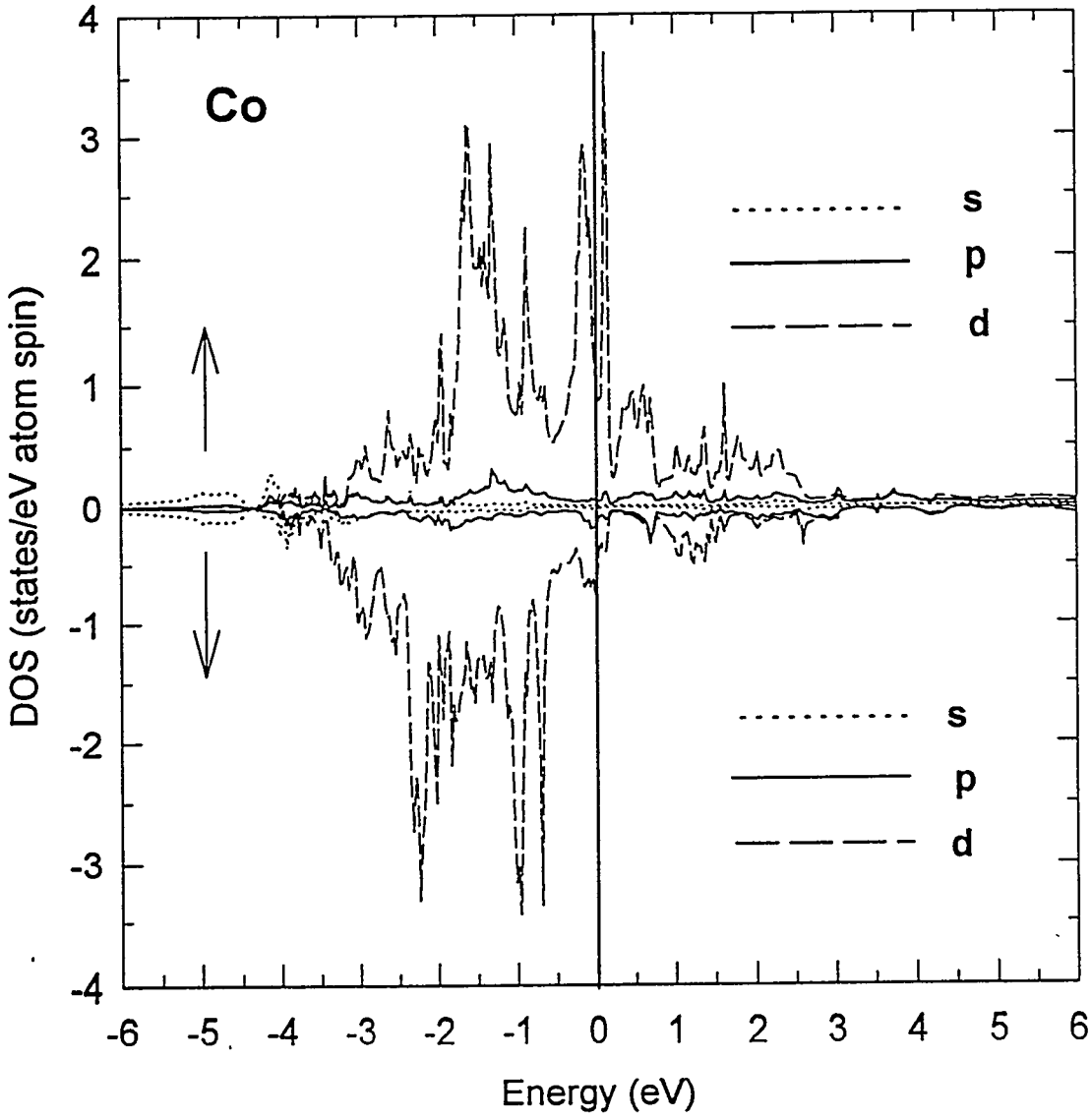

Figure 8.8 The calculated projected density of states of $GdCo_2$ on Co sites using the TB-LMTO method.

unoccupied 4f levels of bulk Gd metal are -8.5 and 3.5 eV with respect to the Fermi level, respectively, from PES and IPES data [123]. The LSDA calculations for $GdFe_2$ by the LMTO method by Hiroshi [124] give the locations of the occupied and unoccupied Gd-4f states to be -3.5 and 0.5 eV with respect to the Fermi level respectively. Our LDA calculation of $GdFe_2$ using TB-LMTO with spin-orbit interactions included gives the positions of Gd-4f occupied and unoccupied states as -3.5 and 1.3 eV with respect to the Fermi level respectively. The differences between experiment and theory based on the LDA of the Gd-4f states are large. The LDA theory, which is an one-electron approximation, does not include the many-body effects of localized 4f electrons which causes the difference.

Figure 8.9 shows the experimental Kerr rotation and ellipticity of $GdFe_2$ and $GdCo_2$ measured at room temperature with an applied magnetic field of 0.5T. The magnitude and shape of the Kerr rotation and ellipticity of $GdFe_2$ and $GdCo_2$ are not so different, as shown in Fig. 8.9. The Kerr rotation of $GdFe_2$ crosses zero at 3.1 eV. For $GdCo_2$, the Kerr rotation crosses zero at 3.8 eV. While there are few features in the diagonal optical conductivity, the MOKE data have many more features. This means that the magneto-optical Kerr spectrometer is very sensitive to the d and f states compared to ordinary optical techniques. The difference in Kerr rotation and ellipticity between the $GdFe_2$ and $GdCo_2$ may come from the different hybridization of Gd-Fe and Gd-Co which affects the density of d states of Gd and Fe(Co). Figure 8.10 shows the experimental data of σ_{2xy} of $GdFe_2$ and $GdCo_2$ measured at room temperature.

$GdCo_2$ shows more clear features in the σ_{2xy} spectrum than $GdFe_2$. There are peaks at 2.0 eV, 4.0 eV, and 5.3 eV in $GdCo_2$. $GdFe_2$ has two weak peaks in the measured spectral range, at 2.0 eV and 3.7 eV. To test the LDA, we calculated σ_{2xy} using the TB-LMTO based on the LDA. The σ_{2xy} component can be obtained directly using the electronic structure. The calculated values can be compared the experimental values. The theoretical σ_{2xy} spectra of $GdFe_2$ and $GdCo_2$ are shown in Fig. 8.11. In Fig. 8.11,

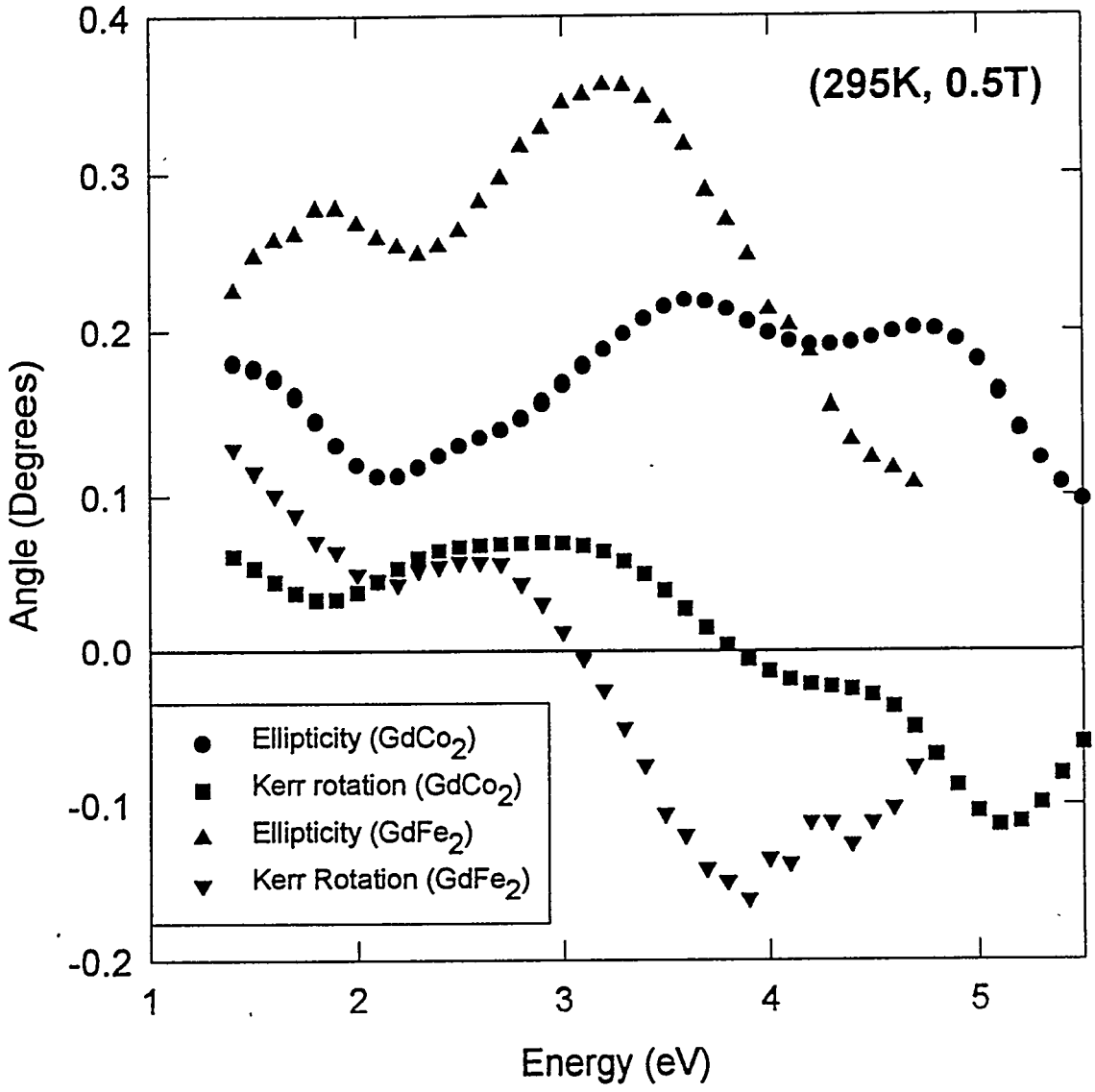

Figure 8.9 The experimental Kerr rotation and ellipticity of $GdFe_2$ and $GdCo_2$ meausred at room temperature with the applied magnetic field of 0.5T.

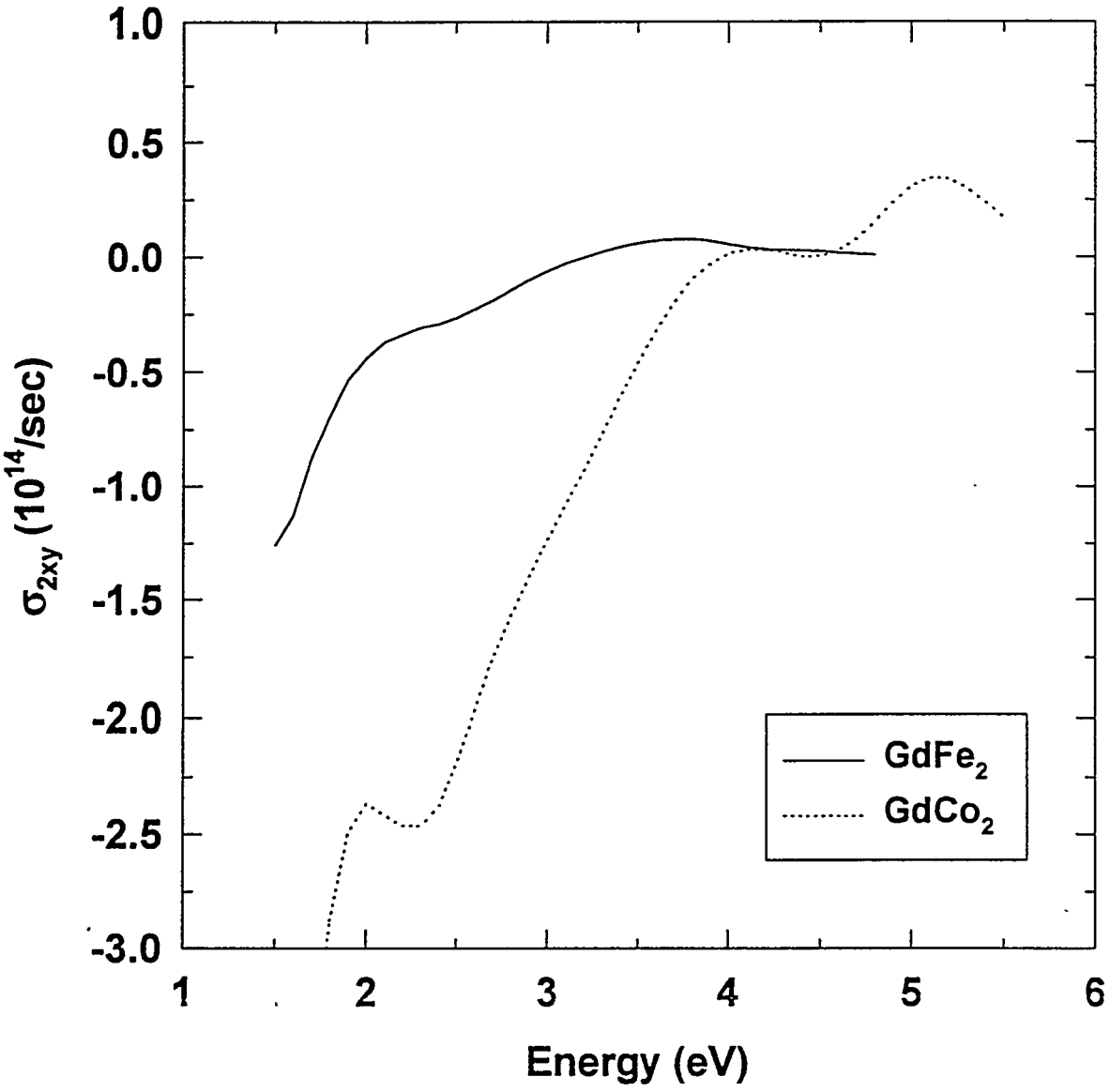

Figure 8.10 The experimental σ_{2xy} values of single crystals of $GdFe_2$ and $GdCo_2$ from experimental Kerr rotation, ellipticity measured at room temperature with an applied magnetic field of 0.5T and optical constants messured at room temperature with no magnetic field applied.

the solid line represents the σ_{2xy} of $GdCo_2$ and the dotted line represents the σ_{2xy} of $GdFe_2$. For both calculations, a constant lifetime broadening parameter of 0.5 eV is used.

As shown in Fig. 8.11, there are noticeable peaks at 0.5 eV, 4.5 eV in $GdCo_2$ and 1.7 eV in $GdFe_2$. The signs of σ_{2xy} for $GdFe_2$ and $GdCo_2$ are mostly negative in the energy range shown in Fig. 8.11. In experiment, $GdFe_2$ and $GdCo_2$ both are negative up to 3.2 eV and 4.0 eV, respectively. The agreement between theory and experiment in $GdCo_2$ and $GdFe_2$ is not good, especially between 3.5 eV and 5.0 eV. The theoretical σ_{2xy} in that region shows negative peaks while the experimental σ_{2xy} shows positive weak peaks. This may indicate the failure of the LDA in describing a strongly correlated system like rare-earth materials with 4f electrons. The Gd-4f states, located near the Fermi level in the calculation based on the LDA, but which should be located far away from it, could be hybridized with the conduction electrons. This could give an incorrect theoretical MOKE spectrum. To remove the occupied and unoccupied Gd-4f states located near the Fermi level, the LDA+U [83] method has been employed.

Summary and conclusion

The study of electronic, magnetic, optical, and magneto-optical properties of $GdFe_2$ and $GdCo_2$ is interesting not only for practical applications but also for the basic investigation of the electronic structure of magnetic materials. Magneto-optical polar Kerr spectroscopy is very useful for the measurement of the imaginary part of the off-diagonal optical conductivity. Because the off-diagonal conductivity is proportional to the product of spin-orbit interaction and net spin polarization, the involvement of d and f states are essential. To analyze the experimental σ_{2xy}, we need information on the density of states obtained by theory or experiment (XPS, BIS). The 4f electrons on the Gd atoms make a theoretical calculation based on the LDA difficult because the LDA can not

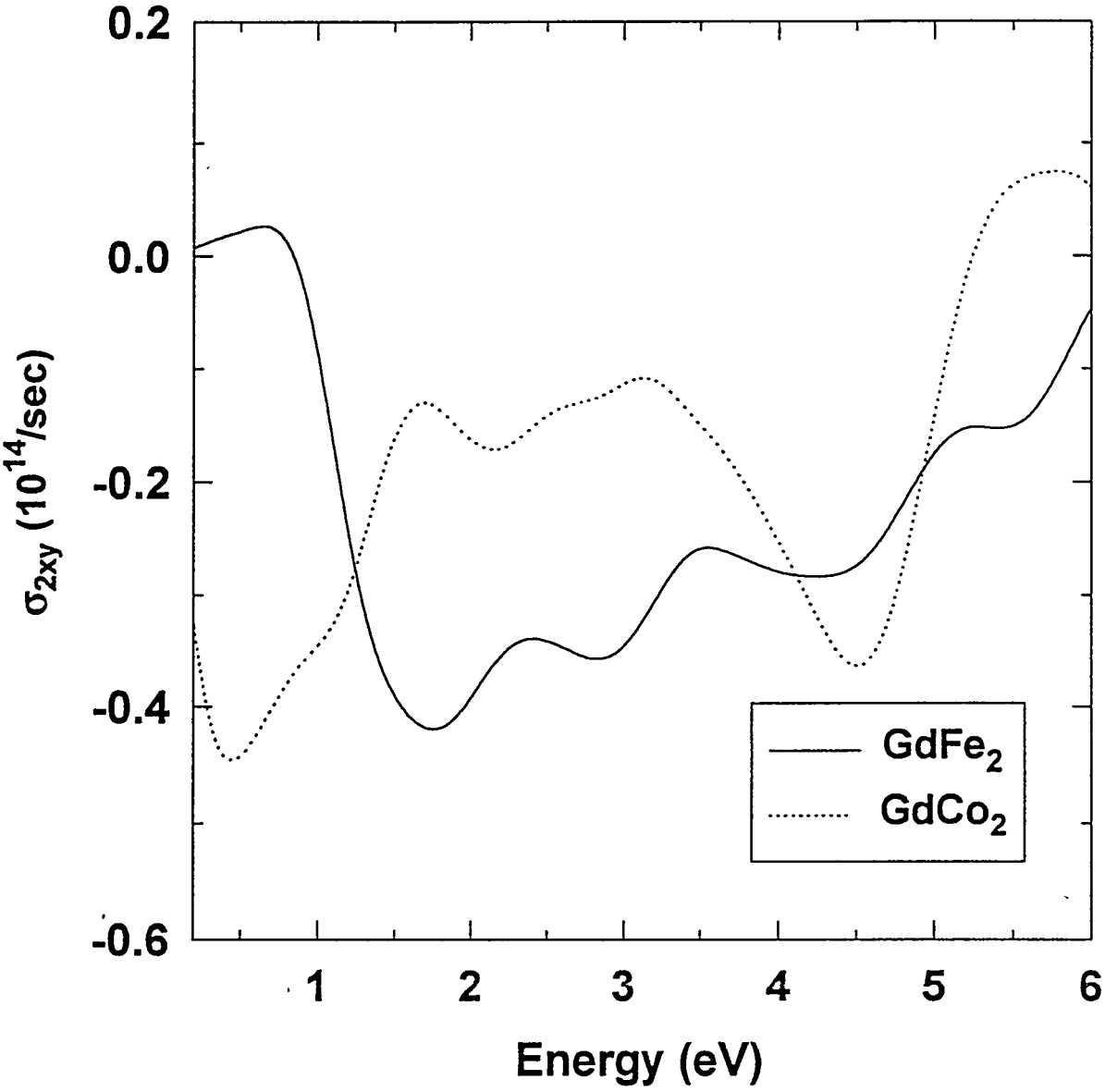

Figure 8.11 The theoretical values of σ_{2xy} of $GdCo_2$ and $GdFe_2$ using the TB-LMTO method based on LDA. The solid line represents the σ_{2xy} of $GdCo_2$ and the dotted line represents the σ_{2xy} of $GdFe_2$. For both calculations, a constant lifetime broadening parameter of 0.5 eV is used.

treat well the many body effects of the strongly localized 4f electrons. The theoretical prediction for 4f states always gives too small an energy separation between the unoccupied and occupied states. Even though the positions of the 4f states are wrong, the theoretical DOS from the TB-LMTO based on LDA explains some of the experimental results reasonably well. The theoretical density of states predicts the reduction of Co-3d magnetic moment in $GdCo_2$. The theoretical and experimental diagonal optical conductivity show one broad peak in the measured spectrum range while the off-diagonal optical conductivity shows more features in both theory and experiment. This means that MOKS is sensitive to the magnetic electrons, d in transition metals and d and f in rare-earth metals. To sort out the contributions to the off-diagonal optical conductivity from p to d, d to f or vice versa, a careful comparison of dipole matrix elements of p to d, d to f or vice versa is necessary. Currently it is being conducted by the author. Diagonal optical conductivity does not give much information about the effects on the density of states due to the Gd-Fe or Gd-Co coupling because the features are similar between the two samples. Compared to the diagonal component of optical conductivity, the off-diagonal optical conductivity shows quite different features between the two samples. This difference is believed come from the different hybridization strength between Gd-Fe and Gd-Co.

9 MAGNETO-OPTICAL PROPERTIES OF $TbFe_2$ AND $HoFe_2$

Magneto-optical properties of $TbFe_2$

The experimental Kerr rotation spectra of $TbFe_2$ were reported by Katayama *et al.* [92] together with a series of RFe_2 intermetallic compounds. They measured the polar Kerr rotation at room temperature with an applied magnetic field of 1.2T. Their measured spectral range was between 1.65 eV $\sim$ 5.0 eV. Among the 5 compounds, RFe_2 (R=Gd, Er, Ho, Dy, and Tb), $TbFe_2$ showed the largest Kerr rotation in the UV region. The maximum negative Kerr rotation appeared at 4.5 eV with a magnitude of 0.41°. The Kerr rotation crossed zero at 3.1 eV from positive in the low-energy region to negative in the high-energy region. They did not measure the ellipticities of their RFe_2 compounds. As far as we know, there have been no reports on the ellipticity of crystalline $TbFe_2$. Therefore we can not compare our ellipticity data with others. Off-diagonal optical conductivity spectra of polycrystalline $GdFe_2$, $TbFe_2$, and $ErFe_2$ are available [101]. Using the measured magneto-optical parameters (Kerr rotation and ellipticity) and optical constants (n and k), we can derive the off-diagonal optical conductivity from Eq. (3.41) and Eq. (3.42). Then we can compare our derived off-diagonal optical conductivity and the data obtained from the transverse Kerr geometry. Figure 2 of [101] was plotted erroneously, that is, the spectrum in Fig. 2 of [101] is the real part of the off-diagonal optical conductivities instead of the imaginary part of the diagonal elements of the dielectric tensor [125]. Figure 9.1 shows the Kerr rotations and ellipticities of

single crystal and polycrystal of $TbFe_2$ measured at different temperatures and applied magnetic fields. The single crystal of $TbFe_2$ was grown by the flux method and the polycrystalline $TbFe_2$ was made by arc-melting. Due to the irregular shape of the back of the single crystal of $TbFe_2$ and its small size, we could not take data in the cryostat because the single crystal sample moved under the large magnetic field and broke into two parts. Therefore we measured, outside the cryostat, with a permanent magnet [94] which can generate a magnetic field about 0.5 T, enough to saturate 60% of the magnetic moment of $TbFe_2$ at room temperature as shown in Fig. 9.2. The back of the polycrystalline sample was flat and the size was adequate for taking data in the cryostat. But the data are unreliable above 4.6 eV due to the weak intensity of the reflected light beam from the sample as compared to that of a reference mirror in the UV region. We noticed that the measured 2f component of the lock-in amplifier, which corresponds to the rotation (Kerr rotation+Faraday rotation for the sample and Faraday rotation for the reference mirror) of the elliptically reflected light from the sample or the reference mirror after normalizing with the DC component, did not increase in the UV region. The rotation mentioned above even bends over the UV region and decreases, especially when the intensity of the reflected light beam is weak.

The reason that the Faraday rotation should increase as the photon energy increases is as follows. The Faraday rotation at constant photon energy increase linearly with applied magnetic field according to,

$$\theta_F = VBl, \tag{9.1}$$

where V is the Verdet coefficient, B is an applied magnetic field and l is the thickness of a window that the light passed. The Verdet coefficient is dependent on the wavelength of light, temperature and is approximately proportional to the square of the light frequency. At constant magnetic field, the Faraday rotation is approximately proportional to the square of the photon energy. Therefore the Faraday rotation should increase as the

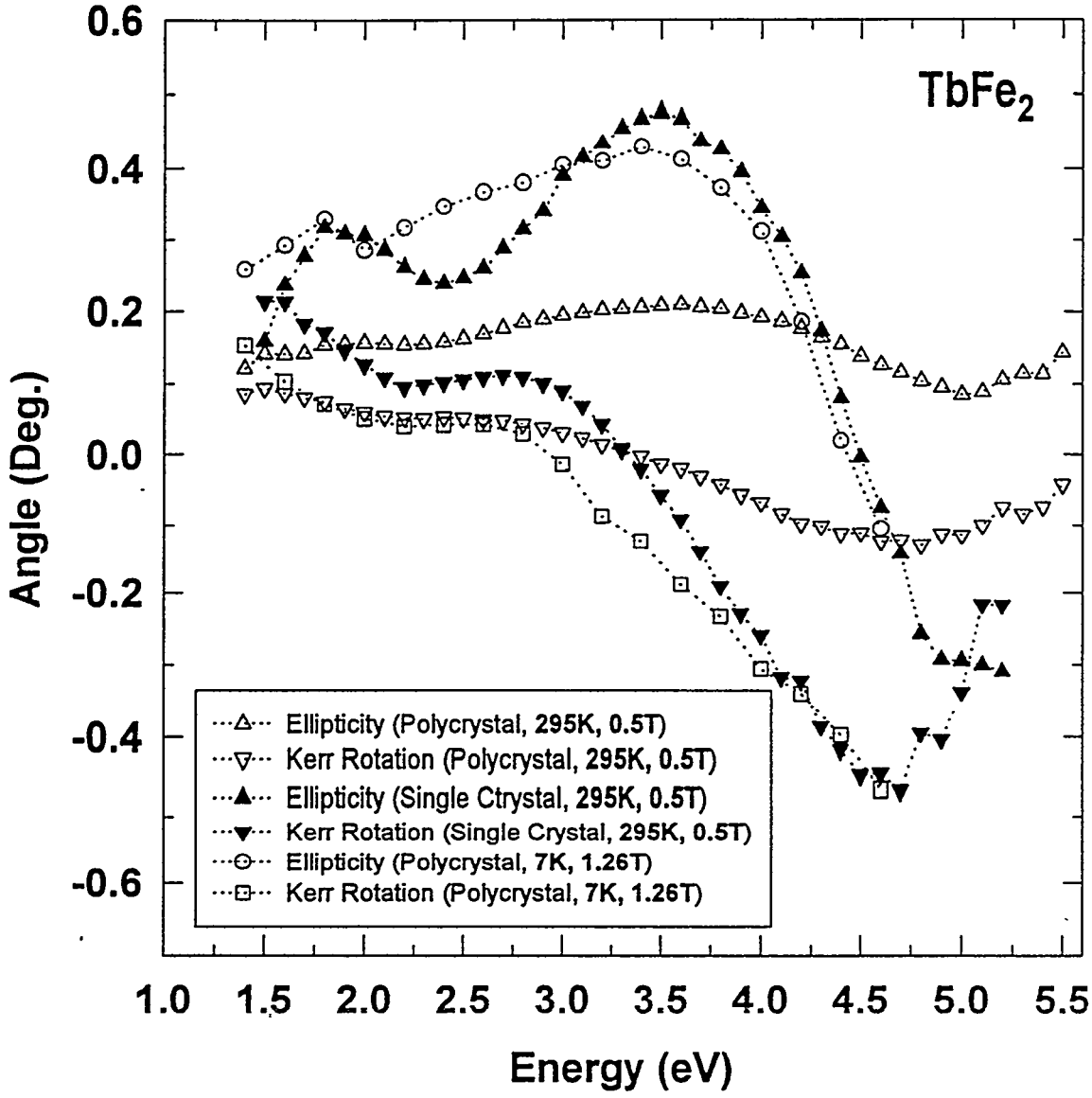

Figure 9.1 The Kerr rotation of single crystal and polycrystal of $TbFe_2$ measured at different temperatures and applied magnetic fields.

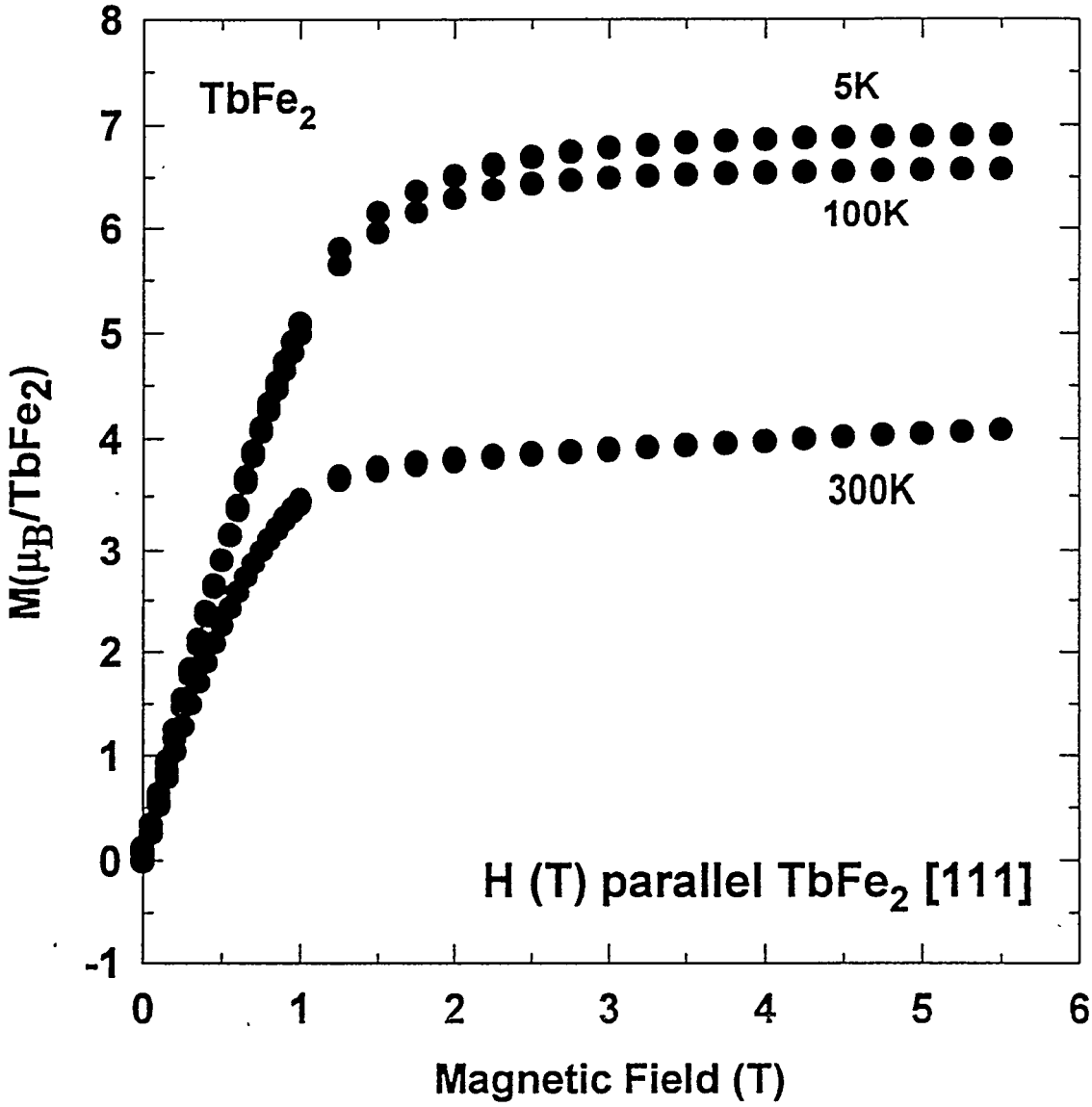

Figure 9.2 Magnetization measurements of $TbFe_2$ at 5K, 100K, and 300K.

photon energy increases. The cryostat has two windows, an inner window attached to the insert and an outer window. The total thickness of the windows is about 5 *mm*, 3 *mm* for the outer window and 2 *mm* for the inner windows. Both windows contribute to the Faraday rotation. But the contribution from the inner window is bigger than that of the outer window, even though the thickness of inner window is slightly thiner than that of the outer window. This is due to the fact that the magnetic fields generated by the superconducting magnet are dipole fields whose magnitude decrease rapidly as the distance becomes larger from the superconducting magnet. For example, the magnetic field at the outer window measured with a gaussmeter is only 0.3 T when we applied current to the superconducting magnet to generate a magnetic field of about 1.6 T. The actual Faraday rotation measured is twice that of Eq 9.1 because the light beam passes through the cryostat windows twice (incoming and outgoing). The Faraday rotation of the cryostat windows at 7 K and 1.6 T is roughly 2° at 2.5 eV while the Faraday rotation is 10° at 5.0 eV. For the above Faraday rotation measurements, the evaporated Al reference mirror was used.

Above 5.0 eV, the magnitude of the apparent Faraday rotation begin to decrease, instead of increasing as expected. The reason for this may be as follows. The intensity of UV radiation on the detector falls because of the weak intensity of the Xe lamp, the low transmittance of the optical elements in the UV, and the lower sample reflectance. As the intensity is lowered, the high voltage on the photomutiplier is raised to keep the DC voltage constant for normalization of the 1f and 2f components. By increasing the DC voltage, the 1f and 2f voltages picked up by the lock-in amplifier also increase according to the DC voltage increase. The DC voltage is proportional to the DC intensity given in Eq. 2.15 and is directly related to the average of the squared Fresnel reflection coefficients for the right- and left-circularly polarized light. The DC component originates from two sources, the real DC signal as defined in Eq. 2.15 and the false DC signal from stray light. In the visible range, the real DC signal is large enough to allow ignoring the stray

light. But in the UV range, the real DC signal is small. In order to raise the small DC voltage to the constant value, a large high voltage from the power supply should be supplied to the PMT tube. The large high voltage also raises the stray-light signal which contributes to the DC component. This makes the magnitude of the portion of the DC component contributed by stray light become a significant fraction of the total DC signal. Suppose in the UV range, the DC component contributed by the real DC signal is I_{DC} and the DC component contributed by stray light is I'_{DC}, then the total DC component will be $I_{DC}+I'_{DC}$. This total DC value is set to constant, 5 mV. Therefore as the relative intensity of stray light increases, the relative component of the real DC value decreases. Similarly, the 2f-component originates from two sources, the real 2f signal of the UV ($I_{2\omega}$) and the stray light contribution ($I'_{2\omega}$) as a form of Faraday rotation. But the Faraday rotation contributed by stray light is smaller because most of stray light comes from the long wavelength light. The total 2f-component can be written as $I_{2\omega} + I'_{2\omega}$. As a result of this, in the large stray light the rotation proportional to $\frac{I_{2\omega}}{I_{DC}}$ is changed into

$$\frac{I_{2\omega} + I'_{2\omega}}{I_{DC} + I'_{DC}} \tag{9.2}$$

While the magnitude of the denominator in Eq. 9.2 is fixed to 5 mV, the magnitude of the numerator is reduced from the value without stray light contribution. Therefore the ratio Eq. 9.2 which is proportional to the rotation is reduced from the real value, with no stray-light contribution. For a sample which is small and not so reflective, the decrease starts earlier than for the Al mirror. Once the wrong DC signal appears, then the data are not reliable because we would be using incorrect rotations in Eq. 2.1. The stray light in the UV range could be reduced by using a few methods. First, a double monochromator or a special filter can reduce the stray light but these will reduce the intensity of the signal a lot. Second, using an Ar or Cd laser as light source could reduce the stray light because they do not produce long wavelength light. Third, to get one

accurate value in the UV spectrum, using a Hg lamp may be useful because it gives one strong line at 5 eV.

We compared the Kerr rotation and ellipticity of the single crystal and polycrystal of $TbFe_2$ as shown in Fig. 9.1. The peak negative Kerr rotation appeared around 4.6 eV for both samples measured at 295 K and 0.5T which is similar to that of Katayama [92]. For polycrystalline $TbFe_2$ measured at 7K and 1.26T, the absolute magnitude of the Kerr rotation at 4.6 eV is quite similar to that of Katayama [92] measured at room temperature and 1.2 T. The magnitude of the Kerr rotation of the single crystal of $TbFe_2$ at 4.6 eV is 0.46° while that of the polycrystal of $TbFe_2$ is 0.12° measured under the same conditions. The Kerr rotation of the single crystal is almost 4 times bigger than that of polycrystalline sample. Compared to the Kerr rotation of Katayama, the magnitude and shape are quite similar in the case of the single crystal, even though we applied a smaller magnetic field. From this, we expect the Kerr rotation of a single crystal of $TbFe_2$ under high magnetic fields in the UV region will be much larger than that of [92]. There is a small flat shoulder between 2.2 eV and 2.8 eV in the Kerr rotation spectrum of $TbFe_2$ of [92]. As shown in Fig. 9.1, we can see also a similar feature between 2.1 eV and 3.0 eV, but the shoulder is a little bit more clear than that of [92]. In the case of our polycrystalline sample, the Kerr rotation is much smaller than their data. This is not surprising because we applied smaller magnetic fields. From the comparison of MOKE data between single crystal and polycrystal $TbFe_2$, we found that the single-crystal shows a larger Kerr rotation and more features than the polycrystal under the same experimental conditions when the magnetic moments are not fully saturated. This may be come from several reasons. First, mechanical polishing of the polycrystal causes surface strain, so the magnetic domains may be more difficult to align compared to samples with unstrained surfaces. To relax the strained surface, annealing the sample may be necessary. However we found annealing the polycrystalline $TbFe_2$ sample in vacuum expedited oxidation. The annealed surface lost its luster due to the oxidation

or due to grain growth, which causes roughening Chemical etching may dissolve one component more than the other component. The surface of the single crystal of $TbFe_2$ grown by the flux method is mirror like, so no further surface treatments were necessary to make the surface suitable for optical measurements. Therefore no surface strain problem arose from mechanical polishing as for the polycrystal sample. The second factor which may affect the surface quality is oxidation. While polishing the surface of polycrystalline sample with alumina solution, contact with water is unavoidable. This may expedite the rate of oxidation. Usually higher humidity increases the oxidation rate [60]. As discussed in Chapter 4, the oxide layer reduces the magnitude of the real part of the optical conductivity. Allen *et al.* [126] found oxidation reduces the reflectivity and the polar Kerr rotation of Tb_xFe_{1-x} ($x \simeq 0.21$). The third factor which affects the MOKE experiment is the purity of the sample. As shown in Fig. 9.3, the crystal grown by flux method has a well defined single phase which does not contain a second phase. Therefore MOKE data of single crystals are more likely to represent the real MOKE spectra of magnetic materials under investigation. Figure 9.4 shows the σ_{1xy}, σ_{2xy}, and $\omega\sigma_{2xy}$ values for the single crystal of $TbFe_2$ from experimental Kerr rotation, ellipticity measured at room temperature with an applied magnetic field of 0.5T, and optical constants, n and k, measured at room temperature with no magnetic field applied. Sharipov *et al.* measured σ_{1xy} and σ_{2xy} of polycrystalline $TbFe_2$ in the energy range of 0.6 eV to 5.0 eV. From Fig. 2 of [125], there are two noticeable peaks in σ_{2xy} of $TbFe_2$ at 2.0 eV and 4.6 eV. As shown in Fig. 9.3, there are two peaks at 2.0 eV and 4.5 eV in σ_{2xy} respectively. We also plotted $\omega\sigma_{2xy}$ in Fig. 9.4. In order to investigate the origin of the Kerr effects for the RFe_2 compounds, we need to have their electronic structures and densities of states. For these, we calculated the electronic structure and DOS of $TbFe_2$ using the TB-LMTO method with the LDA. The total density of states of $TbFe_2$ is shown in Fig. 9.5. The two big peaks are due to the Tb-4f states. The spin-up states are marked by an up-arrow and the spin-down states are marked by a

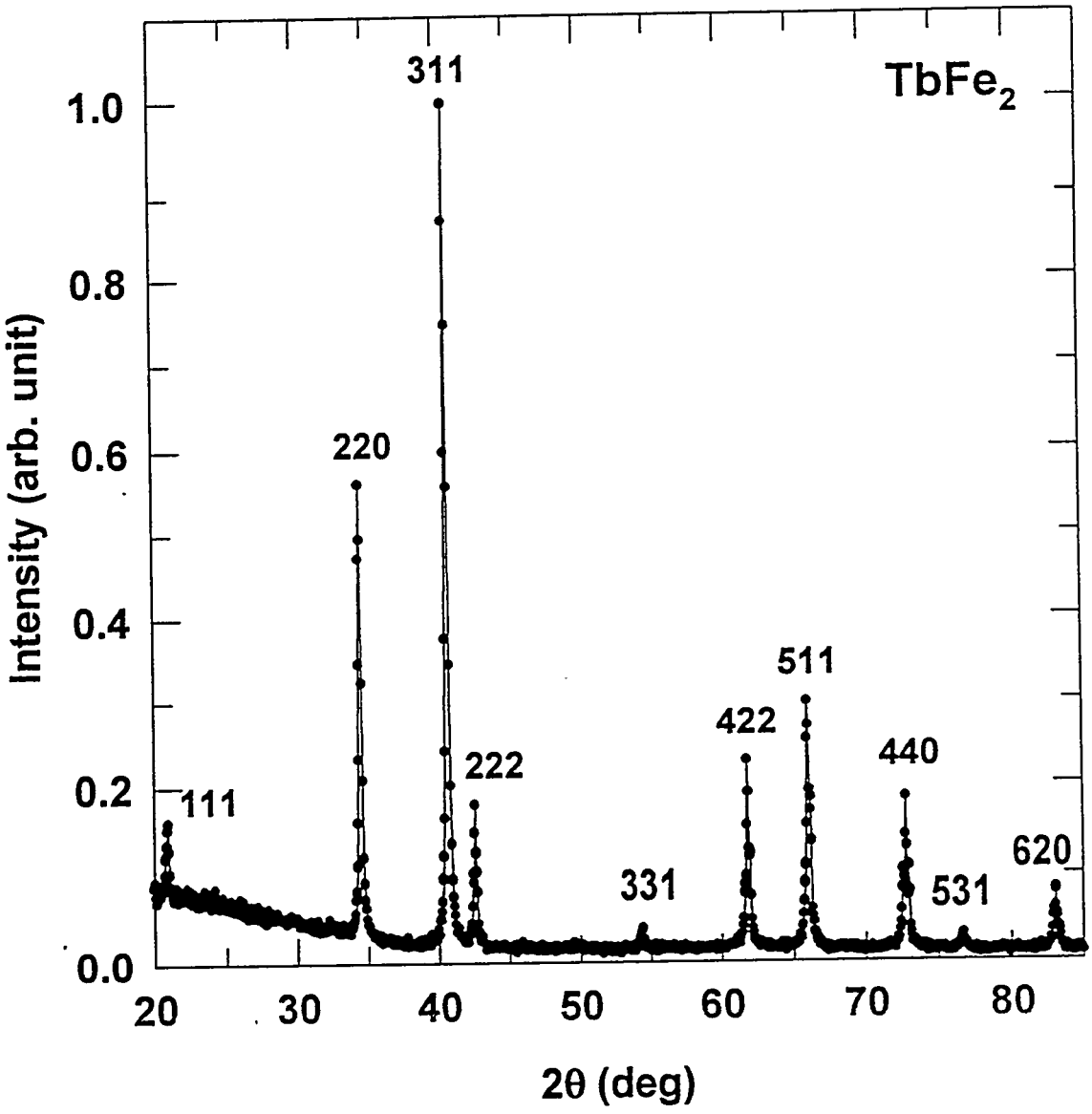

Figure 9.3 Powder X-ray diffraction pattern of crushed $TbFe_2$ single crystal. The peaks are indexed to a fcc unit cell with a lattice parameter a=7.345$\mathring{A}$.

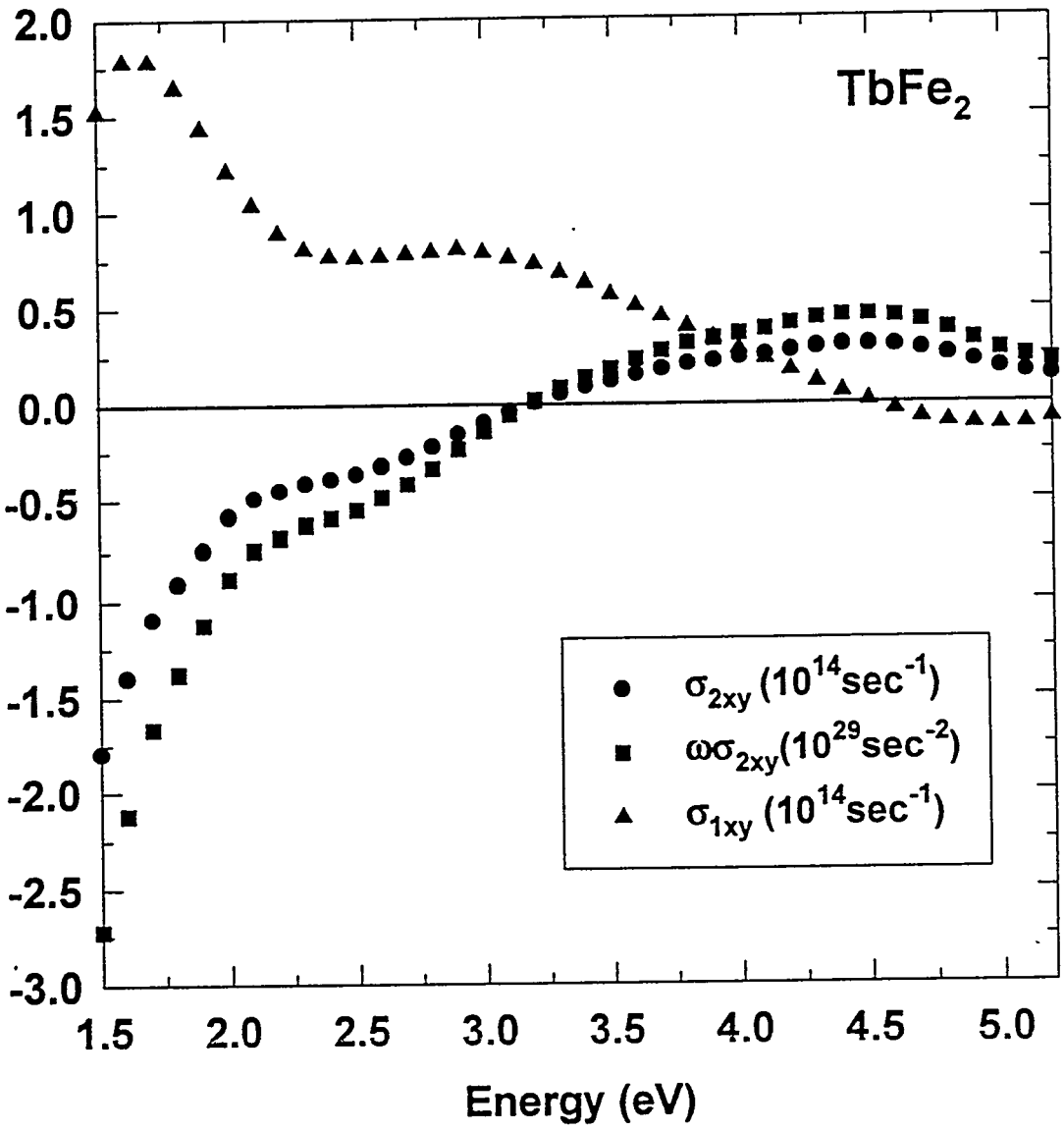

Figure 9.4 Experimental σ_{1xy}, σ_{2xy}, and $\omega\sigma_{2xy}$ spectra of single crystals of $TbFe_2$ from experimental Kerr rotation, ellipticity measured at room temperature with an applied magnetic field of 0.5T and optical constants measured at room temperature with no magnetic field applied.

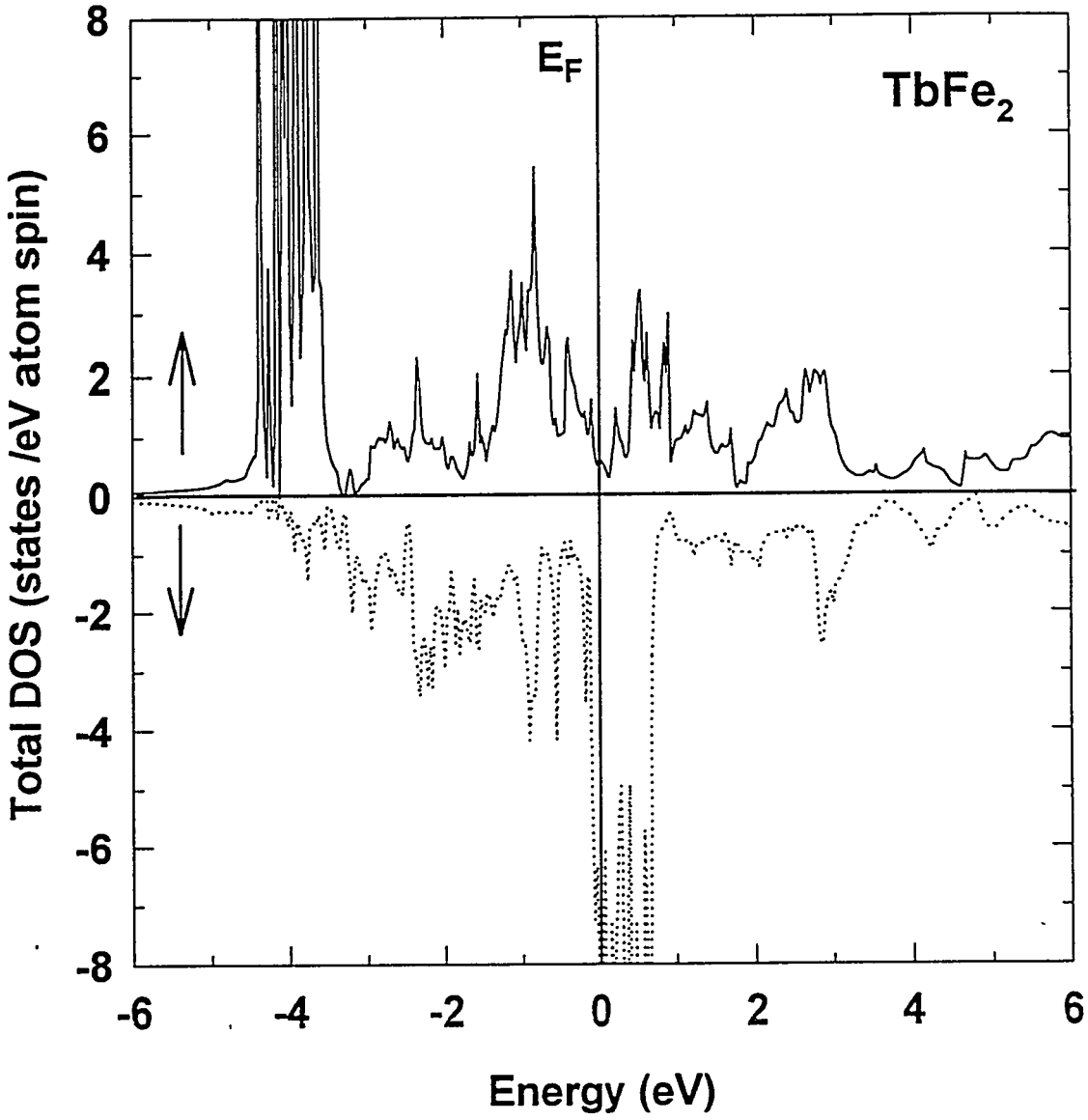

Figure 9.5 Calculated spin-polarized total density of states (DOS) for $TbFe_2$ using the TB-LMTO including spin-orbit interaction.

down-arrow. The partial densities of states of Tb and Fe are shown in Figs. 9.6 and 9.7. The Tb-4f states of spin-up are located 4 eV below the Fermi energy. The Tb-4f states of spin-down are located 0.3 eV above the Fermi energy.

But some of the 4f states are at the Fermi level as shown in Fig. 9.6. This makes the density of states at the Fermi level large. The calculated electronic specific heat coefficient γ is 35.6 $mJK^{-2}mole^{-1}$. The experimental value is 21.0 $mJK^{-2}mole^{-1}$ [127]. Connell *et al.* have studied the density of states of amorphous $Tb_{0.21}Fe_{0.79}$ by photoemission and inverse photoemission. They found the f-electron spectral weight is shifted to lower energy and the f-hole spectral weight is shifted to higher energy, each by 1 eV, compared to the f-electron weight in Tb-metal [128], due to the hybridization between Fe and Tb d-states in the alloy [129]. The center of the occupied f states in Tb metal is located 2.2 eV below the Fermi energy and the center of the unoccupied f states is located 2.7 eV above the Fermi energy. They found the spectra in the vicinity of the Fermi energy are dominated by Fe-d states. We expect the unoccupied 4f states in crystalline $TbFe_2$ to be located at least 3 eV above the Fermi level, while the theory based on LDA located them just 0.3 eV above the Fermi energy. Furthermore part of the theoretical 4f unoccupied density of states is located exactly at the Fermi energy and below the Fermi energy. This discrepancy between theory and experiment comes from the fact that the LDA can not incorporate many-body effects in correlated systems. Figure 9.8 shows the theoretical σ_{2xy} of $TbFe_2$ calculated using the TB-LMTO based on the LDA. We expect the theoretical σ_{2xy} may disagree with experimental values if the theory can not predict well the position of f states in the electronic structure of magnetic materials because the f-electrons play important roles in magneto-optical effects due to their large spin-orbit coupling and exchange splitting. Furthermore the wave function of atomic 5d electrons penetrates deep enough to overlap with the tail of the 4f wavefunction, while the overlap between 6s and 4f is ignorable. In Fig. 9.8, the solid line represents the calculated σ_{2xy} with the $d \rightarrow f$ and $f \rightarrow d$ transitions included, and the dotted line

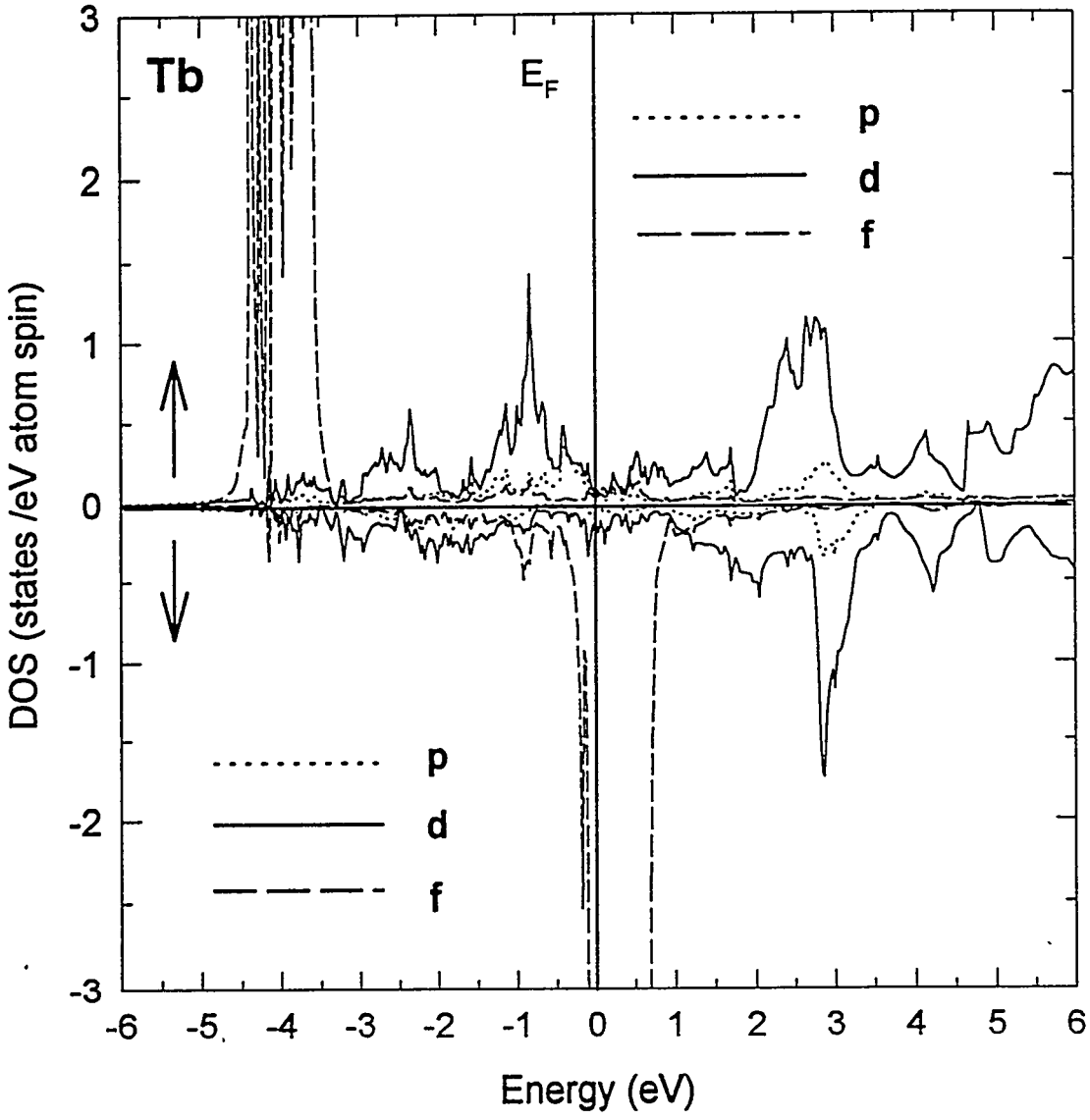

Figure 9.6 Calculated spin-polarized partial density of states (DOS) for Tb using the TB-LMTO including spin-orbit interaction.

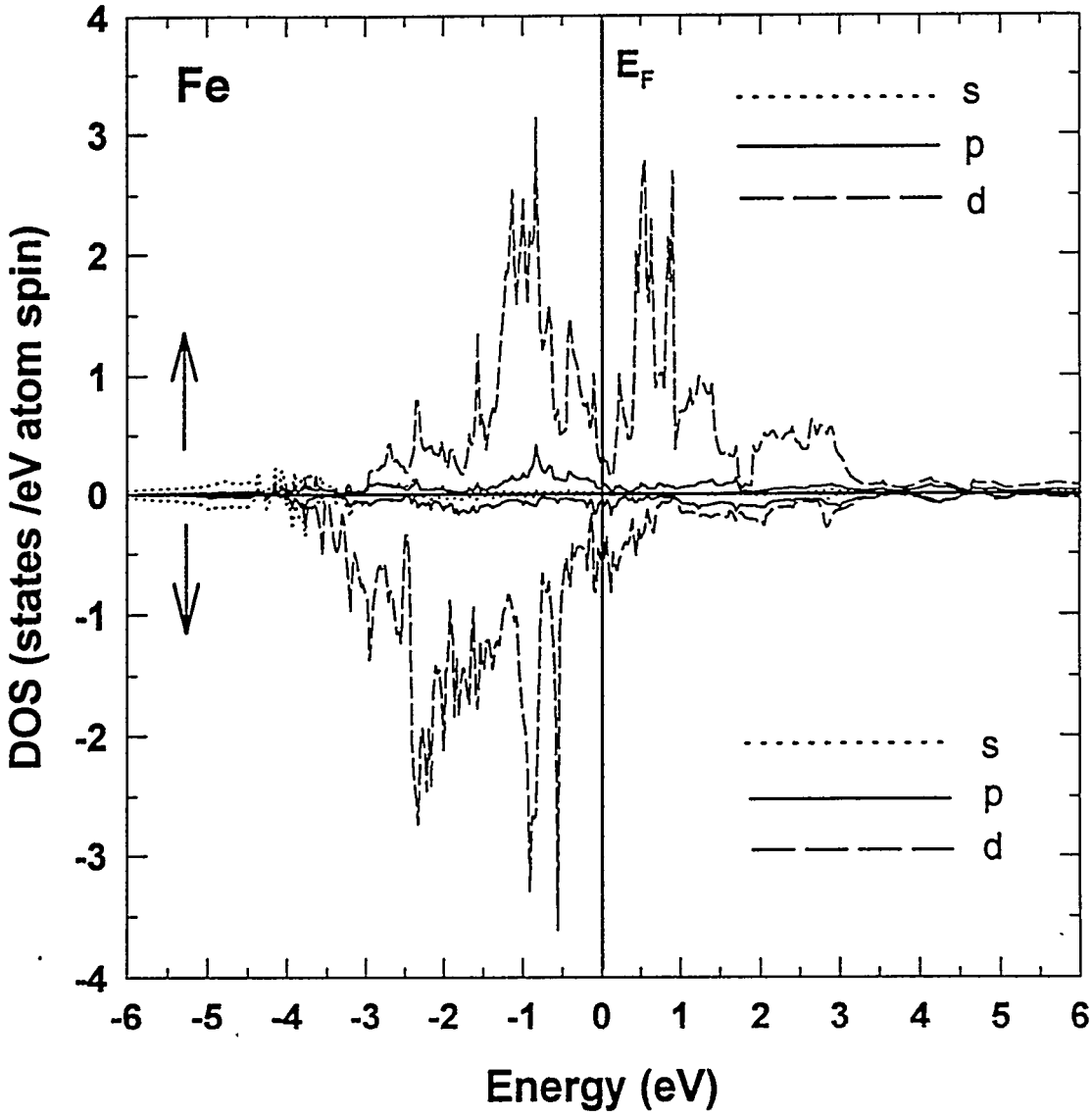

Figure 9.7 Calculated spin-polarized partial density of states (DOS) for Fe using the TB-LMTO including spin-orbit interaction.

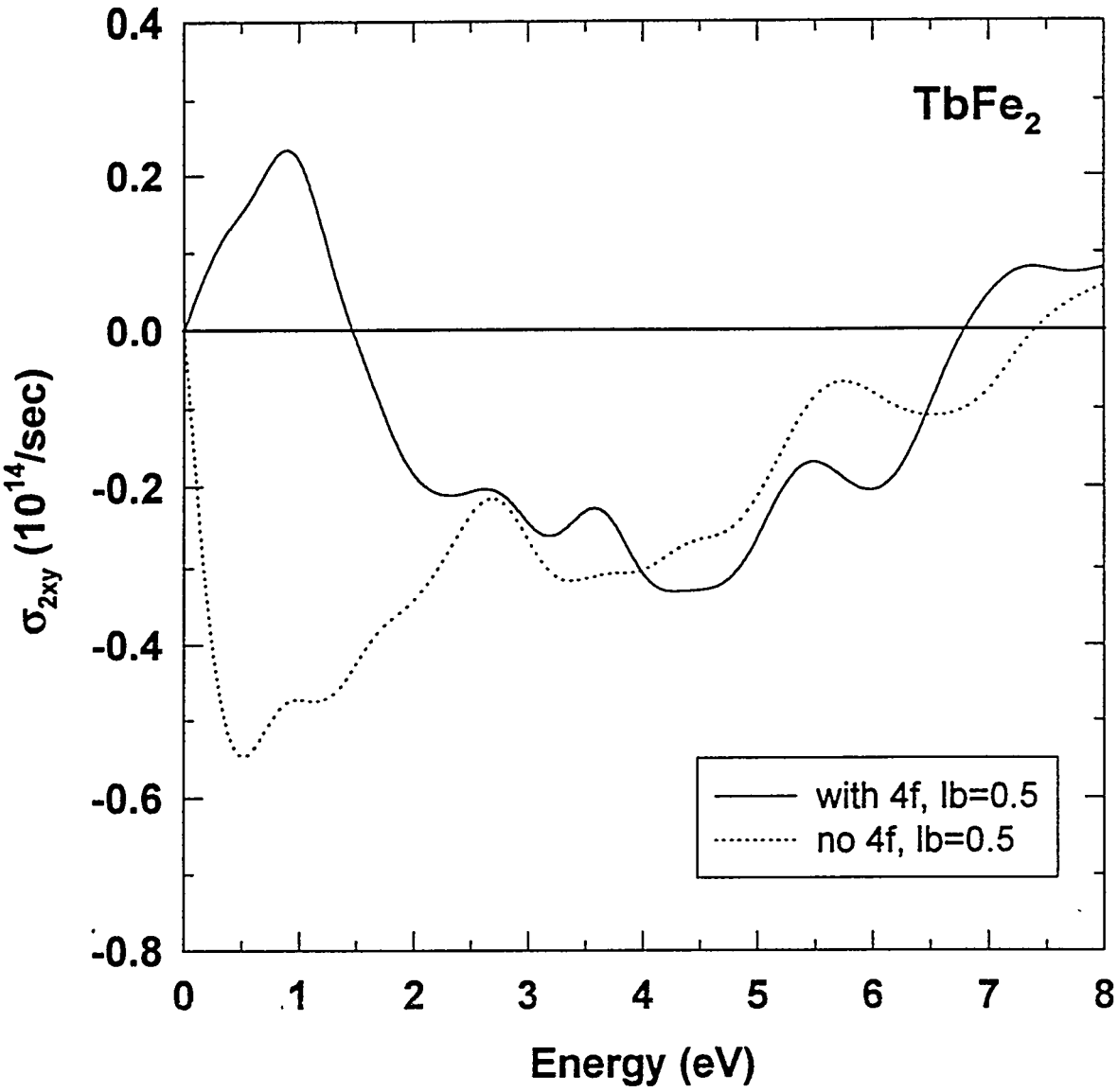

Figure 9.8 Theoretical σ_{2xy} of $TbFe_2$ calculated using TB-LMTO based on LDA. The solid line represents the σ_{2xy} with d-to-f and f-to-d interband transitions are included. The dotted line represents the σ_{2xy} with d-to-f and f-to-d interband transitions are not included. For both calculations, a constant lifetime broadening parameter of 0.5 eV is used.

stands for the calculated σ_{2xy} with the $d \rightarrow f$ and $f \rightarrow d$ transitions turned off. A constant lifetime broadening parameter of 0.5 eV is used for both cases. As shown in Fig. 9.8, the theoretical σ_{2xy} with the $d \rightarrow f$, and $f \rightarrow d$ transitions turned on and turned off are quite different. In the lower energy region, they have opposite signs. As the energy increases, the peak positions in σ_{2xy} do not agree. When compared with the experimental values, σ_{2xy} with the $d \rightarrow f$ and $f \rightarrow d$ transitions turned on shows worse agreement. The sign at lower energy is incorrect. This is not a surprising result when we consider that the unoccupied 4f states stay too close to the Fermi energy, while they should stay at least 3 eV above it. We therefore turned off the d-to-f and f-to-d interband transitions in the calculation to remove the incorrect f contributions to σ_{2xy} due to the wrong 4f states in the electronic structure of $TbFe_2$. The dotted line in Fig. 9.5 shows the theoretical σ_{2xy} without f transitions. As shown in Fig. 9.1, the spectra with f transitions increase as the energy decreases below 2.0 eV, while that without f transitions decrease. This tendency of decreasing spectra below 2.0 eV seems to agree with experimental data except for the small magnitude. But still the theoretical spectra without f-to-d and d-to-f transitions above 2.0 eV do not agree with the experimental data. The experimental σ_{2xy} shown in Fig. 9.4 shows a positive broad peak with a magnitude of $0.27 \times 10^{14} sec^{-1}$ between 4.0 eV and 5.0 eV, while the theoretical spectrum shown in Fig. 9.5 shows negative flat values of σ_{2xy} with a magnitude of $-0.3 \times 10^{14} sec^{-1}$ between 3.5 eV to 5.0 eV. Hence the removal of f transitions does not work well. The experimental broad peak in σ_{2xy} between 4.0 eV to 5.0 eV with the center located at 4.5 eV is expected to come from d-to-f interband transitions. This expectation is quite natural if we consider the location of unoccupied 4f states and 5d bands of rare earths. The 5d electrons in the rare earth metals form broad bands around the Fermi energy. If we assume the unoccupied 4f states are located about 4.0 eV above the Fermi energy, then the occupied 5d states below the Fermi energy could be initial states and the unoccupied 4f states could be final states in interband transitions. From the inverse X-ray

photoemission spectra of amorphous $Tb_{0.21}Fe_{0.79}$, the peak of the 4f electron spectral weight of Tb is at 4.0 eV. The location of the 4f states of the crystalline $TbFe_2$ may not be much different from that of amorphous $Tb_{0.21}Fe_{0.79}$. Therefore the peak at 4.5 eV in σ_{2xy} could be explained with the above analysis. Actually, the involvement of 4f states of RFe_2 intermetallic compounds in the MOKE has been suggested by many authors. Katayama and Hasegawa suggested that the big negative Kerr rotation peaks between 4.0 eV and 5.0 eV in polycrystalline RFe_2 compounds are due to interband transitions between 4f and 5d states of rare-earth atoms, from the studies of Gd by Erskine [29]. Mukimov *et al.* [101] have measured magneto-optical equatorial spectra of RFe_2(R=Gd, Tb, Dy, Ho, and Er) prepared by arc melting. From the analysis of their equatorial Kerr effect data, they found a significant difference in the joint density of states among the RFe_2 intermetallic compounds. This difference can not be explained by the 5d bands, whose variations are small in the rare-earth series. Therefore they suggested the rare-earth 4f electrons are involved in the spectra. Tanaka and Takayama [130] estimated the contributions to the Kerr effects of $Nd_{0.2}Fe_{0.8}$ amorphous alloy from d-to-f transitions and p-to-d transitions by following the argument of Erskine and Stern. They found the d-to-f transitions were expected to be about 50 times larger than that of the p-to-d transitions.

Magneto-optical properties of $HoFe_2$

Similarly to $TbFe_2$, we measured Kerr rotation and ellipticity of $HoFe_2$ at different temperatures and different magnetic fields. Figure 9.9 shows the Kerr rotation and ellipticity of single crystal of $HoFe_2$ measured at 7K, 295K and 0.5T, 1.6T respectively. The negative peak position appeared at 3.7 eV for both samples. The absolute magnitude of the peak Kerr rotation of polycrystalline $HoFe_2$ measured with an applied magnetic field of 1.2T by [92] is only 0.17 °. Compared to that, the absolute magnitude of the

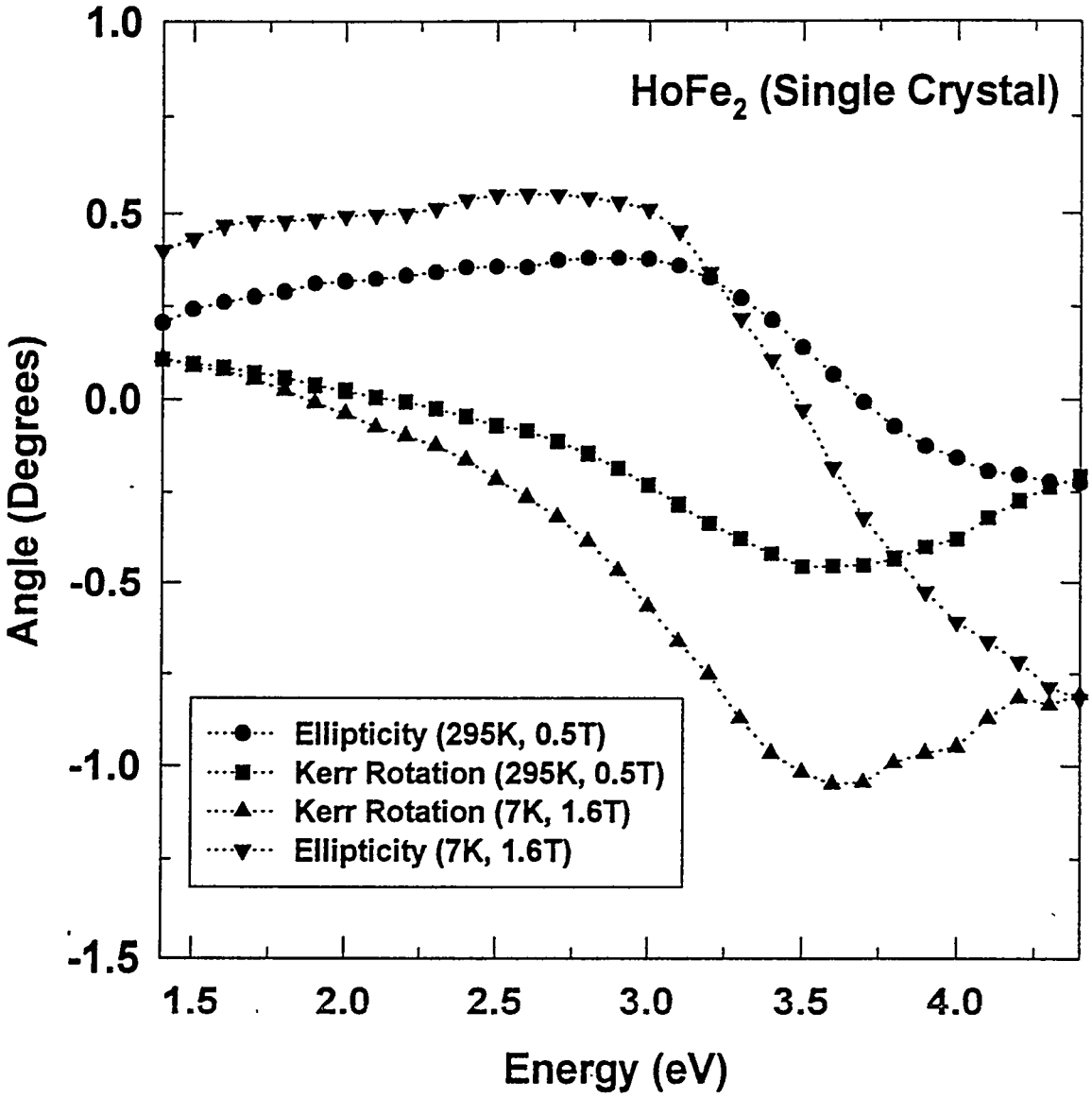

Figure 9.9 The Kerr rotation of single crystal $HoFe_2$ measured at different temperatures and applied magnetic fields. Solid circle and solid square stand for the ellipticity and Kerr rotation measured at the temperature of 295K and with the applied magnetic field of 0.5T. Solid triangle up and solid triangle down represent the Kerr rotation and ellipticity measured at the temperature of 7K and with the applied magnetic field of 1.6T.

peak Kerr rotation of the single crystal of $HoFe_2$ is 1.1°, 6 times larger than that of [92]. Even with an applied magnetic field of 0.5T, the peak Kerr rotation is larger than that of [92]. This comes from the reasons discussed in the $TbFe_2$ section. But the peak position of $HoFe_2$ measured by them is shifted to higher energy by 0.3 eV than ours. This difference might come from the effect of oxidation on the surface of the sample, but this needs to be studied carefully. As shown in Fig. 9.10, magnetic fields of 0.5T and 1.6T will align the magnetic moments of $HoFe_2$ to more than 70% and 90% of the saturated magnetic moments at 300K and 5K respectively.

We calculated the electronic structure and density of states of $HoFe_2$ to investigate the role of f electrons in the magneto-optical effects. For this calculation, the TB-LMTO method with LDA is employed. Figure 9.11 shows the calculated spin-polarized total density of states (DOS) for $TbFe_2$ using the TB-LMTO including spin-orbit interaction. Figures 9.12 and 9.13 show the calculated spin-polarized total density of states (DOS) for Tb and Fe using the TB-LMTO including spin-orbit interaction respectively.
The partial density of spin down 4f states of Ho in $HoFe_2$ is located at the Fermi energy. Even though the experimental density of states for bulk $HoFe_2$ is not available as far as we know, we can expect the unoccupied density of 4f states to be located around 2.0 eV above the Fermi energy because the 4f states in Tb metal are located 2.0 eV above the Fermi energy, if we assume hybridization of the 4f states with the conduction electrons is negligible in $HoFe_2$. The incorrect positions for the 4f states may affect the theoretical calculation of magneto-optical Kerr effects because the correct interband transitions require an accurate band structure. The experimental σ_{1xy}, σ_{2xy}, and $\omega\sigma_{2xy}$ values for single crystals of $HoFe_2$ are obtained from the experimental Kerr rotation and ellipticity measured at room temperature with an applied magnetic field of 0.5T, and optical constants measured at room temperature with no magnetic field applied. We calculated the imaginary part of the off-diagonal optical conductivity of $HoFe_2$ using the band structure obtained with the LDA. In Fig. 9.15, the solid line represents σ_{2xy}

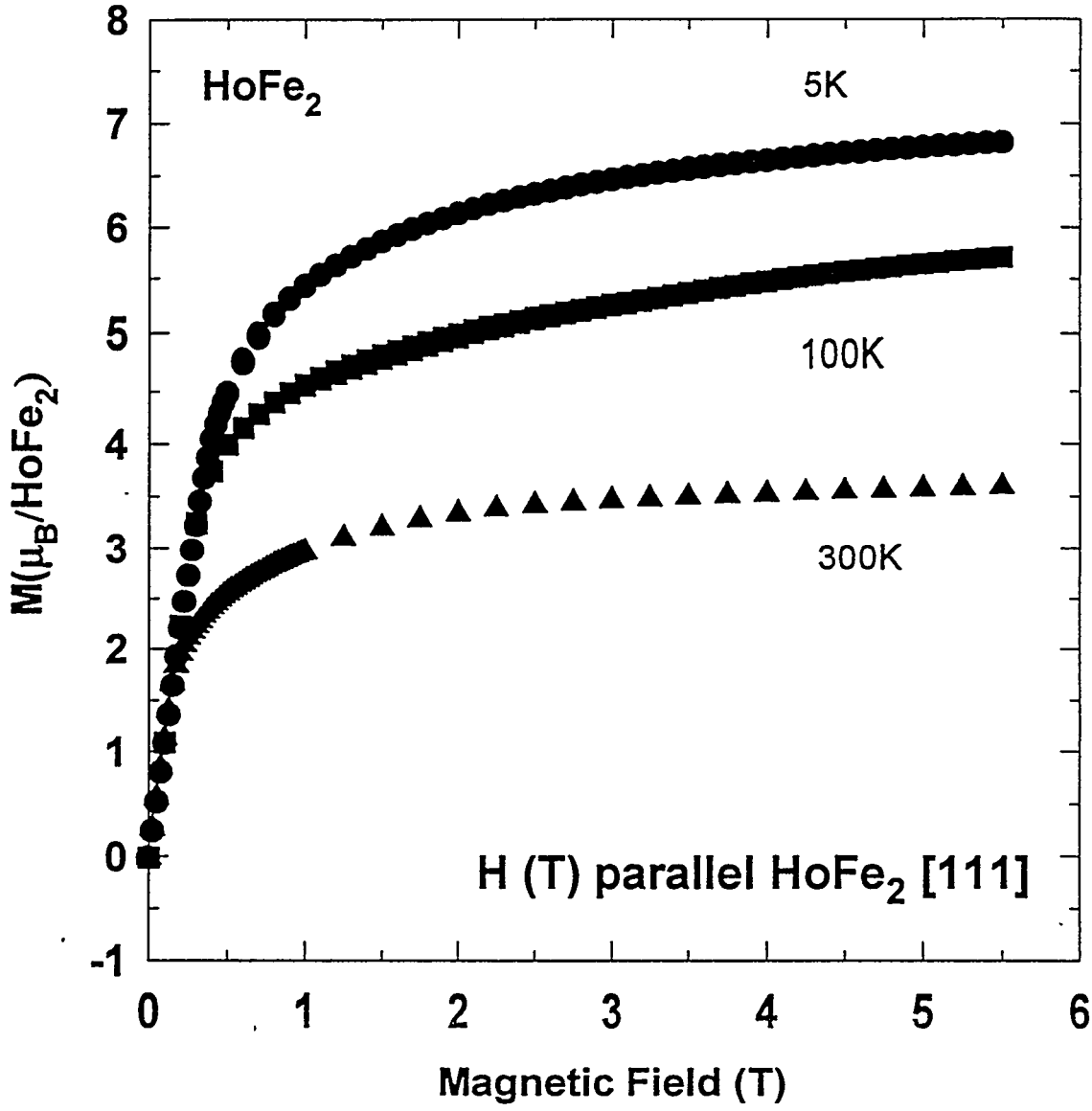

Figure 9.10 Magnetization measurements of $HoFe_2$ at 5K, 100K, and 300K.

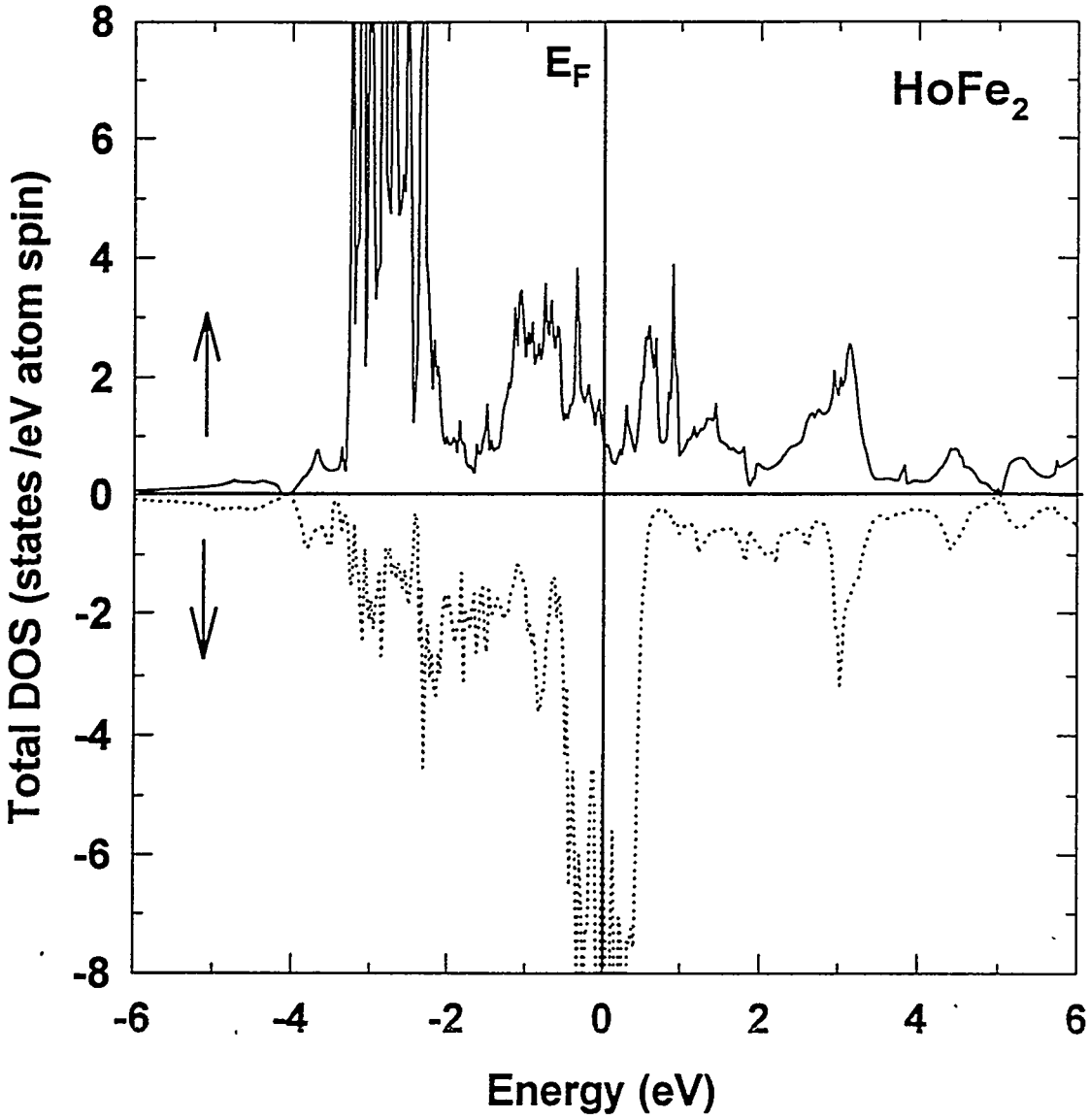

Figure 9.11 Calculated spin-polarized total density of states (DOS) for $HoFe_2$ using the TB-LMTO including spin-orbit interaction.

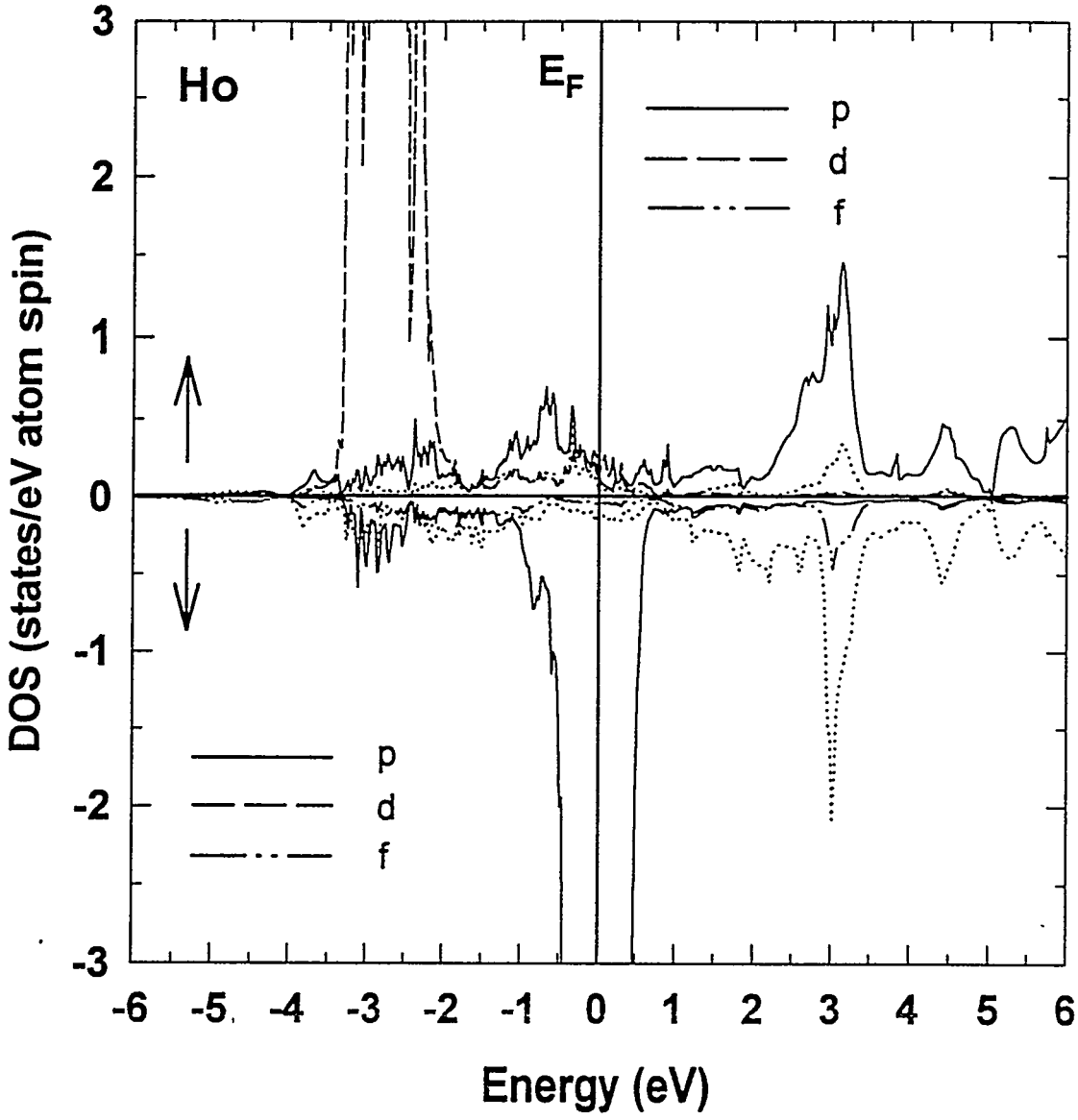

Figure 9.12 Calculated spin-polarized partial density of states (DOS) for Ho using the TB-LMTO including spin-orbit interaction.

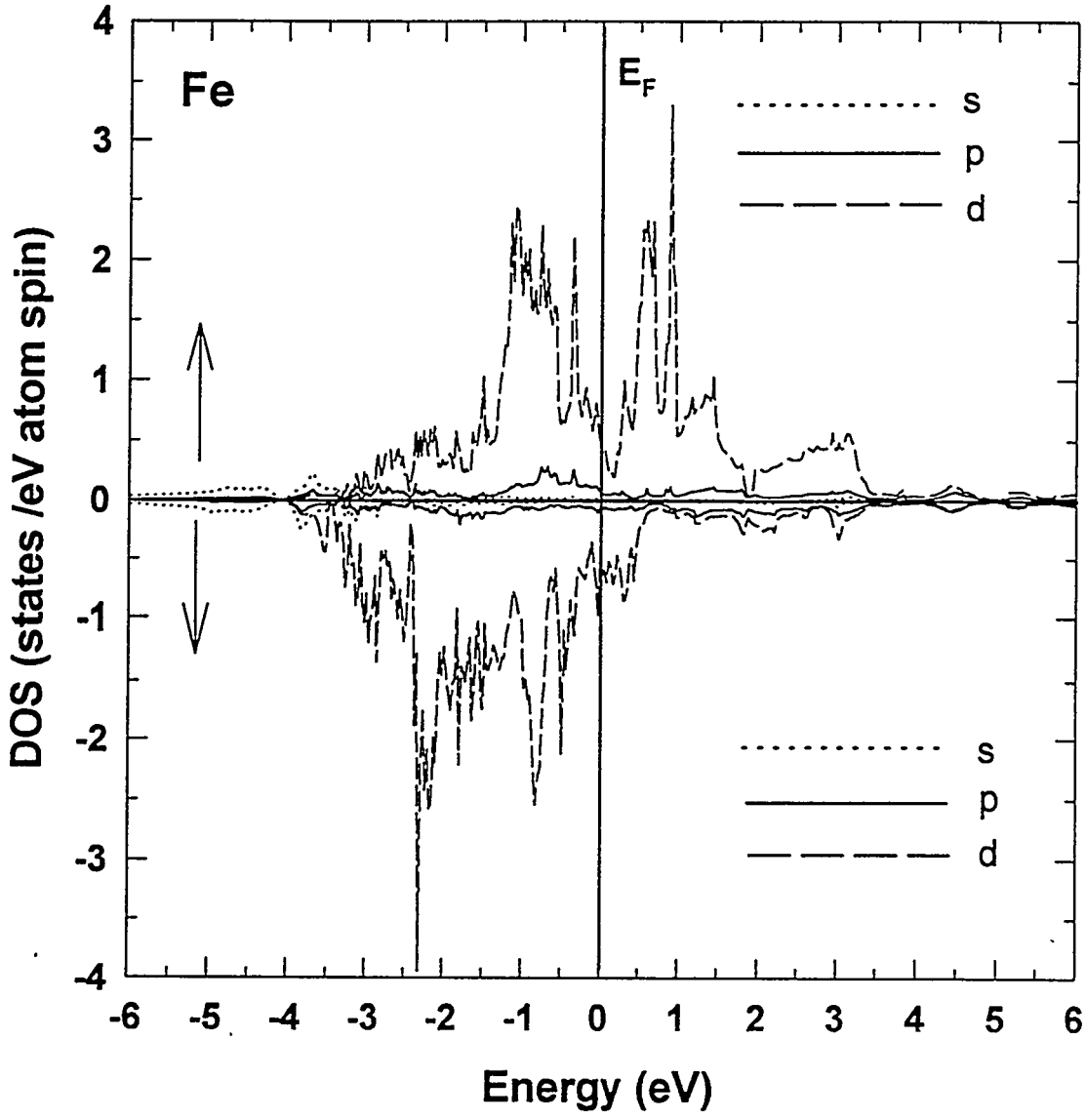

Figure 9.13 Calculated spin-polarized partial density of states (DOS) for Fe using the TB-LMTO including spin-orbit interaction.

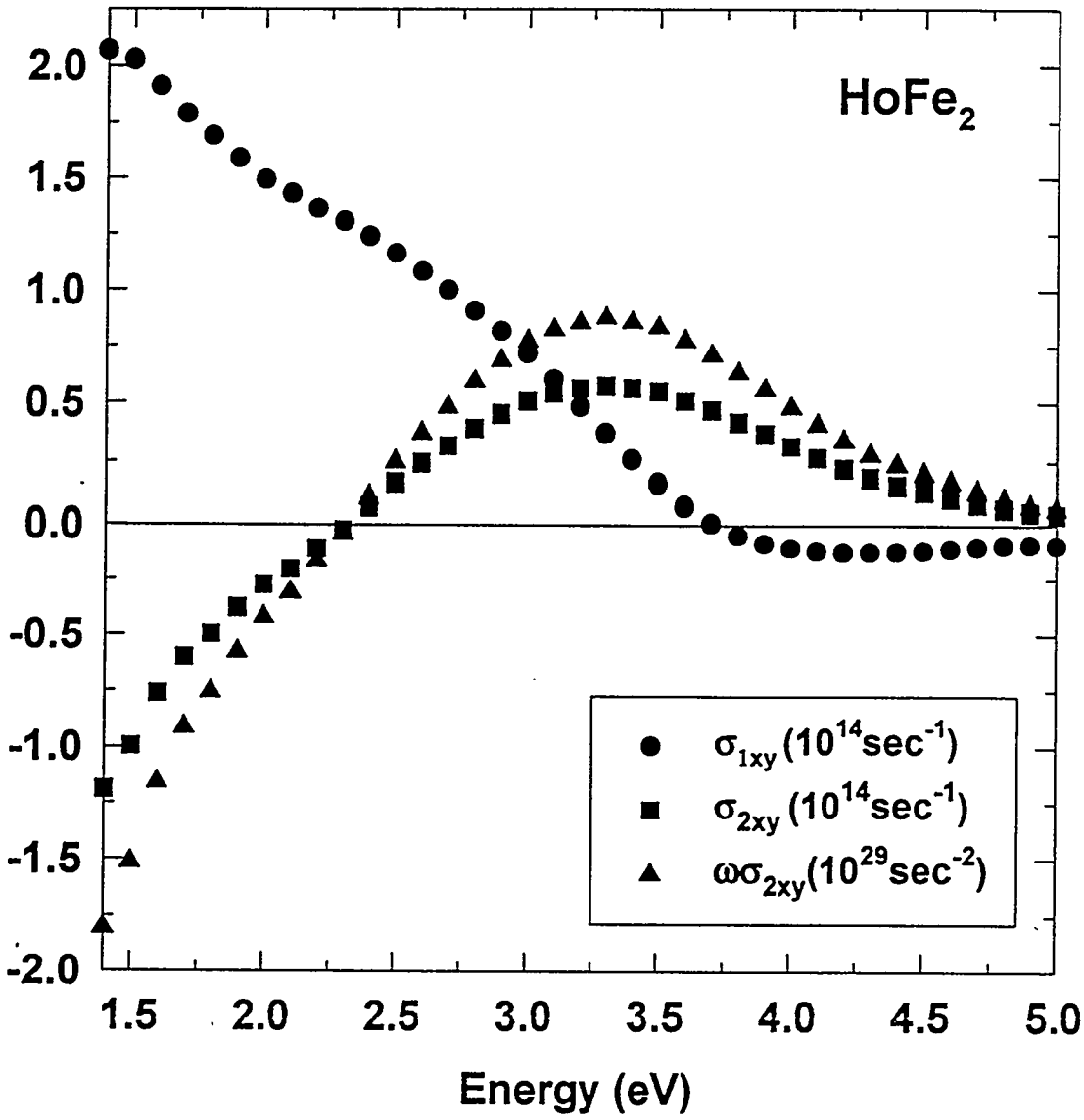

Figure 9.14 The experimental σ_{1xy}, σ_{2xy}, and $\omega\sigma_{2xy}$ values for single crystals of $HoFe_2$ from experimental Kerr rotation and ellipticity measured at room temperature with an applied magnetic field of 0.5T and optical constants measured at room temperature with no magnetic field applied.

with d-to-f and f-to-d interband transitions included. The dotted line represents σ_{2xy} with d-to-f and f-to-d interband transitions not included. The experimental spectrum of σ_{2xy} has a big broad peak at 3.25 eV and a weak peak at 1.8 eV. In the theoretical calculation of σ_{2xy} shown in Fig. 9.15, the two cases are quite different. The calculated spectra with f states involved (solid line), the peak at 3.2 eV is opposite in sign to that of the experimental spectrum and it does not agree with the experimental data. That is, the LDA theory which describes the ground-state properties of materials can not treat well the many body effects of the f electron system. When we remove the f-to-d and d-to-f interband transitions, the spectrum of σ_{2xy} is reduced considerably and it does not agree at all with the experimental σ_{2xy}. This indicates that the peak of σ_{2xy} of $HoFe_2$ may involve the f states in σ_{2xy}. While the σ_{2xy} of the rare-earth are not handled correctly by LDA due to the stronly correlated 4f electrons, the σ_{2xy} of transition metals are treated reasonably well by LDA. This is because in transition metals, the correlation effects are not so strong enough not to use one-electron approximation theory.

Conclusions

It has been shown in this chapter that magneto-optical data combined with ellipsometry data can be used for determining the 4f electron involvement in optical interband transitions. We tried to explain the MOKE effects of $TbFe_2$ and $HoFe_2$ using the TB-LMTO with LDA theory. The theoretical σ_{2xy} does not agree with the experimental σ_{2xy} for both $TbFe_2$ and $HoFe_2$. This comes from the fact that the LDA produces the positions of 4f states too close to the Fermi level due to the lack of incorporating many-body effects of the 4f electron system. To remove the wrong contributions from the f states, we turned off the interband f-to-d and d-to-f transitions. The results show quite different features than those of results with f contributions included. The magnitude and shape of the σ_{2xy} spectra changed considerably. This means that in theory the f electrons take

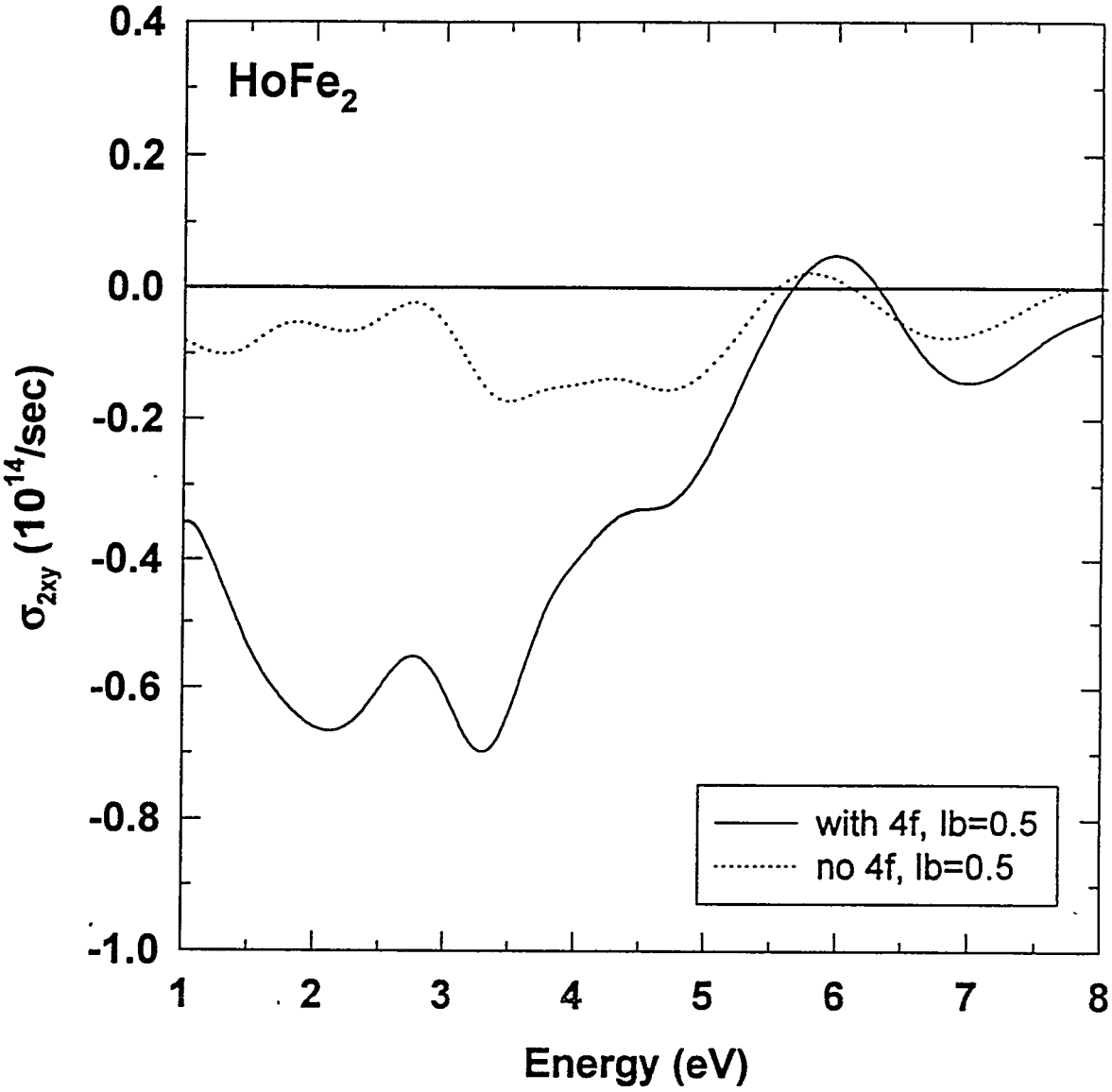

Figure 9.15 Theoretical σ_{2xy} of $HoFe_2$ calculated using TB-LMTO based on LDA. The solid line represents the σ_{2xy} with d-to-f and f-to-d interband transitions are included. The dotted line represents the σ_{2xy} with d-to-f and f-to-d interband transitions are not included. For both calculations, a constant lifetime broadening parameter of 0.5 eV is used.

part in the optical transitions actively. The results without f electron involvement seem better, but still agreement with experimental values are poor. We need a theory which can predict the 4f states well because we found the f electrons participate in the σ_{2xy}. The correct 4f positions are important for producing the correct theoretical spectrum of σ_{2xy}. We found that single crystals grown by the flux method produce superior experimental data compared to the polycrystalline samples. In developing new materials which contain f electrons for magneto-optical storage media, the study of f electrons systematically is important due to their important roles in the magneto-optical effects.

10 CONCLUSIONS

Magneto-optical polar Kerr spectroscopy (MOPKS) was developed for studying the magneto-optical properties of magnetic materials. We have grown single crystals of rare-earth transition (RT) intermetallic compounds by the flux method. The samples have been measured between 5K-295 K under applied magnetic fields of up to 1.6 T. We also have measured the optical constants of these samples using a spectroscopic ellipsometer. By combining the magneto-optical parameters (Kerr rotation and ellipticity) and the optical constants, we can obtain the off-diagonal optical conductivity. The absorptive part of the off-diagonal optical conductivity (σ_{2xy}) can be compared directly with the theoretical σ_{2xy} obtained from electronic structure calculations of the magnetic materials. The comparison of σ_{2xy} between experiment and theory can be a test of the validity and accuracy of the theory. In the case of $LuFe_2$ in which the 4f states are fully occupied, the theoretical and experimental values of the magneto-optical parameters and the off-diagonal optical conductivity agree well with each other. But for other RFe_2 and $GdCo_2$ samples where the 4f states are not fully occupied, the 4f electrons are actively involved in the magnetic properties and electronic properties of the samples. The diagonal parts of the optical conductivity which arise primarily from interband transitions between s and p bands, and p and d bands, due to their large dipole matrix elements, can not discriminate well the parts of the electronic structure arising from the f electrons. Figure 10.1 shows this argument clearly. We measured the absorptive part of the optical conductivity(σ_{1xx}) of RFe_2 (R=Ho, Tb, Gd, and Lu) and $GdCo_2$ compounds. As shown in Fig. 10.1, all of the samples have very similar features in σ_{1xx}, broad peaks

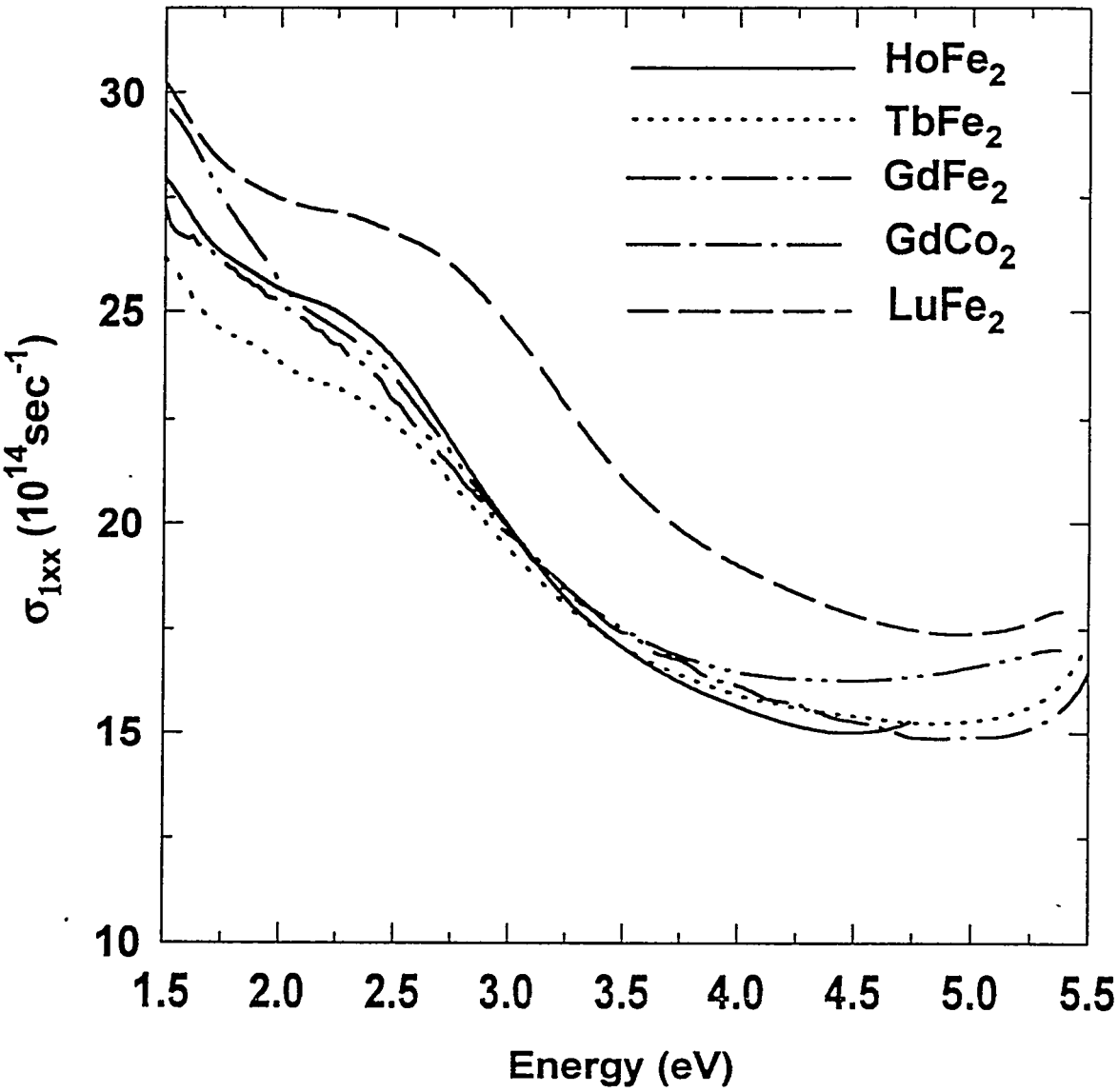

Figure 10.1 Real parts of the diagonal optical conductivity for $HoFe_2$, $TbFe_2$, $GdFe_2$, $GdCo_2$, and $LuFe_2$ single crystals measured at room temperature.

in the energy range of 2.0 eV and 3.25 eV. When we consider the different number of 4f electrons among the RT_2 compounds and different magnetic properties of these materials, ellipsometry measurements can not give enough information to discriminate the different properties of these magnetic materials. Compared to these ellipsometry data, the absorptive part of the off-diagonal optical conductivity, which is directly related to the magneto-optical paramters shown in Fig. 10.2, shows quite diverse features. First, σ_{2xy} of $LuFe_2$ is positive at low energies while those of other samples are negative. This can be explained from the magnetic properties of RFe_2 compounds. In the case of $LuFe_2$, the magnetic moments are dominated by Fe because the 4f states of Lu are fully occupied. Therefore the magnetic moments of Fe are aligned parallel to the applied external magnetic fields. The magnetic moments of the other RFe_2 samples are dominated by rare earths. σ_{2xy}, which is related to Kerr rotation and ellipticity by Eq. (3.43), has generally the opposite sign to that of Kerr rotation. For $LuFe_2$, which has a negative Kerr rotation at lower energies due to the dominant Fe character, the sign of σ_{2xy} is positive. The magnetic moments are ordered ferrimagnetically in RFe_2 and $GdCo_2$ and the magnetic moments of the rare earths are dominant except $LuFe_2$. Therefore the magnetic moments of the rare earths are aligned parallel to the applied magnetic field and the magnetic moment of Fe is aligned anti-parallel to the applied magnetic field. This means that the Kerr rotation in RFe_2 contributed by the Fe character is opposite in sign to that of elemental Fe due to the ferrimagnetic properties of RFe_2. σ_{2xy} discriminates in favor of the optical properties originating from different magnetic properties of magnetic materials. Second, σ_{2xy} of $GdFe_2$ and $GdCo_2$ are quite different. They have different transition metals. The differences arise from different exchange splitting and different strengths of the hybridization between Gd and Fe or Co. Third, the positions of the broad peaks in σ_{2xy} in $HoFe_2$, $TbFe_2$ and $GdFe_2$ are different. In the case of σ_{1xx}, the peaks are located around 2.5 eV. But in σ_{2xy}, the peaks located in the higher energy region are between 3.2 eV and 4.5 eV. The different peak positions among $GdFe_2$ and

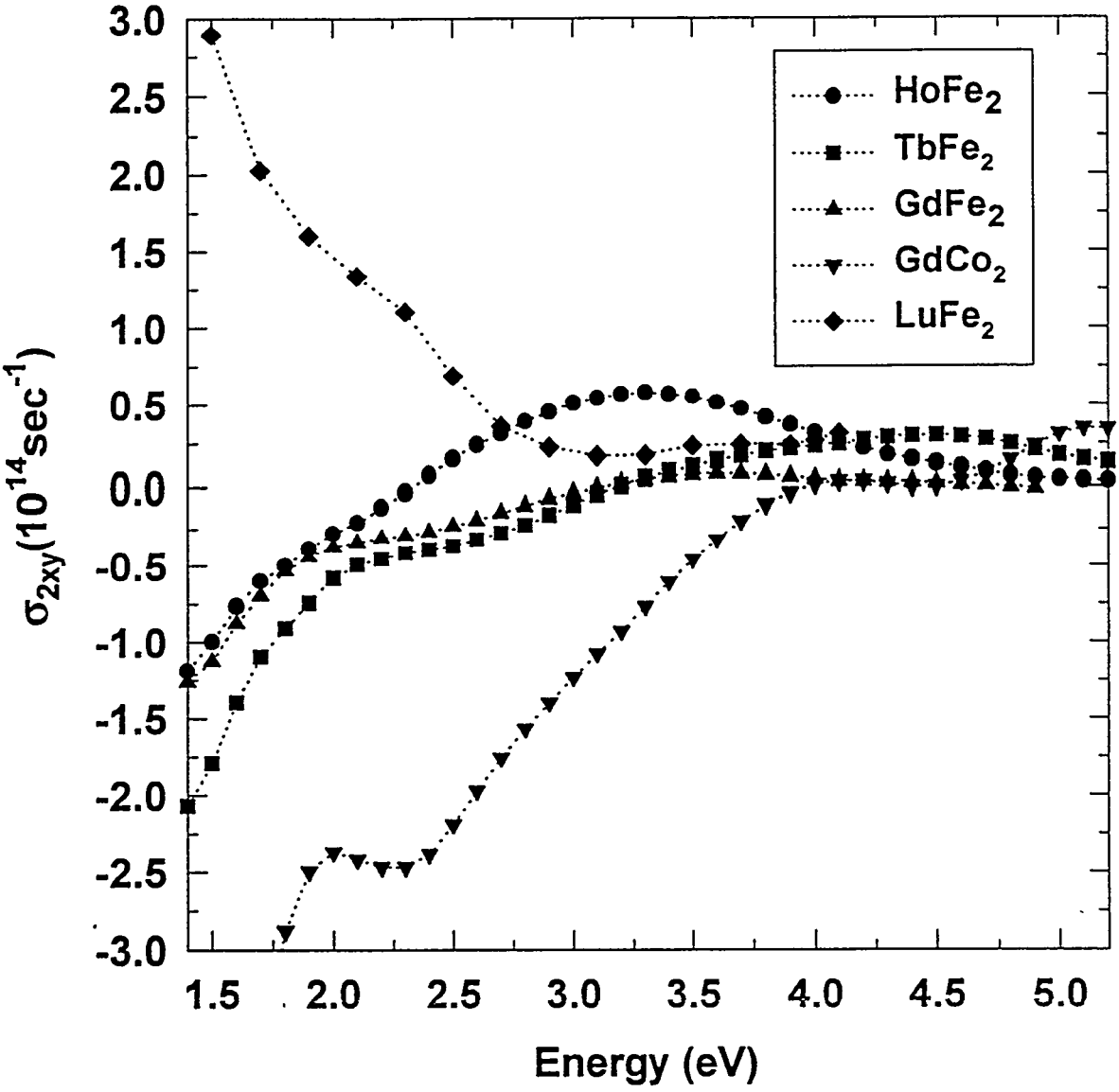

Figure 10.2 The experimental σ_{2xy} values of single crystal of $HoFe_2$, $TbFe_2$, $GdFe_2$, $GdCo_2$, and $LuFe_2$ single crystals from experimental Kerr rotation, ellipticity measured at room temperature with an applied magnetic field of 0.5T and optical constants messured at room temperature with no magnetic field applied.

$HoFe_2$, $TbFe_2$ could be caused by different positions of the unoccupied 4f states of the rare earths relative to the Fermi energy. The exchange-correlation energy splitting Δ_{ex} is largest for Gd and decreases as the number of 4f electrons increases [110]. On the contrary, the spin-orbit splitting Δ_{so} increases as the number of 4f electrons increases [110]. Because Fe is the common element in RFe_2 compounds, the different magnitudes of σ_{2xy} related to MOKE may be related to the different magnitudes of the spin-orbit coupling in rare-earths. The magnitude of the spin-orbit coupling increases from Gd, Tb, to Ho while that of exchange splitting decreases. The magnitudes of the peaks of σ_{2xy}, as shown in Fig. 10.2 in the higher energy region where the 4f electrons are expected to be involved in the MOKE, when we consider the positions of occupied and unoccupied of 4f states with respect to the Fermi energy, increase from $GdFe_2$, $TbFe_2$, $HoFe_2$, consistent with the expectation. Katayama [92] argued that the absolute magnitudes of the peak Kerr rotations in RFe_2 decrease with increasing 4f electron count and the absolute magnitude of the peak Kerr rotation of $TbFe_2$ is two times bigger than that of $HoFe_2$. The above measurements by them are contrary to the fact that the MOKE has a linear dependence on the strength of the spin-orbit interaction parameter [33]. The spin-orbit coupling of Ho is larger than that of Tb [110]. Therefore we expect MOKE to be bigger in $HoFe_2$. As shown in Fig. 10.2, the magnitude of the peak of σ_{2xy} of $HoFe_2$ is larger than that of $TbFe_2$. The Kerr rotation of $HoFe_2$ measured at 295 K in 0.5 T, shown in Fig. 9.9, is similar to that of $TbFe_2$ shown in Fig. 9.1, unlike the measurement of Katayama. The difference arises because they used polycrystalline samples while we have used single crystal samples. The MOKE, which gives the basic principle for the magneto-optical recording method, can be manifested best by single crystals for several reasons, as mentioned in Chapter 9. The effects of oxidation on the diagonal part of the optical conductivity were considered using a three-phase model. The oxidation effects on the magneto-optical parameters were also considered by treating the oxide layer as a nonmagnetic thin transparent layer for both single-crystal and polycrystal samples. It

is found that the corrections change, especially the high-energy region, not only in the magnitude but also in the shape of the optical conductivity and the magneto-optical parameters. This result is reasonable when we consider the penetration depth of UV light is much smaller than that of IR light, so the UV spectral region may be more easily affected by surface contamination like oxidation. From Fig. 6.6, the correction on the Kerr rotation spectrum of $GdCo_2$ in the UV due to oxidation is larger than the correction in the visible.

APPENDIX

SAMPLE CHANGE

1) Stop liquid helium transfer to the sample tube.

2) Close the valve of the mechanical pump attached through the vapor pumping port to the sample tube.

3) Turn off the mechanical pump.

4) Over pressurize (2-3 psi) the sample tube with He gas.

5) Remove the clamp attached on the sample positioner.

6) Take out the positioner from the top of the cryostat carefully to avoid bending it.

7) Install a sealable blank cap on the top of the sample zone.

8) Replace the old sample holder with the new aligned sample holder by unscrewing the old one and screwing on the new sample holder.

9) After replacing the sample, the positioner should be fully dried by LN_2 gas to prevent moisture freezing in the sample tube.

10) When ready, remove the blank cap and re-insert the sample positioner with the new sample.

11) The front face of the sample holder should go down the sample tube as parallel as possible to the outside window of the cryostat to prevent scratching the inside window.

12) Clamp the sample positioner.

Caution

1) Do not remove the sample while the temperature is less than 4.2K or the sample tube pressure is less than an atmosphere.

2) Make sure that you closed the mechanical pump valve before opening the sample tube.

3) During the time the sample positioner is removed from the cryostat, the flow of helium gas (2-3 psi) to the sample tube should be maintained: This will prevent freezing of air in the sample tube.

REFERENCE LIST

[1] A.B. Marchant in *Optical Recording,* (Addison-Wesley, New York 1990).

[2] M. Faraday, Philos. Trans. R. Soc. London **136,** 1 (1846).

[3] J. Kerr, Philos. Mag. **3,** 321 (1877).

[4] P. Chaudhari, J.J. Cuomo, and R.J. Gambino, Appl. Phys. Lett. **22,** 337 (1973).

[5] P. Fumagalli, J. Schoenes, M. Decroux, and O. Fischer, J. Appl. Phys. **67,** 5035 (1990).

[6] K. Sato,Jpn. J. Appl. Phys. **20,** 2403 (1981).

[7] K. Sato, H. Hongu, H. Ikekame, Y. Tosaka, M. Watanabe, K. Takanashi, and H. Fujimori, Jpn. J. Appl. Phys. **32,** 989 (1993).

[8] R. W. Wood, *Physical Optics*, 3d ed., Macmillan, New York, 1934, pp. 356-361.

[9] R. W. Ditchburn, Light, 2d ed., Interscience, New York, 1963*b*, pp. 483-485.

[10] PEM-80 Photoelastic Modulator Systems (Hinds International).

[11] GCA/McPHERSON Instrument.

[12] R.M.A. Azzam and N.M. Bashara, *Ellipsometry and Polarized Light* (North-Holland, Amsterdam, 1977).

[13] URM80ACC with MM2000 controller, Newport Corporation.

[14] Hamamatsu Corporation.

[15] Spectrogon Corporation.

[16] Melles Griot Corporation.

[17] Model 13CC-724-ECO Liquid Helium Dewar, Cryo Industries of America, Inc.

[18] D.E. Aspnes and A.A. Studna, Appl. Opt. **14**, 220 (1975).

[19] J. Y. Rhee, Ph. D. Thesis, Iowa State University, 1992.

[20] P. N. Argyres, Phys. Rev. **97**, 334 (1955).

[21] H. S. Bennett, E. A. Stern, Phys. Rev. **137**, A448 (1965).

[22] M. J. Freiser, IEEE Trans. Magn. MAG-4, 152 (1968).

[23] P. S. Pershan, J. Appl. Phys. **38**, 1482 (1967).

[24] J. C. Suits, IEEE Trans. Magn. MAG-8, 95 (1972).

[25] R. Atkinson, and P. H. Lissberger, Appl. Opt. **31**, 6076 (1992).

[26] L. M. Roth, Phys. Rev. **133**, 542 (1964).

[27] S. E. Schnatterly, Phys. Rev. **183**, 664 (1969).

[28] E. D. Palik, S. Teitler, B. W. Henvis, and R. F. Wallis, Proc. Int. Conf. on Physics of Semiconductors, Exeter (1962).

[29] J. L. Erskine and E. A. Stern, Phys. Rev. B **8**, 1239 (1973).

[30] W. Reim, O. E. Hüsser, J. Schoenes, E. Kaldis, P. Wachter, K. Seiler, J. Appl. Phys. **55**, 2155 (1984).

[31] X. D. Wang, Ph.D thesis, Iowa State University, (1994).

[32] R. Kubo, J. Phys. Soc. Jpn. **12**, 570 (1957).

[33] D. K. Misemer, J. Magn. Magn. Mater. **72**, 267 (1988).

[34] C. M. Schneider, M. S. Hammond, P. Schuster, A. Cebollada, R. Miranda, and J. Kirschner, Phys. Rev. B **44**, 12066 (1991).

[35] S. J. Youn, and B. I. Min, Phys. Rev. B **51**, 10436 (1995).

[36] T. M. Holden, W. J. L. Buyers, and H-G. Purwins, J. Phys. F: Met. Phys. **14**, 2701 (1984).

[37] W. E. Pickett, and B. M. Klein, J. Less-Common Metals **03**, 219 (1983).

[38] T. Jarlborg, and A.J. Freeman, J. Magn. Mag. Mater. **60**, 291 (1986).

[39] K.J. Kim, and D.W. Lynch, J. Phys.: Condens. Matter **5**, 5971(1993).

[40] B. I. Min, H. J. F. Jansen, T. Oguchi, and A. J. Freeman, J. Magn. Magn. Mater. **59**, 277 (1986).

[41] S. B. M. Hagström, P. O. Heden, and H. Löfgren, Solid State Commun. **8**, 1245 (1970).

[42] O. Madelung, *Introduction to Solid-State Theory* (Springer-Verlag, Berlin 1981).

[43] B. I. Min, H. J. F. Jansen, T. Oguchi, and A. J. Freeman, J. Magn. Magn. Mater. **61**, 139 (1986).

[44] T. A. Tibbetts, and B. N. Harmon, Solid State Commun. **10**, 1409 (1982).

[45] B. I. Min, T. Oguchi, H. J. F. Jansen, and A. J. Freeman, Phys. Rev. B **15**, 654 (1986).

[46] K. H. J. Buschow, Rep. Prog. Phys. **40**, 1179 (1977).

[47] K. H. J. Buschow, *Ferromagnetic Materials*, Vol. 4, 493 (1988).

[48] G. Kaindl, B. Reihl, D. E. Eastman, R. A. Pollak, N. Martensson, B. Barbara, Solid State Commun. **41**, 157 (1982).

[49] A. Iandelli, and A. Palenzona, J. Less-Common Metals **29**, 293 (1972).

[50] S.-J. Oh, J.W. Allen, M.S. Torikachvili and M.B. Maple, J. Magn. Mag. Mater. **52**, 183 (1985).

[51] *Binary Alloy Phase Diagrams*, 2d ed., edited by T. B. Massalaski, The Materials Information Society (1992).

[52] U. von Barth, and L. Hedin, J. Phys. **C5**, 1629 (1972).

[53] E. A. Irene, Thin Solid Films **233**, 96 (1993).

[54] T. D. Burleigh, S. Wagner, and T. F. Ciszek, Solar Cells **13**, 179 (1984).

[55] P. J. McMarr, K. Vedam, and J. Narayan, J. Appl. Phys. **59**, 694 (1986).

[56] J. F. McGilp, D. Weaire, C. H. Patterson (eds.), Epioptics, Linear and Nonlinear Optical Spectroscopy of Surfaces and Interfaces (Springer-Verlag, Berlin 1995).

[57] W. H. Press, B. P. Flannery, S. A. Teukolskey, and W. T. Vetterling, Numerical Recipes in C, Cambridge University Press, Cambridge, (1988).

[58] D. A. G. Bruggemann, Ann. Phys. (Leipzig) **24**, 636 (1935).

[59] J.Y. Rhee, X. Wang, B.N. Harmon, and D.W. Lynch, Phys. Rev. B **51**, 17390 (1995).

[60] K. A. Gschneidner, Jr, *Specialty Inorganic Chemicals*, The Royal Society of Chemistry, London (1981).

[61] A.I. Shelykh, A.V. Prokof'ev, and B.T. Melekh, Phys. Solid State **38 (2)**, 236 (1996).

[62] K. Zukowska, Doctor's thesis, Technical University of Wroclaw, Wroclaw, 1975.

[63] K. Zukowska, and E. Oleszkiewicz, Thin Solid Films **224**, 217 (1993).

[64] A. K. Burnham, and G. T. Jameson, J. Vac. Sci. Technol. A **5(4)**, 1713 (1987).

[65] T. Marcinow, Doctor's thesis, Technical University of Wroclaw, Wroclaw, 1975.

[66] A. C. Gossard, V. Jaccarino, and J. H. Wernick, Phys. Rev. **133A**, 881 (1964).

[67] R. E. Hungsberg, and K. A. Gschneidner, Jr., J. Phys. Chem. Solids **33**, 401 (1972).

[68] F. U. Hillebrecht, M. Campagna, *Handbook on the Physics and Chemistry of Rare Earths*, Vol. 10, edited by K. A. Gschneidner, Jr., L. Eyring and S. Hüfner, (Elsevier Science Publishers B. V. 1987) Chapter 70.

[69] B.I. Min, T. Oguchi, H.J.F. Jansen, and A.J. Freeman, Phys. Rev. B **34**, 654 (1986).

[70] P. C. Canfield, and Z. Fisk, Phil. Mag. B **65**, 1117 (1992).

[71] B. K. Cho, Ph.D thesis, Iowa State University, (1995).

[72] S. K. Bose, K. Winer, and O. K. Andersen, Phys. Rev. B **37**, 6262 (1988).

[73] H. C. Skriver, The LMTO Method (Springer, New York, 1984).

[74] R. A. Butera, T. J. Clinton, A. G. Moldovan, S. G. Sankar, and K. A. Gschneidner, J. Appl. Phys. **50**, 7492 (1979).

[75] H. Yamada, and M. Shimizu, J. Phys. F:Met. Phys. **16**, 1039 (1986).

[76] E. Belorizky, M.A. Fremy, J.P. Gavigan, D. Givord, and H.S. Li, J. Appl. Phys. **61**, 3971 (1987).

[77] D. Givord, A.R. Gregory, and J. Schweizer, J. Magn. Mag. Mater. **15-18**, 293 (1980).

[78] Y. Kasamatsu, J.G.M. Armitage, J.S. Lord, P.C. Riedi, and D. Fort, J. Magn. Mag. Mater. **140-144**, 819 (1995).

[79] M. S. S. Brooks, O. Eriksson, and B. Johansson, J. Phys.: Condens. Matter **1**, 5861 (1989).

[80] H. M. Petrilli and S. Frota-Pessôa, J. Alloys and Compounds **225**, 465 (1995).

[81] S. S. Jaswal, D. J. Sellmyer, M. Engelhardt, Z. Zhao, A. J. Arko, and K. Xie, Phys. Rev. B **35**, 996 (1987).

[82] J. C. Slater, Adv. Quantum Chem. **6**, 1 (1972).

[83] V. P. Antropov, A. I. Liechtenstein, B. N. Harmon, J. Magn. Magn. Mater. **140-144**, 1161 (1995).

[84] A. I. Liechtenstein, V. P. Antropov and B. N. Harmon, Phys Rev. B **49**, 2556 (1994).

[85] S. Savrasov and D. Savrasov, Phys. Rev. B **46**, 12181 (1992).

[86] I. S. Dubenko, R. Z. Levitin and A. S. Markosyan, J. Magn. Magn. Mater. **146-148**, 111 (1992).

[87] K. H. J. Buschow and A. S. van Der Goot, J. Less-Common Metals **17**, 249 (1969).

[88] R. M. Moon, W. C. Koehler and J. Farrell, J. Appl. Phys. **36**, 978 (1965).

[89] D. Gignoux, F. Givord and R. Lemaire, Phys. Rev. B **12**, 3878 (1975).

[90] K. Fujiwara, K. Ichinose, and A. Tsujimura, J. Phys. Soc. Japan **56**, 2149 (1987).

[91] T. Katayama and T. Shibata, J. of Crystal Growth **24-25**, 396 (1974).

[92] T. Katayama and K. Hasegawa, Proc. 4th Int. Conf. on Rapidly Quenched Metals 915, Sendai, (1981).

[93] T. Katayama and T. Shibata, J. Magn. Magn. Mater. **23**, 173 (1981).

[94] UGIMAG, 405 Elm St., Valparasio, IN 46383.

[95] E. W. Lee and G. M. Choudhury, J. Less-Common Met. **46**, 305 (1976).

[96] D. H. Shen, Y. Mizokawa, H. Iwasaki, D. F. Shen, T. Numata and S. Nakamura, Jpn. J. of App. Phys. **20**, L757 (1981).

[97] R. B. van Dover, E. M. Gyorgy, R. P. Frankenthal, M. Hong, and D. J. Siconolfi, J. Appl. Phys. **59**, 1291 (1986).

[98] K. H. J. Buschow and P. G. van Engen, Philips J. Res. **39**, 82 (1984).

[99] L. Y. Chen, W. A. McGahan, Z. S. Shan, D. J. Sellmyer, and J. A. Woollam, J. Appl. Phys. 67, 5337 (1990).

[100] L. Y. Chen, W. A. McGahan, Z. S. Shan, D. J. Sellmyer, and J. A. Woollam, J. Appl. Phys. **67**, 7549 (1990).

[101] K. M. Mukimov, Sh. M. Sharipov, and L. A. Ernazarova, Phys. Stat. Sol. (b)**127**, K129 (1985).

[102] W. E. Wallace, *Rare-Earth Intermetallics* (Academic Press, New York 1973).

[103] I. A. Campbell, J. Phys. F **2**, L478 (1991).

[104] M. S. S. Brooks, L. Nordström, and B. Johansson, J. Appl. Phys. **69**, 5683 (1991).

[105] J. P. Liu, F. R. de Boer, P. F. Châtel, R. Coehoorn, K. H. J. Buschow, J. Magn. Magn. Mater. **132**, 159 (1994).

[106] M. Cryot and M. Lavagna, J. de Phys. **40**, 763 (1979).

[107] Sh. M. Sharipov, K. M. Mukimov, L. A. Ernazarova, A. V. Andreyev, and N. V. Kuorevatykh, Phys. Met. Metall. **69**, 50 (1990).

[108] J. P. Petrakian, J. Opt. Soc. Am. **62**, 401 (1972).

[109] J. P. Petrakian, J. Physique **33**, 273 (1972).

[110] B. I. Min, and Y.-R. Jang, J. Phys.: Condens. Matter. **3**, 5131 (1991).

[111] J. F. Herbst, D. N. Lowy, and R. E. Watson, Phys. Rev. B **6**, 1913 (1972).

[112] X. D. Wang, V. P. Antropov, and B. N. Harmon, IEEE Transactions on magnetics **30**, 4458 (1994).

[113] K. H. J. Buschow, Rep. Prog. Phys. **40**, 1179 (1977).

[114] J. A. Cannon, K. Raj, J. I. Budnick, T. J. Burch, and I. Wang, J. Magn. Magn. Mater. **54-57**, 1561 (1986).

[115] K. H. J. Buschow and R. P. van Stapele, J. de Physique **32**, (Supplement C1) C1-672 (1971).

[116] R. Lemaire, and J. Schweizer, Physics Letters **21**, 366 (1966).

[117] M. B. Stearns, in *Numerical Data and Functional Relationships in Science and Technology*, edited by H. P. J. Wijn, Landolt-Börnstein, New Series, Group 3, vol. 19, pt. a (Springer-Verlag, Berlin, 1986); D. Bonnenberg, K. A. Hempel, and H. P. J. Wijn, ibid.

[118] M. Huq, Phys. Stat. Sol. (a) **74**, 667 (1982).

[119] J. L. Erskine, Physica B **89**, 83 (1977).

[120] J. L. Erskine, and E. A. Stern, Phys. Rev. Lett. **30**, 1329 (1973).

[121] Z. Dejuan, W. Zhenxi, X. Kan, and P. Chenhuang, Kexue Tongbao **28**, 1193 (1983).

[122] G. Güntherodt and N. J. Shevchik, in *Magnetism and Magnetic Materials, Proceedings of the 21th Annual Conference on Magnetism and Magnetic Materials*, edited by J. J. Becker, G. H. Lander and J. J. Rhyne, AIP Conf. Proc. No. 29 (AIP, New York, 1976), pp. 174 and 175.

[123] F. Gerken, A. S. Flodström, J. Barth, and C. Kunz, Phys. Scr. **32**, 43 (1985).

[124] H. Tanaka, S. Takayama, and T. Fujiwara, Phys. Rev. B **46**, 7390 (1992).

[125] Sh. M. Sharipov, K. M. Mukimov, and L. A. Ernazarova, Phys. Stat. Sol. (b) **134**, K59 (1986).

[126] R. Allen, and G. A. N. Connel, J. Appl. Phys. 53(3), 2353 (1982).

[127] R. A. Butera, T. J. Clinton, A. G. Moldovan, S. G. Sankar, and K. A. Gschneidner, J. Appl. Phys. **50**, 7492 (1979).

[128] J. K. Lang, Y. Baer, P. A. Cox, J. Phys. F **11**, 121 (1981).

[129] G. A. N. Connell, S. -J. Oh, and R. Allen, J. Non-Cryst. Sol. **61-62**, 1061 (1984).

[130] H. Tanaka, and S. Takayama, J. Appl. Phys. **67**, 5334 (1990).